UNIVERSITY OF BELGRADE

SCHOOL OF ELECTRICAL ENGINEERING

NATHEER AHMED ALWAN

PHASOR ESTIMATION IN RELAY PROTECTION USING MODIFIED COVARIANCE METHOD

-Doctoral Dissertation-

Belgrade, 2026

УНИВЕРЗИТЕТ У БЕОГРАДУ

ЕЛЕКТРОТЕХНИЧКИ ФАКУЛТЕТ

Назир Ахмед Алван

Естимација фазора у релејној заштити коришћењем модификоване коваријантне методе

докторска дисертација

Београд, 2026

ПОДАЦИ О МЕНТОРУ И ЧЛАНОВИМА КОМИСИЈЕ

Ментор:

др Вељко Папић, ванредни професор

Универзитет у Београду, Електротехнички факултет

Чланови комисије:

др Жељко Ђуровић, редовни професор

Универзитет у Београду, Електротехнички факултет

др Жељко Ђуришић, редовни професор

Универзитет у Београду, Електротехнички факултет

др Драган Денић, редовни професор

Универзитет у Нишу, Електронски факултет

Title of doctoral dissertation: PHASOR ESTIMATION IN RELAY PROTECTION USING MODIFIED COVARIANCE METHOD

Abstract:

The reliability of modern power system protection and monitoring depends heavily on the precise estimation of phasors from digitized current and voltage waveforms. However, during fault conditions, these signals are often corrupted by complex transients, including exponentially decaying DC components, harmonic distortion, and interharmonics. Although conventional Discrete Fourier Transform (DFT) methods are extensively utilized, they often have spectrum leakage and resolution constraints when addressing non-periodic components or closely spaced frequencies. This study presents an enhanced filtering architecture known as the Modified Covariance Cleaned Characteristic Harmonic Digital Filter (MC-CCHDF) to address these challenges. The MC-CCHDF framework improves the conventional CCHDF architecture by substituting the standard DFT-based module for interharmonic peak detection with a modified filtering approach that utilizes the high-resolution capabilities of the Modified Covariance Method (MCM) to identify non-harmonic signal components. By integrating this autoregressive estimator into the existing CCHDF structure which relies on BFRP technique for harmonic isolation the system gains the ability to accurately estimate frequency, phase, and magnitude from abbreviated data sets. Comparative analysis reveals that this method significantly outperforms existing techniques in terms of speed and precision, particularly when mitigation the effects of noisy decaying DC offsets in contemporary electrical environments.

Within this thesis, a review of phasor estimation methods for digital protection relays, as well as an analysis of their performance under harsh transient conditions, has been presented. Additionally, the thesis presents an enhanced filtering framework that enables overcoming certain limitations of traditional spectral analysis, such as spectral leakage and low resolution. The newly developed method, which is based on Modified Covariance Method (MCM) integrated into a Cleaned Characteristic Harmonic Digital Filter (CCHDF), can be used to reliable determine the fundamental, harmonic, and interharmonic parameters of electrical signals. Besides that, a more robust approach for handling decaying DC components and frequency instability is proposed. In order to mathematically represent the complex behavior of transient electrical signals, the Biunivocal Frequency of Phasors (BFRP) technique is utilized to isolate directly influences the reliability for protective relaying actions and power system stability. The main hypothesis of the thesis, which the newly developed method is based on, states that high resolution autoregressive spectral estimation techniques can successfully identify non-harmonic components using significantly shorter data widows than conventional Fourier-based method. These parameters are essential indicator for the precise monitoring of modern grids. An auxiliary hypothesis states that replacing traditional windowing and peak-detection blocks with Modified Covariance estimator can overcome the shortcomings caused by interharmonic interference and noise during transient states.

In order to analyze and verify the hypothesis, studies have been conducted using quantitively methods based on comprehensive computer simulations. Using the MATLAB programming language, computer simulations have been conducted in order to analyze the performance of existing phasor estimation algorithms compared to the proposed MC-CCHDF filter. The computer simulation made it possible to study the behavior of the algorithms in different operating conditions, such as frequency deviations, varying levels of harmonic distortion, and the presence of decaying DC offsets. The newly proposed method, which leverages the high-resolution capabilities of the Modified Covariance Method, has also

been developed and tested in MATLAB. Comparative analysis of the existing DFT-based methods and newly developed high-resolution filtering method has been done. On the basis of the simulation data recorded under various transient scenarios, the accuracy and convergence speed of the phasor estimates have been determined.

The results obtained in this thesis are applicable in the power industry, specifically in the development of advanced digital protection relays and monitoring devices. The newly developed algorithm can be easily implemented within a digital signal processor (DSP) or microcontroller to be used in intelligent electronic devices (IEDs) for real-time grid diagnostics. Such a framework would represent a significant advancement in the field and would contribute to the increased reliability of protection systems in the presence of modern, inverter-based energy resources.

Keywords: CCHDF (Cleaned Characteristic Harmonic Digital Filter), Biunivocal Frequency Relationship of Phasors (BFRP), Modified Covariance Method (MCM), MCCCHDF(Modified Covariance CCHDF).

Scientific Field: Electrical Engineering.

Specific Scientific Field: Power System Protection.

Наслов докторске дисертације: Естимација фазора у релејној заштити коришћењем модификоване коваријантне методе

Апстракт:

Поузданост заштите и праћења модерног електроенергетског система у великој мери зависи од прецизне процене фазора из дигитализованих таласних облика струје и напона. Међутим, током кварова, ови сигнали су често загађени сложеним транзијентима, укључујући експоненцијално опадајуће једносмерне компоненте, хармонијска изобличења и интерхармонике. Иако се конвенционалне методе дискретне Фуријеове трансформације (DFT) широко користе, оне често имају ограничења у погледу цурења спектра и резолуције приликом адресирања непериодичних компоненти или блиско распоређених фреквенција. Ова студија представља побољшану архитектуру филтрирања познату као Модификовани коваријантни очишћени хармонијски дигитални филтер (MC-CCHDF) како би се превазишли ови изазови. MC-CCHDF оквир побољшава конвенционалну CCHDF архитектуру заменом стандардног DFT модула за детекцију интерхармонијских пикова приступом модификованог филтрирања који користи високорезолуциону карактеристику Модификоване коваријантне методе (MCM) за идентификацију нехармонијских компоненти сигнала. Интеграцијом овог ауторегресивног естиматора у постојећу CCHDF структуру која се ослања на BFRP технику за хармонијску изолацију, систем добија могућност да прецизно процени фреквенцију, фазу и амплитуду из кратких сетова података. Упоредна анализа открива да ова метода значајно надмашује постојеће технике у погледу брзине и прецизности, посебно када се ублажавају ефекти зашумљених опадајућих једносмерних офсета у савременим електричним мрежама.

У оквиру ове тезе, представљен је преглед метода процене фазора за дигиталне заштитне релеје, као и анализа њихових перформанси у јаким прелазним процесима. Осим тога, теза представља побољшани оквир за филтрирање који омогућава превазилажење одређених ограничења традиционалне спектралне анализе, као што су спектрално цурење и слаба резолуција. Новоразвијена метода, која је заснована на модификованој коваријантној методи (MCM) интегрисаној у хармонијски дигитални филтер очишћених карактеристика (CCHDF), може се користити за поуздано одређивање параметара основног хармоника, виших хармоника и интехрамоника. Поред тога, предложен је робуснији приступ за рад у условима изражених опадајућих једносмерних компонената и фреквенсијске нестабилности. Да би се математички представило сложено понашање прелазних електричних сигнала, користи се техника биунивокалне фреквенције фазора (BFRP) за изоловање директних утицаја на поузданост деловања заштитних релеја и стабилност електроенергетског система. Главна хипотеза ове дисертације, на којој се заснива новоразвијена метода, је да технике ауторегресивне спектралне естимације високе резолуције могу успешно идентификовати нехармонијске компоненте користећи знатно краће секвенце података него конвенционална метода заснована на Фуријеу. Ови параметри су неопходни индикатори за прецизно праћење модерних мрежа. Помоћна хипотеза је да замена традиционалних блокова за прозоровање и детекцију пикова у спектру модификованим коваријантним естиматором може превазићи недостатке изазване интерхармонијском интерференцијом и шумом током прелазних процеса.

Да би се анализирала и верификовала хипотеза, спроведене су студије коришћењем квантитативних метода заснованих на обимним рачунарским симулацијама. Користећи програмски језик MATLAB, спроведене су рачунарске симулације како би се анализирале перформансе постојећих алгоритама за процену фазора у поређењу са предложеним MC-CCHDF филтером. Рачунарска симулација је омогућила проучавање понашања алгоритама у различитим условима рада, као што су девијације учестаности, различити нивои хармонијских изобличења и присуство опадајућих једносмерних офсета. Новопредложена метода, која користи високорезолуциону особину модификовано коваријантне методе, такође је развијена и тестирана у MATLAB-у. Урађена је упоредна анализа постојећих метода заснованих на DFT-у и новоразвијене методе филтрирања високе резолуције. На основу симулација различитих сценарија прелазних процеса, показана је тачност и брзина конвергенције естимације фазора.

Резултати добијени у овој тези применљиви су у електроенергетици, посебно у развоју напредних дигиталних заштитних релеја и уређаја за надзор. Новоразвијени алгоритам може се лако имплементирати у оквиру дигиталног сигналног процесора (DSP) или микроконтролера за употребу у интелигентним електронским уређајима (IED) за дијагностику мреже у реалном времену. Овакав оквир би представљао значајан напредак у овој области и допринео би повећању поузданости система заштите у присуству модерних енергетских извора заснованих на инверторима.

Кључне речи: CCHDF (Хармонијски дигитални филтер очишћених карактеристика), BFRP (Биунивокална фреквенцијска релација фазора), MCM (Модификована коваријантна метода), MC-CCHDF (Модификовани коваријантни CCHDF).

Научна област: Техничке науке - Електротехника

Ужа научна област: Заштита електроенергетских система

First and foremost,

I am extremely grateful to my supervisor, Dr. Veljko Papić (assistant professor) for his continuous support, invaluable suggestions and patience during all the period of my study especially during preparing my Ph.D. thesis.

To my parents and family, every page of this work carries the weight of your sacrifices and the strength of your love. You gave up your comforts so I could chase my dreams, worked tirelessly so I could rest easy, and believed in me even when I doubted myself. This achievement is not mine alone, it belongs to every meal shared around our table, every word of encouragement when the road felt impossible, every silent prayer you whispered for my success. You taught me that love is not just spoken but lived through sacrifice, and that a family's greatest gift is the foundation they build beneath their children's feet.

To my parents, You are the roots that kept me grounded and the wings that helped me soar. Everything I am, everything I will become, begins and ends with you. This is as much yours as it is mine. With all my love and gratitude.

NATHEER

Table of Contents

List of Figures

List of Tables

Chapter 1

Introduction

Introduction

Accurate phasor estimation is essential for electrical power system monitoring and protection. To identify, categories, and isolate errors in real time, digital protection relays and phasor measurement units (PMUs) need accurate voltage and current signal phase and magnitude information. The Discrete Fourier Transform (DFT) provides effective results for sinusoidal signals in steady-state conditions and has traditionally been the basis for phasor estimation. Power system waveforms are increasingly affected by noise, decaying DC components, harmonics, and interharmonics due to the growing integration of power electronic converters, distributed generation, and nonlinear loads. The escalating complexity of modern power systems has rendered conventional spectral analysis techniques, most notably the Discrete Fourier Transform(DFT) and its derivatives, increasingly in adequate. Under transient conditions, these traditional methods often produce significant estimation errors that can compromise the operational integrity of protection systems.

In contemporary electrical networks, the distinction between harmonics and interharmonics is fundamental to understanding signal degradation. While harmonic components are integer multiples of the fundamental frequency typically generated by nonlinear loads interharmonics represent non integer components arising from the proliferation of inverter based renewable energy sources, arc furnaces, and microgrid interconnections. The presence of non-periodic components results in considerable spectral leakage and distortion of the signal. The phenomena negatively affect the accuracy of phasor estimation, which may lead to relay mal-operation, unintended tripping, or delayed fault clearance, thus threatening grid stability.

In recent decades, numerous strategies have been formulated to tackle these challenges, such as least squares estimation, mimic filters, wavelet-based decompositions, and artificial intelligence models. Although these methodologies offer incremental improvements, a complete solution remains elusive for signals that exhibit both harmonic and interharmonic components in noisy environments. Wavelet techniques provide enhanced time-frequency localization; nonetheless, they often involve considerable computational expenses. Likewise, least squares methods, while exhibiting high precision, often demonstrate insufficient numerical efficiency for real-time relaying applications. Moreover, numerous current frameworks concentrate solely on harmonic suppression, neglecting to sufficiently consider the increasing influence of interharmonics in inverter-dominated networks.

The inherent limitations of traditional approaches have necessitated the development of more robust signal decomposition techniques. Recent advancements in the field, as demonstrated by the Cleaned Characteristic Harmonic Digital Filter (CCHDF), have introduced methods that employ sliding filtering and auxiliary signal generation to effectively isolate harmonic and interharmonic phasors.

While these advancements align with international standard such as IEC 61000-4-7 and exhibit resilience against decaying DC offsets, critical obstacles remain. Specifically, there is a persistent need to minimize response times for real-time implementation and enhance accuracy within the highly volatile environment of modern microgrids.

The accurate estimation of harmonic and interharmonic phasors is a crucial aspect of research in power system protection. Accurate signal parameterization is essential for maintaining relay security and facilitating effective wide-area monitoring and fault localization. This thesis presents a filtering framework that is adaptive and computationally efficient, aimed at addressing current technical deficiencies. This study aims to combine theoretical developments in signal processing with the practical

constraints of digital protection, thereby creating a robust basis for future intelligent protective relaying systems.

Literature Review

Digital numerical relays are used in the current protection and surveillance system of an EPS (Electrical Power System). These relays do their jobs by using an internal calculation process with network electrical signal phasors that have been properly processed and digitized (ADC, anti-aliasing filter, etc.). We can get phasors of real frequencies (usually the fundamental) by using digital processing to figure out the harmonic spectrum of the signal you are looking at. A DSP (Digital Signal Processor) does the math and logic needed for phasor estimation in digital processing. It uses special logical-mathematical algorithms that are often called digital filters.

Digital signal processing is how numerical relays function with the settings of an electrical network. This is a key element of how we keep our electrical systems safe to-day. Instead of conventional electromechanical and static relays, these smart electronic devices today use microprocessor-based systems that can undertake com-plicated computational analysis [1]. We now keep things safe in a different way. The main job of these devices is to get phasor data from digital waveforms of voltage and current. Then, algorithms use this information to figure out how to keep something safe.

When one convert from analogue to digital protection systems, you have new issues and new opportunity. Digital relays offer enhanced functionality, increased accuracy, and the capability to perform multiple tasks simultaneously. However, they must also contend with complex signal conditions that may reduce their effectiveness. The fundamental aspect of protective relay operation involves the analysis of phasors, which serve as mathematical representations indicating the magnitude and phase of sinusoidal quantities. Under fault conditions, electrical signals exhibit considerable deviation from ideal sinusoidal characteristics. Multiple components simultaneously alter the waveform, complicating estimation efforts.

Power system failures disrupt steady-state conditions, resulting in transient DC components that diminish over time. The time constant, which indicates the rate of decay, is contingent upon the system's reactance-to-resistance (X/R) ratio. Circuits characterized by high inductance exhibit slower decay rates. This characteristic raises concerns, as traditional Discrete Fourier Transform (DFT) algorithms rely on the assumption of periodic signals and demonstrate suboptimal performance when non-periodic components are present[3]. Harmonic distortion arises from the introduction of harmonic frequencies into the power system, primarily due to nonlinear loads, power electronic converters like inverters, and circuits that demonstrate magnetic saturation. Harmonics, defined as integer multiples of the fundamental frequency, can substantially influence phase estimation if not properly filtered. The growing adoption of renewable energy systems, which depend significantly on inverter-based interfaces, has resulted in an increase in distortions in modern electrical networks[4].

Interharmonic frequencies are distinct from harmonics as they do not represent whole number multiples of the fundamental frequency. The components derive from various sources, such as arc furnaces, rotating frequency converters, wind turbines, and asynchronous switching operations in high-power electronic devices. Frequency-domain analysis reveals that interharmonics induce "spectral leakage," complicating the accurate estimation of both fundamental and harmonic components[5].

Factors such as Electromagnetic Interference (EMI), sensor imprecision, and quantization errors occurring during the Analog-to-Digital (A/D) conversion process contribute to the complexity and ambiguity of the signal processing chain[6]. Protection systems must operate rapidly due to stringent time constraints. To maintain stability in the power system and prevent equipment damage, it is essential to detect, classify, and isolate faults within stringent time constraints, typically measured in cycles or milliseconds. Because of this time pressure, we need to use "algorithms that converge quickly" without losing accuracy. This makes it hard to find the right "balance between speed and precision". When there

are high-magnitude fault currents, Current Transformers (CTs) are likely to reach a state of saturation. This saturation causes severely distorted secondary currents, which have both harmonic content and extra exponential components. The saturation effect induces complex, non-linear distortions, complicating the efficacy of traditional filtering methods [6]. The absence of specific features in the digital filter necessary for optimal device functionality will result in the failure of the protection and/or surveillance equipment to meet established standards. For the filtering algorithm to function effectively, it must possess several characteristics that align it with the ideal digital filter.

The digital filter must provide parameters for protection and fault location functions that are entirely accurate and reliable. The calculations must be performed expeditiously to ensure the relay's prompt response. It should not depend on the fault moment, and there should be no additional unknowns in the equations utilized for calculation. It must operate correctly before, during, and after the fault.

Various strategies have been proposed by researchers over the years to improve the reliability of phasor estimation in adverse conditions. Some focus on identifying and categorizing faults [2]. This field encompasses various methodologies, including: Matrix-Based Least-Squares: Certain methods employ least-squares estimation (LSE) to determine unknown phasor parameters by formulating the signal model as a system of linear equations [7–8].These methods are mathematically sound, but they often have problems with numerical stability because of ill-conditioned matrices, especially when the decaying DC time constant is unknown or when noise is present. Mimic filters work like analog circuits that get rid of the decaying DC component before using DFT-based phasor extraction [9]. Their performance is contingent upon prior knowledge of system parameters (e.g., time constant τ), which is seldom accessible during unpredictable fault conditions, despite being effective in idealized scenarios. Changed DFT Algorithms: There have been a number of improvements to the standard DFT, such as offset compensation using extra samples or recursive formulations [10–12]. These do help with DC-induced errors, but they also make things more sensitive to noise and need very precise timing for faults to start, which makes them less useful in real-world relaying situations [13]. Methods Based on Wavelet Transform: The Discrete Wavelet Transform (DWT), especially through multiresolution analysis (MRA), gives time–frequency localization that is helpful for transient analysis [14–16]. Wavelet-based estimators, on the other hand, usually need longer data windows and more processing power, which makes them less useful for protection schemes that work quickly and only last a few post-fault cycles.

Researchers have looked into using ANNs for fault detection and classification [17,18], but they haven't been used much for precise phasor estimation yet. They can't be used in adaptive protection systems because they need a lot of training data and can't work with different grid topologies and fault types. Mixed methods have been explored by researchers who combine techniques such as wavelet-ANN and LSE-DFT hybrids to leverage their distinct advantages [19–23]. Many of these methods exhibit insufficient robustness in managing interharmonics and do not deliver accurate magnitude and phase information when faced with noisy transients.

Different Approaches to Signal Processing Emerging techniques that employ mathematical morphology or iterative computational schemes demonstrate potential; however, they are still experimental and have not undergone extensive evaluation in real-time relay contexts. The current literature insufficiently addresses interharmonic and subharmonic components, which are non-integer multiples of the fundamental frequency produced by power electronics, variable-speed drives, and other nonlinear loads [27].Many phasor estimation algorithms operate under the assumption that signals consist solely of harmonics and DC transients, despite the increasing prevalence of such conditions as acknowledged by standards such as IEC 61000-4-7. Spectral leakage from interharmonics adversely affects the precision of DFT-based estimates, which may result in failures of protection systems [28].

Recent studies on the identification of interharmonics using adaptive windowing [29], iterative DFT [30], or adaptive notch filters [31] frequently necessitate the collection of 10 or more cycles of data, which surpasses the typical fault-clearing window in transmission systems. This renders them inadequate for real-time protection. Vazquez et al. [32] devised a filter utilizing a sliding technique to remove decaying DC components while maintaining harmonic information. Nonetheless, it is still vulnerable to interharmonic distortion. The C-CharmDF method improves this framework by explicitly modeling and extracting interharmonics, facilitating the recovery of clean harmonic phasors even under highly transient conditions.

The dissertation is divided into seven chapters that progress the research from theoretical foundations to methodological innovation and performance validation. The first chapter discusses the study challenge, aims, and assumptions, as well as a review of existing phasor estimating strategies for protective relays. Chapter 2 describes the architecture of digital protection systems, covering signal collecting, sampling, and digital processing. Chapter 3 discusses the theoretical concepts of phasor estimation, with a focus on the Discrete Fourier Transform and its limitations in transient and off-nominal scenarios. Chapter 4 examines spectrum estimation approaches, with a focus on high-resolution parametric techniques and the Modified Covariance Method. Chapter 5 presents the proposed Modified Covariance Cleaned Characteristic Harmonic Digital Filter (MC-CCHDF) and its mathematical formulation. Chapter 6 assesses the suggested strategy using simulated studies and a comparative performance study with standard accuracy indices. Finally, Chapter 7 summarizes the key findings and discusses their practical consequences.

Chapter 2

Architecture and Signal Processing of Digital Protection Relays

2.1 Architecture and Signal Processing of Digital Protection Relays

The transition from electromechanical devices to sophisticated digital systems in power system protection represents a significant technological leap within the field of electrical engineering. Early protection schemes relied on mechanical elements, magnetic circuits, and analogue electronics to detect system anomalies and initiate remedial actions. While these systems demonstrated dependable performance over extended periods, they were inherently constrained by limitations in precision, versatility, and their capacity to accommodate intricate operational contexts. The advent of microprocessor technology during the 1970s and 1980s, however, opened up new avenues for the development of protection systems.

Digital relays represent sophisticated instruments capable of simultaneously performing multiple protection functions, alongside offering enhanced monitoring, communication, and diagnostic capabilities. Unlike their analogue counterparts, digital relays possess the capacity to execute intricate algorithms, store historical data, and adapt their operational parameters to fluctuating system states. This technological advancement has been driven by several key factors, including the increasing intricacy of power systems, the imperative for faster fault-clearing procedures, the need for heightened reliability and selectivity, and the desire for improved system monitoring functionalities. Modern digital relays are a product of the convergence of developments in signal processing, computer science, and power system engineering [1].

2.2 Core Structure of Digital Protection Relays

Numerical relays, which incorporate computer components, employ digital techniques to acquire current and voltage data from power systems through current transformers (CT) and potential transformers (PT). These data, known as analogue inputs, are processed to ascertain the appropriate action for the associated circuit breaker, specifically whether to initiate a trip. The online computational element is typically a high-speed microprocessor or digital signal processor (DSP). The entire sequence, from data acquisition to the final decision, is completed within approximately 20 milliseconds, equivalent to one cycle. The relay's operation is governed by integrated software, which incorporates the parameters defined by the relay's tripping logic. Furthermore, these settings are adjustable via communication interfaces, including local, remote, or HMI (Human Machine Interface) channels[1].

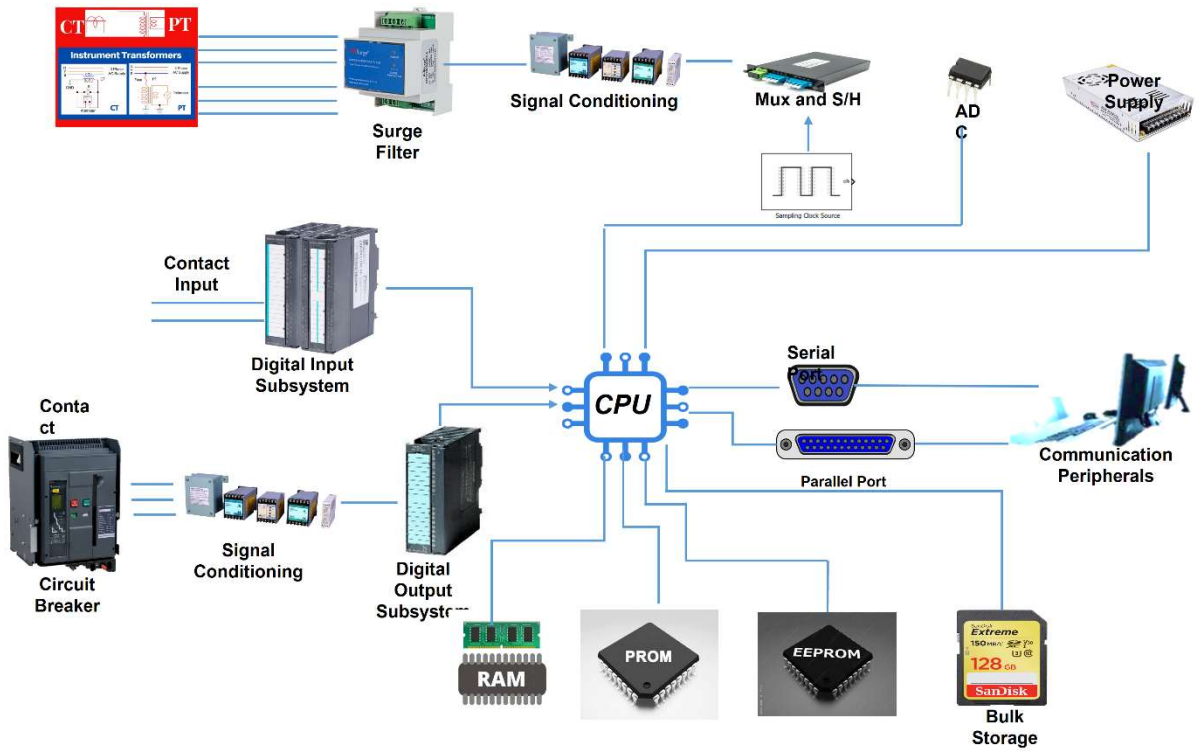

Fig. 2.1 *Numerical Relay internal architecture*

Figure 2.1 presents a block diagram depicting the internal architecture of a numerical relay. The components constituting a numerical relay are categorized as follows:

1) **Analogue Input Subsystem:** This subsystem acquires analogue signals, including currents and voltages, directly from the substation's switchyard. These analogue signals undergo multiplexing, sampling, and conversion into digital signals. This process, known as discretization, is a fundamental operation in digital signal processing. Furthermore, surge filters are employed to protect the low-voltage digital components from voltage spikes. Signal conditioning is essential for adjusting and aligning voltage levels to match the input range of an analog-to-digital converter (ADC). An analog low-pass filter is also required to reduce higher, unwanted frequency components, thereby preventing aliasing.
2) **Digital Input Subsystem:** Digital Input Subsystem Digital input encompasses the status of supplementary relays and the circuit breaker (open or closed) within the relevant network.
3) **Central Processing Unit:** Central Processing Unit Historically, high-speed microprocessors and microcontrollers were frequently used. Presently, digital signal processors (DSPs) are integrated into numerical relays, offering greater speed compared to microcontrollers. Earlier, DSPs utilized specialized multiplication hardware and instructions to enable rapid multiplications, and they incorporated additional hardware, such as large accumulator registers, to improve numerical accuracy. Contemporary standard DSPs now operate at clock rates ranging from 50 MHz to 100 MHz, with the most recent DSPs exceeding 200MHz. Certain sophisticated DSP processors incorporate dual multiplication units, thereby facilitating the execution of two instructions per cycle. Consequently, at a frequency of 200MHz, each instruction pair requires only 5 ns.

4) **Storage of Data and Programs:** The Random-Access Memory (RAM) of a computer is responsible for storing the sampled data acquired from the input system. Furthermore, it acts as a buffer for additional samples, accommodating scenarios where the relaying algorithm necessitates extended processing time. Beyond this, the RAM functions as a data scratch pad, providing temporary storage during the execution of filtering and relay algorithms. The program itself is permanently stored in Read-Only Memory (ROM).The relay logic and the monitoring program, which facilitate user and operator interaction, are stored in ROM. EEPROM (Electrically Erasable Programmable Read-Only Memory) is employed to store parameters that require periodic updates, including relay configurations; however, Flash memory has become more prevalent in this application. Archiving old data files necessitates substantial storage capacity. This capacity is used to store time-stamped event data, fault-related data tables, and documentation of significant transient events within the power system. The digital filter program is essential for all relaying applications, processing data samples obtained from the RAM. Subsequently, the techniques for phasor extraction are addressed.
5) **Digital Output System:** This subsystem provides trip signals, alert notifications, and control signals to the external system.
6) **Power Supply:** The relay must remain functional even in the absence of station power supply. Consequently, a continuous direct current supply is delivered to the numerical relay using battery-charger units.
7) **Communication Devices and Protocols:** The communication facility is equipped with multiple ports, including RS 232/485 and RJ 45. Communication between the numerical relay and a personal computer can be made using Ethernet and fiber optic lines. A defined collection of communication regulations is referred to as a protocol. Every relay manufacturer possesses proprietary protocols for communication with their relays. Communication protocols vary across relays from the same manufacturers across different platforms, such as SPA, Modbus, Profibus, LON, and the IEC 60870 series. Patented communication methods do not pose an issue, as individual communication remains feasible. However, with the contemporary notion of substation integration and automation (i.e., SCADA and EMS), the interoperability of relays utilizing a standard communication protocol must be achieved. In these systems, all relays within the substation are interconnected over a shared network for both substation-level operations and distant communication. A standardized communication protocol, IEC 61850, has been established to address this requirement.

Inputs may include CT, PT, external contacts, etc., whilst outputs will consist of contacts utilized for various executions. Each organization possesses own software for relay configuration, LED assignment, and related tasks. Human-Machine Interface (HMI) Certain primary data may be accessible on the unit's local display, specifically via a menu on a personal computer. The data will include service values, fault current and voltage before and during the fault, relay operation time, fault distance, impacted phase indicators and tripping, carrier inter-trip, and carrier signal transmission and reception. Conveyance of information The relay is operated by the PC via software specific to the relay's manufacturer. The relay can be established, configured, and monitored via a PC, and the saved data can be retrieved for analysis on the PC. The Disturbance Recorder (DR) relay has the ability to store both events and disturbances. It can capture voltage and current waveforms for each phase, including the neutral phase. The relay carefully records the duration of its decisions, operational time, tripping time, and carrier transmission/reception. This feature is useful for analysis, potentially helping to improve coordination equipment if needed. Logic Charts can be created within the relay to assign specific functions in addition to the relay's existing functions. Moreover, the numerical relays include metering capabilities, such as maximum and minimum recordings. Group Configurations Typically, four groups of configuration

variables can be retained, with any one being activated. The current collection of active groups is accessible in the menu.

2.3 DIGITAL SIGNAL PROCESSING(DSP)

A solid understanding of numerical relaying requires a strong grasp of the theoretical principles behind digital signal processing. Typically, undergraduate electrical engineering programs include a separate course on digital signal processing. However, this discussion will examine these concepts to provide a thorough understanding of the subject. Figure 2.2 provides a block diagram of digital signal processing. The following sections will explain the different components and elements involved in digital signal processing.

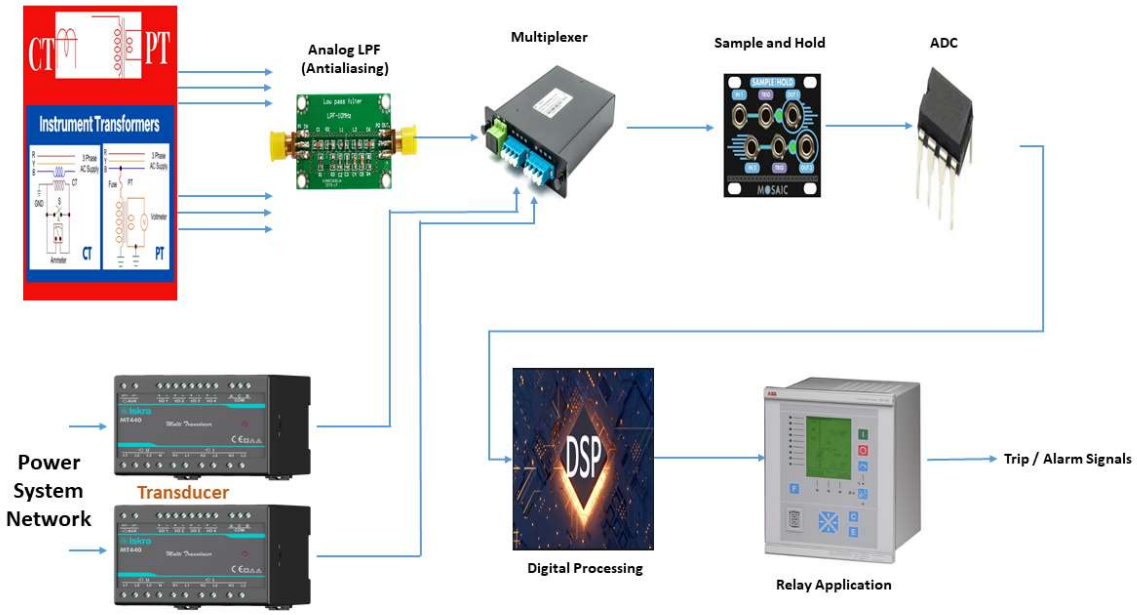

Fig. 2.2 *Block diagram of DSP*

2.3.1 Signal Acquisition Subsystem

Figure 2.2 shows the main parts of a data acquisition system. Current and potential transformers serve two main purposes. First, they reduce voltage levels so they can be handled by the digital subsystem. Second, they provide electrical isolation between the power circuit and the measurement and protection devices. These reduced analog signals must be changed into voltage signals suitable for digital conversion. The voltage across a resistor connected to the secondary of a current transformer provides

current to the numerical relay. In addition, a resistive voltage divider connected to the P.T.'s secondary produces the required voltage output.

Transducers are used to convert electrical and thermal signals into corresponding direct current (DC) analog values. The numerical relay receives digital inputs, usually contact statuses from other relays or circuit breakers. When digital inputs come from yard contacts, surge filtering and/or optical isolation are essential to protect the numerical relay from transient surges. These surges can occur on wiring connected to relays, including those for power supply, analog, and digital inputs. Industry standards define the requirements for surge filtering. The IEEE standard C 37.90a, often called the SWC standard, describes the surge wave as follows:

- Oscillatory wave at 1–1.5 MHz, 2.5–3 kV, with a decline to half value exceeding 6ms.
- Unidirectional (Fast Transient) 4 – 5 kV, rising duration under 10ms, decline to half value within 100 – 200ms.

Figure 2.1 shows surge filters designed for analog signals. These surges can be caused by faults and switching actions within the electrical system or the control room. To reduce these surges, it's important to carefully ground and shield leads and equipment, along with using low-pass filtering. Surge filters, which are a type of low-pass filter, have cutoff frequencies in the hundreds of kilohertz. They don't affect the transmission of input signals. In some designs, nonlinear energy-absorbing Metal Oxide Varistors (MOVs) can be used with low-pass filters.

2.3.2 Implementation of Sample-and-Hold Circuit (S/H)

The sampling-and-hold circuit is an analogue circuit that functions as a voltage memory device. The analogue input voltage is captured and retained on a high-quality capacitor , which has low leakage and low dielectric absorption properties. An electronic switch is linked to the hold capacitor. OPAMP-1 is an input buffer amplifier with high input impedance. OPAMP-2 is the output amplifier It stabilizes the voltage on the hold capacitor. Figure 2.3 presents a simplified representation of the sample-and-hold mechanism.

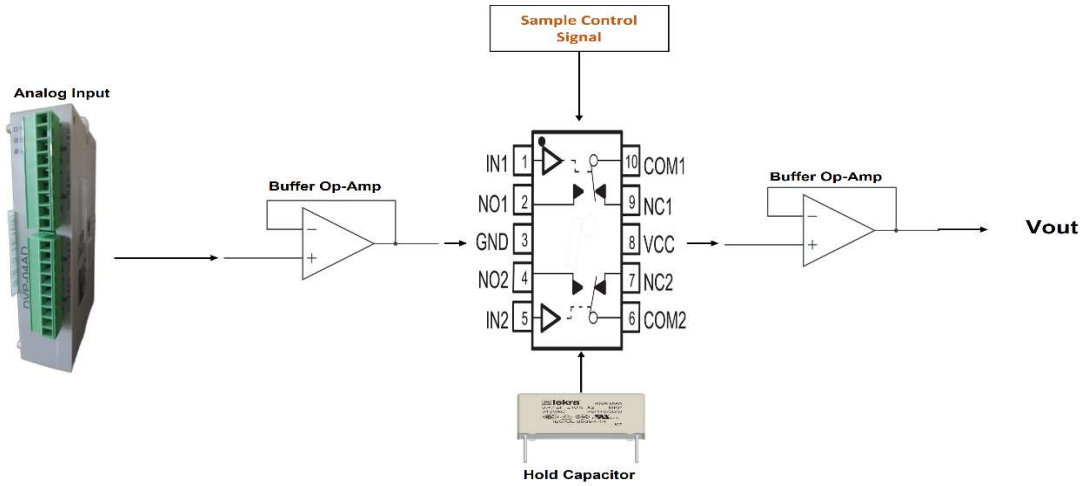

Fig. 2.3 *S/Hf circuit*

Two sampling strategies are available: Non-simultaneous sampling, Simultaneous sampling. In a relaying application, it is typically necessary to acquire the three-phase currents and three-phase voltages. The magnitude and phase of each signal are significant; therefore, all signals must be sampled simultaneously. Therefore, a synchronous sampling strategy is favored. Figure 2.4 illustrates a synchronous sampling methodology.

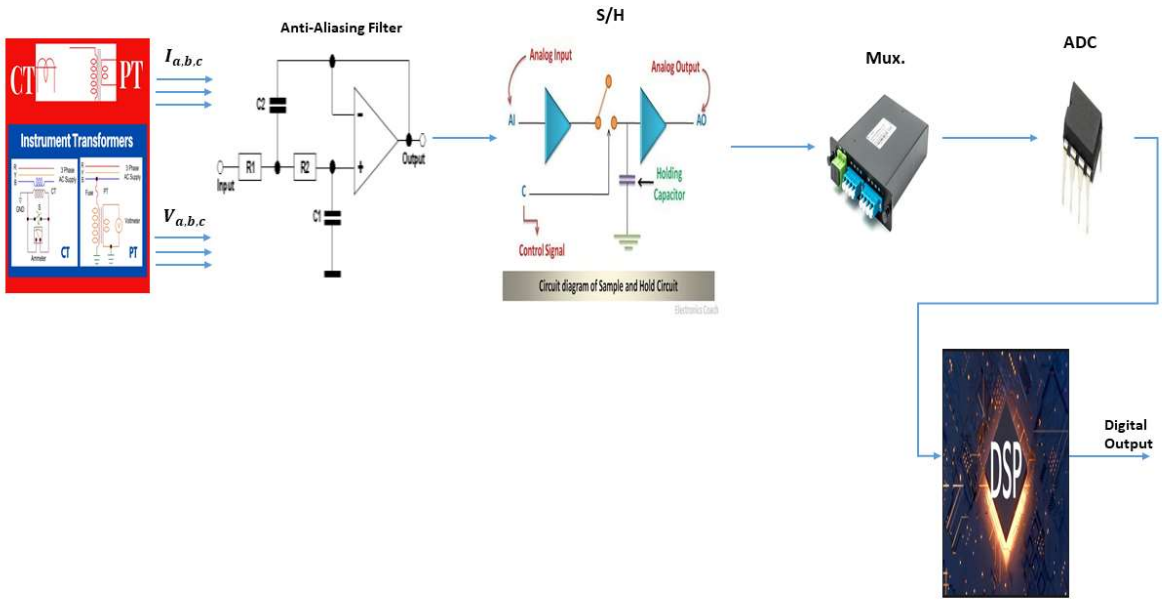

Fig. 2.4 *Simultaneous sampling scheme with single ADC*

All input analogue signals are sampled simultaneously. The multiplexer sequentially processes various signals, while the ADC interface is managed through appropriate programming. Currently, multichannel ADCs with concurrent sampling are accessible. The sample-and-hold and multiplexer functions are integrated within the ADC. Typically, successive approximation type ADCs with conversion times between 15 and 30ms are employed for relaying applications. The interval between two sampling moments must account for the ADC's conversion time and permit the processor to retrieve the digital value from the input buffer RAM. The sampling rate must satisfy the Nyquist criterion. Discretization presents specific challenges, which can be addressed as detailed below.

2.3.3 Anti-Aliasing Filters

Anti-aliasing filters (AAFs) are used before sampling to strictly limit the bandwidth of the input signal. Acting as a low-pass filter, the AAF requires software adjustments, such as algorithmic correction or compensation, due to its magnitude scaling and phase shifting properties. The AAF's cut-off frequency, denoted as f1, is determined by the algorithm's specifications, which are designed to protect specific equipment. Figure 2.5 shows how an AAF works. It removes high-frequency noise and unwanted

signals, thus preventing aliasing during sampling. As shown in Fig. 2.5, the frequency domain after sampling reveals repeating spectra, which are essentially pseudo-spectra.

These spectrums experience a shift by f_s Hz. The aliasing phenomenon, as previously noted, obfuscates the distinction between the original signal lobe and its replicated counterparts. A separation between these spectrums is therefore essential. This divergence stems from the condition $f_s > 2f_1$. If f_s is precisely $2f_1$, an interval will be absent, thereby enabling clear demarcation. Conversely, if f_s equals $2f_1$, overlap will ensue, rendering demarcation difficult. Digital filtering algorithms are subsequently utilized within the processor to remove these pseudo-spectrums.

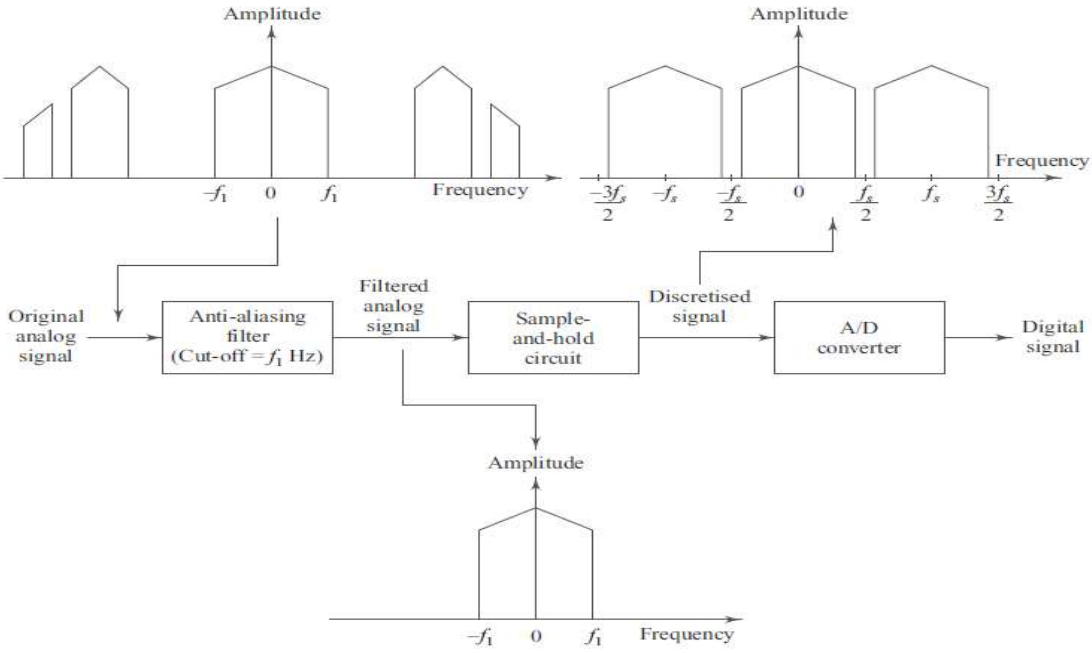

Fig. 2.5 *Anti-aliasing filtering prior to sampling at a rate of* f_s *Hz*

2.3.4 Process of Analog-to-Digital Conversion

Analogue-to-digital conversion (ADC) is the process of transforming a continuous-time analogue signal into its equivalent digital representation for subsequent processing or control. Several ADC techniques exist, including successive approximation, flash, dual-slope, and counter-based methods. A basic counter-type conversion scheme is shown in Fig. 2.6 (Kester, 2005; Franco, 2015). In this method, the analogue input is connected to the non-inverting (+) terminal of an operational amplifier, which acts as a comparator. The comparator's output then controls an up/down counter. The counter counts up when the control line is high and counts down when the control line is low. It receives a continuous stream of pulses from a clock source. As the counter's value changes, it triggers a digital-to-analog converter (DAC), which then produces a feedback voltage. The comparator constantly checks the difference between the analog input and the DAC feedback signal. When the comparator finds that the feedback matches the input, indicated by a change in the comparator's output, the counter stops adjusting. At this point, the counter's value represents the stable digital version of the analog input. This simple counter-

based ADC is conceptually important because it illustrates the basic closed-loop operation found in many ADC systems, even though it's slower than other practical designs like successive approximation or sigma-delta converters.

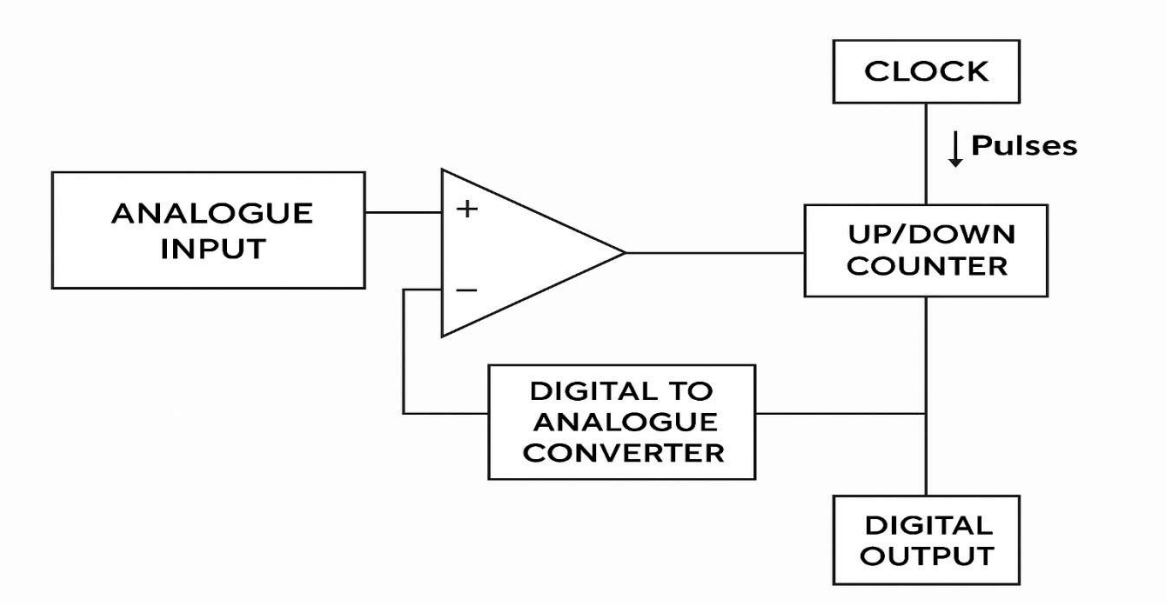

Fig. 2.6 *ADC circuit*

The sample-and-hold circuit operates by capturing instantaneous signal values at specific intervals, dictated by the sampling clock. To prevent aliasing, the sampling frequency must, in accordance with the Nyquist-Shannon sampling theorem, be at least twice the highest frequency component present in the signal. Moreover, the quantization process converts continuous amplitude values into discrete levels, which are determined by the resolution of the analog-to-digital converter. Contemporary protection relays typically employ analog-to-digital converters (ADCs) with resolutions ranging from 12 to 16 bits. Consequently, this provides a resolution capable of representing between 4096 and 65536 distinct levels. Binary encoding transforms quantized amplitude levels into digital representations appropriate for computer processing. The encoding scheme defines the representation of analogue values in the digital domain and influences subsequent computational processes.

2.3.5 Process of Digital -to- Analog Conversion

A key procedure in contemporary electronics is digital-to-analog conversion, which converts discrete digital signals into continuous analogue waveforms. Applications like music playback, video display, and control systems are made possible by this conversion, which is necessary for connecting digital and analogue systems.

A digital input, usually a binary integer that stands for a discrete amplitude value, starts the DAC process. This digital word goes into the DAC circuit, where it goes through a number of steps. A basic counter-type conversion scheme is illustrated in Fig. 2.7. First, the binary input is decoded and given a weight based on how important each bit is. For example, in a weighted resistor DAC, each bit controls a switch that is connected to a network of resistors with binary-weighted values (R, 2R, 4R, 8R, etc.).

When a bit is "1," the switch that goes with it closes, letting current flow via that branch. An operational amplifier in a summing setup is usually used to add up the weighted currents from all the active bits at a common node. After that, this summed current is turned into a voltage output, which makes a stepped version of the intended analogue signal. The number of bits (n) in the DAC's resolution determines how many discrete levels it can show. This is equal to 2^n potential values.

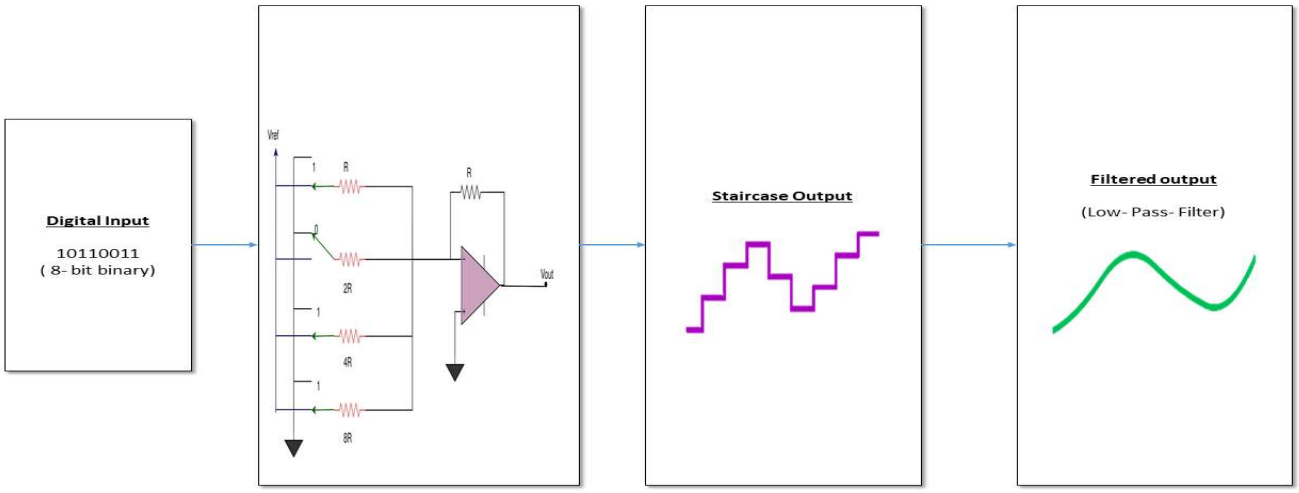

Fig. 2.7 *DAC circuit*

The raw DAC output makes a staircase waveform that is close to the desired analogue signal. A reconstruction filter, which is usually a low-pass filter, is used to turn this stepped output into a continuous waveform. This filter gets rid of high-frequency parts and sampling artefacts, leaving a clean analogue stream. The Nyquist-Shannon sampling theorem says that the sampling frequency must be at least twice the highest frequency component in the analogue signal to avoid aliasing and make sure that the signal can be accurately reconstructed[33-35].

Chapter 3

Digital Filters in Contemporary Protection Relay Algorithms

3.1 Digital Filters in Contemporary Protection Relay Algorithms

The shift from electromechanical and solid-state devices to microprocessor-based protective relays marked a fundamental change in power system protection philosophy. These modern relays function as intelligent analyzers that execute sophisticated numerical computation. At their core, they depend on processing digitized measurements of system quantities primarily voltage and current waveforms to drive critical operational parameters. However, acquired digital samples inevitably contain disturbances such as electrical noise, harmonic distortion, and transient phenomena generated by circuit breaker operations, fault initiation, and the behavior nonlinear loads. Consequently, digital filtering is not merely a supplementary feature but an indispensable requirement for dependable relay performance. These filters serve to condition input signals by attenuating undesired frequency components, thereby allowing protection algorithms to reliably determine fundamental system characteristics including magnitude, phase angle, and frequency. This discussion presents the fundamental purpose of digital filtering techniques, examines prevalent algorithmic approaches for their implementation, and evaluates the application within specific protective relay functions [36].

3.2 The Importance of Signal Conditioning in Relaying

The accuracy and dependability of protective relay operation are fundamentally governed by the integrity of measured input signals. When system faults occur, the secondary outputs from instrument transformers both current and voltage types contain numerous extraneous components that can mask the primary power system frequency component (50 or 60Hz). The contaminating signal components include:

- Aperiodic DC offset with exponentially decay characteristics: this phenomenon results from instantaneous changes in current waveforms when faults are initiated, often leading to magnetic saturation in current transformer cores and resulting waveform deformation.
- Elevated frequency disturbances: Generated by electromagnetic transients propagating through transmission lines and by breaker switching operations.
- Distortion at harmonic frequencies (multiples of fundamental frequency): these originate from nonlinear operating characteristics of power electronic equipment and the saturation behavior of transformer magnetic circuits.

In the absence of effective signal conditioning, these unwanted frequency components cause considerable errors when determining the fundamental frequency phasor quantities, potentially resulting in relay malfunction either spurious operation due to oversensitivity of failure to respond to actual fault conditions due to inadequate sensitivity. Digital filtering techniques serve the essential purpose of attenuating these undesired frequency-domain elements thus yielding a refined fundamental frequency signal for downstream processing algorithms that preform protective action determination. Figure 3.1 presents the complete signal conditioning framework.

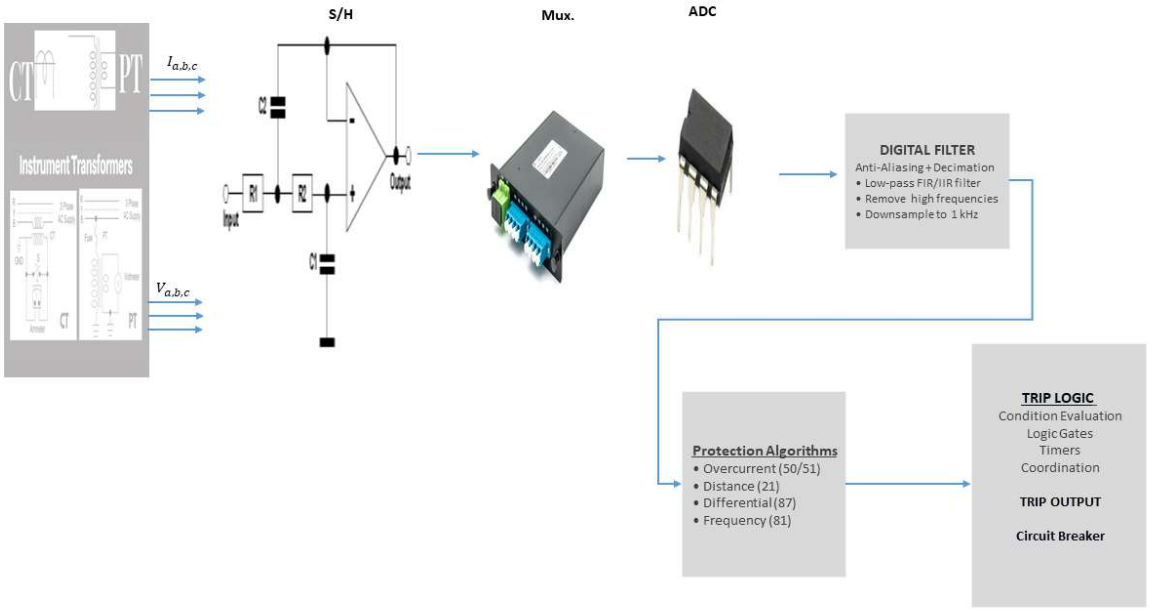

Fig. 3.1 *The complete signal conditioning frameworks.*

3.3 Theoretical foundations of Phasor Estimation Computation

Protective relays employ various protection algorithms tailored to detected and respond to distinct frequency characteristics (base frequency and/or harmonic components) present in their measured input quantities. The majority of protection functions operate based on fundamental frequency measurements(such as overcurrent, undervoltage, and impedance-based elements), while certain specialized functions depend on specific harmonic frequency analysis(for instance, second harmonic detection for discriminating transformer magnetizing inrush currents, third harmonic monitoring for generator stator earth fault identification, or broadband harmonic assessment for equipment thermal overload protection). Clearly, the precision of these measurements is critical, as protection algorithm rely on this data to distinguish between acceptable system operating conditions and abnormal fault scenarios. When system faults occur, especially those involving bolted or low- impedance short circuits, the pure sinusoidal character of the fundamental frequency waveform becomes degraded by non-periodic DC offset components, spectral distortion from harmonics, and high-frequency transient disturbances. Consequently, protective relays systemically employ signal conditioning technique to improve measurement precision and prevent corruption of critical information by these unwanted signal constituents these filtering strategies are designed to retain the frequency components of interest while attenuating undesired elements.

Following appropriate signal filtering, digital relay conventionally calculate phasor representations complex quantities that have remained the predominant analytical tool in power system protection. The phasor concept, introduced by Charles Proteus Steinmetz in 1893 [37], represents a sinusoidal quantity as a complex number encoding both magnitude and angular phase, applicable when the waveform's

amplitude, frequency, and phase remain constant over time. According to this mathematical framework, a sinusoidal signal:

$$x(t) = X_m \cos(\omega t + \varphi) \tag{3.1}$$

In this expression X_m denotes the peak value of the signal $x(t)$. Angular frequency is defined as $\omega = 2\pi f$, with f indicating the frequency in hertz. The phase angle at initial time zero $x(t)$ expressed by:

$$x(t) = \Re\{X_m e^{j(\omega t+\varphi)}\} = \Re\{e^{j\omega t} X_m e^{\varphi}\} = \Re\{X_m e^{\varphi}\} \tag{3.2}$$

The Root Mean Square (RMS) quantities play a fundamental role in the evaluation of electrical power and energy transfer. Its corresponding phasor representation $\bar{X}$ for a time-domain signal x(t) is defined as follows:

$$\bar{X} = \frac{X_m}{\sqrt{2}} e^{j\varphi} \tag{3.3}$$

Phasor theory remains valid for any constant frequency component, making it particularly advantageous in digital relay applications where analysis spans both the fundamental frequency and associated harmonic orders. Digital protective devices routinely calculate phasor quantities to support most of their protective functions. Signal filtering and phasor determination can be combined into a unified computational process, enabling simultaneous execution of these operations. This combined approach is termed the phasor extraction algorithm. Phasor extraction algorithms are assessed based on several performance criteria, including:

- Capability to attenuate frequency content at integer multiples of fundamental.
- rejection non-fundamental frequency elements.
- Tolerance to variations in power system frequency.
- Robustness against measurement noise.
- Suppression of aperiodic DC offset contributions.
- Swift computational execution to satisfy protection system timing constraints .
- Robust transient response characteristics during sudden signal discontinuities.
- Minimal computational burden to optimize processor utilization.

An ideal phasor extraction method satisfying all these performance metrics simultaneously does not exist in practice. Selection of an appropriate algorithm typically balancing competing objectives: relay operating speed, operational dependability, and measurement accuracy. In contemporary commercial relay designs, phasor calculation predominantly employs Discrete Fourier Transform methodology.

3.4 The Discrete Fourier Transform

The French mathematician and physicist Jean Baptiste Joseph Fourier delivered his treatise on December21,1807,"On the Propagation of Heat in Solid Bodies" before the institute de France, presenting his research on thermal conduction phenomena[38]. Within this work, he proposed that any continuously varying periodic function could be represented as an infinite series of sinusoidal and cosinusoidal components[39]. This principle founded on the premise that any periodic signal can be represented as fundamental frequency together with its associated integer harmonic components. This mathematical representation is designated as the Fourier Series (FS) and belongs to the wider Fourier Transform(FT) class of methods. The FT serves as an umbrella term encompassing four distinct categories, each corresponding to one of four fundamental signal classifications commonly encountered engineering applications:

Continuous-Periodic Signals As previously mentioned, the Fourier analysis of continuously varying periodic waveforms is designated as the Fourier Series.

Continuous-Aperiodic Signals The mathematical technique for representing any arbitrary continuous time-domain function, not restricted to periodic behavior, as a summation of harmonic component is referred to simply as Fourier Transform.

Discrete-Periodic Signals Analogous to its continuous counterpart, the FT applied to sampled periodic data is termed the Discrete Fourier Series(DFS).

Discrete-Aperiodic Signals This FT classification corresponds to Discrete Time Fourier Transform(DTFT).

To comprehend the DFT methodology, it is instructive to begin with the continuous FT formulation. In its mathematical expression, the FT consolidates the sinusoidal and cosinusoidal trigonometric terms into a compact exponential representation through application of Euler's identity. This reformulation allows the FT to be expressed as:

$$X_{\omega} = \int_{-\infty}^{\infty} x(t)\, e^{-j\omega t}\, dt \tag{3.4}$$

Modern digital relays inherently employ signal processing techniques operating on sampled data rather than continuous waveforms. All calculations are therefore conducted in the discrete temporal domain, working with datasets obtained via the sampling mechanism detailed thoroughly in section 3.5.4. at this juncture, it suffices to recognize that a sampled signal results from periodically measuring a continuous analog waveform at distinct time points. These measurements are termed samples and form a numeric array suitable for digital computational methods. From this perspective, Eq.(3.4) proves inapplicable to protective relay implementation, as the standard Fourier Transform addresses continuous signals while the DTFT is expressly designed for discrete sequences. Given an unbounded series of samples $x_i[n]$, the DTFT formulation is given by:

$$X_{(\omega)} = \sum_{n=-\infty}^{\infty} x_i\,[n] e^{-j\omega n} \tag{3.5}$$

Where n denotes the discrete sample number, n ∈ ℤ. Obviously, it is impractical for any digital processor to execute an unbounded summation operation over infinite data points, rendering the direct implementation of Eq.(3.5) within microprocessor-based protective devices infeasible. To address this computational limitation, a finite segment must be selected from the continuous stream of sampled values *xi*[n]. this segmentation is accomplished through application of a discrete-time windowing operator *w*[n]. The bounded sequence *x*[n] is thereby define over *N* consecutive samples. The reduction of the unlimited sequence *xi*[n] to finite number of samples *x*[n] produces the Discrete Fourier Transform, whose standard formulation appears in Eq.(3.6).

$$\bar{X}(k) = \frac{1}{G}\sum_{n=-\infty}^{N-1} \omega[n]\, x[n] e^{-j\frac{2\pi}{N}nk}, \quad 0 \le k \le N-1 \tag{3.6}$$

Where k represent's the harmonic number being analyzed, and *G* denotes the normalization factor of data window , $G = \sum_{n=-\infty}^{N-1} \omega[n]$.
the standard DFT formulation reveals several significant properties. Primarily, periodicity of the sample sequence x[n] is not a prerequisite for transforming it into the frequency domain representation. Errors are introduced in the DFT estimates when the signal is not periodic within the data window, as discussed in Section 3.6. The subsequent explanation assumes, without loss of generality, that the signal under analysis is a pure cosine wave at its fundamental frequency. Therefore, the DFT will be adjusted to the fundamental frequency, specifically $k = 1$, to estimate the phasor of the fundamental component. Under these conditions, a DFT formulated according to Eq.(3.6) is alternatively termed a one-cycle DFT, wherein *N* samples span exactly one complete period of the cosine waveform. Furthermore, when the most basic uniform(rectangular) window function, characterized by:

$$\omega[n] = \begin{cases} 1 & if\ 0 \le n \le N-1 \\ 0 & Otherwise \end{cases} \tag{3.7}$$

The normalization factor G is numerically equal to N, and the precise phasor determination is achieved by multiplying Eq. (3.6) with the multiplicative factor $\sqrt{2}$, (under this arrangement, the DFT spectral magnitude of the cosine signal corresponds to $Xm/2$). Furthermore, when the sinusoidal waveform described in Eq. (3.1) undergoes sampling at rate of N samples per fundamental period, its discrete-time equivalent is represented by the sample sequence:

$$x[n] = X_m \cos\left(\frac{2\pi}{N}n + \varphi\right) \tag{3.8}$$

When employing a uniform (rectangular) window function, the phasor of the fundamental frequency phasor is determined from Eq. (3.6) by setting $k = 1$ and applying $\sqrt{2}$ scaling factor as indicated:

$$\bar{X}(1) = \frac{\sqrt{2}}{N}\sum_{n=0}^{N-1} x(n)\cos\left(\frac{2\pi}{N}\, n\right) - j\frac{\sqrt{2}}{N}\sum_{n=0}^{N-1} x(n)\sin\left(\frac{2\pi}{N}n\right) \tag{3.9}$$

$$= X_{\Re} - jX_{\Im}$$

$$X_{\Re} = \frac{\sqrt{2}}{N}\sum_{n=0}^{N-1} x(n)\cos\left(\frac{2\pi}{N}n\right) = \frac{X_m}{\sqrt{2}}\cos\varphi \tag{3.10}$$

$$X_{\Im} = \frac{\sqrt{2}}{N}\sum_{n=0}^{N-1} x(n)\sin\left(\frac{2\pi}{N}n\right) = -\frac{X_m}{\sqrt{2}}\sin\varphi \tag{3.11}$$

Substituting equations (3.10) and (3.11) into equation (3.9) yields the expected phasor $\overline{X(1)} = \left(X_m/\sqrt{2}\right)e^{j\varphi}$. The phasor of a cosine wave at its fundamental frequency is derived directly through application of DFT coefficients to the sampled input data. From a protective relay implementation standpoint, DFT-based algorithm are realized using Finite Impulse Response (FIR) filter structures [40]. The computation the output at sampling instant *m* based on *N* previously acquired samples (data values retained in buffer memory). The response $yk[m]$ of the FIR filter with coefficients $hk[n]$ for the k^{th} order harmonic is expressed as follows:

$$y_k[m] = \sum_{n=0}^{N-1} h_k[n]x[m-n] \tag{3.12}$$

Where $y_k[m]$ represent the output sample for k^{th} harmonic components, $x[m-n]$ denote the input data sequence (buffered sample values), $N-1$ indicates the filter length (N denotes filter taps), and $h_k[n]$ represents the weighting coefficients of the filter. The coefficients $h_k[n]$ are directly associated with the real and imaginary components of the complex exponential in the DFT, serving as approximations of cosinusoidal and sinusoidal functions. Therefore, two orthogonal FIR filters are necessary to execute the DFT filtering operation for the k^{th} order harmonic. For a specified harmonic *k*, the orthogonal filters formulation are expressed as follows:

$$h_{k,c}[n] = \frac{\sqrt{2}}{N}\sum_{n=0}^{N-1}\cos\left(\frac{2\pi}{N}nk\right) \tag{3.13}$$

$$h_{k,s}[n] = \frac{\sqrt{2}}{N}\sum_{n=0}^{N-1}\sin\left(\frac{2\pi}{N}nk\right) \tag{3.14}$$

The FIR filters defined in Eqs. (3.13) and (3.14) are referred to as the "full-cycle cosine filter" and the "full-cycle sine filter," respectively. The frequency response for each harmonic can be assessed by multiplying Eqs. (3.13) and (3.14) by the complex exponential $e^{-j\omega n}$ as demonstrated:

$$H_{k,c}\left[e^{j\omega}\right] = \frac{\sqrt{2}}{N}\sum_{n=0}^{N-1}\cos\left(\frac{2\pi}{N}nk\right)\cdot e^{-j\omega n} \tag{3.15}$$

$$H_{k,s}\left[e^{j\omega}\right] = \frac{\sqrt{2}}{N}\sum_{n=0}^{N-1}\sin\left(\frac{2\pi}{N}nk\right)\cdot e^{-j\omega n} \tag{3.16}$$

By computing the magnitudes of $H_{k,c}\left[e^{j\omega}\right]$ *and* $H_{k,s}\left[e^{j\omega}\right]$, the frequency amplitude characteristics for each harmonic component can be displayed graphically. Figure 3.20 presents an illustration for $k = 1$ (fundamental frequency phasor) using $N = 48$, a typical sampling rate per cycle employed in protective relay applications. Note that the angular frequencies have been expressed in terms of harmonic orders for convenience. The magnitude characteristics appear as continuous curves because they were calculated at angular frequency increments of 2 rad/s.

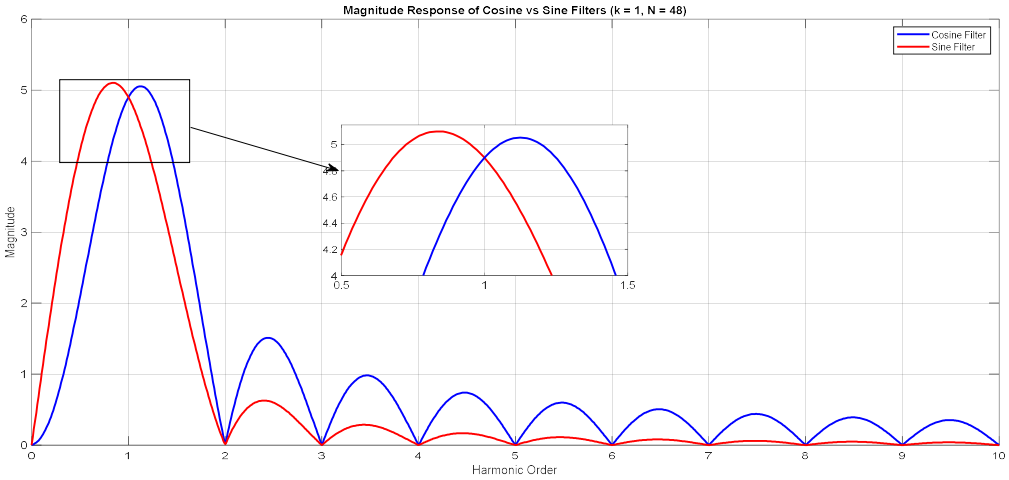

Fig. 3.2 *Cosine and sine filters magnitude responses*

Figure 3.20 illustrates that both the cosine and sine filter structures exhibit band-pass frequency characteristics with unity gain $(1/\sqrt{2})$ precisely at the fundamental frequency. Furthermore, because these filters produce zero gain at DC (representing steady-state offsets) and at harmonic frequency levels, they effectively suppress these undesired components when present alongside the fundamental frequency content. After processing the input signals through the one-cycle sine and cosine filtering operations, the magnitude and phase angle can be calculated as illustrated in Figs. 3.2 and 3.3, modified from [41].

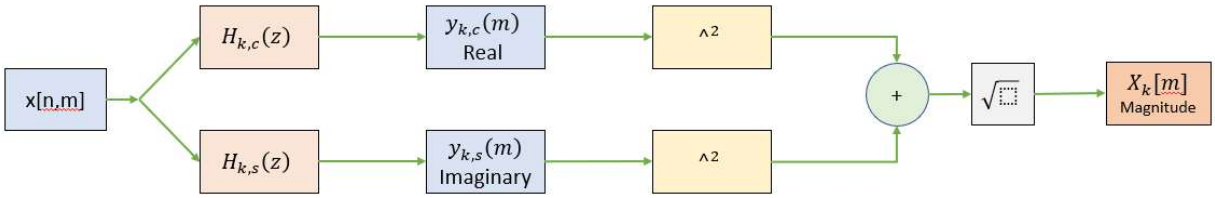

Fig. 3.3 *Magnitude estimation algorithm for Microprocessor-based relay*

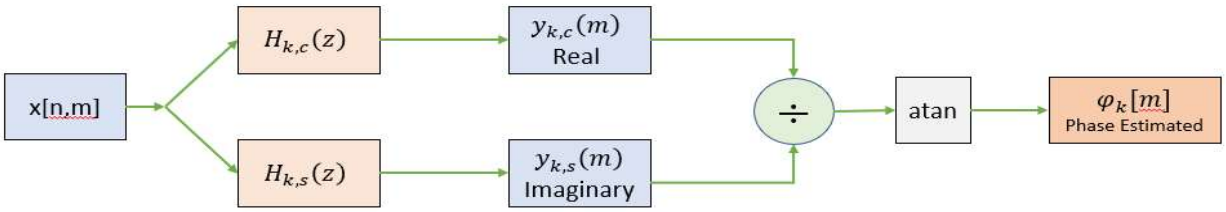

Fig. 3.4 *Phase estimation algorithm for Microprocessor-based relay*

3.4 Review of non-DFT phasor estimators

Modern relays frequently use the full-cycle DFT filter for a number of reasons. It may reject DC and all of its harmonics, to start. Then, as shown by its bandpass properties, it can withstand slight frequency deviations. Lastly, it has a good transient reaction and is quick and accurate. Over time, a number of other algorithms have been put forth to rival the DFT-based algorithm's performance. These include Kalman filters, Least Error Squares (LES), and Infinite Impulse Response (IIR). Although the DFT has been thoroughly compared to these unconventional filters, no one has been able to replace it. Below is a quick summary of the shortcomings of the previously described approaches.

IIR filters Differing from FIR architectures, IIR filter computations intrinsically rely upon the accumulated input record extending indefinitely into the past. As a result, when fault occur, IIR-based approaches demonstrate lower sensitivity to FIR counterparts since the IIR methodology perpetually retains data from before the fault inception. This behavior necessarily produces slower fault identification, which may threaten the dynamic stability of the electrical network.

LES filters The fundamental idea behind the LES approach is to minimize the mean-square error between a mathematical model of the waveform and the actual waveform. The fundamental frequency component, the fading DC offset, and the harmonics of designated orders are often included in the model [42]. The accuracy of the LES method is high if the waveform under consideration matches its mathematical model. However, as demonstrated in [41], an LES-based filter's frequency response indicates that its upper boundary is higher than the DFT filter's, indicating that more errors are incorporated into the phasor estimates.

Kalman filters The Kalman filter requires a signal model since it is a generalized version of the LES filters. To get precise phasor measurements, its model must take into account every potential undesirable element that the Kalman filter is meant to filter out. Phasor estimations will deteriorate if a component is not well modelled since the filter will squeeze it into the fundamental and harmonics. Furthermore, as mentioned in [43], the Kalman filter necessitates a greater computing effort than the DFT, with the cost of fundamental operations for modelling the noise, DC, and second and third harmonics being 13 times higher than the DFT. The aforementioned explanation leads to the conclusion that while there are DFT-based algorithm alternatives, they are not tailored for protection relaying. For this reason, the study will solely look at the DFT.

3.5 Architecture of microprocessor-based relays

Digital protective relays are designed to identify system fault and irregular operating conditions by evaluating voltage and current signals presented at their terminals. Upon fault recognition, these devices issue trip commands to associated circuit breakers, which then mechanically interrupt current flow through their contacts in response to the received signal. The physical interruption is therefore executed by the circuit breaker, which forms an integral part of the protection scheme wherein the digital relay functions as the decision-making center. Obviously, such microprocessor devices cannot directly handle the transmission-level voltages reaching hundreds of kilovolts or currents in the kiloampere range carried by overhead conductors and buried cables. These quantities are instead scaled down to relay-compatible levels by instrument transformers(ITs) positioned within electrical substations. Potential transformers(PTs) or capacitor voltage transformers(CVTs) reduce voltage magnitude to nominally 67V-rms(line-to-ground), while current transformers(CTs) scale to 1 or 5 A-rms during normal conditions. The complete protection architecture, comprising these three principal elements-digital relay, ITs, and circuit breaker- is illustrated in Figure 3.4, modified from[44], which also presents the fundamental structure of microprocessor-based relays. Digital relay architecture consist of three core functional modules. The initial module focuses on precise acquisition of voltage and current parameters via the data acquisition pathway, commencing with the secondary outputs of instrument transformers(CTs and VTs, described in Section 3.1) and terminating at the analog-to-digital converter(ADC), which converts continuous-time analog signals into discrete sample sequences. After conversion to digital form, these sampled values are processed using digital signal processing techniques where essential system state quantities are computed (such phasor extraction) and protection logic is executed. The collection of software routines executing all protective logic is termed the firmware. The final functional block encompasses external communication capabilities, including digital input/output(I/O) circuits, the Human-Machine Interface(HMI), and standardized communication protocols. Optical isolators may provide circuit breaker status information to the relay, while digital output modules drive physical contacts that transmit trip signals to the breaker. The HMI provides operators with immediate access to numerous relay parameters such as configuration data, digital I/O states, and real-time measurements generated by the device. Where the central challenge of this research is emphasized. In essence, protective relays constitute critical elements within substation automation system(SAS) due to the essential operational data they maintain, which serves multiple stakeholder groups throughout the utility organization. Consequently, protective relays, along with other intelligent electronic devices(IEDs) comprising the SAS, incorporate various communication protocols to facilitate data exchange primarily with the supervisory control and data acquisition(SCADA) infrastructure.

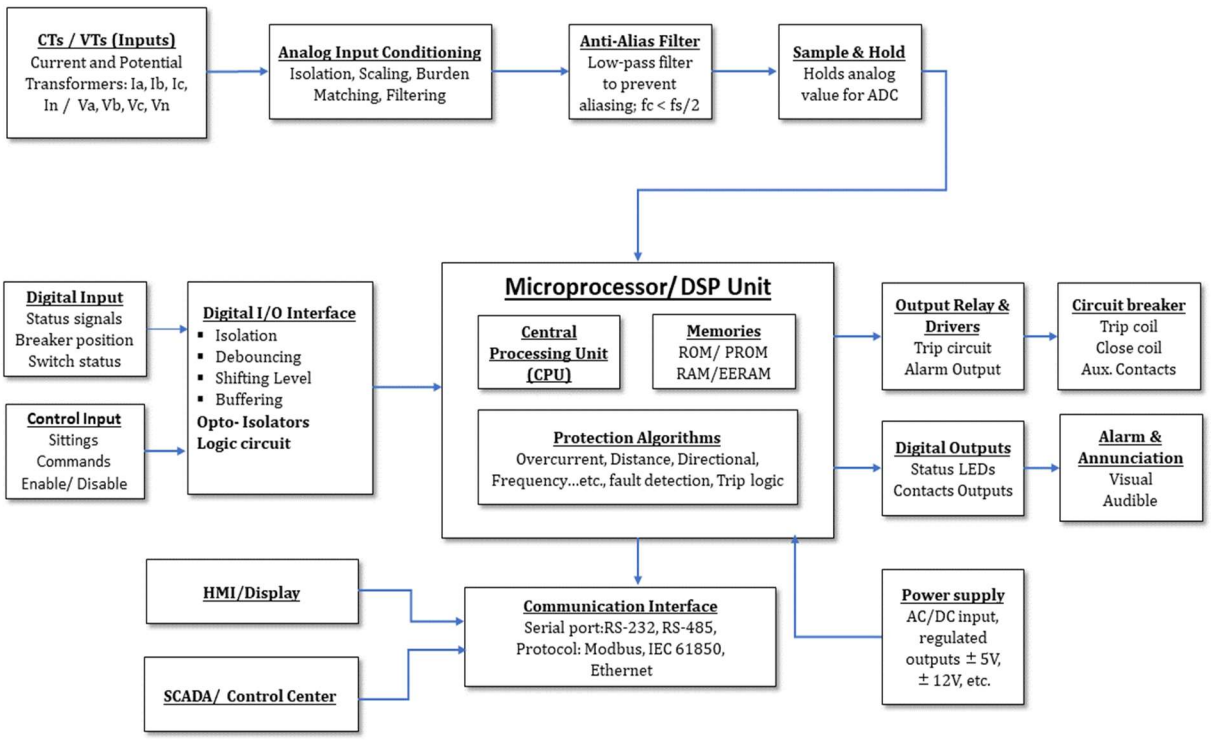

Fig. 3.5 *Architecture of microprocessor-based relays*

Given that this research primarily address the algorithmic aspects of next-generation digital protective relays a brief discussion of firmware architecture provides valuable context regarding its structural organization. The microprocessor serves as the core element of both the relay firmware and the device itself, as it orchestrated protection algorithm execution and manages communication with peripheral hardware. The three memory types illustrated in Figure3.4 constitute vital relay components, each fulfilling a distinct operational requirement. The Read-Only-Memory(ROM) houses the protection software to be executed. These programs are permanently stored and remain intact even during power-off conditions. Program execution can occur directly from ROM if memory access speeds are adequate for real-time operation. Otherwise, program instructions are transferred from ROM to Random-Access-Memory(RAM) during an initialization sequence(shadowing process) where actual execution takes place. This method is usually used because RAM is much faster than ROM, often more than 15 times faster. Also, RAM is used to store digitized data from the ADC that need to be processed by algorithms. Also, digital protection switches can't be used in substations until they are set up. This configuration process includes changing the setting file so that it works with the network design. Understandably, once parametrized, these setting must persist in memory to prevent reconfiguration requirements following power cycling. For this purpose, the setting file resides in Electrically-Erasable Programable-Read-Only-Memory(EEPROM), which provides non-volatile programmable storage. Finally, it warrants mention that the timing circuit depicted in Figure3.4 represents a critical component and foundational element of

this investigation. Synchronizing time-base with an absolute temporal reference enables multiple applications, including the Phasor Measurement Unit(PMU) functionality addressed in section3.9.

The following parts describe the Data Acquisition System (DAS) and talk about the main technical problems that come up when trying to use DFT-based estimate methods.

3.5.1 Interposed current and voltage transformers

The main components of protective relay DAQs are auxiliary (or intervened) current and voltage transformers. are employed for two primary purposes. First, their transformer ratio reduces the levels of the principal signals to acceptable levels that the ADC requires. In fact, ADCs usually operate at a voltage level of ±10 volts, which is ten times lower than the secondary of the power system's traditional VTs. Additionally, before the ADC can process the outputs of auxiliary CTs, they must be transformed to voltages. As illustrated in Fig. 3.4, a resistive shunt attached to the secondary of auxiliary CTs converts current into voltage. Second, galvanic isolation is provided by interposed ITs. Before the signal is converted, this type of analogue isolation introduces a nonlinear gain and some offset errors, but it shields the ADC from high or transient voltages [45]. Let's concentrate on the interposing CT equivalent circuit, also known as the secondary side, shown in Fig. 3.5 to comprehend the effects of the distortions applied to the analogue signals.

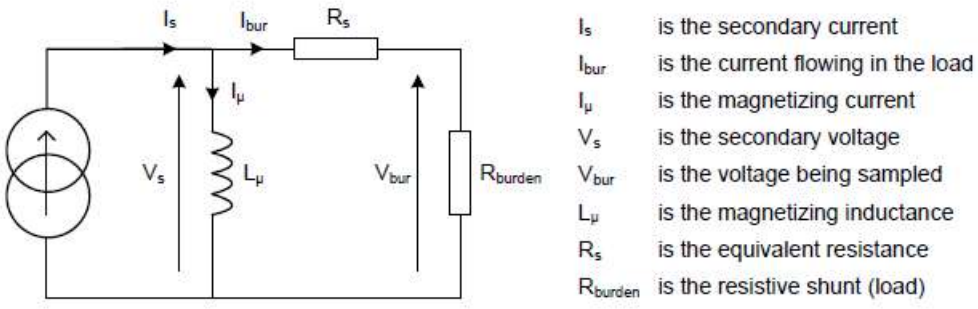

Fig. 3.6 *secondary-side equivalent circuit model for CT*

Assume that $R_t = R_s + R_{burden}$. The following formula can be used to calculate the transfer function $H_{CT}(s)$, which is connected to the interposed CT schematic in Figure 3.5:

$$H_{CT}(s) = \frac{V_s(s)}{V_{bus}(s)} = \frac{sL_\mu}{R_t + sL_\mu} = \frac{\frac{s}{\omega_C}}{1 + \frac{s}{\omega_C}} \tag{3.17}$$

Where the cutoff frequency denoted ω_c is expressed in (rad/s). Initially, Eq.(3.17) suggests that the auxiliary CT can be approximated as a first-order high-pass filter, with a cutoff frequency of $f_c = R/(2\pi L\mu)$ Hz. Consequently, the selection of winding turns and the load impedance must be executed

with precision to minimize the cutoff frequency, thereby preventing the exclusion of significant frequencies. Notably, R_{burden} serves as a crucial parameter for eliminating the direct current (DC) component from the fault current, which is advantageous for preserving the accuracy of phasor measurements during fault conditions. Figures 3.7 and 3.8 illustrate the frequency response representation, with R_s = 42.5, R_{burden} = 5.5, and L_μ = 390 mH. These parameters are representative of a single auxiliary CT, as detailed in the research presented in [46].

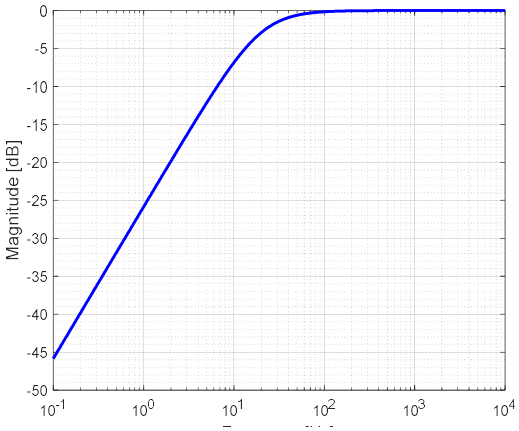

Fig.3.7 *Auxiliary CT frequency response magnitude*

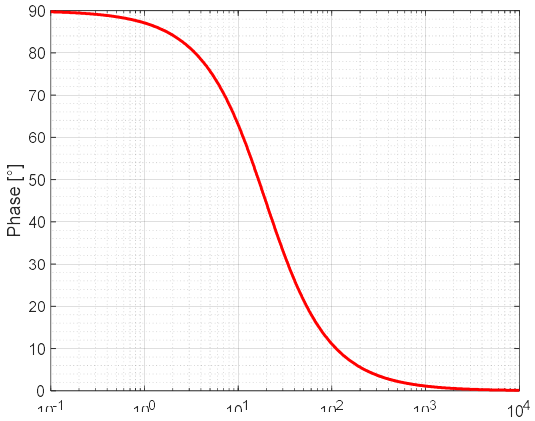

Fig.3.8 *Auxiliary CT frequency-domain phase response*

According to Figures. 3.7 and 3.8, the attenuation is approximately 0.9311 at 50 Hz, and the phase shift introduced is 21.39 degrees. Similarly, at 60 Hz, the attenuation is about 0.9506, and the phase shift is 18.08 degrees. Because faults may be identified, they can be remedied throughout the calibration process. Typically, the calibration operation is carried out at the fundamental frequency (50 and 60 Hz) for each harmonic utilized by protective algorithms. If the auxiliary CTs for three-phase currents are similar, correction is unnecessary as the current waveforms shift by the same amount. If the CTs are not exactly the same, a phasor rotation in software is required to achieve a 120-degree phase shift between the phases. Clearly, lowering the cutoff frequency reduces the magnitude and phase angle errors, which may be ignored. Signals are sampled for digital processing after being calibrated and adjusted to allow for acceptable voltage levels.

3.5.2 The procedure for sampling and its effects

The sampling procedure involves extracting samples from an analog continuous-time signal; these samples represent the amplitude of the signal at the specific instants when the samples are acquired. This process is executed through Sample and Hold (S/H) circuits. In most instances, the samples are acquired at a constant interval, denoted as T_s, referred to as the sampling period. The number of samples produced within one second denotes the sample rate, or sampling frequency, denoted as $F_s = 1/T_s$, and measured in Hertz. Clearly, the continuous variable t can no longer be used in the discrete-time domain, as the resulting samples occur solely at specific instants determined by the sampling interval, as illustrated. particular instants related to the sampling interval; it is evident that the continuous variable t can no longer be employed in the discrete time domain:

$$t = nT_s \quad , \qquad n \in z \tag{3.18}$$

This demonstrates how the sampling procedure disregards the interval between two successive samples. Therefore, one may naturally question if the samples obtained are sufficiently representative of the analogue signal or not, keeping in mind that it is impracticable to sample the input signal at an arbitrary high sample rate. Stated differently, what is the lowest value of F_s that ensures the data from the analogue signal is retained after sampling? The answer to this question can actually be stated as follows: can the analogue signal be reconstructed from the samples without information loss? The sampling process's mathematical model serves as the foundation for answering this query.

Initially, let us presume that the signal $x(t)$ possesses a spectrum inherently limited to the frequency f_{max}, such that $X(f) = 0$ for all $f > f_{max}$. This restriction may also be artificial, resulting from the application of specific filters as demonstrated later in Section 3.3. In the time domain, the sampling procedure is equivalent to multiplying the signal $x(t)$ by a series of unit impulses. Consequently, the acquired signal consists of a sequence of successive impulses whose amplitude is modulated by that of the sampled signal. Furthermore, the aforementioned series of unit impulses is known as the Dirac comb (or impulse train), comprising an infinite sequence of Dirac delta functions evenly spaced by the sampling interval T_s, that is:

$$\text{Ш}_{T_s} \stackrel{\text{def}}{=} \sum_{n=-\infty}^{\infty} \delta(t - nT_s) \tag{3.19}$$

According to Eq. (3.19), Ш_{T_s} (shah/Comb function) represents an infinite sequence of "spikes" (Dirac delta functions), and the sampled signal $x_s(t)$ can be expressed as follows if the sampling procedure is perfect, that is, if the samples are created instantly at $t = nT_s$ ("Hold" function is ignored):

$$x_s(t) = x(t) \times \text{Ш}_{T_s}$$

$$x_s(t) = x(t) \cdot \sum_{n=-\infty}^{\infty} \delta(t - nT_s)$$

$$= \sum_{n=-\infty}^{\infty} x(nT_s)\, \delta(t - nT_s) \tag{3.20}$$

Practical implementation of the sampling process cannot achieve the theoretical ideal of infinitesimally narrow impulses. In reality, each sampling pulse persists for a finite time interval τ_p during which the signal value is maintained at a fixed level(implementing a "Sample-and-Hold" operation). The actual sampled waveform therefore consists of a pulse train recurring with period T_s, where each pulse has finite width τ_p . The magnitude assigned to these pulses depended on the specific sampling methodology employed, either instantaneous or averaged sampling. The instantaneous sampling approach assigns pulse amplitudes equal to the input signal value at the precise sampling instant, maintained throughout the duration τ_p (illustrated in Fiigure3.9) The averaged sampling technique assigns pulse amplitudes corresponding to the time averaged value of the input signal over the interval τ_p (illustrated in Figure 3.10). the spectral implications of these two sampling methodologies are examined in Appendix A. Specifically, when the pulse duration is negligibly small relative to the period of the highest frequency content in the input signal, both instantaneous and averaged sampling

approaches closely approximate ideal impulse sampling. Under this assumption, the subsequent analysis proceeds using the ideal sampling model.

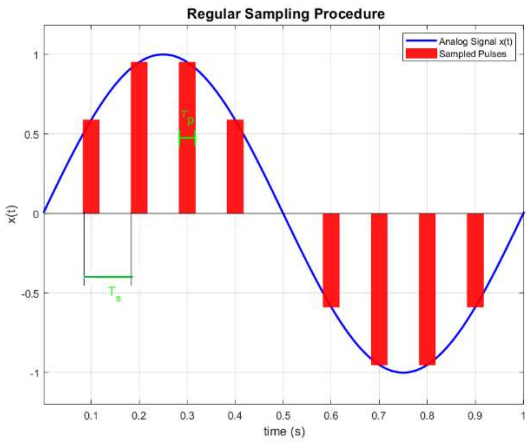

Fig.3.9 *Regular sampling procedure*

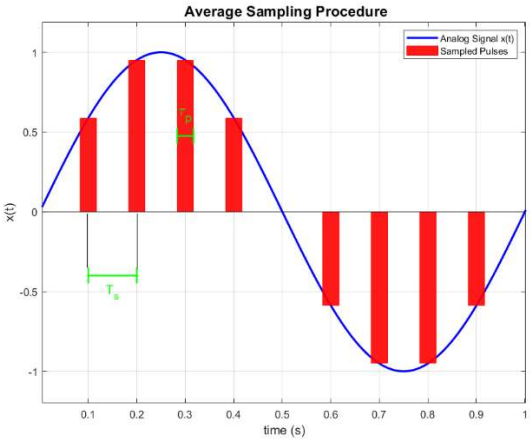

Fig.3.10 *Average sampling procedure*

Eq.(3.20) describes the sampling mechanism within the time domain. To evaluate sampling's influence on spectral content, however, conversion of Eq.(3.20) to the frequency domain becomes necessary. Such conversion permits direct comparison of the sampled signal spectrum $X_s(f)$ against the continuous input signal spectrum $X(f)$. Spectral equivalence would confirm complete information preservation through the sampling process. Achieving this frequency-domain representation requires employing the Discrete Time Fourier Transformer(DTFT). Noting that a time-domain impulse train transforms via DTFT into a frequency-domain impulse train, the spectrum of the samples train, the spectrum of the sampled waveform may be written as:

$$F\{x_s(t)\} = X_s(f) = F\left\{x(t) \cdot \sum_{n=-\infty}^{\infty} \delta(t - nT_s)\right\}$$

$$= X(f) * \left[F_s \cdot \sum_{m=-\infty}^{\infty} \delta(f - mF_s)\right]$$

$$= F_s \cdot \sum_{m=-\infty}^{\infty} X(f - mF_s) \tag{3.21}$$

Consequently Eq.(3.21) demonstrates that the frequency spectrum of an ideal sampled signal comprises the original signal spectrum centered *f=0*, analog with periodic replicas displaced by integer multiples of F_s in both positive and negative frequency directions. This effect is termed spectral replication or aliasing-free periodization. The spectrum centered at *f=0* constitutes the primary band (or baseband) of $X_s(f)$, whereas the additional spectral copies represent frequency-shifted replicas of $X_s(f)$. Figure 3.11 illustrates both temporal and spectral representations of sampling the signal $x(t) = 2\cos(2f_{max}t)$ at a rate $F_s = 6 \times f_{max}$.In contrast to the spectrum *X(f)*, which is constrained to a maximum frequency f_{max}, the sampled signal $x_s(t)$ extends infinitely due to spectral replication across the whole frequency range of $f \in [-\infty\,;\,+\infty]$. Moreover, as illustrated in Figure 3.11, the original

information stored in *x(t)* is retained post-sampling, as both the primary band and frequency-shifted replicas exhibit identical spectral characteristics. This information preservation occurs because F_s is sufficiently elevated to prevent spectral overlap between adjacent replicas.

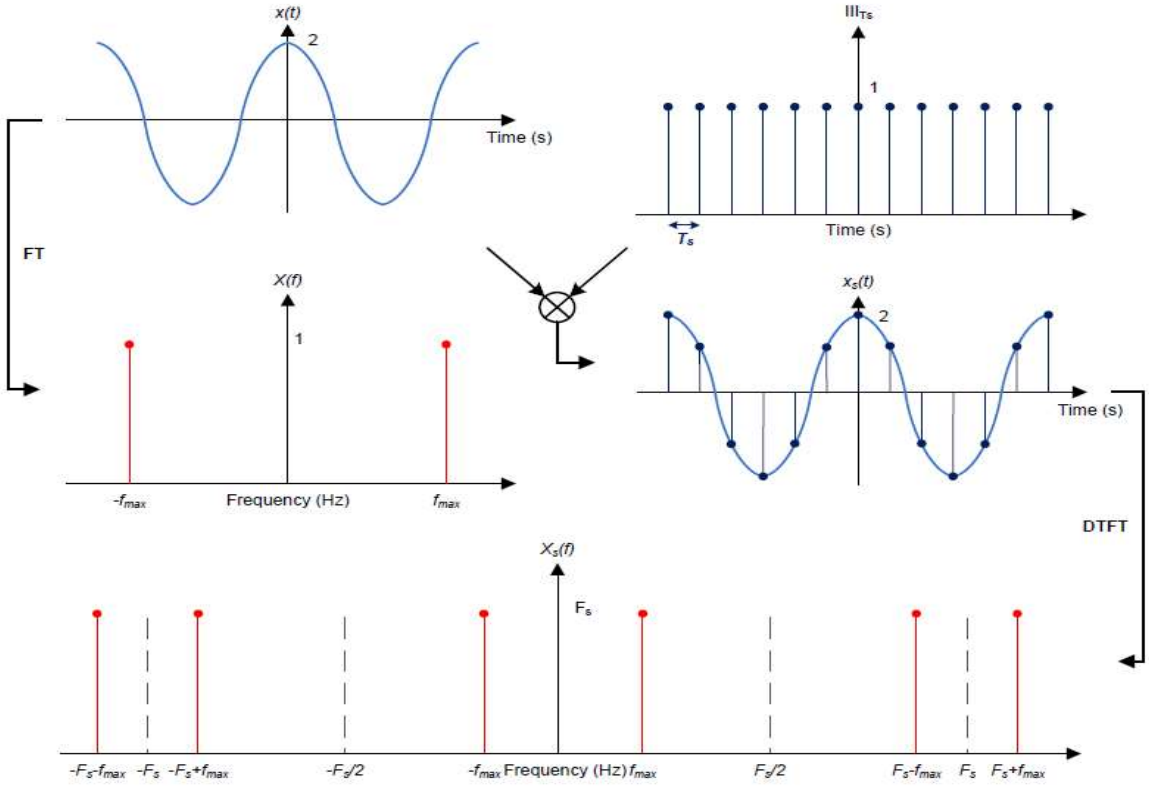

Fig. 3.11 *Frequency domain representation of spectrum periodization*

Closer examination of the frequency axis reveals that a critical minimum sampling rate exists below which spectral replication results in overlapping. This criterion corresponds to the well-known Nyquist-Shannon sampling theorem, stated as follows:

First theorem: Let $x(t)$ be a periodic continuous signal with a bandwidth $\Omega_{max} = 2\pi f_{max}$ rad/s. For the signal $x(t)$ to be perfectly reconstructed without information loss, the sampling rate needs to be more than twice the maximum frequency, which is:

$$F_s \geq 2 \cdot f_{max} \tag{3.22}$$

As mentioned earlier, the ability to retriever the continuous signal $x(t)$ from its sampled signal $x_s(t)$ validated satisfaction of the sampling theorem. In practice, signal reconstruction is accomplished by extracting the baseband component $X_{sb}(f)$ from the periodic spectral replicas, followed by application of the inverse transform. This extraction process employs an ideal low-pass filter with cutoff frequency $f_c = Fs/2$. This half sampling frequency $Fs/2$ is termed the Nyquist frequency(alternatively, the Shannon frequency). The filtering operation, mathematically equivalent to rectangular frequency

window, can be expressed as $\Pi_{Fs}(f)$. following this framework, x(t) can be reconstructed by reversing the sampling procedure beginning with the baseband component of $x_s(t)$:

$$F^{-1}\{X_{s,b}(f)\} = x_{s,b}(t) = F^{-1}\{X_s(f) \cdot \prod_{F_s}(f)\}$$

$$= x_s(t) * [F_s \cdot sinc(\pi F_s t)]$$

$$= F_s \cdot \left[x_s(t) * \frac{sin(\pi F_s t)}{\pi F_s t}\right]$$

$$= F_s \cdot \left[\sum_{n=-\infty}^{\infty} x(nT_s)\delta(t - nT_s) * \frac{sin(\pi F_s t)}{\pi F_s t}\right]$$

$$= F_s \cdot \left[\sum_{n=-\infty}^{\infty} x(nT_s) * \frac{sin\big(\pi F_s(t - nT_s)\big)}{\pi F_s(t - nT_s)}\right] \quad (3.23)$$

The Whittaker-Shannon interpolation, often known as equation (3.23), which enables an exact reconstruction of the continuous analog signal $x(t)$ from discrete samples acquired at intervals $t = nT_s$. In conclusion, if the Nyquist theorem is satisfied, then ideal sampling preserves all of the information present in the original signal $x(t)$ after sampling. But if that isn't the case, what may the implications be for the spectrum? A graphical illustration of the answer to this question may be seen in Fig. 3.12, where $F_s = 1.8 \times f_{max}$. The spectral lines at f_{max} and $-f_{max}$ are outside the region enclosed by the Nyquist frequency, $[-F_s/2\ ;\ F_s/2]$, as shown in Figure 3.12. Consequently, these frequency components at f_{max} and $-f_{max}$ are reflected into the baseband as $F_s - f_{max}$ and $-F_s + f_{max}$, respectively. Generally, when the sampling theorem is violated, any frequency component f_{alias} within the interval $[F_s/2;\ F_s]$ is reflected to the frequency $F_s - f_{alias}$. This spectral overlap phenomenon is termed aliasing (or frequency folding) and causes spectrum corruption. Due to aliasing, the reflected component of f_{alias} manifests as an apparent spectral line in the reconstructed analogue signal, despite its absence at that frequency in the original waveform. When an aliased spectral component appears at a frequency that a DFT-based approach cannot adequately suppress, phasor estimation accuracy degrades. The most problematic frequency for DFT-based estimator is $F_s - f_k$, where f_k denoted the target frequency component.

3.5.3 Analogue Anti-aliasing Filtering Implementation

Digital protective relays are engineered to function within a defined frequency range where each measured frequency serves specific metering and protection purposes. Frequency components beyond this operational bandwidth, which may exist in electrical power system, constitute unwanted interference requiring elimination for two critical reasons. First, these components serve no functional purpose for relay operation. Second, their presence can trigger aliasing distortion. Consequently, artificial bandwidth limitation of analog input signals becomes necessary. The standard approach employs an analog low-pass anti-aliasing preceding the sampling stage. The ideal anti-aliasing filter magnitude characteristic resembles the rectangular window function and is commonly termed a "brick-wall filter". This theoretical filter provides unity gain with zero distortion throughout the passband, and instantaneous transitions between these regions. However, physical realization of such filter is impossible; practical implementations approximate this behavior based on the following design parameters:

- Passband gain, Gpass
- Stopband attenuation, Gstop
- Passband corner frequency(or cutoff frequency), Fpass
- Stopband edge frequency, Fstop

Figure3.13 presents a representative magnitude response for such filters, where the frequency domain extends from DC to theoretically infinite frequency. The horizontal axis displays three distinct filter regions: passband, transient region, and stopband. These zones are delimited by the four previously mentioned specifications. Throughout the passband, filter gain may fluctuate between 0dB and Gpass. Likewise, stopband attenuation varies between Gstop and − ∞dB. In both regions, these gain variations are termed ripple. Passband ripple introduces magnitude errors in the filter output across the entire operational frequency range. These amplitude errors require software compensation as they compromise calculation precision.

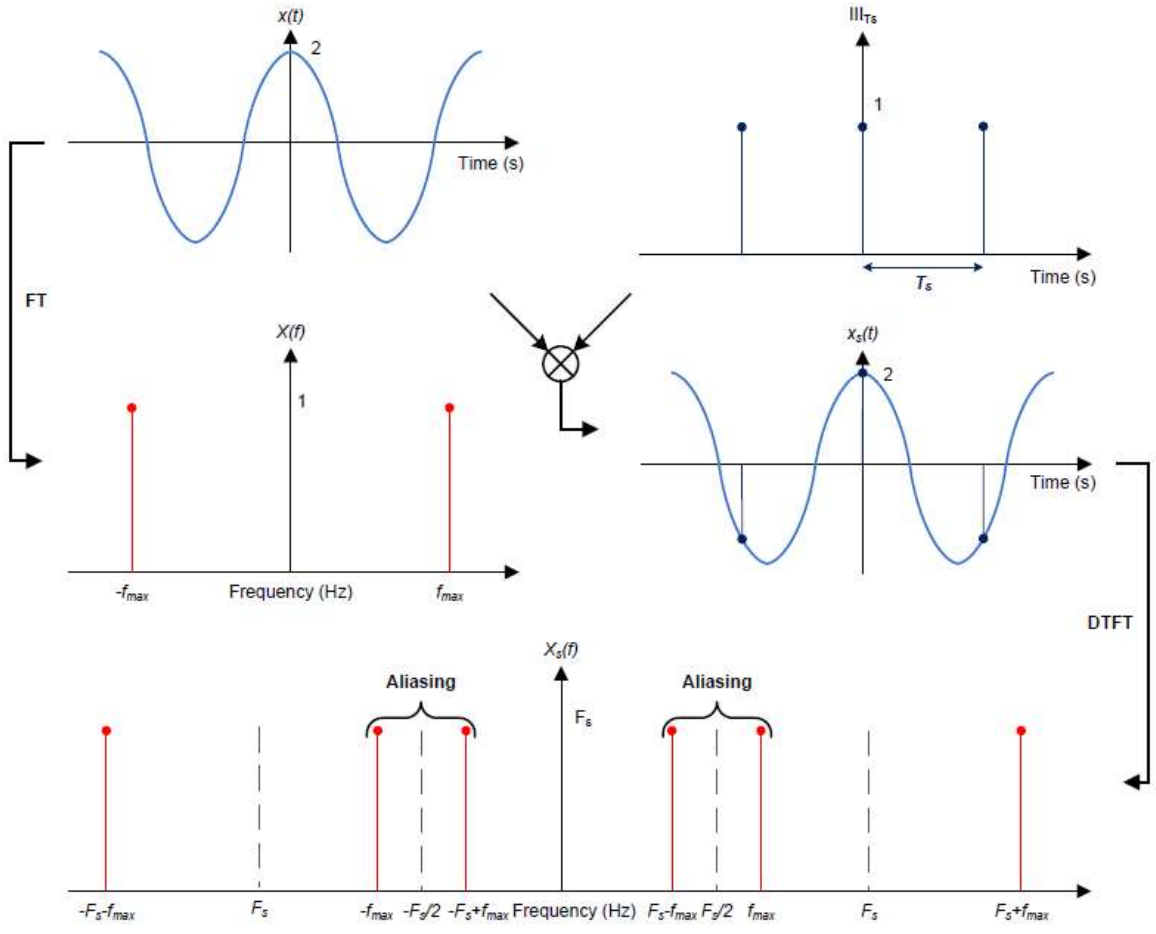

Fig. 3.12 *Frequency spectrum showing aliasing mechanism*

An additional critical parameter is filter order, which governs the steepness of the transition region, also referred to as roll-off rate. Generally, the rate-off is engineered to achieve the specified attenuation at the lowest frequency that aliases onto the frequency of interest.

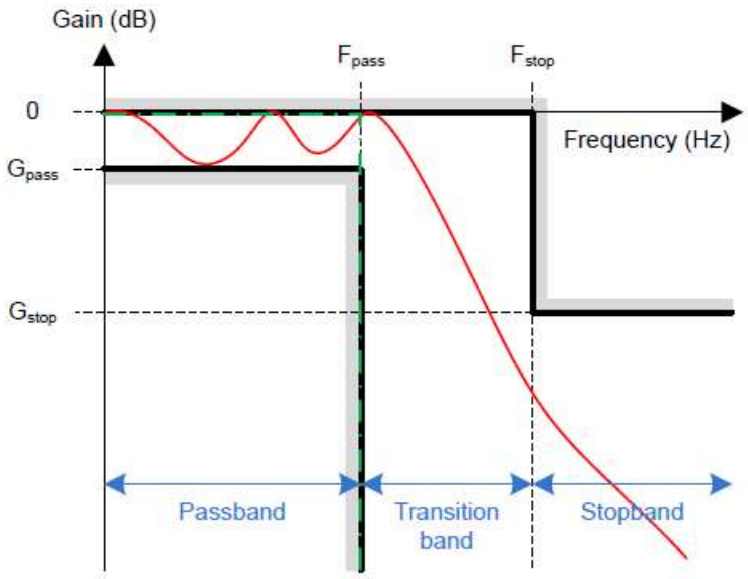

Fig. 3.13 *Magnitude frequency characteristics of theoretical (green) and realizable (red) anti-aliasing low-pass filters*

Assuming linear roll=off characteristics, the relationship between roll-off rate, required attenuation, sampling frequency, and target frequency can be demonstrated as shown. [47]:

$$\Delta R = \frac{A \log 2}{log\left[\frac{F_s - f_k}{f_k}\right]} \tag{3.24}$$

ΔR specifies the attenuation slope in dB per decade, A indicates the necessary stopband rejection in dB, and f_k represents the target frequency in Hz. Higher-order filters typically attain sharper transition characteristics; nevertheless, they demonstrate a slower transient response and contribute more signal delay relative to lower-order designs. Ultimately, such elevated filter orders adversely affect protective relay operation speed. The group delay, G_d, measured in seconds, directly correlates with the phase characteristic according to the following expression:

$$G_d = -\frac{1}{2\pi} \cdot \frac{d\varphi(f)}{df} \tag{3.25}$$

Where $d\varphi(f)$ represents the filter's characteristic. Different frequency components of the signal experience different phase shifts due to the phase response effect; the frequency derivative of a phase characteristic that shows linear frequency dependency stays constant. Consequently, according to Eq.(3.26), Gd maintains a constant value across all frequencies while phase linearity is upheld. This property is particularly advantageous as it preserves signal waveform integrity throughout a wide frequency range: the output waveform is a time-delayed replica of the input, offset by Gd. Consequently, phase compensation is simplified and continues to be effective even under off-nominal frequency conditions.

Beyond cutoff frequency and filter complexity, the specifications Gpass, Gstop, Fpass, and Fstop establish the filter transfer function and, subsequently, its frequency response characteristics. Numerous approximation methodologies have been developed historically to approach ideal filter behavior while minimizing filter order requirements. Butterworth, Chebyshev, and Bessel designs exemplify such approximation techniques. Butterworth filter feature maximally flat passband characteristics. Conversely, Bessel filter optimization prioritize group delay uniformity throughout the passband. This attribute leads to their alternative designation as maximally linear-phase filters. The principal limitation of Bessel approximations is their broader transition regions compared to Butterworth and Chebyshev implementations. Chebyshev approximation enables steeper passband-to-stopband transitions, though at the cost of passband ripple. Traditionally, protective relays employ one of these three approximation methods due to their balanced time-domain and frequency-domain performance. Nevertheless, Butterworth filters receive preference for their constant passband gain characteristics[1].

3.5.4 The Process of Converting Analog-to-Digital and Oversampling

For reliable conversion results, analog-to-digital converters need a steady and consistent voltage level at their input. This is done by using S/H circuits that perform two tasks. Initially, the signal strength is preserved while sampling. The conversion function is executed while the signal is maintained for a duration τ_p (refer to Figs. 3.9 and 3.10). Quantization is the process of translating the signal being sampled into its equivalent digital code. The primary goal of quantization is to use a finite number of bits to approximate the infinitely accurate analog signal as closely as possible. This is accomplished by splitting the ADC's entire scale voltage range into several sub-ranges of the same amplitude, known as steps or Least Significant Bits (LSB). Every step has a corresponding number, which is a signed integer in the case of protection relays. The resolution, which is typically stated in bits, is the total number of discrete values that may be produced across the entire scale range. Because of this, the steps are typically a power of two for convenience. The range of an analog value that may be encoded by an ADC with a resolution of 16 bits is -32,768 to 32,767, or one in 2^{16} = 65,536 levels. Furthermore, the easiest way to determine the precision of an analog value's encoding is to express the resolution as a function of the full scale and bit count as follows:

$$R = \frac{V_{f_s}}{2^{N_{bits}} - 1} \tag{3.26}$$

Where: R denotes the ADC resolution (in Volts), V_{fs} represents the complete voltage range (in Volts) and N_{bits} denotes the bit word length. According to Eq. (3.27), if the specified ADC possesses a full-scale range of ±10 V, its resolution R is approximately 0.305 mV. If the ADC input voltage is 0.2 mV, the digitized output will be inaccurate due to insufficient resolution. The added error is referred to as quantization error or quantization noise. Assuming the analogue signal extends beyond few LSBs, the quantization noise constitutes a time-varying error characterized by a saw-tooth shape, with a zero mean value and uniformly distributed between −1/2 LSB and 1/2 LSB 3 (see to Figure 3.14) [49].

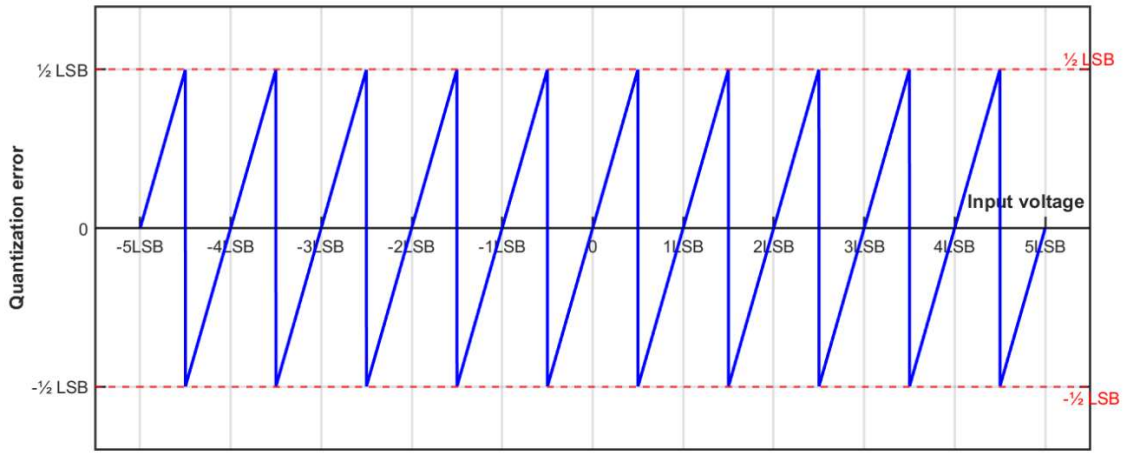

Fig. 3.14 *Progression of the quantization error*

Thus, the quantization process superimposes Gaussian noise onto the input signal. Based on these assumptions, the average power, P_{ϵ}, of this noise is delineated below [49]:

$$P_{\epsilon} = \frac{LSB^2}{12} \tag{3.27}$$

In the frequency domain, P_{ϵ} , the power spectral density, D_{ϵ}, is essentially evenly distributed across the Nyquist bandwidth, which ranges from direct current (DC) to half the sampling frequency (Fs/2), is given by [49]:

$$D_{\epsilon}(f) = \frac{2P_{\epsilon}}{F_s} \tag{3.28}$$

The frequency range of interest for the analogue signal is defined as [0, f_{max}]. According to Eq. (3.22), the Nyquist rate is $2f_{max}$. When an analogue signal is sampled at the Nyquist rate, white noise with a spectral density of $(2P_{\epsilon})/Fs$ will be distributed across the entire passband. If the sampling frequency is increased by a factor L, such that $L \cdot 2f_{max} = L \cdot F_s$ with $L > 1$, the white noise density decreases by the same factor L and spreads over the interval $[0; (LF_s)/2]$. The noise in the passband is consequently reduced by a factor of $1/L$, as illustrated in Fig. 3.15. Oversampling refers to the practice of sampling at a rate significantly exceeding the Nyquist rate [50].

Oversampling not only reduces noise but also simplifies the features of the analogue low-pass anti-aliasing filter. As seen in Fig. 3.10, the spectrum replicas are now shifted by LF_s rather than F_s. This eliminates the need for an analogue anti-aliasing filter with a severe cutoff and stopband at $F_s/2$. Instead, the stopband is at $(LF_s)/2$, which is distant from the passband. As a result, the transition band fades gradually, yielding a reduced order filter.

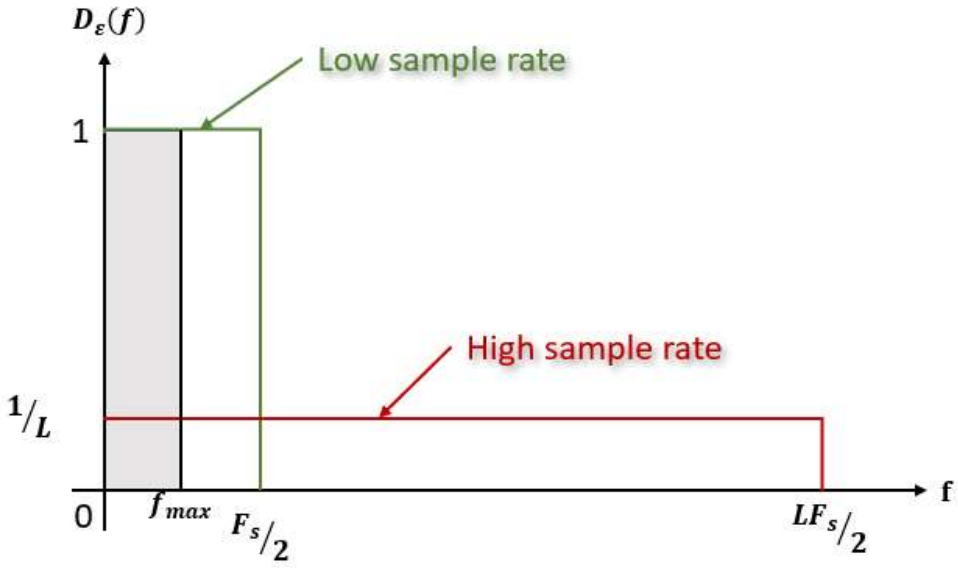

Fig. 3.15 *Spectral density of quantization noise, comparing scenarios with and without oversampling.*

The analogue anti-aliasing filter does not reject frequency values inside the range [Fs/2;\ (LFs)/2], hence they must be filtered in software. This occurrence is represented in Figure. 3.16.

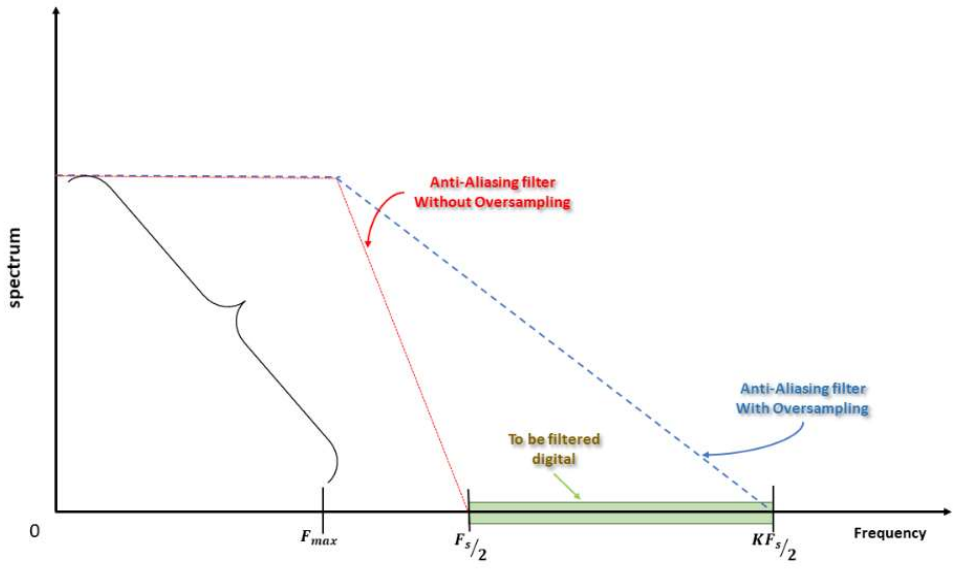

Fig. 3.16 *The Characteristics of Anti-aliasing Filters in scenarios with and without Oversampling*

3.5.5 Configuration of Multi-Channel

In the preceding three subsections, the descriptions were provided with regard to a singular input signal. However, multiple measurements must be analyzed and processed by the numerical relay. To meet this requirement, two primary multi-channel configurations are commonly utilized: the non-multiplexed structure and the multiplexed structure. To obtain multiple signals, the simplest approach involves duplicating each fundamental component of the DAQ system m times, where m represents the number of input signals to be converted. This produces the structure illustrated in Fig. 3.17, with the interposed CTs and VTs omitted for the sake of simplicity. With this configuration, filtering, sampling, and quantization processes are executed concurrently across all channels. Now, if the S/H functions are governed by a common signal, it indicates that the input signals are sampled concurrently. Thanks to this feature, there is no phase difference between the channels. This constitutes a significant advantage in scenarios where a protection algorithm analyzes the phase angles across multiple channels, such as in directional protection. The primary disadvantage of the non-multiplexed configuration is its cost, as the ADC is typically the most expensive element of the data acquisition system. [51].

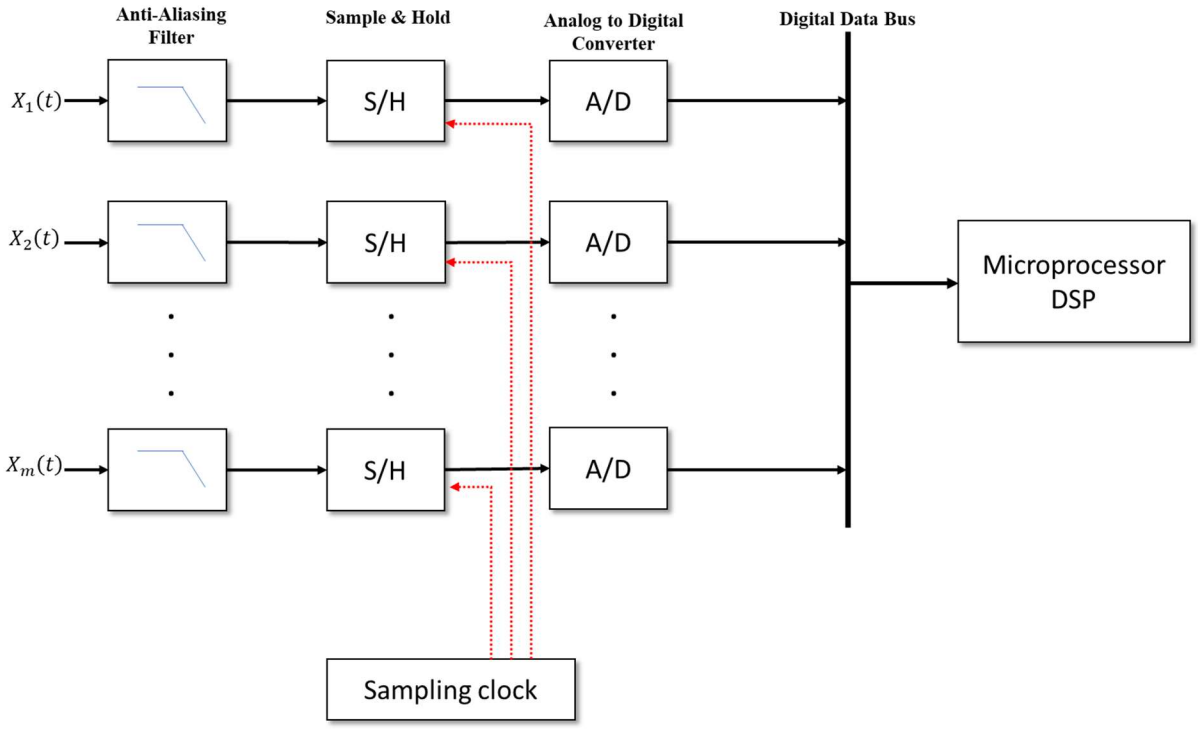

Fig. 3.17 *Non-multiplexed DAQ structure*

The DAQ may incorporate a multiplexer to minimize costs and structural complexity, as shown in Fig. 3.5. In this system, input signals are multiplexed before being sequentially transmitted to a single ADC. To mitigate phase inaccuracies, it is essential to utilize sample-and-hold circuits for each channel.

Employing a solitary S/H circuit directly preceding the ADC results in a phase discrepancy. This structure offers significant benefits for industrial applications.

3.6 Impact of Off-Nominal Frequencies on DFT-Based Algorithms

To analyze how frequency variations influence DFT-based estimators, we begin by considering a pure sinusoidal signal $x(t)$, with frequency f_0, the mathematical expression is given by:

$$x(t) = X_m \cos(2\pi f_0 t + \varphi_x) \tag{3.29}$$

where: Xm denotes the peak value of $x(t)$ and φ_x represents the beginning phase angle of $x(t)$. Eq.(3.30) models the signal assuming nominal power system frequency operation. Correct phasor computation using DFT necessitates defining the relationship linking sampling frequency Fs to the fundamental system frequency according to:

$$F_s = N \times f_0 \tag{3.30}$$

Sampling signal $x(t)$ at constant frequency F_s generates the discrete sequence x[n] described in Eq.3.8 contains N samples collected over exactly one cycle of the fundamental component. In this setup, the one-cycle DFT approach described in Eq.(3.9) allows for error-free fundamental phasor estimate as long as aliasing distortion has been successfully removed by anti-aliasing filters. Power systems do not consistently operate at their nominal frequency. Dynamic load variations and generation-demand discrepancies, exacerbated by the widespread utilization of intermittent renewable energy sources and dispersed generation assets, result in constant fluctuations of the real frequency *f*. Under these circumstances, the sample plan specified in Eq.(3.31) is rendered inappropriate for universal application. To illustrate this limitation, consider a sinusoidal waveform *y(t)* at a perturbed frequency *f*, expressed as:

$$y(t) = Y_m \cos\left(2\pi f_0 t + \varphi_y\right) \tag{3.31}$$

Where: Y_m denotes the peak value of $y(t)$ and φ_y represents the beginning phase angle of $y(t)$

The sample set $y[n]$, derived from the sampling procedure according to Eq. (3.31), is presented below:

$$y(t) = Y_m \cos\left(\frac{2\pi f}{N f_0} n + \varphi_y\right) \tag{3.32}$$

Sampling frequency F_s ceases to be an integer multiple of f since Eq.(3.33) admits no integer simplification. This mode of sampling is termed asynchronous sampling, characterized by data windows spanning non-integer cycle counts. DFT methodology fundamentally assumes that discretized signals repeat periodically with period equal to the N-point observation window. Asynchronous sampling invalidates this premise the implied periodic repetition no longer constitutes a pure cosine function and manifests endpoint discontinuities. Such abrupt windowing of off-nominal frequency signals produces inaccurate phasor determinations. This adverse phenomenon commonly known as the leakage effect[52]. Figure 3.18 illustrates this behavior through full-cycle DFT application. Two test signals appear:

$m(t) = \sqrt{2}\,cos(2\pi f_0 t)$ and $n(t) = \sqrt{2}\,cos(2\pi(f_0 + 5)t)$, both digitized at 2400Hz with DFT processing executed at t=0.04s. The selected data windows are highlighted, and their spectral representations are shown within $[0;\ F_s/2]$ for presentational clarity. Signal *m(t)* yields 48 samples per signal complete cycle, and spectral analysis verifies error- free fundamental phasor magnitude extraction expected. In contrast, n(t)'s 48 samples encompass slightly more than one cycle. As a result, spectral demonstrates fundamental frequency amplitude reduction accompanied by energy spreading into neighboring spectral components.

The impact of spectral leakage on the target phasor can be demonstrate analytically and visualized graphically. Consider a cosine waveform with off-nominal angular frequency ω, formulated as:

$$x(t) = X_1\,cos(\omega t + \emptyset_1) \tag{3.33}$$

X_1 denotes the fundamental component peak amplitude. ω is the non-nominal angular frequency, $\omega = 2\pi f = \omega_0 + \Delta\omega$, and $\emptyset_1$ represents the initial phase angle of the fundamental component.

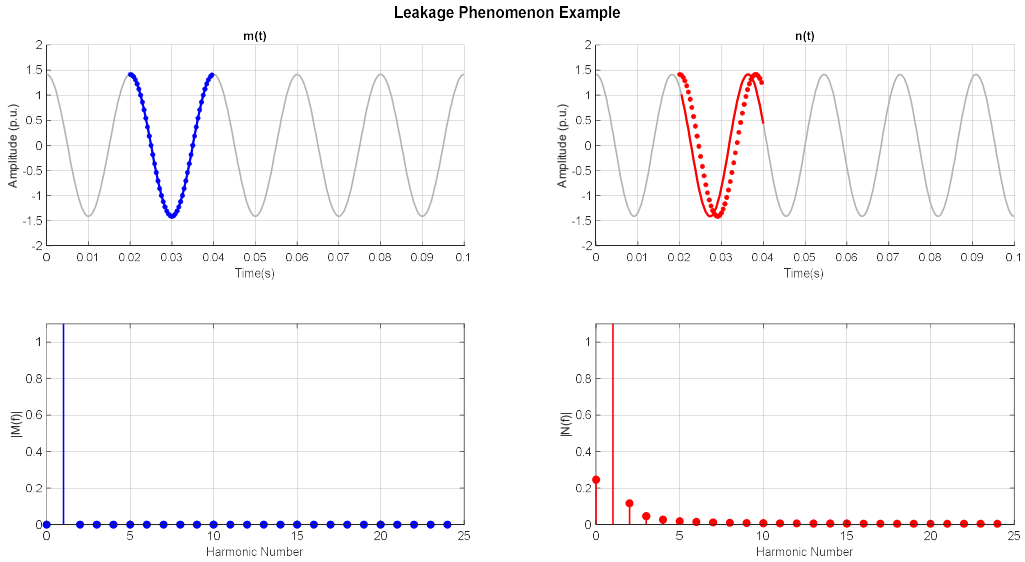

Fig. 3.18 *Leakage phenomenon example*

The calculated fundamental frequency phasor, $\overline{X^{(r)}}$, evaluated at discrete time index r, is presented below (Mathematical derivation appears in Appendix B, where an off-nominal angular frequency ω cosine waveform with superimposed m^{th} harmonic components demonstrates the relationship between the ideal phasor and the computed result.):

$$\bar{X}^{(r)} = \bar{P}_1^{(r)}\bar{X}_1 + \bar{Q}_1^{(r)}\bar{X}_1^* \tag{3.34}$$

$$\bar{P}_1^{(r)} = \frac{sin\left(\frac{\pi\Delta f}{f_0}\right)}{N\,sin\left(\frac{\pi\Delta f}{f_0}\right)}\, e^{j\pi\frac{(N-1)}{N}\frac{\Delta f}{f_0}}\, e^{\frac{2\pi\Delta f}{f_0}r} \tag{3.35}$$

$$\bar{Q}_1^{(r)} = \frac{sin\left(\frac{\pi\Delta f}{f_0}\right)}{N\, sin\left(\frac{\pi\Delta f}{f_0}\right)}\, e^{-j\pi\frac{(N-1)}{Nf_0}(\Delta f + 2f_o)} e^{-j\frac{2\pi}{Nf_0}(\Delta f + 2f_o)r} \tag{3.36}$$

where $\Delta f = f - f_0$ and f is the frequency deviation.
Equation (3.35) expresses the erroneous computed phasor $X^{(r)}$ as a function of the true phasor $\overline{X_1}$. To gain deeper insight into the estimation errors affecting the accurate fundamental frequency phasor, initially consider that the input signal undergoes evaluation at sampling instant $r = 0$. Under this condition, Eq. (3.35) might be reformulated as follows:

$$\bar{X}^{(0)} = \frac{sin\left(\frac{\pi\Delta f}{f_0}\right)}{N\, sin\left(\frac{\pi\Delta f}{f_0}\right)}\, e^{j\pi\frac{(N-1)}{N}\frac{\Delta f}{f_0}} e^{\frac{2\pi\Delta f}{f_0}r}\, \overline{X_1} + \frac{sin\left(\frac{\pi\Delta f}{f_0}\right)}{N\, sin\left(\frac{\pi\Delta f}{f_0}\right)}\, e^{-j\,\frac{(N-1)}{Nf_0}(\Delta f + 2f_o)} e^{-j\frac{2\pi}{Nf_0}(\Delta f + 2f_o)r}\, \bar{X}_1^* \tag{3.7}$$

The phasor estimation that is computed can be broken down into two distinct parts: a phasor and its complex conjugate, which rotate in opposite directions within the complex plane. While the phasor $\overline{X_1}$ rotates in a counterclockwise with an angular velocity $\Delta\omega$ rad/s, while complex conjugate of rotates clockwise at $\Delta\omega + 2\omega_0$ rad/s. Additionally, both phasors $\overline{X_1}$ and $\overline{X_1^*}$ are scaled by complex weight factors $\overline{P_1^{(0)}}$ and $\overline{Q_1^{(0)}}$ respectively, whose magnitudes depend on the frequency deviation. at $\Delta\omega$ rad/s. Additionally, a complex factor, and, respectively, is multiplied by each of the two phasors, $\overline{X_1}$ and $\overline{X_1^*}$, and the values of these factors depend on the frequency deviation. Qualitatively, these complex gains both attenuate and angularly displace the phasors the complex gains shift the phasors $\overline{X_1}$ and $\overline{X_1^*}$ in the complex plane, illustrated in Fig. 3.19.

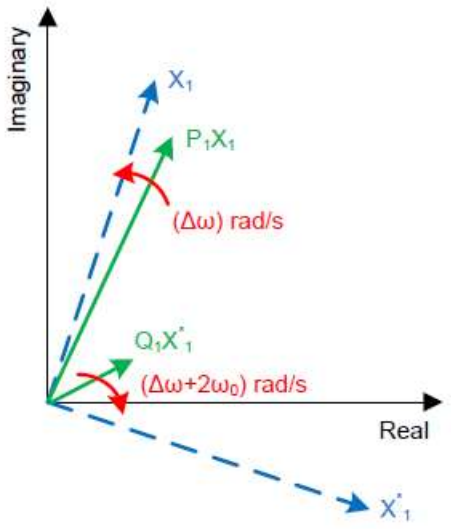

Fig.3.19 *Qualitative representation of DFT-based estimation at off-nominal frequency*

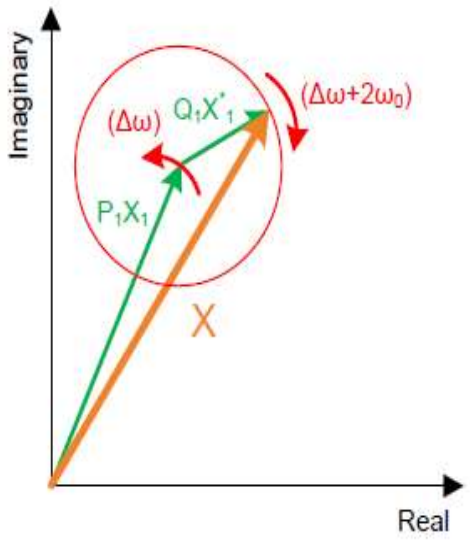

Fig.3.20 *Overall estimation error of DFT-methods at off-nominal frequency*

The red circular trajectory depicted in Fig. 3.20 represents the combined influence of complex coefficients $\bar{P}_1^{(0)}$ and $\bar{Q}_1^{(0)}$, on $\bar{X}^{(0)}$ on the estimated phasor $\bar{X}^{(0)}$. The phasor $\bar{X}^{(0)}$'s position along this circle, rotating at $\Delta\omega$ rad/s angular rate, varies with the sampling time "r" . the path described by phasor $\bar{X}^{(r)}$ constitutes an ellipse whose angular orientation is depends on $\overline{X_1}$ initial phase angle. To verify this assertion Eq. (3.38) may be expressed in more recognized notation through decomposition into real and imaginary parts:

$$\left(\frac{\Re\{\bar{X}^{(0)}\}}{\left(\Re\left\{\bar{P}_1^{(0)}\right\} + \Re\left\{\bar{Q}_1^{(0)}\right\}\right)|\overline{X_1}|}\right)^2 + \left(\frac{\Im\{\bar{X}^{(0)}\}}{\left(\Re\left\{\bar{P}_1^{(0)}\right\} - \Re\left\{\bar{Q}_1^{(0)}\right\}\right)|\overline{X_1}|}\right)^2 = 1 \qquad (3.38)$$

$\left(\Re\left\{\bar{P}_1^{(0)}\right\} + \Re\left\{\bar{Q}_1^{(0)}\right\}\right)|\overline{X_1}|$ is the major radius , $\left(\Re\left\{\bar{P}_1^{(0)}\right\} - \Re\left\{\bar{Q}_1^{(0)}\right\}\right)|\overline{X_1}|$ is the minor radius.

Equation (3.39) demonstrates that ellipse eccentricity increases with growing frequency deviation magnitude. From a graphic perspective, the leakage effect distorts the phasor trajectory from an ideal circular path, a circle with radius matching the RMS value of the input waveform. Instead, all phasor estimates trace an elliptical locus, signifying that estimation magnitude varies continuously as a function of sample index. This observation holds only when the input signal remains free from harmonic contamination. The influence of harmonic content during frequency deviations can be analyzed through graphical examination, particularly by considering the frequency response characteristics of the full-cycle DFT algorithm. For this analysis, the methodology presented in [41] is employed. Reference [41] established that DFT-based estimator constitute non-linear algorithm since both the magnitude and phase computations involve non-linear operations, as illustrated in Figs. 3.3 and 3.4. These non-linear operations comprise square root extraction and arctangent calculation. According to Fig. 3.3,and considering the cosine waveform Eq.(3.8), namely $x[n] = X_m cos((2\pi n)/N + \varphi)$, the fundamental magnitude estimate $\overline{X1[n]}$ can be formulated as follows:

$$\overline{X_1[n]} = \frac{1}{\sqrt{2}}\left(H_{1,c}^2 + H_{1,s}^2 + \sqrt{H_{1,c}^4 + H_{1,s}^4 + 2\cdot H_{1,c}^2 + H_{1,s}^2 \cdot \cos\left(2\left(\theta_{1,c} - \theta_{1,s}\right)\right)} \cdot \cos(2\omega n T_s + \theta)\right)^{\frac{1}{2}} \cdot \overline{X_1} \qquad (3.39)$$

$$H_{1,c} = \left|H_{1,c}(\mathcal{Z})\right| \qquad see\ (3.15)$$

$$H_{1,s} = \left|H_{1,s}(\mathcal{Z})\right| \qquad see(3.16)$$

$$\theta_{1,c} = \angle H_{1,c}(\mathcal{Z})$$

$$\theta_{1,s} = \angle H_{1,s}(\mathcal{Z})$$

$$\theta = arctan\left(\frac{H_{1,c}^2 \sin\left(2\left(\varphi + \theta_{1,c}\right)\right) + H_{1,s}^2 \sin\left(2\left(\varphi + \theta_{1,s}\right)\right)}{H_{1,c}^2 \cos\left(2\left(\varphi + \theta_{1,c}\right)\right) + H_{1,s}^2 \cos\left(2\left(\varphi + \theta_{1,s}\right)\right)}\right)$$

Eq. (3.40) demonstrates that the magnitude estimate fluctuates depending on the sample "n" in this case as well. Letting $cos(2\omega nTs + \theta) = 1$ yields the highest value, while $cos(2\omega nTs + \theta) = -1$ yields the lowest. Thus, by examining the magnitude estimate's variation range, which is bounded by two limits, It is possible to look at the magnitude reaction of a full-cycle DFT. Below are the normalized top and lower envelopes, respectively:

$$\frac{max\left(\overline{X_1[n]}\right)}{\overline{X_1}} = \frac{1}{\sqrt{2}}\left(H_{1,c}^2 + H_{1,s}^2 + \sqrt{H_{1,c}^4 + H_{1,s}^4 + 2 \cdot H_{1,c}^2 + H_{1,s}^2 \cdot \cos\left(2\left(\theta_{1,c} - \theta_{1,s}\right)\right)}\right)^{\frac{1}{2}} \quad (3.40)$$

$$\frac{min\left(\overline{X_1[n]}\right)}{\overline{X_1}} = \frac{1}{\sqrt{2}}\left(H_{1,c}^2 + H_{1,s}^2 - \sqrt{H_{1,c}^4 + H_{1,s}^4 + 2 \cdot H_{1,c}^2 + H_{1,s}^2 \cdot \cos\left(2\left(\theta_{1,c} - \theta_{1,s}\right)\right)}\right)^{\frac{1}{2}} \quad (3.41)$$

Figure 3.21 illustrates the operating limits of a DFT-based phasor estimation algorithm when nominal system frequency 50Hz is assumed. Although this may not be immediately apparent, the amplitude response of the DFT differs slightly from that of ideal cosine and sine filters. The shaded region in the figure represent the magnitude values produced by algorithm for arbitrary input frequencies, highlighting the effect of spectral leakage. When the input signal exactly matches the nominal fundamental frequency, the algorithm maintains a constant gain of $1/\sqrt{2}$, thereby yielding an accurate phasor estimate. However, deviations from the nominal frequency introduce oscillation in estimated magnitude, with an angular frequency equal to the sum of the nominal angular frequency and the frequency deviation for the fundamental component($\omega_0 + \Delta\omega$ rad/s). When harmonics are present in addition to an off-nominal fundamental component, the corresponding magnitude variations of each harmonic can be directly inferred from the algorithm's frequency response. As shown in Figure 3.21, a fundamental frequency deviation of +5 Hz causes the estimated phasor magnitude to oscillate between approximately 93.66% of the true value, corresponding to transient underestimation, and about 103.07%, corresponding to transient overestimation. Such inaccuracies can significantly affect how well protection systems work. Underestimating values might delay or prevent relays from working correctly during faults.

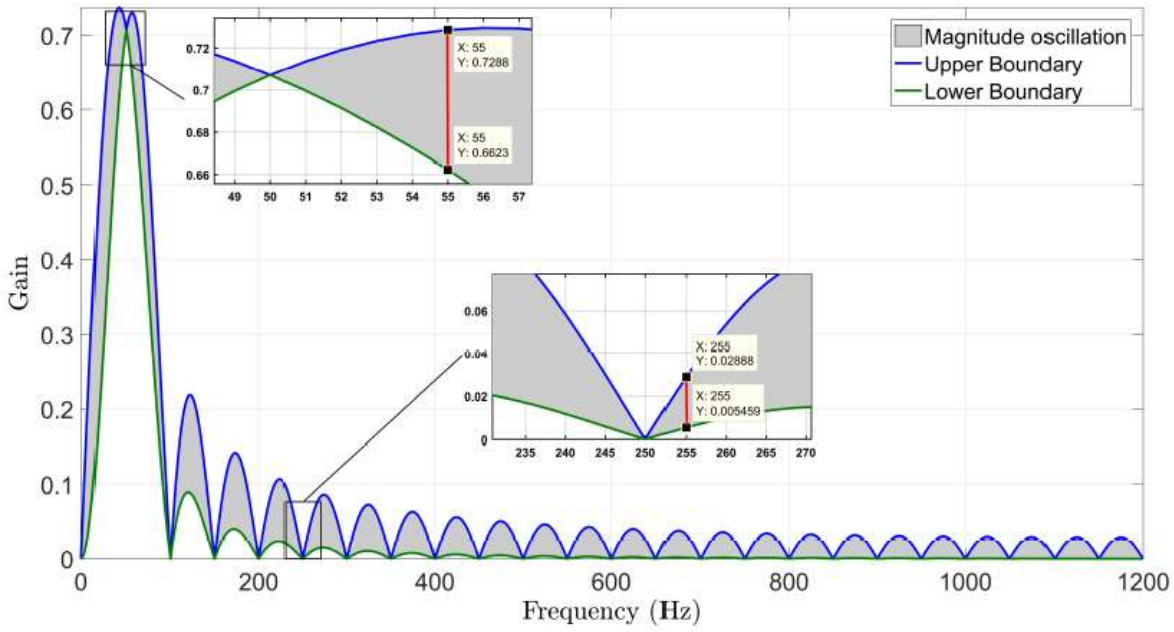

Fig. 3.21 *Effect of Off-nominal Signal Frequency on Phasor Estimation*

In contrast, overestimating values could cause unnecessary tripping during normal operation. For example, an instantaneous overcurrent relay with a $1p.u.$ pickup setting will trip if the incorrect value is above this threshold. In this case, the relay's reach is about $1 - 1/1.0307 \approx 2.98\%$ farther than its set value. Conversely, at 55Hz, the same relay shows an underreach of roughly $1/0.9366 - 1 \approx 6.78\%$, which could reduce its ability to detect faults. If a fifth harmonic component is superimposed on the off-nominal fundamental signal, additional errors are introduced. Rather than being fully attenuated, the harmonic magnitude estimate fluctuates between approximately $5.46 \times 10^{-3}\ p.u.$ and $28.88 \times 10^{-3}\ p.u.$, as illustrated phasor calculation, exacerbating the overall estimation error.

In conclusion, the DFT-based phasor estimation technique is the most prevalent method in commercial numerical relays, owing to its simplicity, robustness, and typically excellent accuracy in steady-state conditions. Nevertheless, spectral leakage inherent to the DFT framework degrades estimation accuracy whenever the signal frequency departs from its nominal value. While the resulting errors are typically modest for small frequency deviations, they become increasingly significant under large frequency excursions. Such condition relevant in generator protection applications. For instance, hydroelectric units may experience speed up to 1.5 times the nominal value following load rejection, whereas gas turbines and pumped-storage units may operate at frequencies as low as 0.3 per unit during startup phases. Consequently, protective relays intended for generator protection must deliver reliable and accurate phasor measurements across a wide frequency range in order to prevent erroneous overreach or underreach and to ensure dependable protection performance during sever frequency deviations.

3.7 Reducing the impact of leakage on DFT estimators

3.7.1 Frequency Synchronization Techniques

Frequency tracking and frequency error compensation are the two primary conventional methods used in protective relays to address the DFT leakage issue during frequency variations. The most well-known method is frequency tracking, which was originally used in [54]. Fig. 3.22, which considers the standard oversampling method, illustrates the technique's basic idea.

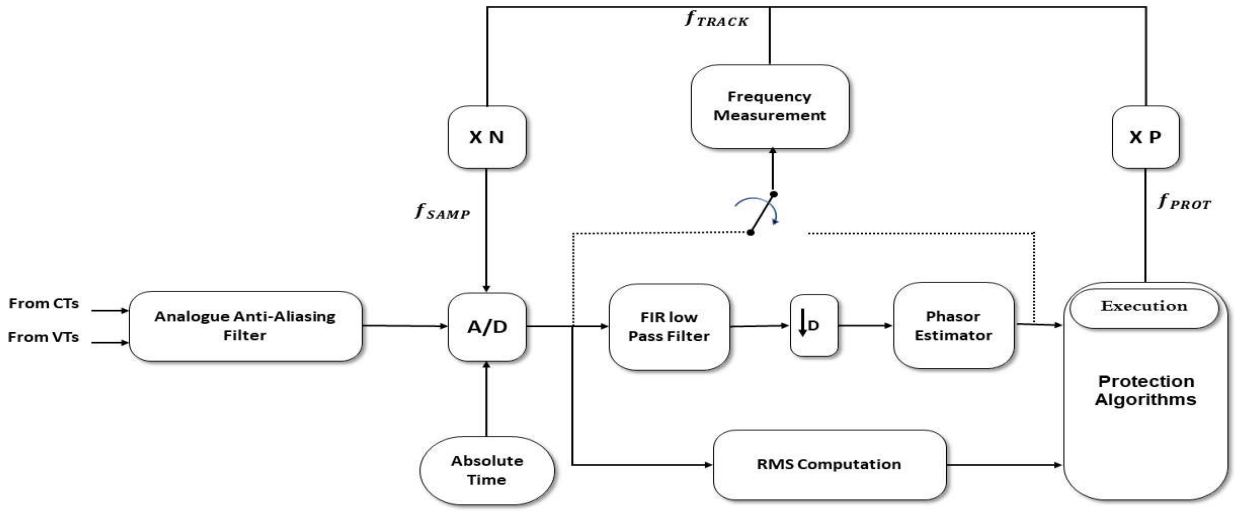

Fig. 3.22 *Conceptual diagram of Frequency Tracking implementation in digital protective relays*

Successful frequency tracking implementation requires initial accurate determination of the actual system frequency. This measurement can be accomplished using one of the algorithms described in section 3.8. assuming sufficient frequency estimation accuracy, the measured frequency value enables sampling rate synchronization by multiplying this estimate by the sample count N yield f_{SAMP}. This adjustment is achieved by modifying the sampling clock frequency. So, if N=48 and $f_0 = 50\ Hz$, when the system frequency changes to 55Hz, the relay samples at $Fs = 48 \times 55 = 2,640\ Hz$, not 2,400Hz. So, no matter how much the system frequency changes, the samples-per-cycle ratio stays the same. This lets you get a correct DFT phasor estimate. In terms of graphics, frequency tracking changes the full-cycle DFT frequency response in a way that the unity gain $(1/\sqrt{2})$ stays locked to the system frequency that it is at the moment. The protection function execution at a specific rate f_{PROT}, which is conventionally associated with the tracked frequency, f_{TRACK}. This enables the protection functions to be carried out each time the required quantity of samples has been collected. For example, the output contacts, logic schemes, and protection elements are changed twice every cycle, or per $N/2$ samples, if P equals 2. Over time, the frequency tracking system shown in Fig. 3.22 has changed to take advantage of advancements in DSP processing power. The full-digital frequency tracking solution serves as the

foundation for the new techniques. [55] provides an illustration of this type of implementation. By using interpolations (resampling schemes), these techniques aim to replicate the frequency tracking with drivable ADC implementation. The ADC's sample clock is now fixed with regard to Fig. 3.23 and can be synchronized to an absolute time reference. To enhance the resolution of integrated digital fault recorder functionality, the ADC f_{SAMP} sample rate can be set higher than the one utilized to execute the protection algorithms (f_{RESAMP}).

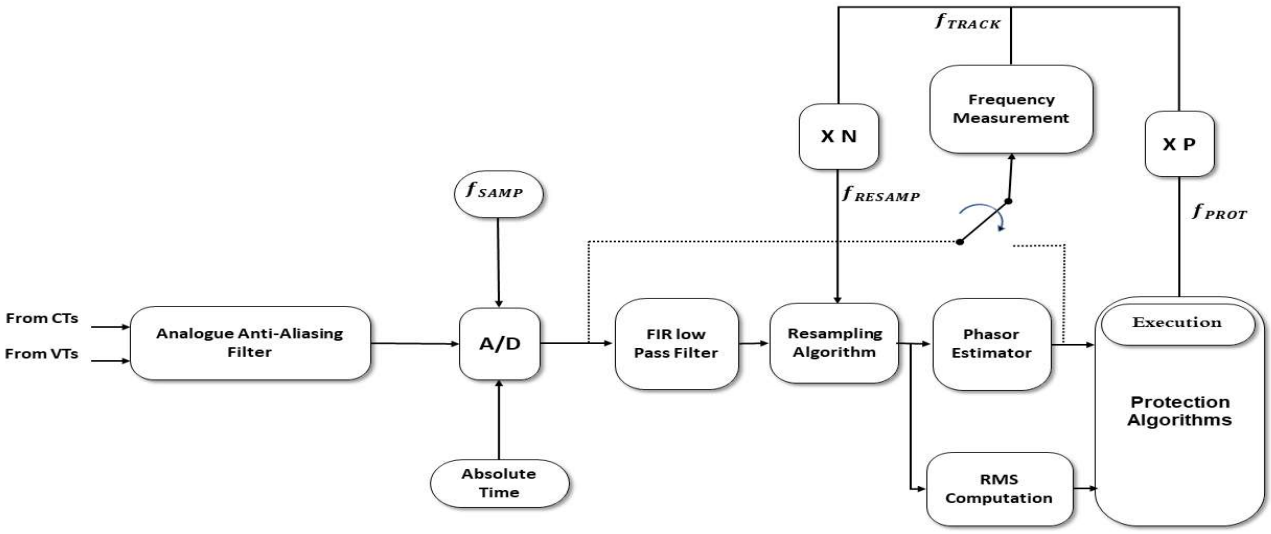

Fig. 3.23 *Conceptual diagram of Frequency Tracking implementation through resampling algorithm*

3.7.2 Compensation for frequency errors

The uniform sample rate architecture serves as the foundation for the frequency error compensation technique. The essential idea is to use calibration factors, as shown in Fig. 3.24, to estimate the predominant system frequency in order to correct the influence of the leakage phenomena. [56] contains one potential implementation of the method. In order to calculate the precise phasor using the complex gains $\overline{P_1^{(r)}}$ and $\overline{Q_1^{(r)}}$ in Eqs. (3.36) and (3.37), this technique uses a post-processing layer. Starting from Eq. (3.35), the correction coefficients along with erroneous phasor estimate $\overline{X^{(r)}}$, the true phasor $\overline{X_1}$ and its conjugate $\overline{X_1^*}$ are first expressed using their Cartesian components. These component values are then organized into a 2×2 matrix structure as indicated:

$$\begin{bmatrix} \Re\{\overline{X_1}\} \\ \Im\{\overline{X_1}\} \end{bmatrix} = \begin{bmatrix} \Re\left\{\overline{P_1^{(r)}}\right\} + \Re\left\{\overline{Q_1^{(r)}}\right\} & \Re\left\{\overline{Q_1^{(r)}}\right\} - \Re\left\{\overline{P_1^{(r)}}\right\} \\ \Im\left\{\overline{P_1^{(r)}}\right\} + \Im\left\{\overline{Q_1^{(r)}}\right\} & \Re\left\{\overline{P_1^{(r)}}\right\} - \Re\left\{\overline{Q_1^{(r)}}\right\} \end{bmatrix}^{-1} \cdot \begin{bmatrix} \Re\{\overline{X_1}\} \\ \Im\{\overline{X_1}\} \end{bmatrix} \tag{3.42}$$

$$\Re\left\{\overline{P_1^{(r)}}\right\} = \frac{\sin\left(\frac{\pi\Delta f}{f_0}\right)}{N\sin\left(\frac{\pi\Delta f}{Nf_0}\right)} \cos\left(\left(\frac{\pi\Delta f}{Nf_0}\right)(N - 1 + 2r)\right) \tag{3.43}$$

$$\Im\left\{\overline{P_1^{(r)}}\right\} = \frac{\sin\left(\frac{\pi\Delta f}{f_0}\right)}{N\sin\left(\frac{\pi\Delta f}{Nf_0}\right)}\sin\left(\left(\frac{\pi\Delta f}{Nf_0}\right)(N-1+2r)\right) \tag{3.44}$$

$$\Re\left\{\overline{Q_1^{(r)}}\right\} = \frac{\sin\left(\left(\frac{\pi}{f_0}\right)(\Delta f+2f_0)\right)}{N\sin\left(\frac{\pi\Delta f}{Nf_0}+\frac{2\pi}{N}\right)}\cos\left(\left(-\frac{\pi(\Delta f+2f_0)}{Nf_0}\right)(N-1+2r)\right) \tag{3.45}$$

$$\Im\left\{\overline{Q_1^{(r)}}\right\} = \frac{\sin\left(\left(\frac{\pi}{f_0}\right)(\Delta f+2f_0)\right)}{N\sin\left(\frac{\pi\Delta f}{Nf_0}+\frac{2\pi}{N}\right)}\sin\left(\left(-\frac{\pi(\Delta f+2f_0)}{Nf_0}\right)(N-1+2r)\right) \tag{3.46}$$

The correction matrix specified in Equation. (3.43) can undergo off-line computation for a range of frequency shifts Δ*f*, memory storage through look-up table implementation, followed by direct utilization for erroneous phasor correction. This technique eliminates runtime matrix calculation requirements each time precise phasor values are needed, conserving processing resources. The same procedure applies to harmonic component phasors, but demands dedicated correction matrices each harmonic frequency analyzed. Note that frequency offset compensation methods inherently presume harmonic-free input signals without unwanted spectral content. Consequently, adequate signal conditioning must ensure input waveform contain exclusively the desired component.

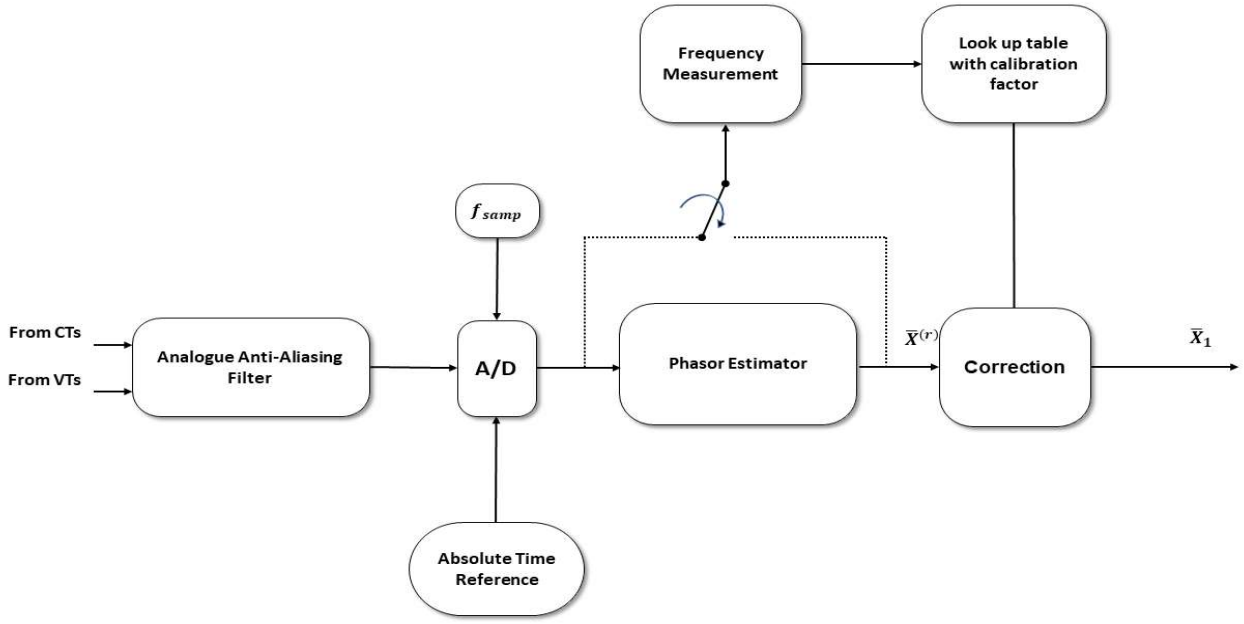

Fig.3.24 *Simplified frequency error compensation implementation*

3.8 Review of power system frequency estimate techniques

Section 3.6 demonstrated the DFT's susceptibility to frequency variations and characterized the spectral leakage phenomenon. Following this, Section 3.7 presented two conventional protection relays strategies for addressing leakage: frequency synchronization and frequency compensation. Frequency synchronization employs frequency estimates either to modify the sample rates or to execute digital resampling algorithms. Conversely, frequency correction approaches utilize measured frequency values to apply calibration factors to DFT results. Both methodologies share frequency estimation as their foundational requirement. This constitutes one key reason why protective relays must achieve accurate system frequency measurement. Furthermore, numerous protection and control algorithms dependent on frequency measurements are routinely deployed on safeguard power systems under diverse operating scenarios. For instance, under-frequency schemes enable automatic load shedding [56], while over-frequency algorithms provide overspeed protection [57].

Protective relays must deliver rapid, real-time fundamental frequency estimations within noisy environments experiencing dynamic operation conditions. Under such circumstances, The optimal frequency measurement technique would exhibit accuracy, implementation simplicity, rapid convergence to expected values, rejects noise, and minimal computational requirements. numerous frequency measurement techniques have been proposed in technical literature attempting satisfy these objectives. Here are a few of them, however they are not all-inclusive: phasor-based , demodulation , Kalman filters , zero-crossing , and least error square . Because they are straightforward and inexpensive to compute, zero-crossing and phasor-based are the two methods most frequently used in protective relays . Both approaches are described below. Generally, voltage signals maintain higher amplitude levels and experience less contamination from noise, harmonics, and the DC offset compare to the current waveforms [58-64].

3.8.1 Using zero-crossings to assess frequency

The zero-crossings technique operating in the time domain, utilizing the temporal interval between successive zero-crossings moments when the polarity reverses between adjacent samples. given the inverse relationship between time and frequency, frequency can be derived from measured time intervals. Mathematically, for discrete sample sequence x[n], the number of zero-crossings within a specified data window containing M samples may be expressed as follows:

$$ZC = \sum_{n=r}^{r+M-1} |sgn(x[n]) - sgn(x[n-1])| \tag{3.47}$$

Where ZC represents the quantity of zero-crossings. The sign function is indicated by sgn. In Eq. (3.48), zero-crossings are detected regardless of transition direction, encompassing both rising(negative-to-positive) and falling (positive-to-negative) transitions. Consequently, the interval between two successive zero-crossings represents half the input signal's fundamental period. Alternative implementations exist, such as measuring complete cycles between unidirectional zero-crossings. Following the determination of ZC, the frequency is calculated as indicated below [65].

$$f = \frac{1}{2} \cdot \frac{ZC - 1}{t_m - t_1} \tag{3.48}$$

where the expected frequency is represented by f. The last zero-crossing in the observation window happens at tm. The first zero-crossing in the observation window happens at t_1. As shown in Fig. 3.25, sample timestamps are linearly interpolated to get the instants of time t_1 and t_m . While alternative interpolation methods can be employed, they require greater computational effort than straightforward linear interpolation. Considering the fixed sample interval T_s, the time t_1 is computed as follows:

$$t_1 = t[n-1] - \frac{x[n-1]}{x[n] - x[n-1]} T_s \tag{3.49}$$

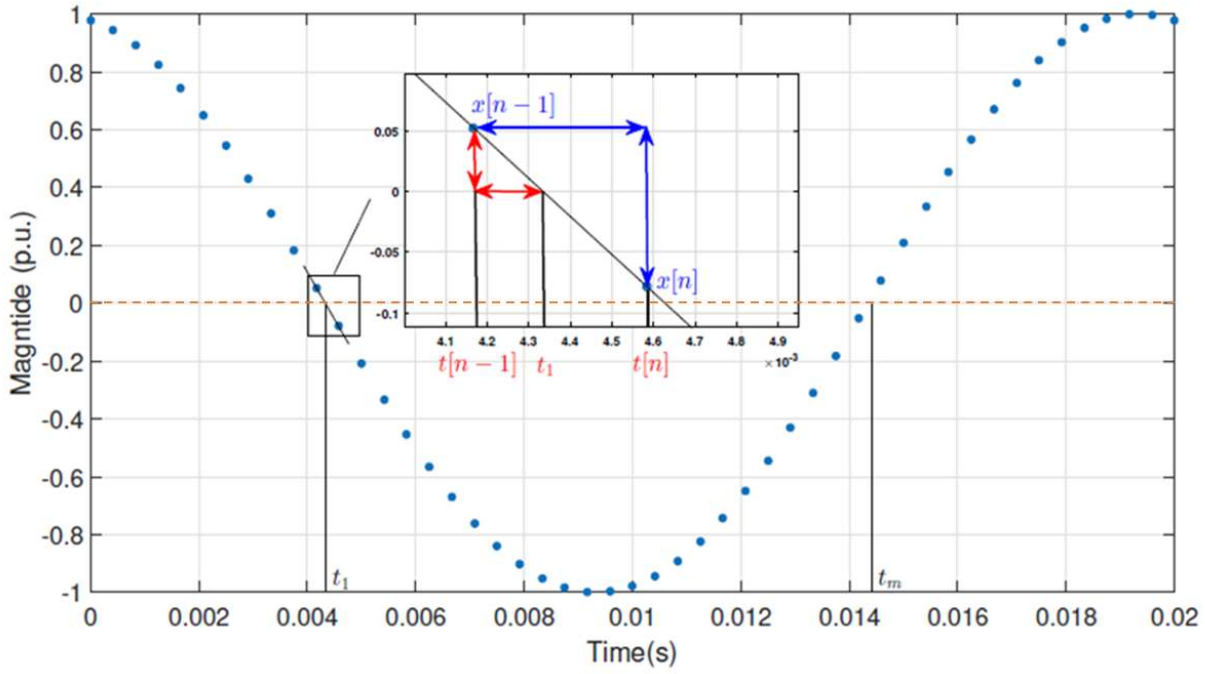

Fig. 3.25 *Zero-crossing time instant determination through interpolation*

The primary limitation of zero-crossing algorithms lies in in their complete dependence on waveform morphology. When extraneous frequency components are present alongside the fundamental, spurious zero-crossings events proliferate. Consequently, input signals require filtering prior to algorithmic processing. This filtration process takes place in two distinct stages. Initially, a pre-filtering stage eliminates specific undesirable waveform components. Pre-filtering employs either low-pass or band-pass filter configurations. Subsequently, additional post-filtering is generally employed to improve the robustness of the algorithm. This post-processing entails either aggregating multiple consecutive frequency estimates or employing specialized nonlinear filters to remove residual spurious zero-crossings that persist after pre-filtering. [65].

3.8.2 The technique based on phasors

The phasor-based approach emulates the mechanical frequency analogy of synchronous generators by calculating, within the complex plan, the angular velocity of a measured phasor [63], as shown in Fig. 3.26. This methodology was originally presented in [58], where it operated on DFT-derived positive-sequence phasors of the three-phase voltages quantities. Utilizing positive-sequence components offers advantages owing to their intrinsic filtering property during frequency variations. Specifically, under balanced system conditions, the influence of the $\overline{Q_1^{(r)}}$ term in Eq. (3.35) can be eliminated utilizing positive sequence phasors [66]. Thus, Equation (3.35) can be restructured as:

$$\overline{X^{(r)}} = \frac{\sin\left(\frac{\pi\Delta f}{f_0}\right)}{N\sin\left(\frac{\pi\Delta f}{f_0}\right)} e^{j\pi\frac{(N-1)}{N}\frac{\Delta f}{f_0}} e^{j\frac{2\pi\Delta f}{Nf_0}r} \overline{X_1} = \bar{P}_1^{(r)} \bar{X}_1 \tag{3.50}$$

The factor $\bar{P}_1^{(r)}$ provides the angular speed of the phasor $\bar{X}^{(r)}$. When the N-point DFT is executes once every n samples, Eq. (3.52) delivers $\bar{X}^{(r+n)}$:

$$\bar{X}^{(r+n)} = \frac{\sin\left(\frac{\pi\Delta f}{f_0}\right)}{N\sin\left(\frac{\pi\Delta f}{f_0}\right)} e^{j\pi\frac{(N-1)}{N}\frac{\Delta f}{f_0}} e^{j\frac{2\pi\Delta f}{Nf_0}(r+n)} \overline{X_1} \tag{3.51}$$

The phase angle differential between $\bar{X}^{(r+n)}$ and $\bar{X}^{(r)}$ is calculated as follows:

$$\Phi_{r+n} - \Phi_r = \frac{2\pi\Delta f}{Nf_0} n \tag{3.52}$$

In the implementation of Eq.(3.53), the phase angles Φ_{r+n} and Φ_r are derived by applying the four-quadrant arctangent function to the complex phasors estimates $X^{(r+n)}$ and $X^{(n)}$, respectively. Given the frequency deviation is defined as $\Delta f = f - f_0$ (Where f_0 represents the nominal frequency), the instantaneous system frequency can be extracted by analyzing the phase shift, $\Delta\Phi_r = \Phi_{r+n} - \Phi_r$, between these two phasors:

$$f = \left(\frac{N\,\Delta\,\Phi_r}{2\pi n} + 1\right)\cdot f_0 \tag{3.53}$$

Unlike zero-crossing methods, the phasor-based approach is less sensitive to harmonics or DC offset. This is because phasors are calculated using the Discrete Fourier Transform (DFT) filter. Therefore, the pre- and post-filtering steps are not required. Therefore, the phasor-based method is preferred for estimating frequency.

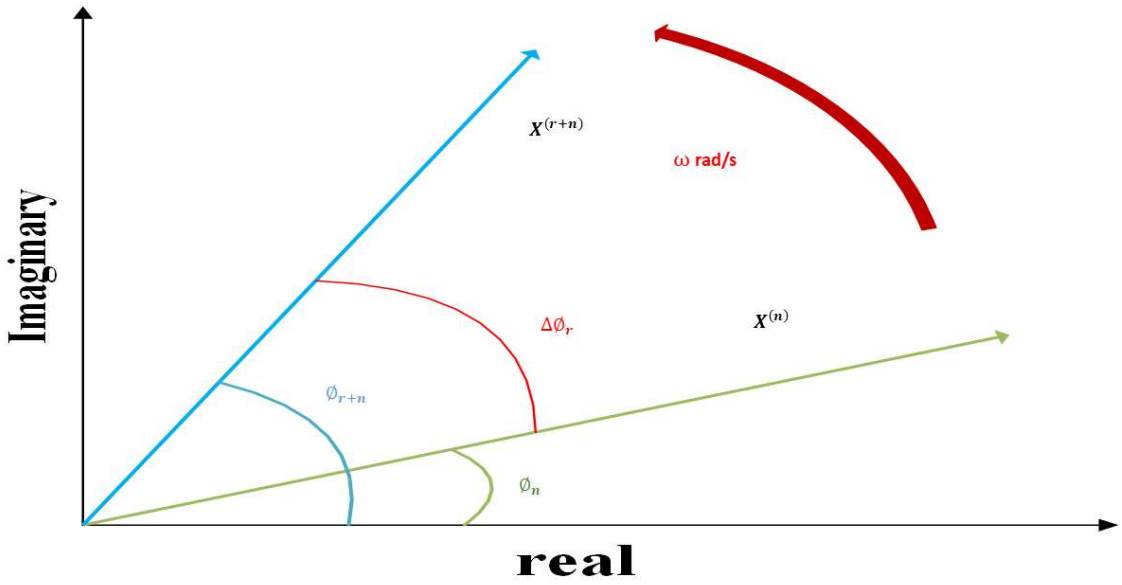

Fig. 3.26 *Rotation of phasors for frequency estimation*

3.9 The Unit of Phasor Measurement

An intelligent electronic device (IED) that provides time-synchronized, real-time measurements of voltage and/or current signals in the form of phasors is called a Phasor Measurement Unit (PMU)[67].The development of PMU technology can be traced back to earlier advances in protective relaying, most notably the Symmetrical Component Distance Relay(SCDR) introduced in the 1980s. this relay enabled the direct estimation of one of the most informative quantities in power system analysis the positive-sequence component of three-phase voltages[68]. Owing to its strong correlation with overall system operating conditions, the positive-sequence component plays a central role in power system state estimation and monitoring. The capacity to perform synchronized phasor measurements across geographically dispersed stations is a significant achievement in PMUs. Aligning all measurements to a standardized and accurate time base facilitates the direct comparison of phasors derived from various substations. By making it easier to create reliable system-wide "snapshots," this synchronized measurement framework enhances the effectiveness of power system operation, protection, monitoring, and control. [69,70].

Synchronized measurements across multiple locations become feasible by coordinating sampling clocks among deployed power system equipment. Achieving system-wide clock synchronization for all IEDs demands particular accuracy levels dictated by target application specifications. Analysis in [71] established that timing precision better than 1μs-equivalent to roughly 0.02 electrical degree at 60Hz proves necessary for coordinated phasor determination. Global Positioning System(GPS) technology satisfies this accuracy requirement. GPS provides an absolute time standard with peak timing precision of ±0.2μs. The system generates a One Pulse-Per-Second (1PPS) synchronization reference. GPS enables accurate timestamping of PMU sample data by broadcasting time-tagged data with full temporal information (year, day, hour, minute, and second). These time references follow the Coordinated Universal Time (UTC) standard [67].

All PMUs theoretically produce time-aligned phasors at specified moments, the issue of transmitting these quantities for operational use naturally emerges. Phasor data transmission of encompasses message formatting requirements and telecommunications infrastructure. Early PMU deployments prioritized data exchange between PMUs at separate geographic locations. To support these implementations, preliminary research suggested dedicated communication channels using modern-based transmission [67]. The original message structure incorporated minimal required information using binary encoding. Communication medium availability and bandwidth limitations influenced this architectural choice. Conventional 4,800-baud communication channels standard, permitting individual phasor message delivery in roughly 30ms [72].

3.9.1 Historical Overview of PMU Standards

The Institute of Electrical and Electronics Engineers (IEEE) Standard 1344, finalized in 1995, was the inaugural formal standardization of the synchronized phasor measurement concept for power systems [73]. To enhance the accuracy of time-synchronized phasor measurements, the IEEE initiated efforts to transition from Standard 1344 to Standard C37.118 in 2003. This development was driven by post-incident analyses of the 2003 North American blackout, which affected approximately 50 million individuals across the United States and two Canadian provinces [74]. By 2005,[73] was replaced by IEEE synchro-phasor Standard C37.118-2005. This revision introduced the fundamental compliance testing metric termed Total Vector Error (TVE), which quantifies the synchronized phasors measurement accuracy. To verify conformance with[73], steady-state condition tests were established. Furthermore, [73] specified the message structure for encoding phasor data.

In 2005,Brazil's Operator of National Electricity System(ONS), the Independent System Operator for the Brazilian Interconnected National Power System (NIPS), spearheaded a significant initiative for Brazilian electric power sector by implementing a large-scale Synchro-Phasor Measurement System (SPMS), for NIPS. The SPMS design objectives encompassed post-disturbance analysis, wide-area monitoring capabilities, and Energy Management System (EMS) / SCADA enhancement. As part of SPMS deployment strategy, all procured and installed PMUs required certification to guarantee the overall SPMS performance. Subsequently, ONS organized in 2009 workshop to evaluate and certify PMUs from eight vendors: ABB, Arbiter, Areva, General Electric, Qualitrol, Reason, Schweitzer Engineering Laboratories, and Siemens. The ONS PMU certification program built upon the IEEE Standard C37.118-2005 steady-state testing, supplemented with additional ONS requirements addressing dynamic performance evaluation. This marked the first comprehensive testing of various manufacturers PMUs under dynamic operating conditions. To ensure SPMS performance, identical behavior across all eight PMUs was anticipated for the test scenarios considered. However, results contradicted this expectation, yielding three significant findings [75]:

- Most tested PMUs satisfied the majority of steady-state performance criteria.
- PMU behavior under dynamic conditions exhibited substantial variation.
- The 2005 amendment of IEEE Standard C37.118 was necessary to add considerations of the dynamic performance of Phasor Measurement Units (PMUs).

Following this workshop, [73] was divided into two distinct standards: IEEE Standard C37.118.1-2011 [76] and IEEE Standard C37.118.2-2011 [77], both published in December 2011. This separation addressed two key needs. First, given the rapid advancement of communication technologies compared

to power system technology evolution, separate treatment become necessary. Second, IEEE recognized the requirement to align the real-time messaging format defined in [77] with International Electrotechnical Commission (IEC) communication standard 61850, which gained industry adoption. This harmonization enables seamless integration of synchronized phasor estimation into substations, utilizing IEC61850. An overview of [76] and [77] follows:

The IEEE Standard C37.118.1-2011 outlines the methodology for synchronized phasor measurements in power systems. This standard delineates the definitions of synchro phasors, frequency, and the measurement of Rate of Change of Frequency (ROCOF) across all operating conditions. This document outlines methods for assessing these measurements and stipulates compliance requirements with the standard in both steady-state and dynamic conditions. The standard includes requirements for time tagging and synchronization. Performance is verified using a comprehensive reference model. Moreover, the standard does not specify particular hardware, software, or computational methods for calculating phasors, frequency, or the Rate of Change of Frequency (ROCOF). Rather, the IEEE Standard C37.118.2-2011 provides a mechanism for several pieces of equipment in a power system to exchange real-time synchronized phasor measurement data. It specifies messaging compatible with any appropriate real-time communication protocol between PMUs, phasor data concentrators (PDC), and other applications. Message types, content, and utilization are defined. Data types and formatting are specified. A representative measurement system architecture, along with communication alternatives and requirements, is described.

Post-publication analysis of the signal processing reference model defined in[76] revealed its inability to satisfy most frequency and ROCOF performance specifications. Additionally, PMU Manufacturers cited excessive stringency of [76] requirements, particularly those concerning frequency and ROCOF measurements [78]. Addressing these concerns, the 2011 standard version was amended by IEEE Standard C37.118.1a-2014 [77]. Steady-state and dynamic performance requirements were relaxed to facilitate the deployment of fully compliant PMUs.

Currently, IEEE and IEC are collaborating on publishing IEC standard for PMUs, incorporating several modifications from previous IEEE versions and introducing new elements. The IEC/IEEE standard, designated as IEC Standard 60255-118-1, currently exists in draft form [IEC15]. Principal revisions include:

- Expanded reporting rate allowances,
- Reconsidered frequency definition,
- Phase angle test removal,
- Clarified step response tests procedures,
- Consideration of PMU accepting sampled values as input signals (versus analog inputs).

This work references requirements specified in the IEC Standard 60255-118-1 draft version, as it will supersede amended PMU standard upon completion.

3.9.2 Synchronized phasor measurements definition

The synchronized phasor, or synchro-phasor, of signal $x(t)$ represents the phasor defined in Eq. (3.3), where φ denotes the instantaneous (absolute) phase angle referenced to UTC. Under this framework, a nominal-frequency cosine function the synchronized to UTC serves as the reference waveform. This convention establishes that φ equals zero at UTC second transitions(1PPS timing signal), coinciding with the cosine waveform $x(t)$ reaching maximum amplitude, as illustrated in Fig.3.27. In contrast, when a positive-going zero-crossing happens at $t=0$, as shown in the sine waveform $y(t)$, the synchro-phasor angle is -90 degrees at that moment.

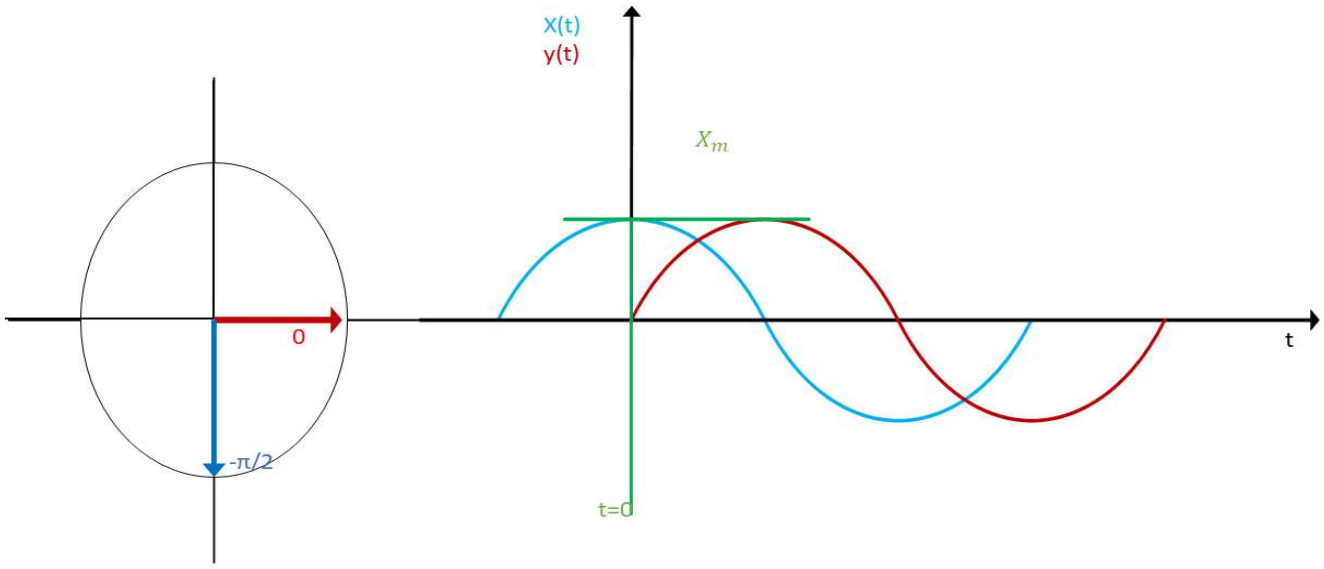

Fig. 3.27 *Illustration of synchro phasors*

Furthermore, the PMU standard defines a number of reporting rates. The number of time-tagged phasors calculated in a one-second period (between two successive 1 PPS signals) is provided by these reporting rates, which are denoted F_R in frames per second (fps). The reporting rates are set numbers that are multiples of the network's basic cycles (50/60 Hz). The following Table 3.1 reports them:

Table 3. 1 *Reporting rates permitted by the PMU standard*

System frequency (Hz)	**50**	**60**
Reporting rates (fps)	10 25 50 100	10 12 15 20 30 60 120

Generally, elevated reporting rates suit for protection and control functions requiring rapid tracking of power system transients, while reduced reporting rates serve SCADA system applications such as state

estimation and power flow analysis [77]. For illustration, a 50-fps reporting rate indicates that timestamped synchro-phasors must characterize the monitored signal at intervals $k = \{0, T_R, 2T_R, 3T_R, \ldots 50T_R, \ldots\}$, where $T_R = 1/F_R$ in seconds. Consequently, for pure 50 Hz cosine input signal, the calculated phase angles equal 0 degrees at each T_R interval. However, this condition fails when the cosine waveform exhibits non-nominal frequency f. because synchro-phasors are delivered at constant rate F_R, the phase angles of non-nominal signals advance steadily at $2\pi(f - f_0)T_R$ radians, as illustrated in Fig. 3.28, where bullet symbols • indicates estimation instants. Notably, phase angles are typically bounded within [−180; 180] range as specified in the standard [78].

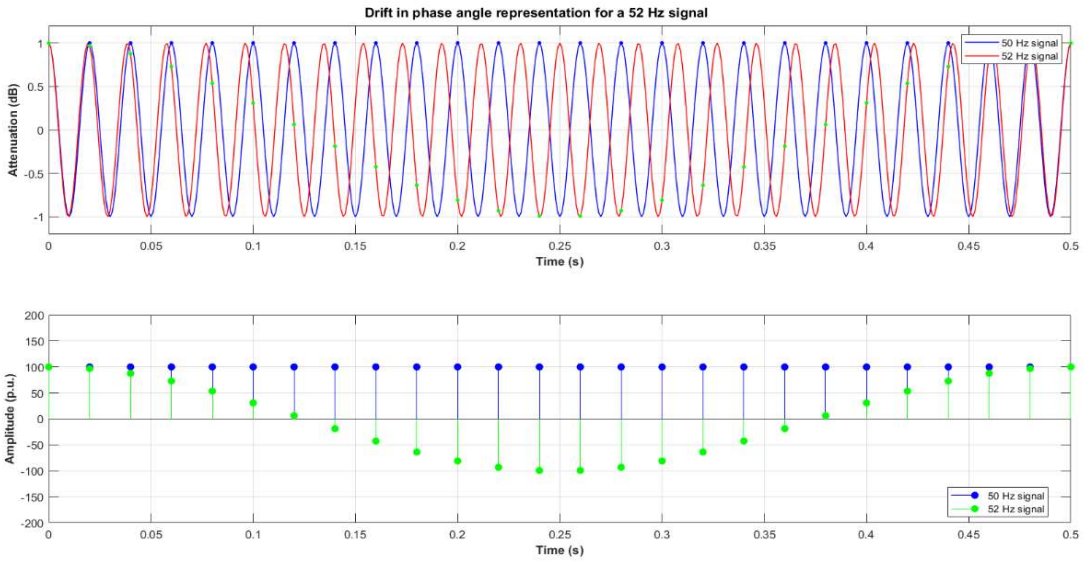

Fig. 3.28 *Drift in phase angle representation for a 52 Hz signal*

The synchro-phasor definition applies to both performance classes specified in the standard. These classifications, designated P-Class and M-Class, corresponding to protection-oriented applications and measurement-oriented applications, respectively. The principal distinction between these performance categories involves the capability to effectively suppress spurious sensitive to frequency component that may overlap the fundamental component. Typically, applications sensitive to harmonics and interharmonic distortion but accepting longer response delays require M-Class PMUs, which implement extensive filtering. Conversely, applications demanding minimal delay when responding to dynamic system changes should employ P-Class PMUs. However, this guideline connecting P and M designations to application types may not be universally apply across all potential PMU deployment scenarios. As explicitly stated in [78], the system designer bears responsibility for selecting the performance class optimally suited to specific application requirements. Finally, PMU manufacturers are no obligated to support both performance classes; vendors may offer a device conforming to only one of the two standardized classifications.

3.9.3 Measurement Requirements for PMUs

Estimation of electrical system parameters(magnitude, phase angle, frequency, and rate-of-change-of-frequency (ROCOF)), is governed by measurement precision requirements. As with any instrumentation, PMUs introduce unavoidable errors when quantifying parameters of interest. For synchro-phasor estimation, disparities between an ideal theoretical values and actual computed results are aggregated into single figure-of-merit, previously designated as TVE. This TVE metric comprises a combined measure capturing both magnitude and angular deviations. Since phase determination depends on UTC-synchronized time references, temporal errors translate directly into angular errors. To illustrate, a 1\ \mu s time discrepancy produces a 0.018 degrees phase error in 50 Hz system networks, 0.0216 degrees in 60 Hz system networks. Thus, the TVE criterion implicitly accounts for synchronization errors that vary proportionally with nominal frequency. Per [78], TVE is calculated as percentage using real and imaginary components of ideal and estimated phasor quantities:

$$TVE(k) = \sqrt{\frac{\left(\hat{X}_r(k) - X_r(k)\right)^2 + \left(\hat{X}_i(k) - X_i(k)\right)^2}{X_r(k)^2 + X_i(k)^2}} \times 100 \tag{3.54}$$

Where k represents the moment of measurement $\hat{X}_r$ represents estimated synchro-phasor real component. X_r represents theoretical synchro-phasor real component of the. $\hat{X}_i$ represents the imaginary component of the estimated synchro-phasor. X_i represents the imaginary component of the theoretical synchrophasor. For the majority of the test scenarios specified in the standard, synchro-phasor estimation must achieve maximum total vector error (TVE) of 1%. This 1%TVE threshold is reached when magnitude estimation error reaches ±1%, assuming zero phase angle error. Conversely, a phase angle deviation of ±0.01 radians alone produces1% TVE, while synchronization discrepancies of ±31μs and ±26μs at 50 Hz and 60 Hz, respectively, yield equivalent TVE values.

Following their introduction in [76], the frequency and ROCOF concepts have been refined in the most recent PMU standard revision, which endeavored to clarify instantaneous frequency interpretation. The adopted definitions utilize phase angle derivatives. To understand this approach, recall that phase angle estimates carry timestamps. Deriving frequency and ROCOF from phase angles streamlines temporal alignment across all three measurements. The standard [78] provides frequency and ROCOF definitions as follows:

"Given a sinusoidal signal:

$$x(t) = X_m \cos[\psi(t)] \tag{3.55}$$

Frequency is defined

$$f(t) = \frac{1}{\sqrt{2}} \frac{d\psi(t)}{dt} \tag{3.56}$$

The rate of change of frequency (ROCOF) is

$$ROCOF\ (t) = \frac{df(t)}{dt} \tag{3.57}$$

Frequency and ROCOF measurement errors, designated FE and RFE respectively, are calculated as the deviation between the estimated and theoretical values at identical time instants. Compared to definitions in prior standard version, the revised formulation exclude absolute values. These expressions are presented below:

$$FE(k) = f_{est}(k) - f_{th}(k) \tag{3.58}$$

In this context, FE is denoted in Hertz (Hz), f_{est} represents the estimated frequency, and f_{th} indicates the theoretical frequency.

$$FRE(k) = \frac{f_{est}(k_2) - f_{est}(k_1)}{t_{k2} - t_{k1}} - \frac{f_{th}(k_2) - f_{th}(k_1)}{t_{k2} - t_{k1}} \tag{3.59}$$

Where RFE is measured in Hz/s, t_{k1} denote the time-tag at instant $k1$ associated with the phase angle at $k1$, and t_{k2} represents the time-tag at instant $k2$. The difference between the nominal and actual frequencies, assuming that frequency is a function of time, can be written as $g(t) = f(t) - f_0$. The following is the expression for the cosine wave *x*(t) in Eq. (3.56):

$$x(t) = X_m \cos\left[2\pi \int f(t)\, dt + \varphi\right] \tag{3.60}$$

$$x(t) = X_m \cos\left[2\pi f_0 t + \left(2\pi \int g(t)\, dt\right) + \varphi\right] \tag{3.61}$$

In view of the instantaneous frequency $f(t)$, the signal's synchro-phasor is formulated by mapping the time-varying phase onto the nominal frequency reference frame as follows:

$$\overline{X(t)} = \frac{X_m}{\sqrt{2}}\, e^{j(2\pi \int g(t)\, dt + \varphi)} \tag{3.62}$$

According to the formulation introduced in Eq. (3.61) instantaneous synchro-phasor computation would, in theory, be feasible if the observation window were limited to a single sample. Digital implementation of Park's transformation are capable of such rapid estimation and have been extensively validated in [79]. In practical applications, however, phasor estimation typically performed over a finite observation interval, as is the case for DFT-based techniques. Under these conditions, the resulting phase estimate inherently aggregates the signal behavior occurring within the analysis window and therefore represents an averaged manifestation of the underlying dynamics rather than a truly instantaneous value. This observation extends equally to frequency and rate-of-change-of-frequency(ROCOF) measurements, implying that exact instantaneous estimations of these parameters are not achievable in practice. The 2011 edition of the PMU standard, which suggests placing the time-tag in the middle of the data frame used for estimation, expressly acknowledges this constraint. Consequently, the estimated phase angle corresponds to a cosine waveform referenced to the midpoint of the observation window, as illustrated in Fig. 3.28, where the window boundaries are indicated by vertical markers for a window length of *N = 9* samples.

A key implication can be inferred from Fig. 3.29. Although the synchro-phasor time reference at $T_R = 0.02\,s$, the actual computation of the synchro-phasor estimate cannot be completed until an additional $[N/2 - 1]$samples have been acquired beyond this reference instant in order to fully populate the estimation window. The overall latency of the PMU is directly influenced by the additional samples, leading to a processing delay of $([N/2 - 1] \times \Delta t_0)$seconds. Any synchro-phasor estimation approach utilizing a finite data window invariably incurs a delay of approximately half the window period.

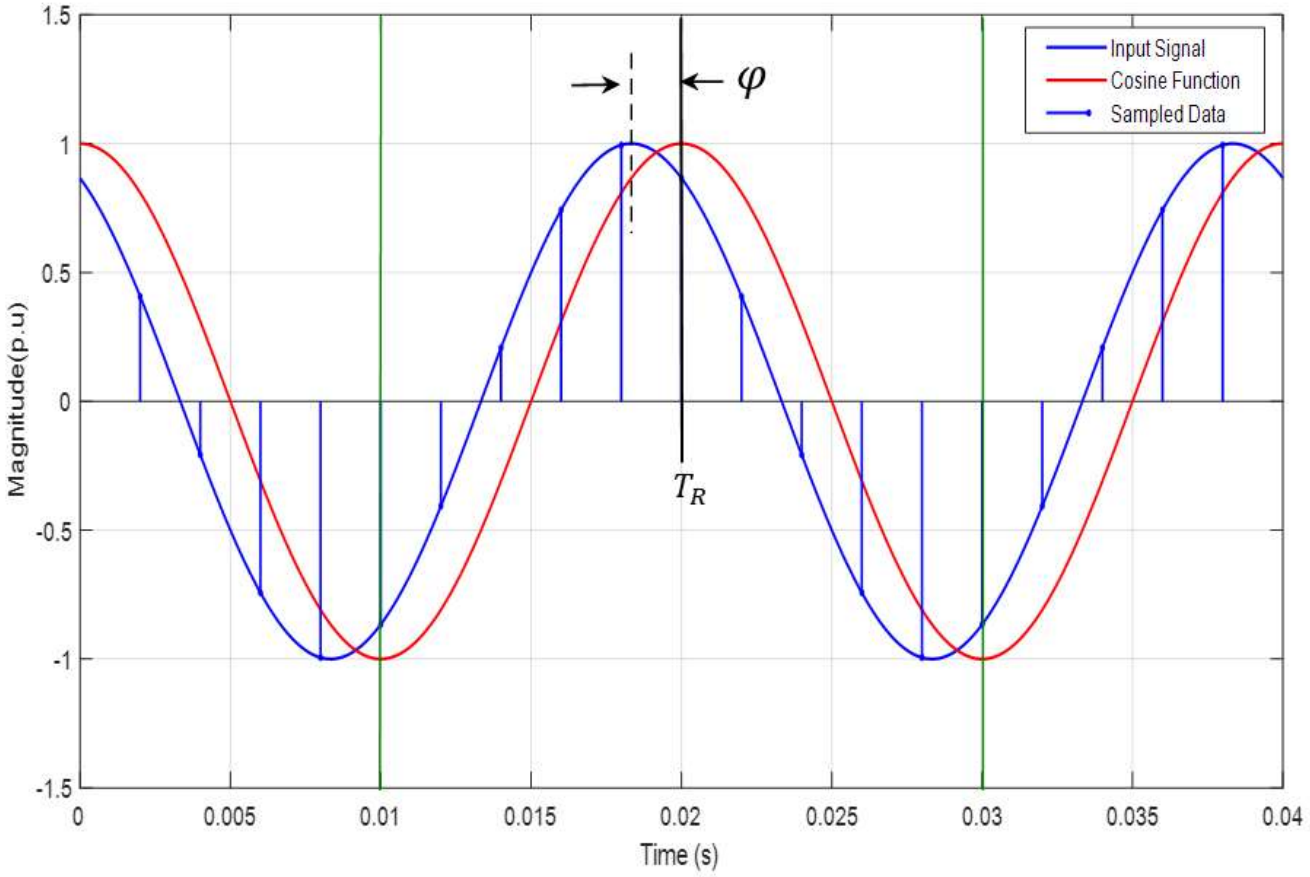

Fig. 3.29 *Time-tag assignment referenced to the midpoint of measurement window*

$$t_{lat} = \frac{2}{F_s}, \qquad being \;\; F_s = f_{nom}, \qquad for \;\; F_s > f_{nom} \tag{3.63}$$

The IEC 60255-118-1 standard formally defines this delay as PMU reporting latency. For P-Class PMU the standard specifies an upper bound on the allowable reporting latency, expressed in second. From Eq. (3.63), it becomes evident that synchro-phasor-based estimation algorithms must be designed such that no more than two fundamental-frequency cycles of data are required beyond the reporting time T_R. This constraint is crucial for ensuring precise and prompt measurements for protection and monitoring applications, while also ensuring compliance with latency standards.

3.9.4 Model for Processing Reference Signals

To satisfy the steady-state and dynamic performance requirements specified by the PMU standard, two comprehensive signal-processing reference models are presented in Appendix B of the IEC documentation[78], one corresponding to P-Class PMUs and another for M-Class PMUs. Although intended for different application objectives, both models are founded on the same underlying algorithmic principle. Specifically, they employ a quadrature demodulation, or correlation-based, approach in which the input signal is multiplied by a complex exponential synchronized with the nominal system frequency f_0, followed by the suppression of the undesired component appearing at twice the nominal frequency. Under ideal conditions namely, when the input consist of pure sinusoidal waveform at the fundamental frequency this process yield an exact synchro-phasor representation of the signal.

The complex exponential used in demodulation is broken down into its in-phase (cosine) and quadrature (sine) components in Fig. 3.30, which shows the PMU reference obtained from the IEC standard. The standard model additionally presumes that the samples obtained from the analog-to-digital converter accurately represent the original analog signal and that any delays introduced by the measurement and acquisition process are comprehensively compensated. By neglecting front-end nonidealities, the focus is placed exclusively on the algorithmic structure governing synchro-phasor estimation. Within this framework, the synchro-phasor is directly computed from a discrete set of signal samples x_k according to the following expression:

$$\bar{X}(k) = \frac{\sqrt{2}}{G} \sum_{n=-N/2}^{N/2} x[k+n] \cdot \omega[n] \cdot e^{-\frac{2\pi}{N}(k+n)} \tag{3.64}$$

In this context, N denotes FIR low-pass filter order, while $\omega[n]$ denotes FIR filter coefficients, which are contingent upon the performance class. G represents the gain of the filter, calculated using the formula $G = \sum_{n=-N/2}^{N/2} \omega[n]$.

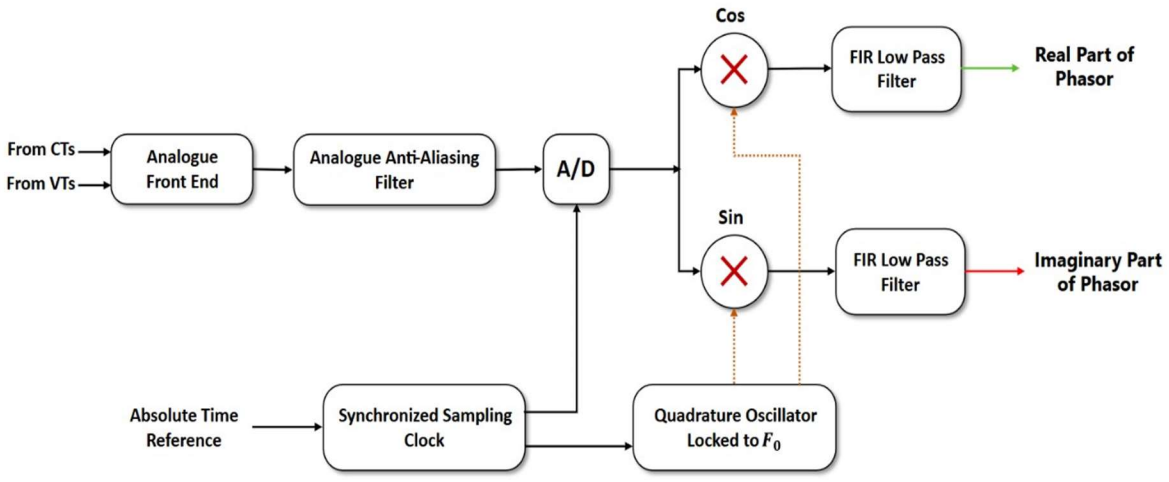

Fig. 3.30 *Simplified single phase PMU signal processing model*

Following eq.(3.64), the reference model's critical challenge involves precisely designing filters to ensure estimated synchronized phasors, frequency, and ROCOF satisfy performance class requirements. Additionally, particular attention must be address phasor computation methodology. Specifically, because the filter exhibits finite impulse response characterized (with symmetrical coefficients), its group delay equals $G_d = N/2$ samples within the passband. Since this delay shifts samples rightward relative to given window, phasor computed from shifted samples will be erroneous unless the time-stamp aligns with the window midpoint. To mitigate this effect, the estimate $X(k)$ at synchronized sample time k is obtained by selecting the $N/2$ "earliest" samples and the $N/2$ "most recent" samples surrounding $x[k]$. Figure 3.28 illustrates this approach where 9 samples span exactly one fundamental cycle, yielding $N = 8$ (corresponding to 9filter taps). When estimation occurs at sample index $x[k + N/2]$ with the timestamp positioned precisely at the observation window, natural group delay compensation occurs, producing a correct synchro-phasor. Note that this methodology inherently introduces phasor estimation delay of $(N/2)Ts$ seconds. Equivalently, a synchro-phasor representing power system condition at instant t becomes available at the PMU output at time $(t + (N/2)Ts)$ seconds, excluding additional processing delays.

3.9.5 Practical Implementation of Synchronized Phasor Measurement

Synchronized phasor measurement technology provides an effective methodology for monitoring real-time operational status within Wide-Area Measurement System (WAMS), substantially enhancing system reliability, observability, integrity, and security [79]. When WAMS incorporates monitoring, protection, and control capabilities, it is classified into a Wide-Area Monitoring, Protection, And Control (WAMPAC) infrastructure[80]. WAMPAC implementations necessitate PMUs deployment across adequate electrical grid nodes to establish complete system observability [81]. However, utilities have determined that synchro-phasor system deployment costs average between $40,000 and $180,000 per PMU. Labor expenses, encompassing installation and commissioning, constitutes a substantial cost component, whereas the PMU hardware itself typically represent under 5% of total deployment cost [82]. Given this economic context, extensive PMU deployment may encounter constraints, prompting utilities to seek alternative, more cost-effective solutions. The incorporation of the PMU function into pre-pursue more alternatives. One practical strategy is to include PMU capability into digital relays that are currently in use in power systems. These dual-purpose devices provide real financial advantages by removing the extra costs related to wiring, engineering, and testing needed for standalone (dedicated) PMUs [80].

Initially, apparent discrepancies exist between the synchro-phasor reference models and conventional numerical protection relay architectures, despite both Intelligent Electronic Devices (IEDs) perform a shared fundamental phasor estimation processes. The former employs demodulation techniques with uniform sampling scheme, while the latter typically utilizes frequency tracking combined with DFT-based algorithms. Consequently, examining how synchronized phasor measurement implementations appear in commercial products becomes pertinent. Additionally, investigating whether alternative synchro-phasor algorithms can satisfy standard requirements merits consideration. This subsection addresses both questions.

The preliminary implementation strategy is integrating synchro-phasors without altering the sampling procedure (adaptive sampling) to mitigate the danger of interfering with other relay functions (protection, control, and metering). The utilization of integrated Central Processing Unit (CPU) and Digital Signal Processing (DSP) architecture for sample timestamping accomplishes this goal. This method is especially appropriate for relay signal processing systems with adjustable ADCs (Fig. 3.22). The DSP regulates the ADC sampling clock, producing samples asynchronously in relation to the

absolute time reference (ADC output samples in Fig. 322). Subsequently, synchro-phasor processing transpires. The data window center is initially calculated by averaging the timestamps according to the DSP time reference. Thereafter, the CPU, aligned with the 1PPS signal, ascertains the timing for synchro-phasor reporting inside the designated window. An initial synchro-phasor estimate is computed using a four-parameter model based on a first-order Taylor expansion, aimed at improving the accuracy of the classical Fourier technique in dynamic system settings [80]. The discrepancy between the averaged timestamps and the absolute time reference is ultimately computed. This facilitates the rectification of the estimated synchro-phasor through phasor rotation.

The convolution synchro-phasor algorithm, as detailed in [80], offers an alternative to the four-parameter model synchro-phasor algorithm. This approach essentially replicates the demodulation-based reference algorithm, but it is modified to accommodate asynchronous sampling through the use of convolution integrals. As with the previous method, samples are produced asynchronously, with the CPU supplying absolute time markers for each sample. The input signal is then convolved with a specific FIR low-pass filter, utilizing the corresponding timestamps to estimate the synchro-phasors. These asynchronously generated samples are processed immediately upon acquisition, while filter values are dynamically estimated to correspond with the irregularly spaced timestamps. This is possible because the filter's characteristics are predetermined during the design phase, thereby facilitating its creation. Filter values at each time step are computed using numerical methods, like linear interpolation. Algorithms in [80, 83] have the same feature: they use the same variable-rate sample streams for both protection algorithms and synchro-phasor estimation. The synchro-phasor estimation is a new software that runs alongside the existing protection algorithms. As a result, changes to the hardware are kept to a minimum, which helps to lower costs.

Another way to include synchronized phasor measurements in protective relays uses fixed sampling rates, as shown in Figs. 3.23 and 3.24. With a constant ADC sampling rate, synchronization to an absolute time reference allows synchro-phasor algorithms to use timestamped samples directly. This idea was first described in [84], where synchro-phasors were estimated using the demodulation-based method recommended by the PMU standards. In contrast to the algorithms previously discussed, synchro-phasors were employed in conjunction with a line differential protection algorithm (ANSI 87L). The protection relay, in particular, integrates communication functionalities that facilitate the exchange of synchronized phasors with comparable relays. Consequently, when two such relays are situated at line terminals and engage in synchro-phasor exchange, line differential protection is activated.

Most contemporary PMU algorithms utilize a uniform sample rate architecture, as this approach streamlines data acquisition and signal processing analysis [85]. Therefore, protection relays that utilize fixed sampling frequencies are capable of processing a variety of implementations for synchro-phasor algorithms. The estimation of synchro-phasors within this architectural framework is categorized into two primary groups: DFT-based algorithms and non-DFT algorithms. DFT is the most widely used method, mainly because it's simple, elegant, and precise for estimating phasors [66]. However, DFT-based algorithms often have spectrum leakage problems, and many solutions have been proposed in the literature. Three main types of solutions help DFT regain its ability to accurately predict target parameters.

The first method uses a variable DFT window length to reduce leakage errors by aligning the DFT window with the expected frequency [86, 87]. This approach only works for signals with a single fundamental frequency. Therefore, the method has a significant limitation: errors in phasor estimations occur when the Discrete Fourier Transform (DFT) is applied to signals with different fundamental frequencies.

The second solution utilizes combinations of windowing functions [88] with the Interpolated-Discrete Fourier Transform (IpDFT), first presented in [89]. This method mitigates both long-range and short-range leakages, as illustrated in [90], where Hanning windows exhibited the superiority of IpDFT with tapering compared to traditional IpDFT algorithms. As a result, this method was implemented for synchro-phasor estimation, with algorithm performance assessed using the TVE criterion under both steady-state and dynamic situations, in accordance with IEEE Standard C37.118.1-2011 for M-Class PMUs in [91]. Subsequently, comprehensive investigations delineated tapered IpDFT concerning windowing functions [92] and observation interval size [93] for both performance classes (P-Class and M-Class PMU). The suggested enhanced-IpDFT (e-IpDFT) effectively compensates for spectral interference from negative DFT spectrum images, exhibiting promising performance in real-time implementation. In summary, the majority of references address DFT leakage issues for off-nominal frequencies in both steady-state and dynamic settings, rendering IpDFT algorithms exceptionally appealing methodologies. Nonetheless, the previously described IpDFT algorithms utilizing the Hanning window necessitate sampling rates far surpassing the fundamental frequency (often in the tens of kHz) to prevent aliasing effects and facilitate the requisite approximations of the process. Furthermore, a minimum of two-cycle window widths guarantees adequate spectral line separation for efficient leakage reduction by windowing techniques.

The third approach employs resampling methods. These methods adjust input samples to align with optimal signal sample sequences, ensuring their sampling frequency matches the power system frequency. Subsequently, phasor estimation is performed using the resampled data. Reference [66] demonstrates that phasors derived from resampled data exhibit minimal estimation errors. The resampling technique referenced utilizes trigonometric functions, thereby excluding harmonic effects; consequently, high-order filters are required to provide a pure sinusoidal signal to the algorithms. Conversely, when harmonic phasors are needed, FIR filter banks become essential. The use of high-order filters introduces delays, which in turn slows the system's response.

Several alternative algorithms, not based on DFT, are available for phasor estimation. Recent algorithms have used dynamic phasor models, which are based on the first-order Taylor expansion. This method was later improved by using the second-order Taylor expansion in six-parameter models, which helped to improve measurement accuracy during large frequency changes. The accuracy of synchro-phasor estimation can be increased by optimizing the coefficients of Taylor's series using least squares error and applying a spectral window. The four-cycle LES method is a particularly promising Taylor's series technique, as shown by simulations in [93]. However, these methods require processing complex-valued data, which leads to a significant computational burden and is a major drawback in practical use.

Chapter 4

Spectral Estimation

4.1 Spectral Estimation

Frequency domain analysis represents a critical signal processing methodology that examines how signal power distribution through the frequency spectrum. Comprehending spectral structure within waveform is vital for electrical engineering disciplines, communication systems, biomedical instrumentation, and power system protective applications. Such comprehension facilitates detection of concealed harmonic components, non-integer harmonic components, system disturbances, periodic oscillations, and stochastic noise elements.

Spectral estimate functions simultaneously as a diagnostic instrument and a core algorithmic foundation in digital protective relays technology, phasor measurement units (PMUs), and harmonic phasor estimation (HPE) systems, supporting protective relaying, control functions, and operational awareness. This chapter provides a thorough overview of spectrum estimation methods. This study covers traditional approaches, modern techniques, and parametric procedures, all supported by mathematical explanations and practical examples [52,96,97].

4.2 Energy Spectral Density (ESD) and Power Spectral Density (PSD)

Energy-spectrum(or power-spectrum) analysis focuses on characterizing signal energy or power distribution throughout the frequency domain. For deterministic discrete-time signal, the energy-spectral density is defined as:

$$E(f) = |X(f)|^2 = \left| \sum_{m=-\infty}^{\infty} x(m)\, e^{-2\pi f m} \right|^2 \tag{4.1}$$

The energy spectral density of the signal $x(m)$ can be formulated as the Fourier transform of its autocorrelation function:

$$E(f) = |X(f)|^2 = X(f)\, X^*(f)$$

$$= \sum_{m=-\infty}^{\infty} r_{xx}(m)\, e^{-2j\pi f} \tag{4.2}$$

Here, $r_{xx}(m)$ denotes the autocorrelation function of the signal $x(m)$. From theoretical standpoint, the Fourier transform is strictly defined only for signals with finite energy. However, an important and widely studied class of stationary stochastic processes which due to their stationarity property, extend indefinitely in time and therefore possess infinite energy. As a result, such signals do not admit a conventional Fourier transform representation. For stochastic processes, spectral characterization is instead achieved through the power spectral density, which is defined as the Fourier transform of the signal's autocorrelation function:

$$P_{xx}(f) = \sum_{m=-\infty}^{\infty} r_{xx}(m) e^{-j2\pi f} \tag{4.3}$$

where $r_{xx}(m)$ represent auto-correlation as follows:

$$r_{xx}(m) = E[x(n)\, x(n+m)] \tag{4.4}$$

In practice, the auto-correlation function, which measures how similar a signal is to its delayed form, is calculated from a signal record that is N samples long as:

$$\hat{r}_{xx}(m) = \frac{1}{N-m} \sum_{k=0}^{N-m-1} x(k)\, x(k+m) \tag{4.5}$$

As shown in Equation (4.5), when the correlation lag, *m*, approaches the length of the data, *N*, the estimator $\hat{r}_{xx}(m)$ uses fewer samples. This leads to greater variability in the estimation. To reduce this effect, a triangular weighting function can be used to lessen the impact of correlation estimates related to larger lag values. The triangle window is defined as follows:

$$w(m) = \begin{cases} 1 - \dfrac{|m|}{N}, & |m| \le N-1 \\ 0, & Other\ wise \end{cases} \tag{4.6}$$

When multiply Equation (4.5) by the window of Equation (4.6), we get:

$$\hat{r}_{xx}(m) = \frac{1}{N} \sum_{k=0}^{N-m-1} x(k)\, x(k+m) \tag{4.7}$$

The expected value of the windowed correlation estimate $\hat{r}_{xx}(m)$ is :

$$E[\hat{r}_{xx}(m)] = \frac{1}{N} \sum_{k=0}^{N-m-1} E[x(k)x(k+m)] \tag{4.8}$$

$$= \left(1 - \frac{|m|}{N}\right) r_{xx}(m)$$

Jenkins and Watts demonstrated that the variance of $r_{xx}(m)$ can be expressed as:

$$Var[\hat{r}_{xx}(m)] \approx \frac{1}{N} \sum_{k=-\infty}^{\infty} [r_{xx}^2(k) + r_{xx}(k-m)\, r_{xx}(k+m)] \tag{4.9}$$

Equations (4.8) and (4.9) show that $\hat{r}_{xx}(m)$ is an estimate that is asymptotically unbiased and consistent.

4.3 Non-Parametric Power Spectrum Estimation(NPPSE)

The earliest and most widely recognized approach for estimating the power spectral density of a finite record consisting of $N-sample$ is periodogram method, originally proposed in the late of nineteenth century. This technique defines the spectral estimate as follows:

$$\hat{P}_{xx}(f) = \frac{1}{N}\left|\sum_{m=0}^{N-1} x(m)e^{-j2\pi f}\right|^2 = \frac{1}{N}|X(f)|^2 \tag{4.10}$$

The power spectral density, commonly referred to as the power spectrum and defined in Eq.(4.10), constitutes the foundation of non-parametric spectral techniques. Due to the finite duration of available data records and the inherent randomness of the most practical signals, spectral estimates obtained from different realizations exhibit random fluctuations around a mean spectral profile. To address this variability, several approaches have been proposed to reduce the variance associated with the periodogram estimator.

4.3.1 Mean and Variance of the Periodograms

The expected value of the periodogram is determined by evaluating the statistical expectation of the expression given in Eq. (4.10):

$$E\left[\hat{P}_{xx}(f)\right] = \frac{1}{N}E[|X(f)|^2]$$

$$= \frac{1}{N}E\left[\sum_{m=0}^{N-1} x(m)e^{-j2\pi fm}\sum_{n=0}^{N-1} x(n)e^{j2\pi fn}\right] \tag{4.11}$$

$$= \sum_{m=-(N-1)}^{N-1}\left(1-\frac{|m|}{N}\right)r_{xx}(m)\,e^{-j2\pi f}$$

As we have the number of signal samples N goes up.

$$\lim_{N\to\infty} E\left[\hat{P}_{xx}(f)\right] = \sum_{m=-\infty}^{\infty} r_{xx}(m)\,e^{-j2\pi f} = P_{XX}(f) \tag{4.12}$$

For a Gaussian stochastic sequence, the variance periodogram estimator can be expressed as follows:

$$Var\left[\hat{P}_{XX}(f)\right] = P_{XX}^2(f)\left[1+\left(\frac{sin2\pi fN}{Nsin2\pi f}\right)^2\right] \tag{4.13}$$

As the record length N increases, the expected value of the periodogram approaches the true power spectral density $P_{XX}(f)$, while the variance of estimator $\hat{P}_{XX}(f)$ converges to $P_{XX}^2(f)$. Consequently,

although the periodogram provides an unbiased estimate of the power spectrum, it does not satisfy the criterion of consistency, since its variance does not diminish with increasing data length. The periodograms may be computed either directly from the DFT of the signal *x*(m) or from FT of the estimated auto-correlation sequence $\hat{r}_{xx}(m)$. Furthermore, the original data record can be divided into multiple, possibly overlapping, segments to generate several individual periodograms, which are subsequently averaged to improve statistical reliability. The following sections examine these approaches and analyze their influence on reducing the variance of periodogram-based spectral estimates.

4.3.2 Averaging Periodograms (AP) (Bartlett Method)

This method averages many periodograms from different parts of a signal to lower the periodogram's variance. We may get the Bartlett periodogram by averaging K periodograms.

$$P_{XX}^{B}(f) = \frac{1}{K}\sum_{i=1}^{k} \hat{P}_{XX}^{(i)}(f) \tag{4.14}$$

where $\hat{P}_{XX}^{(i)}(f)$ is the periodogram for the i^{th} part of the signal. The expected value of the Bartlett periodogram $\hat{P}_{XX}^{B}(f)$ is expressed as:

$$E[P_{XX}^{B}(f)] = E\left[\hat{P}_{XX}^{(i)}(f)\right]$$

$$= \sum_{m=-(N-1)}^{N-1}\left(1 - \frac{|m|}{N}\right) r_{xx}(m)e^{-j2\pi f} \tag{4.15}$$

$$= \frac{1}{N}\int_{-1/2}^{1/2} P_{XX}(v)\left[\frac{sin\pi(f-v)N}{sin\pi(f-v)}\right]^2 dv$$

Here, the term $(sin\pi fN/\, sin\pi f\,)^2/N$ represents the frequency response of the triangular window defined by $1-|m|/N$. As indicated by Eq. (4.15), the Bartlett periodogram exhibits asymptotic unbiasedness. Moreover, the variance of the Bartlett spectral estimate $P_{XX}^{B}(f)$ is reduce to *1/K* of the variance associated with the standard periodogram and can be expressed as follows:

$$Var\left[\hat{P}_{XX}^{B}(f)\right] = \frac{1}{K}P_{XX}^{2}(f)\left[1 + \left(\frac{sin2\pi fN}{Nsin2\pi f}\right)^2\right] \tag{4.16}$$

4.3.3 Averaging Periodograms from Overlapped and Windowed Segments (Welch method)

In this method, a signal $x(m)$ of M samples is split into K overlapping segments of length N. Each segment is then windowed before the periodogram is calculated. The i^{th} section is defined as

$$x_i(m) = x(m + iD), m = 0, \ldots, N-1 \quad , i = 0, \ldots, K-1 \tag{4.17}$$

D is the area of overlap. $D = N/2$ for half-overlap, and $D = N$ for no overlap. The periodogram for the i^{th} windowed segment is expressed by:

$$\hat{P}_{XX}^{(i)}(f) = \frac{1}{NU} \left| \sum_{m=0}^{N-1} w(m) x_i(m) e^{-j2\pi fm} \right|^2 \tag{4.18}$$

In this expression, $w(m)$ denotes the applied window function, while U represents the corresponding window power, defined as:

$$U = \frac{1}{N} \sum_{m=0}^{N-1} w^2(m) \tag{4.19}$$

The spectrum of a signal with a finite length usually has side-lobes because there are breaks at the ends. The window function $w(m)$ smooths out the gaps and keeps the spectral energy from spreading too far into the spectrum's side-lobes. The Welch power spectrum is the mean of K periodograms derived from overlapping and windowed portions of a signal:

$$\hat{P}_{XX}^{W}(f) = \frac{1}{K} \sum_{i=0}^{K-1} P_{XX}^{(i)}(f) \tag{4.20}$$

We may find the expected value of $\hat{P}_{XX}^{W}(f)$ by using Equations (4.18) and (4.20):

$$E[P_{XX}^{W}(f)] = E\left[P_{XX}^{(i)}(f)\right]$$

$$= \frac{1}{NU} \sum_{n=0}^{N-1} \sum_{m=0}^{N-1} w(n) w(m) \, E[x_i(m) x_i(n)] e^{-j2\pi f(n-m)}$$

$$= \frac{1}{NU} \sum_{n=0}^{N-1} \sum_{m=0}^{N-1} w(n) w(m) \, r_{xx}(n-m) e^{-j2\pi f(n-m)}$$

$$= \int_{-1/2}^{1/2} P_{XX}(v) \, W(v-f) dv \tag{4.21}$$

Where:

$$W(f) = \frac{1}{NU}\left|\sum_{m=0}^{N-1} w(m)e^{-j2\pi fm}\right|^2 \tag{4.22}$$

$$Var\left[\hat{P}_{XX}^{W}(f)\right] = \frac{1}{K^2}\sum_{i=0}^{K-1}\sum_{j=0}^{K-1} E\left[\hat{P}_{XX}^{(i)}(f)\hat{P}_{XX}^{(j)}(f)\right] - \left(E\left[\hat{P}_{XX}^{W}(f)\right]\right)^2 \tag{4.23}$$

Welch has demonstrated that under the scenario of no overlap, $D = N$:

$$Var\left[\hat{P}_{XX}^{W}(f)\right] = \frac{Var\left[\hat{P}_{XX}^{(i)}(f)\right]}{K_1} \approx \frac{P_{XX}^2(f)}{K_1} \tag{4.24}$$

for half-overlap, $D = N/2$:

$$Var\left[\hat{P}_{XX}^{W}(f)\right] = \frac{9}{8K_2} P_{XX}^2(f) \tag{4.25}$$

4.3.4 Blackman–Tukey Method

In the Blackman-Tukey approach, the power spectral density of a signal is estimated by applying the Fourier transform to a windowed version of the estimated autocorrelation function, expressed as:

$$\hat{P}_{XX}^{BT}(f) = \sum_{m=-(N-1)}^{N-1} w(m)\,\hat{r}_{xx}(m)e^{-j2\pi f} \tag{4.26}$$

For a finite data record consisting of N samples, the number of observations contributing to the estimation of the autocorrelation at lag m, denoted $\hat{r}_{xx}(m)$, decreases as m approaches N. As a result, the variance of the autocorrelation estimate increase for larger lag values m, reducing the reliability of those estimates. The application of a window function w(m) mitigates this issue by assigning lower wights to autocorrelation coefficients near the endpoints, where estimation uncertainty is highest. Under this framework, the expected value of the Blackman–Tukey power spectral estimation is given by:

$$E\left[\hat{P}_{XX}^{BT}(f)\right] = \sum_{m=-(N-1)}^{N-1} E[\hat{r}_{xx}(m)]\,w(m)e^{-j2\pi f} \tag{4.27}$$

$E[\hat{r}_{xx}(m)] = r_{xx}(m)w_B(m)$ now, where $w_B(m)$ is the Bartlett or triangular window. We can write equation (4.27) as:

$$E\left[\hat{P}_{XX}^{BT}(f)\right] = \sum_{m=-(N-1)}^{N-1} r_{xx}(m)\,w_c(m)e^{-j2\pi fm} \tag{4.28}$$

where $w_c(m) = w_B(m)w(m)$. The expression on the right-hand side of Eq.(4.28) may be reformulated in terms of the Fourier transforms of both the autocorrelation function and the applied window functions as:

$$E\left[\hat{P}_{XX}^{BT}(f)\right] = \int_{-1/2}^{1/2} P_{XX}(v)\, W_c(f-v)dv \tag{4.29}$$

Where $W_c(f)$ denotes the Fourier transform of the composite window $w_c(m)$. The variance of the Blackman–Tukey spectral estimate is expressed as:

$$Var\left[\hat{P}_{XX}^{BT}(f)\right] \approx \frac{U}{N} P_{XX}^2(f) \tag{4.30}$$

Where U is the energy of the window $w_c(m)$.

4.3.5 Power Spectrum Estimation Using Autocorrelation of Overlapped Segments

Within the Blackman–Tukey methodology, compute *N*-length correlation sequence from an *N*- length signal record results in progressively fewer samples contributing to the estimate $\hat{r}_{xx}(m)$ estimation as lag m approaches signal length *N*. Consequently, $\hat{r}_{xx}(m)$ variance increases with increasing lag *m*. this limitation can be addressed by utilizing a *2N*-sample signal for computing *N* correlation values. In a generalized extension of this technique, the signal record *x*(m), containing *M* samples, is partitioned in to *K* overlapping segments, each of length *2N*. the i^{th} segment is expressed as:

$$x_i(m) = x(m + iD)\,, \qquad m = 0,\ldots,2N-1\,, \quad i = 0,\ldots.,K-1 \tag{4.31}$$

Where D is the overlap. The correlation function for each segment of length $2N$ in the range $0 \geq m \geq N$ is given by:

$$r_{xx}(m) = \frac{1}{N}\sum_{K=0}^{N-1} x_i\,(K)x_i(K+m) \quad , \quad m = 0,\ldots.,N-1 \tag{4.32}$$

In Equation (4.32), each correlation value estimate is derived by averaging the sum of N product terms.

4.4 Model-Based Power Spectrum Estimation

Non-parametric spectral power estimation methods are based on the assumption that the autocorrelation function is zero for lags $|m| \geq N$, which sets a limit on the range of lags where estimates can be made. In contrast, parametric or model-based methods use signal processing models to extend autocorrelation functions beyond the $|m| \leq N$ range, where data is available. As a result, model-based spectral estimators offer better resolution compared to periodogram techniques, mainly because they don't assume zero correlation for lag intervals where data is missing.

In spectral estimation using linear models, the signal *x*(*m*) is regarded the output of a linear, time-invariant system. This system is activated by a random input that has a uniform spectrum. Because the input is assumed to have a flat spectrum, the shape of the output power spectrum is determined solely by the system's frequency response. The following equation describes the input-output relationship in a generalized discrete linear time-invariant model:

$$x(m) = \sum_{K=1}^{P} a_K\, x(m-K) + \sum_{K=0}^{Q} b_K\, e(m-K) \tag{4.33}$$

In this context, $x(m)$ denotes the model's output, $e(m)$ signifies the input, and the model coefficients are indicated by the parameters a_k and b_k. Equation (4.33) constitutes an auto-regressive-moving-average (ARMA) model. The transfer function H(z) for the discrete linear time-invariant model delineated in Eq. (4.33) is articulated as:

$$H(z) = \frac{B(z)}{A(z)} = \frac{\sum_{K=0}^{Q} b_K\, Z^{-K}}{\sum_{K=1}^{P} a_K\, Z^{-K}} \tag{4.34}$$

Where the autoregressive is given by $1/A(z)$ and $B(z)$ denotes the moving-average components of $H(z)$, respectively. The power spectral density of $x(m)$ equals the input signal power spectrum multiplied by the squared magnitude frequency response of the system:

$$P_{XX}(f) = P_{EE}(f)|H(f)|^2 \tag{4.35}$$

Where $H(f)$ represents the frequency response of the model and $P_{EE}(f)$ denotes the input spectral power density. When the input is assumed to be a white noise process having unit variance, specifically $P_{EE}(f) = 1$, Eq.(4.35) simplified into:

$$P_{XX}(f) = |H(f)|^2 \tag{4.36}$$

A fundamental principle of model-based spectral analysis is that the estimated power spectrum is derived directly from model's frequency response, calculated as its absolute value squared. The accuracy of the resulting spectrum is therefore heavily dependent on the chosen model type, commonly categorized as autoregressive(AR), moving-average(MA), or a combined ARMA structure.

4.4.1 Maximum–Entropy Spectral Estimation

For stationary signal, the power spectrum is mathematically given by the Fourier transform of its autocorrelation function:

$$P_{XX}(f) = \sum_{n=-\infty}^{\infty} r_{xx}(m)\, e^{-j2\pi f m} \tag{4.37}$$

A fundamental practical challenge arises when implementing Eq.(4.37): while it requires the complete autocorrelation sequence $r_{xx}(m)$, only a finite set of estimates within $|m| \leq P|$ is available. Infinite possible extensions exist for the unknown the lag m inside the interval $\pm\infty$. Standard non-parametric techniques adopt the simplest extension-setting these values to zero an assumption that leads to undesirable spectral leakage and limited resolution. The maximum-entropy estimate offers an alternative by choosing the extension that yields the signal with the greatest randomness(entropy) while perfectly matching the measured correlation values within the range $|m| \leq P|$ match the observed values. The maximum-entropy approach is favored because it avoids introducing unwarranted constraints. Here, a signal's entropy, reflective of its bandwidth and spectral distribution, is given by:

$$H[P_{XX}(f)] = \int_{-1/2}^{1/2} ln\, P_{XX}(f) df \tag{4.38}$$

To derive the maximum-entropy correlation estimate, we compute the derivative of Eq.(4.38) concerning the unknown correlation coefficients and equate it to zero:

$$\frac{\partial H[P_{XX}(f)]}{\partial r_{xx}(m)} = \int_{-1/2}^{1/2} \frac{\partial\, ln\, P_{XX}(f)}{\partial r_{xx}(m)}\, df = 0 \;\; for\; |m| > P \tag{4.39}$$

According to Eq.(4.3), the partial derivative of the power spectrum with respect to the autocorrelation coefficients is expressed as:

$$\frac{\partial P_{XX}(f)}{\partial r_{xx}(m)} = e^{-j2\pi f} \tag{4.40}$$

The derivative of the log-power spectrum, derived from Eq.(4.40), is given by:

$$\frac{\partial\, ln\, P_{XX}(f)}{\partial r_{xx}(m)} = P_{XX}^{-1}(f) e^{-j2\pi} \tag{4.41}$$

The next step in the derivation is to substitute Eq.(4.41) into Eq.(4.39), which gives:

$$\int_{-1/2}^{1/2} P_{XX}^{-1}(f)\, e^{-j2\pi fm}\, df = 0 \;\; for\; |m| > P \tag{4.42}$$

It could be linked to an autocorrelation sequence $c(m)$ if $P_{XX}^{-1}(f)$ is integrable, as:

$$P_{XX}^{-1}(f) = \sum_{m=-\infty}^{\infty} c(m)\, e^{-j2\pi fm} \tag{4.43}$$

Where:

$$c(m) = \int_{-1/2}^{1/2} P_{XX}^{-1}(f) e^{j2\pi fm}\, df \tag{4.44}$$

Equations (4.42) and (4.44) give us that, for $|m| > P, c(m) = 0$. Therefore, using Equation (4.43), the Fourier transform of a finite-length autocorrelation sequence can yield the inverse of the maximum-entropy power spectrum as:

$$P_{XX}^{-1}(f) = \sum_{m=-P}^{P} c(m)\, e^{-j2\pi f m} \tag{4.45}$$

and the spectrum of maximal entropy power is provided by:

$$\hat{P}_{XX}^{ME}(f) = \frac{1}{\sum_{m=-P}^{P} c(m) e^{-j2\pi f}} \tag{4.46}$$

Given the symmetry of the denominator polynomial in Equation (4.46), there is a zero at radius $1/r$ for any zero of this polynomial located at radius r. Therefore, it is possible to factorize and express this symmetric polynomial as:

$$\sum_{m=-P}^{P} c(m) z^{-m} = \frac{1}{\sigma^2} A(z) A(z^{-1}) \tag{4.47}$$

where $A(z)$ is a polynomial of rank P defined as follows, and $1/\sigma^2$ is a gain term.

$$A(z) = 1 + a_1 z^{-1} + \cdots + a_P z^{-P} \tag{4.48}$$

Equations (4.46) and (4.47) allow for the expression of the maximum-entropy power spectrum as

$$\hat{P}_{XX}^{ME}(f) = \frac{\sigma^2}{A(z)A(z^{-1})} \tag{4.49}$$

Eq.(4.49) establishes that the maximum-entropy power spectrum estimate is equivalent to the power spectrum of an autoregressive (AR) model. This result derived by maximizing the spectral entropy with respect to the unknown autocorrelation lags. Consequently, the known autocorrelation values can be directly utilized to calculate the coefficients of the AR model of Eq.(4.49), a procedure detailed in the subsequent section.

4.4.2 Autoregressive Power Spectrum Estimation(ARPSE)

The previous section establish the equivalence between the maximum-entropy power spectrum and the spectrum of an autoregressive(AR) signal model. An autoregressive or linear prediction model formally define by the relation:

$$x(m) = \sum_{K=1}^{P} a_K\, x(m-K) + e(m) \tag{4.50}$$

And the random signal of variance σ_e^2 is represented by $e(m)$. An autoregressive process's power spectrum is provided by:

$$P_{XX}^{AR}(f) = \frac{\sigma_e^2}{|1 - \sum_{k=1}^{P} a_K e^{-j2\pi f}\ |^2} \tag{4.51}$$

A key property of the AR model is its ability to extend, or predict, the correlation sequence for lags where data is unavailable. This relationship is formalized mathematically by multiplying Eq.(4.50) by $x(m-j)$ applying expectation operator as follows:

$$E[x(m)x(m-j)] = \sum_{K=1}^{P} a_K E[x(m-K)x(m-j)] + E[e(m)x(m-j)] \tag{4.52}$$

The random input $e(m)$ for the ideal model coefficients is now orthogonal to the historical data, and Equation (4.52) turns into:

$$r_{xx}(j) = \sum_{k=1}^{P} a_K r_{xx}(j-K), \qquad j = 1, 2, \cdots \tag{4.53}$$

The AR coefficients a_k can be obtained by solving Equation (4.53) given $P + 1$ correlation values. The correlation sequence can also be extrapolated using equation (4.53).

4.4.3 Power Spectrum Estimation Using Moving-Average (MA)

The moving-average(MA) model, also referred to as an all-zero or finite impulse response (FIR) filter, describes a signal $x(m)$ as a weighted sum of a finite sequence of input samples. This process is mathematically defined by:

$$x(m) = \sum_{k=0}^{Q} b_k e(m-k) \tag{4.54}$$

In this model, $e(m)$ represents a zero-mean random input signal, and Q denotes the model order. The cross-correlation function between the input and output of the moving-average process is expressed as:

$$r_{xe}(m) = E[x(j)\, e(j-m)]$$

$$= E\left[\sum_{k=0}^{Q} b_k e(j-k)\, e(j-m)\right] = \sigma_e^2 b_m \tag{4.55}$$

Following from this, the autocorrelation function of the moving-average process is defined as:

$$r_{xx}(m) = \begin{cases} \sigma_e^2 \sum_{k=0}^{Q-|m|} b_k b_{k+m}, & |m| \le Q \\ 0, & |m| > Q \end{cases} \tag{4.56}$$

Therefore, as established by Eq.(4.56), the power spectrum derived from the Fourier transform of the autocorrelation sequence is identical to that of a moving-average(MA) signal model. This equivalence

implies that the spectrum of an MA process can be calculated directly via the Fourier transform of its autocorrelation function:

$$P_{XX}^{MA} = \sum_{m=-Q}^{Q} r_{xx}\ (m)\, e^{-j2\pi f} \tag{4.57}$$

It is important to note MA spectral estimation is equivalent to the Blackman–Tukey method for periodogram estimation via autocorrelation sequence.

4.4.4 Power Spectrum Estimation Using Autoregressive Moving-Average (ARMA)

The autoregressive moving-average(ARMA), or pole-zero, model is defined Eq.(4.33). The relationship linking the ARMA parameters to the autocorrelation sequence is derived by multiplying both sides of this Eq.(4.33) by $x(m-j)$ and applying the expectation operator as follows:

$$r_{xx}(j) = \sum_{k=1}^{P} a_k\, r_{xx}\ (j-k)\ + \sum_{k=0}^{Q} b_k r_{xe}(j-k) \tag{4.58}$$

In Eq.(4.58), the moving-average component affects the autocorrelation sequence only values lags up to its order *Q*. Consequently, for the autoregressive component the following relation holds:

$$r_{xx}(m) = \sum_{k=1}^{P} a_k\ r_{xx}(m-k) \qquad for\ m > Q \tag{4.59}$$

Therefore, Eq.(4.59) is first used to solve for AR coefficients a_k. These values are then substituted into Eq.(4.58) to determine the MA coefficients b_k. Once all ARMA model's parameters are identified, the power spectral estimate is given by:

$$P_{XX}^{ARMA}(f)\ = \sigma_e^2 \frac{\left|\sum_{k=0}^{Q} b_k e^{-j2\pi f}\ \right|^2}{\left|\sum_{k=1}^{Q} a_k e^{-j2\pi f}\ \right|^2} \tag{4.60}$$

Where σ_e^2 represents the ARMA model's input variance. Generally speaking, the zeros represent the signal spectrum's anti-resonances, while the poles represent its resonances.

4.5. Spectral Estimation at High Resolution Using Subspace Eigen-Analysis

The eigenvalue decomposition (EVD) of a signal's autocorrelation matrix is a key part of subspace-based decomposition methods. These methods are generally used to find the parameters of sinusoidal components that are mixed with additive white Gaussian noise (AWGN). This method allows for a clear separation of the data into two independent subspaces:

1) The signal subspace, which is made up of the principal eigenvectors linked to the largest eigenvalues.
2) The noise subspace, which is made up of the smallest eigenvalues.

The fundamental principle of the eigen-analytical methods discussed here is the exploitation of this geometric separation to enhance the resolution and accuracy of parameter estimation.

4.5.1 Pisarenko Harmonic Decomposition (PHD)

The second-order autoregressive (AR) model provides a complete representation for a real-valued sine wave. In this model, the system poles lie on the unit circle at an angular frequency corresponding to that of the sinusoid As seen in Figure 4.1. For a sine wave of frequency F_i sampled at rate F_s, the defining AR model is:

$$x(m) = 2\cos\left(\frac{2\pi F_i}{F_s}\right) x(m-1) - x(m-2) + A\delta(m-t_0) \tag{4.61}$$

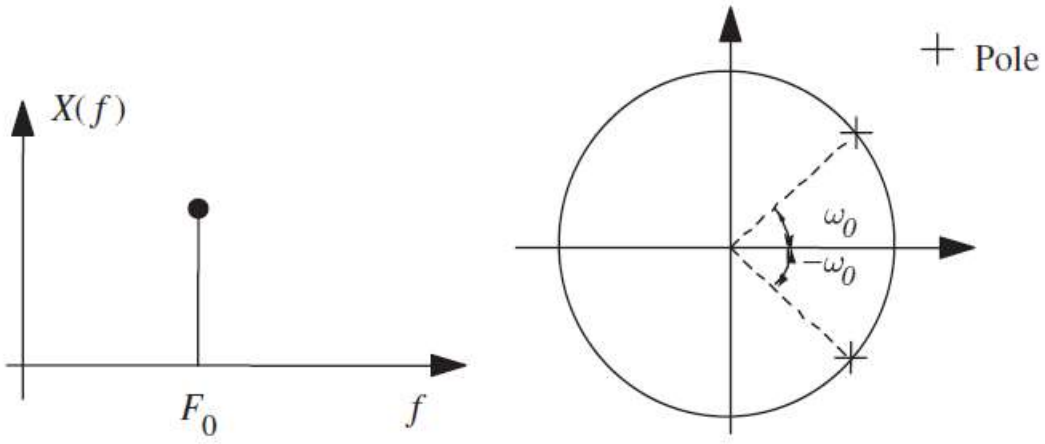

Fig. 4.1 *An all-pole model of a sinusoidal signal of second order.*

Where $A\delta(m-t_0)$ denotes the initiating impulse for a sine waveform having amplitude A. In the general case, a composite signal containing P real sinusoids admits representation through an AR model of order $2P$ according to:

$$x(m) = \sum_{k=1}^{2P} a_k\, x(m-k) + A\delta(m-t_0) \tag{4.62}$$

The AR model's transfer function is provided by

$$H(z) = \frac{A}{1-\sum_{k=1}^{2P} a_k\, z^{-k}} = \frac{A}{\prod_{k=1}^{P}(1-e^{-j2\pi F_k}\, z^{-1})(1-e^{+j2\pi F_k}\, z^{-1})} \tag{4.63}$$

Where the pole angular location on the unit circle, $e^{\pm j2\pi F_k}$, correspond to the sinusoidal angular frequencies. for P real sinusoidal components embedded in additive white noise, the expression becomes:

$$y(m) = x(m) + n(m)$$

$$= \sum_{k=1}^{2P} a_k \; x(m-k) + n(m) \tag{4.64}$$

When $x(m-k)$ is substituted for $[y(m-k) - n(m-k)]$ in Equation (4.64), the result is:

$$y(m) - \sum_{k=1}^{2P} a_k \; y(m-k) = n(m) - \sum_{k=1}^{2P} a_k \; n(m-k) \tag{4.65}$$

According Eq.(4.65), the noise-contaminated sinusoidal signal $y(m)$ admits representation as an ARMA process where the AR and MA components are equivalent, with the noise process serving as the input. Eq.(4.65) can alternatively be expressed in vector form as:

$$y^T a = n^T a \tag{4.66}$$

Where $a^T = [1, a_1, \ldots, a_{2P}]$, and $y^T = [y(m), \ldots, y(m-2P)]$. Additionally, $n^T = [n(m), \ldots, n(m-2P)]$. We take the expectation and multiply both sides of Eq.(4.66) by the vector y to get the parameter vector a:

$$E[yy^T]a = E[yn^T]a \tag{4.67}$$

or

$$R_{yy}\, a = R_{yn}\, a \tag{4.68}$$

where $E[yy^T] = R_{yy}$, and $E[yn^T] = R_{yn}$ can be written as:

$$R_{yn} = E\,[(x+n)n^T]$$

$$= E[nn^T] = R_{nn} = \sigma_n^2 I \tag{4.69}$$

Where the noise variance is denoted by σ_n^2. Used equations (4.69) and (4.68) to obtain:

$$R_{yy}\, a = \sigma_n^2\, a \tag{4.70}$$

Eq.(4.70) takes the form of an eigenvalue equation. When the matrix R_{yy} has dimensions exceeding$2P \times 2P$, the $2P$ largest eigenvalues correspond to eigenvectors representing the noise-contaminated sinusoids, while the smallest eigenvalue equals noise variance σ_n^2 . The parameter vector a is derived as the eigenvector of R_{yy} having unit first element and corresponding to the minimum eigenvalue. From this AR parameter vector, a, sinusoidal frequencies can be extracted by initially computing the polynomial roots:

$$1 + a_1 z^{-1} + a_2 z^{-2} + \cdots + a_2 z^{-2P+2} + a_1 z^{-2P+1} + z^{-2P} = 0 \tag{4.71}$$

It is important to observe that in the case of sinusoidal signals, the AR coefficients constitute a symmetric polynomial defined by the relationship $a_k = a_{2P-k}$. Consequently, the frequencies F_k of these sinusoids can be determined by identifying the roots z_k of Eq.(4.71) and applying the corresponding conversion formula:

$$z_k = e^{j2\pi F_k} \tag{4.72}$$

To compute the power of the sinusoids, we proceed as follow. When observing P sinusoidal components corrupted by additive white noise, the autocorrelation function is defined by the equation:

$$r_{yy}(k) = \sum_{i=1}^{P} P_i \cos 2\pi k F_i + \sigma_n^2 \delta(k) \tag{4.73}$$

In this context, $P_i = A_i^2/2$ denotes the power of the sinusoidal component $A_i \sin(2\pi F_i)$. Since the white noise contribution is restricted to the zero-lag autocorrelation $r_{yy}(0)$, Eq.(4.73) can be reformulated for the lags $k = 1, \ldots, P$, as follows:

$$\begin{pmatrix} \cos 2\pi F_1 & \cos 2\pi F_2 & \ldots & \cos 2\pi F_P \\ \cos 4\pi F_1 & \cos 4\pi F_2 & \ldots & \cos 4\pi F_P \\ \vdots & \vdots & \ddots & \vdots \\ \cos 2P\pi F_1 & \cos 2P\pi F_2 & \ldots & \cos 2P\pi F_P \end{pmatrix} \begin{pmatrix} P_1 \\ P_2 \\ \vdots \\ P_P \end{pmatrix} = \begin{pmatrix} r_{yy}(1) \\ r_{yy}(2) \\ \vdots \\ r_{yy}(P) \end{pmatrix} \tag{4.74}$$

Once frequencies F_i have been determined via Eqs.(4.71) and (4.72), and the autocorrelation function $\hat{r}_{yy}(k)$ has been estimated, Eq.(4.74) can be utilized to solve for the sinusoidal power Pi. Subsequently, the variance of the noise is derived from Eq.(4.73) as follows:

$$\sigma_n^2 = r_{yy}(0) - \sum_{i=1}^{P} P_i \tag{4.75}$$

4.5.2 Spectral Estimation via Multiple Signal Classification (MUSIC)

The MUSIC algorithm functions as an eigen- decomposition subspace technique to estimate the frequencies of complex sinusoids in additive white noise. To begin, we consider a signal *y*(*m*) defined as:

$$y(m) = \sum_{k=1}^{P} A_k e^{-j(2\pi F_k m + \emptyset_k)} + n(m) \tag{4.76}$$

The noisy signal's $N - sample$ vector $y = [y(m), \ldots, y(m + N - 1)]$ can be expressed as:

$$y = x + n = Sa + n \tag{4.77}$$

where the definition of the signal vector $x = Sa$ is:

$$\begin{pmatrix} x(m) \\ x(m+1) \\ \vdots \\ x(m+N-1) \end{pmatrix} = \begin{pmatrix} e^{j2\pi F_1 m} & e^{j2\pi F_2 m} & \cdots & e^{j2\pi F_P m} \\ e^{j2\pi F_1 (m+1)} & e^{j2\pi F_2 (m+1)} & \cdots & e^{j2\pi F_P (m+1)} \\ \vdots & \vdots & \ddots & \vdots \\ e^{j2\pi F_1 (m+N-1)} & e^{j2\pi F_2 (m+N-1)} & \cdots & e^{j2\pi F_P (m+N-1)} \end{pmatrix} \begin{pmatrix} A_1 e^{j2\pi \emptyset_1} \\ A_2 e^{j2\pi \emptyset_2} \\ \vdots \\ A_P e^{j2\pi \emptyset_P} \end{pmatrix} \quad (4.78)$$

Definitions for the matrix S and vector a are provided on the right-hand side Eq.(4.78). The autocorrelation matrix of the noisy signal y is constructed by summing the autocorrelation matrices of the signal x and the noise, yielding:

$$\boldsymbol{R_{yy} = R_{xx} + R_{nn} = SPS^H + \sigma_n^2 I} \quad (\mathbf{4.79})$$

Where the diagonal matrix P specifies the strength of the sinusoids, the exponent H indicates the Hermitian transpose, and the autocorrelation matrices of the signal and noise processes are $R_{xx} = SPS^H$ and $R_{nn} = \sigma_n^2 I$.

$$P = aa^H = diag[P_1, P_2, \cdots, P_P] \quad (4.80)$$

Where the strength of the complex sinusoid $e^{-j2\pi F_i}$ is represented by $P_i = A_i^2$. Another way to express the signal's correlation matrix is as follows:

$$R_{xx} = \sum_{k=1}^{N} P_k S_k S_k^H \quad (4.81)$$

Where $[1, e^{j2\pi F_k}, \cdots, e^{j2\pi(N-1)F_k}]$ is the value of S_k^H. Examine the $N \times N$ correlation matrix R_{xx} eigen-decomposition now.

$$R_{xx} = \sum_{k=1}^{N} \lambda_k v_k v_k^H$$

$$R_{xx} = \sum_{k=1}^{P} \lambda_k v_k v_k^H \quad (4.82)$$

In this context, λ_k and v_k, denote the eigenvalues and eigenvectors of the matrix R_{xx}, respectively. The reasoning relies on the assumption that the autocorrelation matrix, which is formed by P complex sinusoids, has exactly P non-zero eigenvalues, with the remaining values satisfying $\lambda_{P+1} = \lambda_{P+2}, \ldots, \lambda_N = 0$. Given that the sum of the outer products of the eigenvectors yields the identity matrix, the diagonal autocorrelation matrix of the noise can be reformulated using the eigenvectors of R_{xx} of P complex sinusoids, $\lambda_{P+1} = \lambda_{P+2}, \ldots, \lambda_N = 0$. The diagonal autocorrelation matrix of the noise can also be expressed in terms of the eigenvectors of R_{xx} as follows:

$$R_{nn} = \sigma_n^2 I \; = \; \sigma_n^2 \sum_{k=1}^{N} v_k \, v_k^H \tag{4.83}$$

Using the eigenvectors and their corresponding eigenvalues, the correlation matrix of the noisy signal can be formulated as follows:

$$R_{yy} \; = \; \sum_{k=1}^{P} \lambda_k v_k v_k^H + \sigma_n^2 \sum_{k=1}^{N} v_k \, v_k^H$$

$$= \sum_{k=1}^{P} (\lambda_k + \sigma_n^2) v_k v_k^H + \sigma_n^2 \sum_{k=P+1}^{N} v_k \, v_k^H \tag{4.84}$$

The noisy signal's correlation matrix's eigenvectors and eigenvalues can be divided into two disjoint subsets using Equation (4.84) (see Figure 4.2). The primary eigenvectors are the set of eigenvectors $\{v_1, \ldots, v_P\}$ that span the signal subspace and are connected to the P greatest eigenvalues.

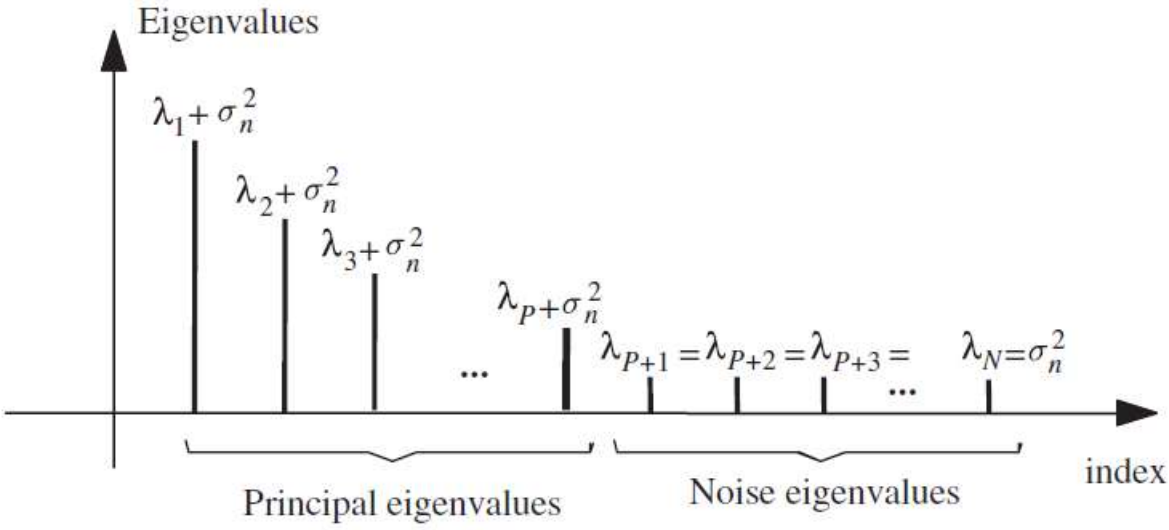

Fig. 4.2 *Decomposition of the eigenvalues of a noisy signal into signal-dominant and noise-dominant.*

In this framework, the signal subspace is spanned by the principal eigenvectors, meaning every signal vectors S_i is a linear combination of these vectors. Conversely, the eigenvectors, $\{v_{P+1}, \ldots, v_N\}$, with eigenvalues equal to the noise variance σ_n^2 define the noise subspace. The orthogonality between the two sets of eigenvectors directly implies that the signal and noise are subspaces are mutually orthogonal. Therefore, a sinusoidal signal vectors S_i in the signal subspace is orthogonal to every vector in the noise subspace leading to the condition:

$$S_i^H(f)\, v_k = \sum_{m=0}^{N-1} v_k\,(m) e^{-j2\pi F_i m} = 0\,, \quad i = 1, \cdots, P \quad , \quad k = P+1, \cdots, N \tag{4.85}$$

It follows from Eq.(4.85) that the frequencies of the P sinusoids can be determined by identifying the zeros of the polynomial function of the frequency variable f defined below:

$$\sum_{k=P+1}^{N} S^H\,(f)\, v_k \tag{4.86}$$

The power spectrum estimation in the MUSIC method is described as

$$P_{XX}(f) = \sum_{k=P+1}^{N} |S^H(f)\, v_k|^2 \tag{4.87}$$

Where $\{v_{P+1}, \ldots, v_N\}$ are the eigenvectors in the noise subspace and $s(f) = [1,\ e^{j2\pi f}, \ldots, e^{j2\pi(N-1)f}]$ the complex sinusoidal vector give as the following:

$$P_{XX}(f_i) = 0\,, \quad i = 1, \cdots, P \tag{4.88}$$

The reciprocal of $P_{XX}(f)$has its poles at the sinusoidal frequencies since $P_{XX}(f)$ has its zeros at those frequencies. The definition of the MUSIC spectrum is

$$P_{XX}^{MUSIC}(f) = \frac{1}{\sum_{k=P+1}^{N} |S^H(f) v_k|^2} = \frac{1}{S^H(f)\, v(f)\, v^H(f)\, S(f)} \tag{4.89}$$

Where the noise subspace's matrix of eigenvectors is represented by $V = [v_{P+1}, \ldots, v_N]$. Since PMUSIC(f) sharply peaks at the frequencies of the signal's sinusoidal components, the MUSIC estimations are determined by taking the frequencies of its peaks.

4.5.3 Estimation of Signal Parameters via Rotational Invariance Techniques (ESPRIT)

ESPIRIT is an eigen-decomposition approach used to find the frequencies of complex sinusoids hidden in additive white noise. We consider a signal, $y(m)$, which is made up of P complex sinusoidal components and additive white noise:

$$y(m) = \sum_{k=1}^{P} A_k e^{-j(2\pi F_k m + \emptyset_k)} + n(m) \tag{4.90}$$

The sinusoidal component of the signal vector $y(m) = [y(m), \ldots, y(m + N - 1)]^T$ and that of the time-shifted vector $y(m + 1) = [y(m+1), \ldots, y(m+N)]^{\mathrm{T}}$ have a deterministic relationship that the ESPIRIT algorithm takes use of. The noisy vector $y(m)'s$ signal component can be written as:

$$x(m) = Sa \tag{4.91}$$

Here, S represents the complex sinusoidal matrix, and a denotes the vector of sinusoidal amplitudes and phases, as described in Eqs.(4.76) and (4.77). Multiplying a complex sinusoid $e^{j2\pi F_i}$ by the phase factor $e^{j2\pi F_i m}$ effectively shifts it by one sample in time. Consequently, the time-shifted signal vector $x(m+1)$ can be derived from $x(m)$ by applying a phase-shift to every complex sinusoidal component, resulting in the following expression:

$$x(m+1) = S\emptyset a \tag{4.92}$$

The $P \times P$ phase matrix of Φ is defined as:

$$\emptyset = diag\left[e^{j2\pi F_1}, \quad e^{j2\pi F_2}, \quad \cdots, e^{j2\pi F_P}\right] \tag{4.93}$$

The diagonal elements of Φ represent the relative phases between the neighboring samples of the sinusoids. Because it links the time-shifted vectors $x(m)$ and $x(m+1)$, the unitary matrix Φ is also referred to as a rotation matrix. The noisy signal vector $y(m)$ autocorrelation matrix can be expressed as:

$$R_{y(m)y(m+1)} = SPS^H + \sigma_n^2 I \tag{4.94}$$

Where the powers of the complex sinusoids $P = diag[A_1^2, \cdots, A_P^2] = aa^H$ are the diagonal elements of the diagonal matrix P. The vectors $y(m)$ and $y(m+1)$ have a cross-covariance matrix that is

$$R_{y(m)y(m+1)} = SP\emptyset^H S^H + R_{n(m)n(m+1)} \tag{4.95}$$

where the definitions of the autocovariance matrices $R_{y(m)y(m+1)}$ and $R_{n(m)n(m+1)}$ are

$$R_{y(m)y(m+1)} = \begin{pmatrix} r_{yy}(1) & r_{yy}(2) & r_{yy}(3) & \cdots & r_{yy}(N) \\ r_{yy}(0) & r_{yy}(1) & r_{yy}(2) & \cdots & r_{yy}(N-1) \\ r_{yy}(1) & r_{yy}(0) & r_{yy}(1) & \cdots & r_{yy}(N-2) \\ \vdots & \vdots & \vdots & \ddots & \vdots \\ r_{yy}(N-2) & r_{yy}(N-3) & r_{yy}(N-4) & \cdots & r_{yy}(1) \end{pmatrix} \tag{4.96}$$

$$R_{n(m)n(m+1)} = \begin{pmatrix} 0 & 0 & \cdots & 0 & 0 \\ \sigma_n^2 & 0 & \cdots & 0 & 0 \\ 0 & \sigma_n^2 & \cdots & 0 & 0 \\ \vdots & \vdots & \ddots & \vdots & \vdots \\ 0 & 0 & \cdots & \sigma_n^2 & 0 \end{pmatrix} \tag{4.97}$$

It is possible to estimate the correlation matrix of the signal vector $x(m)$ as:

$$R_{x(m)x(m)} = R_{y(m)y(m)} - R_{n(m)n(m)} = SPS^H \tag{4.98}$$

and the signal vector $x(m)$ crosscorrelation matrix with its time-shifted form $x(m\ +\ 1)$ is found to be:

$$R_{x(m)x(m+1)} = R_{y(m)y(m+1)} - R_{n(m)n(m+1)} = SP\emptyset^H S^H \tag{4.99}$$

A proportion $\lambda_i = e^{-j2\pi}$ is subtracted. Equation (4.97) divided by the F_i of Equation (4.98) produces:

$$R_{x(m)x(m)} - \lambda_i R_{x(m)x(m+1)} = SP(I - \lambda_i \phi^H)S^H \tag{4.100}$$

The roots of Equation (4.100) can be used to estimate the sinusoids' frequencies based on Equations (4.93) and (4.100).

Chapter 5

Development of Modified Covariance Enhanced CCH Filter

5.1 Development of Modified Covariance Enhanced CCH Filter

An accurate calculation of the phasor is an essential component of modern digital protection relays. As outlined in preceding sections, conventional techniques like the Discrete Fourier Transform (DFT) exhibit considerable accuracy loss when analyzing transient signals, which are distinguished by decaying DC offsets, harmonics, and, crucially, interharmonics. Although the initial Cleaned Characteristic Harmonic Digital Filter (CCHDF) provided a strong foundation for eliminating exponential decays, its dependence on DFT-based spectral estimation for interharmonic detection constrained its resolution and convergence rate.

The Modified Covariance Cleaned Characteristic Harmonic Digital Filter (MC-CCHDF) is an improvement to the CCHDF design that is talked about in this chapter. The most important theoretical development in this study is replacing the usual DFT spectral block with the Modified Covariance Method (MCM), which is a high-resolution autoregressive estimator. The next parts will talk about the math behind the recommended method, such as the Biunivocal Frequency Relation of Phasor (BFRP), the signal decomposition technique, and how to use MCM to accurately characterize interharmonics [98-101].

5.2 Signal Modeling and Problem Formulation

The analyzed fault signal incorporated multiple components: continuous offset, decreasing exponential components, the system's fundamental frequency f, harmonic and interharmonic contents, plus measurement noise. Signal digitization occurred at sampling frequency of $f_s = 1/T_s$, satisfying the Nyquist–Shannon sampling criterion [1], yielding the following mathematical representation:

$$y(t) = C_{dc} + C \cdot e^{\frac{-nT_s}{\tau}} + \sum_{h=1}^{l} A_h \cdot cos(2\pi f \cdot h \cdot nT_S + \alpha_h) + i[n] + z[n] \quad (5.1)$$

Here, C_{dc} represents the constant DC component, while C and τ denote the magnitude and decay time constant of exponential transient, respectively, the term $z[n]$ corresponds to additive noise contamination, and $i[n]$ characterizes interharmonic content relative to the fundamental frequency, expressed as a summation of sinusoidal components:

$$A_i \cdot cos(2\pi f_i \cdot h \cdot nT_S + \alpha_i) \quad with \quad f_i \neq f \cdot h \quad (5.2)$$

within this framework, A_h and A_i indicate the magnitudes, while $\alpha_h$and α_i represent the phase angles of harmonic components(Where h=1 designates the fundamental frequency) and periodic interharmonics, respectively.

The Discrete Fourier Transform serves as a powerful technique for determining amplitudes and phases of sinusoidal signals when their periods correspond to integer fractions of the analysis window. Under these circumstances, each sinusoidal component's spectral power concentrates at a discrete frequency location, manifesting as an impulse function(Dirac Delta) at the appropriate frequency point.

The DC offset component does not degrade DFT performance, since it appears exclusively at zero frequency, maintaining spectral separation from all other frequency components. However, when analyzing a signal of the form given in (5.1), the accuracy of DFT- based phasor estimation for fundamental component or its harmonics deteriorates due to the presence of non-synchronous signal components relative to the analysis window. Specifically, exponentially decaying terms introduce broadband spectral content that interferes with estimation of other frequency components. In practical fault scenarios, the unknown magnitude and exact mathematical form of these exponential transient further degrade the reliability of the resulting phasor estimates. In addition, the presence of interharmonic components leads to spectral leakage, causing energy spreading across multiple frequency components of interest [31]. As illustrated in Figure5.1 the combined effect of decaying exponential terms and interharmonics results in significant distortion of the spectral components that are otherwise synchronous with the analysis window, affecting not only their magnitudes but also their phase angles.

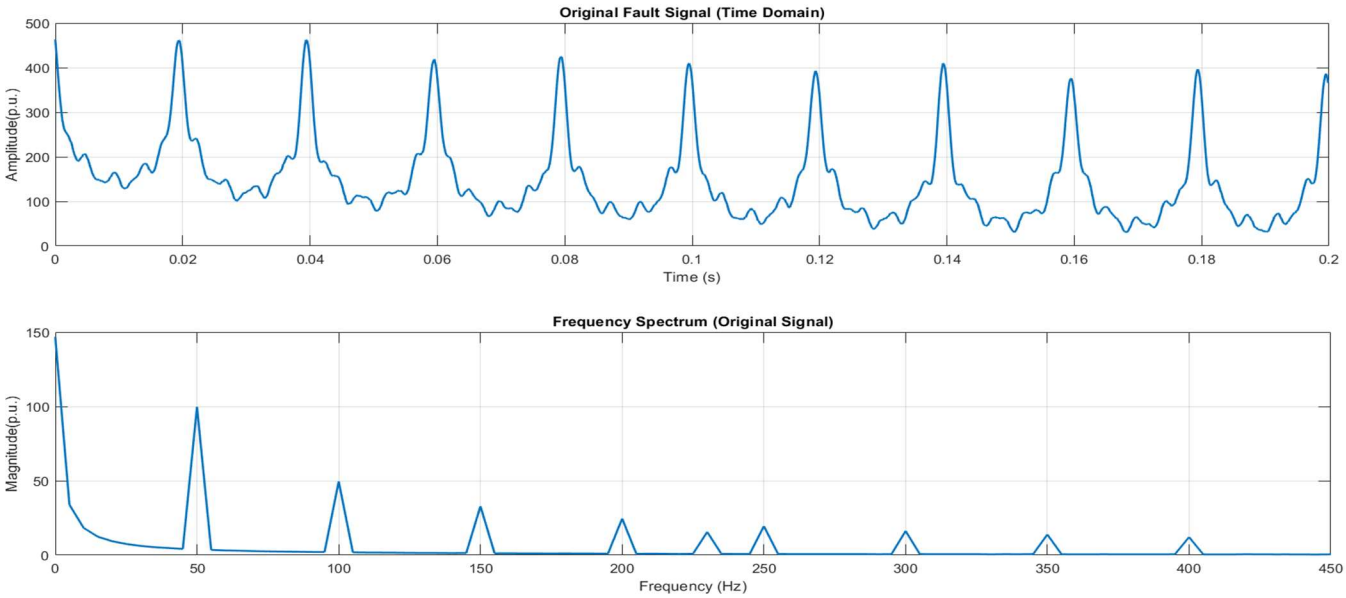

Fig. 5.1. *Spectral magnitudes representation of waveform exhibiting constant DC component, time-decaying exponential, and harmonic and interharmonic frequencies.*

The Modified Covariance Cleaned Characteristic Harmonic digital filter (MC-CCHDF) technique is funded on the generation of an auxiliary signal that is deliberately free from components capable of distorting the fundamental and harmonic quantities used for phasor estimation. This auxiliary signal is constructed such that constant (DC) offset, exponentially decaying transient components and interharmonic terms are effectively removed from the original waveform. At the same time, the essential periodic harmonic information of the original signal is preserved, enabling accurate and stable estimation of harmonic phasors in subsequent stages. The proposed framework extends beyond merely improving the estimation of fundamental and harmonic phasors, the proposed framework introduces the capability to accurately resolve interharmonic components. Crucially, this is accomplished without degrading the fidelity of the standard harmonic content, marking a significant methodological improvement over traditional techniques.

The original Cleaned Characteristic Harmonic Digital Filter (CCHDF) introduced in earlier work focused on constructing an auxiliary signal that retained harmonic information while being immune to

exponential transients. Although that approach is recognized for its robustness and relatively low computational burden, its performance degrades when interharmonic components are present in the signal. Un-der such condition, the efficacy of the filtering process degrades, resulting in errors within the phasor estimation. To mitigate this, this study introduces the concept of the (CCH wave). This variable is defined as a pure harmonic representation of the original, effectively purged of all non-harmonic elements, including interharmonics signal de-rived from the original wave, devoid of any non-harmonic components.

The suggested MC-CCHDF (Modified Covariance Clean Characteristic Harmonic Digital Filter) method enhance the original CCHDF approach by integrating the Modified Covariance Method for superior interharmonic detection and characterization. The fundamental architecture maintains its foundation of generating an auxiliary signal that is free of components that can affect the fundamental and/or harmonic components whose phasor estimation will carried out.

5.3 Theoretical foundation: Biunivocal Frequency Relationship of Phasors(BFRP)

The STF (Sliding Technique Filter) method operates by processing pairs of data points from a sinusoidal signal that are separated by a fixed interval, referred to as the 'slip'(s). By subtracting these sample pairs, the method reveals a deterministic link between the phasors of the input and the output signals, known as the BFRP. Crucially, this operation alters the amplitude and phase of the signal but preserves the original frequency, ensuring a direct spectral correspondence. As depicted in Figure5.2, this process transforms an acquired sinusoidal signal $x[n]$ (with frequency f', and window length N corresponding to period $T = f^{-1}$) into derived signal $u[n]$.

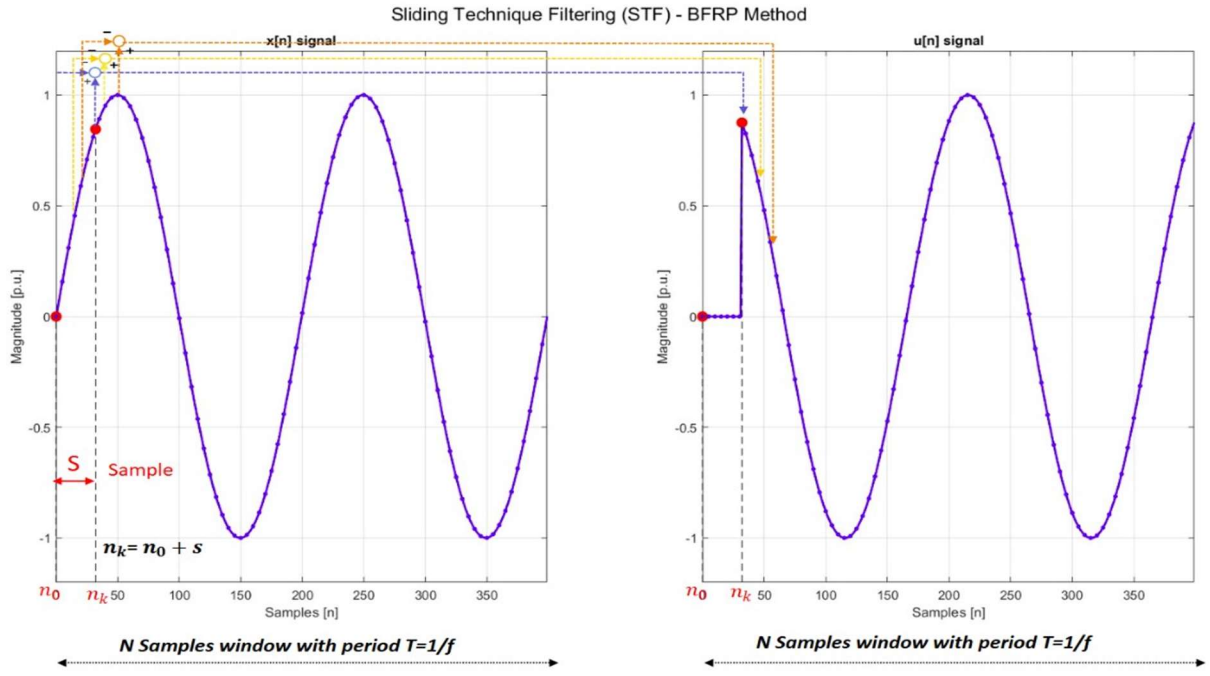

Fig. 5.2. *STF Process transform original signal x[n] into derived signal u[n].*

The sample at index n_0 of the signal $x[n]$ corresponds to the initial time instant t_0 , while the sample n_k corresponds to the instant t_k, at which the formation of the $u[n]$ signal begins. These indices are related by the equation $n_k = n_0 + s$. The values constituting the $u[n]$ signal are derived through analytical methods.

$$u[n_0] = 0$$

$$u[n_1] = 0$$
$$\vdots$$
$$\vdots$$
$$u[n_{k-1}] = 0$$

$$u[n_k] = x[n_k] - x[n_0] = x[n_k] - x[n_{k-s}] \tag{5.3}$$

$$u[n_{k+1}] = x[n_{k+1}] - x[n_1] = x[n_{k+1}] - x[n_{k+1-s}]$$

$$u[n_{k+2}] = x[n_{k+2}] - x[n_2] = x[n_{k+2}] - x[n_{k+2-s}]$$

In the phasor representation shown in Figure 5.3, the phasor corresponding to the signal $x[n]$ are depicted at several time instants. The instantaneous phasors associated with the samples n_0 and n_k , referenced to their respective time instants, are denoted as A^{t_0} and A^{t_k}. The phasor U^{t_k} of derived $u[n]$ signal at the instant t_k , corresponding to the sample n_k, is then obtained by performing a vector subtraction between these two phasors of $x[n]$.

$$\underline{U^{t_k}} = \underline{A^{t_k}} - \underline{A^{t_0}} \tag{5.4}$$

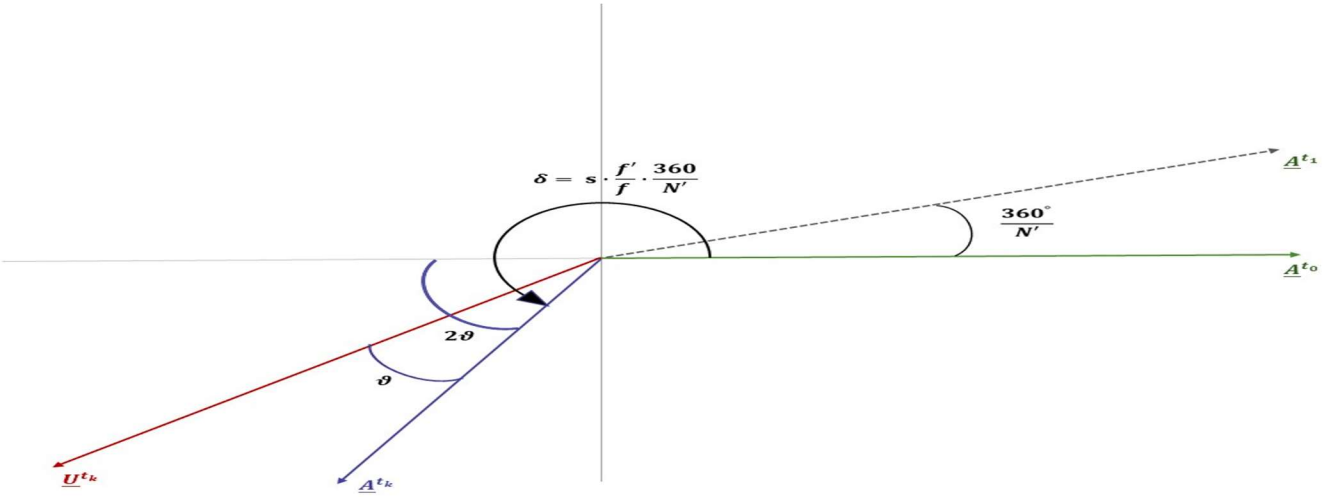

Fig. 5.3 *x[n] and u[n] signals phasor representation.*

Given that a full period of the $x[n]$ signal is represented by N' samples, the phase increment (or equivalent angle) separating two adjacent phasors, A^{t_0} and A^{t_1} is calculated as:

$$\measuredangle(x[n_0], x[n_1]) = \measuredangle\left(\underline{A^{t_0}}, \underline{A^{t_1}}\right) = \frac{360}{N'} \text{ (degree)} \tag{5.5}$$

Accordingly, the angular displacement between the samples n_0 and n_k, which corresponds to the phase shift between the phasors A^{t_0} and A^{t_k}, is given by:

$$\delta = \measuredangle(x[n_0], x[n_k]) = \measuredangle\left(\underline{A^{t_0}}, \underline{A^{t_k}}\right) = s \cdot \frac{360}{N'} \text{ (degree)} \tag{5.6}$$

For given a sampling frequency f_s , the time length of the data window T can be expressed as the number of samples N multiplied by the sampling period T_s :

$$T = N \cdot T_s \tag{5.7}$$

Similarly, with a duration of the $x[n]$ signal, we have:

$$T' = N' \cdot T_s \tag{5.8}$$

Using the expressions given in Equations (5.7) and (5.8), the following relation can be derived:

$$\frac{N}{N'} = \frac{T}{T'} = \frac{f'}{f} \tag{5.9}$$

Consequently, the expression given in equation (5.6) can be reformulated as:

$$\delta = s \cdot \frac{f'}{f} \cdot \frac{360}{N'} \text{ (degrees)} \tag{5.10}$$

From the geometric relationships among the phasors illustrated in Figure5.3, the phase displacement between the phasors A^{t_k} and U^{t_k} can be determined as:

$$\vartheta = \measuredangle\left(\underline{A^{t_0}}, \underline{U^{t_k}}\right) = \frac{\text{wrapTo360}(\delta) - 180}{2} \text{ (degrees)} \tag{5.11}$$

Here, the angle δ is constrained to interval (0°, 360°) (using a wrap-to-360 operation) in order to generalize scenarios where δ is greater than 180° or is less than 180°, to ensure that the numerator in the subtraction remains positive.

Under these conditions, a BFRP in the phase of the terms of phase is established between of the signals $x[n]$ and $u[n]$:

$$\beta = \alpha + \vartheta \ (degrees) \tag{5.12}$$

with $\beta = arg\{\underline{A^{t_k}}\}$ *and* $\alpha = arg\{U^{t_k}\}$

After determining the angular position of the phasors shown in Figure 5.3, it becomes possible to relate the magnitude of the phasors of the A^{t_0}, A^{t_k}, and U^{t_k}. The vector subtraction expressed in (5.4) yield a triangular geometric configuration formed by these magnitudes employing the law of sines along with straightforward trigonometric identities. A BFRP with respect to the magnitude can be established between the phasors of corresponding signals:

$$\left|\underline{A}^{t_k}\right| = \left|\underline{U^{t_k}}\right| \cdot K \tag{5.13}$$

K can be represented as a function of (11):

$$K = \frac{1}{2\cos\vartheta} \tag{5.14}$$

Accordingly, when the STF is applied to a sinusoidal signal, the amplitude and phase of the resulting phasor U can be uniquely determined through the BFRP at any time instant, provided that the phasor A of the original signal is known, and vice versa.

5.4 Obtaining the MC-CCH Wave Integration

The acquisition of the MC-CCH signal is delineated into two essential components with the key enhancement being the integration of MCM for interharmonic detection. Initially, beginning with the original signal as specified in (5.1), the goal is to derive a signal devoid of the exponential component. This signal is referred to as the Wave Dirtied Characteristic Harmonic Wave (DCH) because it comprises characteristic signals formed by harmonic terms, although it is "dirty" due to the presence of interharmonic components. The STF approach will be employed to obtain this signal by the successive subtraction of sample pairs that are separated by a distance or slip of s.

By applying a first-order McLaurin polynomial approximation to the exponential component in the original signal expression (5.1) at an initial generic time t_0, the following expression is obtained:

$$y[n_0] = C_{dc} + C \cdot \left(1 - \frac{n_0\, T_s}{\tau}\right) + \sum_{h=1}^{\iota} A_h \cdot \cos(2\pi f \cdot h \cdot n_0 T_s + \alpha_h) + i[n_0] + z[n_0] \tag{5.15}$$

Moreover, at a later instant t_k , associated with a slip of s samples, the corresponding expression becomes:

$$y[n_k] = C_{dc} + C \cdot \left(1 - \frac{n_k\, T_s}{\tau}\right) + \sum_{h=1}^{\iota} A_h \cdot cos(2\pi f \cdot h \cdot n_k T_s + \alpha_h) + i[n_k] + z[n_k] \tag{5.16}$$

The DCH signal results from subtracting (5.16)and (5.15). For consecutive sample pairs, this signal is generally given by:

$$DCH[n] = -\frac{C \cdot s \cdot T_s}{\tau} + u[n] + z'[n] \tag{5.17}$$

In this context, $u[n]$ represents the cumulative difference between the global contributions of all harmonic and interharmonic contributions over a span of s samples, while $z'[n]$ accounts for the intrinsic white noise within the transformed signal.

Consequently, the derived DCH signal is synthesized from three distinct elements consisting of a function incorporating harmonic and interharmonic periodic components, noise, and a continuous offset defined as $(-\frac{C \cdot s \cdot T_s}{\tau})$. The magnitude of this offset term is governed by specific parameters. Its influence is minimized by a slower exponential decay (indicated by a larger time constant τ), the reduced initial amplitude (C), or a smaller value for the slip (s). Furthermore, the sampling frequency (f_s) is a critical factor; a higher sampling rate corresponds to a shorter sampling period (T_s), which directly attenuates the impact of this offset term.

Given the indeterminacy of the exponential component values (C and τ), system optimization relies exclusively on adjusting the sampling f_s and the slip s. The practical upper limit of f_s is dictated by the digital signal processor (DSP) performance specifications, particularly its ability to execute the necessary algorithms within the available time window between consecutive samples. Consequently, we rationally consider minimizing the value of the slip s.

While it may be presumed that the optimal slip value is $s = 1$ (indicating two consecutive samples), it is essential to consider that subtracting samples that are in close proximity may obscure the inherent noise in the signal, thereby distorting the measurement of the estimated wave. In this scenario, the noise may dominate the signal's value, resulting in an undesirable signal to noise ratio (SNR) that complicates phasor estimation.

Consequently, the selection of the optimal slip parameter s necessitates a strategic trade-off between minimizing the exponential offset and mitigating signal noise. Extensive simulations corroborate that a slip value of s = N/16 specifically within the context of N=128 samples per period, standard for modern protection relay DSPs, is optimal. This configuration not only ensures an acceptable SNR but also maintains robust filter performance in the presence of fast decaying exponentials, while simultaneously minimizing the latency required to generate the auxiliary signal.

After generating DCH signal, the subsequent key step consists of deriving a signal that contains exclusively the interharmonic periodic components associated with the network fundamental frequency. This is achieved by applying a procedure analogous to the previous one, based on the Sliding Technique Filter (STF), in which pairs of samples are subtracted using a slip value s=N. As a result, the Removed All Harmonics wave (RAH wave) is obtained, in which the harmonic components as well as any remaining constant terms present in the DCH signal are effectively eliminated.

For a subsequent instant corresponding to a fundamental period *T*, that is a slip $s = N$ samples, the DCH signal is giving by:

$$DCH[n+N] = -\frac{C \cdot s \cdot T_s}{\tau} + u[n+N] + z'[n+N] \tag{5.18}$$

Computing the difference between expression(5.18) and (5.17) achieves a dual filtering effect. Primarily, it nullifies the continuous offset associated with the exponential component of the original signal. Simultaneously, the operation eliminates all periodic components that are synchronous with the fundamental period T. Consequently, the resulting RAH signal is defined as:

$$RAH[n] = u'[n] + z''[n] \tag{5.19}$$

For sample pairs spaced by N, $u'[n]$ reflects the residual interharmonic difference found in the DCH signal , $z''[n]$ accounting for the signal's white noise. The relationship between the original signal and the derived DCH and RAH waves is illustrated in Figure 5.4.

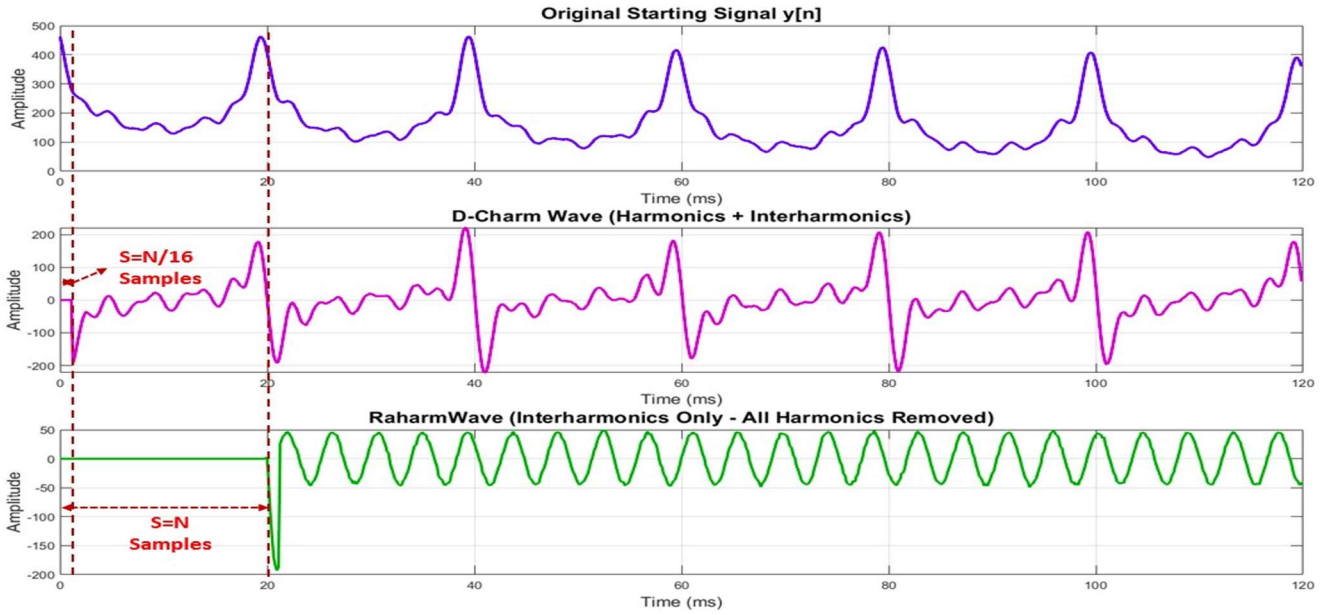

Fig. 5.4. *The relationship between the original signal and the derived DCH and RAH waves.*

The theoretical derivation RAH and DCH components assumes a perfect alignment where the sampling window N samples correspond to one fundamental period. However, in practical grid scenarios, the fundamental frequency f often deviates from the nominal f0. This results in a "slip", where the window length $T_w = N/F_s$, is no longer an integer multiple of the actual signal period T = 1/f. This asynchrony can potentially lead to spectral leakage, which might degrade the performance of harmonic cancellation techniques that rely on exact periodicity. To verify the robustness of the proposed DCH/RAH methodology, and to evaluate the robustness of the proposed algorithm under off-nominal operating situations, its performance was examined using a frequency deviation of +200mHz. Figure 6 displays the resultant fundamental magnitude and phase estimates for this test case.

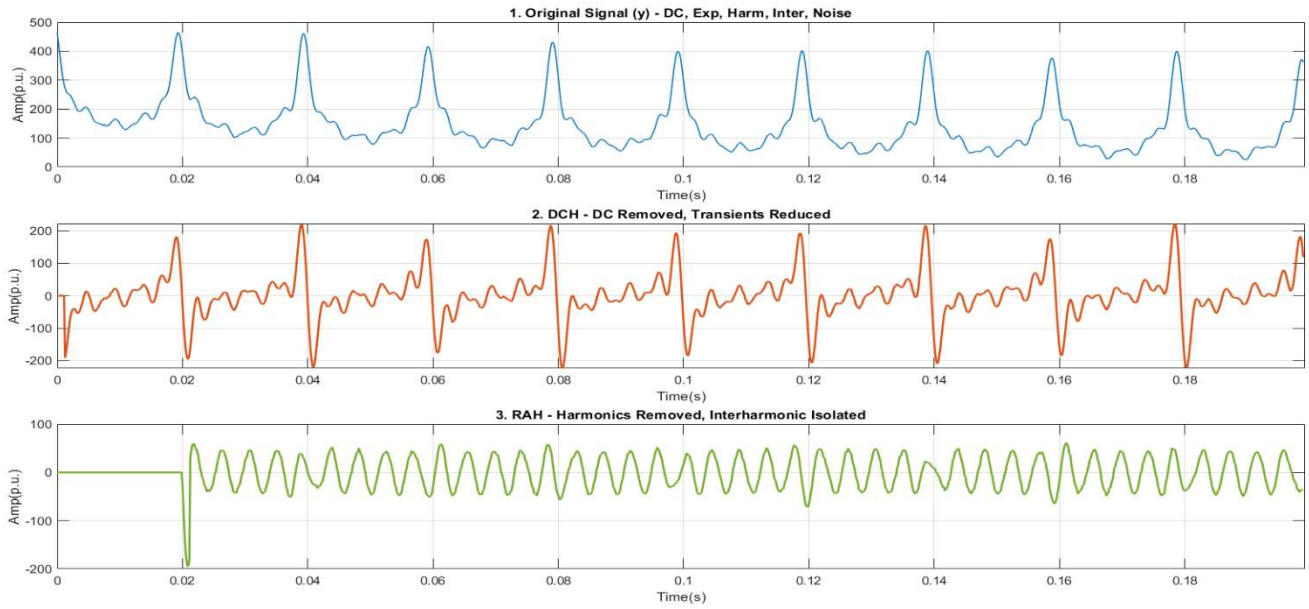

Fig. 5.5. *Robustness of DCH/RAH when fundamental frequency is off-nominal.*

At this stage, the aim is to estimate the interharmonic components contained in the RAH signal in order to construct a new signal whose phasor values are referenced to the DCH signal. To this end, the BFRP is applied to the phasor quantities estimated from the RAH signal. The resulting signal represents the interharmonic and subharmonic characteristic content of the original waveform and is referred to as the CISH wave (Characteristical Inter/Sub-Harmonic Wave). finally, the MC-CCH signal is computed by subtracting the CISH wave from the DCH wave, thereby isolating the desired harmonic components.

If the set of interharmonic in the RAH signal represented by $U_i' = \{U_{i1}', U_{i2}', \ldots, U_{ip}'\}$, then each phasor can be uniquely described by its modulus, phase angle, and corresponding interharmonic frequency:

$$U_i' = \begin{Bmatrix} U_{i1}' \\ U_{i2}' \\ \vdots \\ U_{ip}' \end{Bmatrix} \Longrightarrow \begin{Bmatrix} |\underline{U}_{i1}'| \\ |\underline{U}_{i2}'| \\ \vdots \\ |\underline{U}_{ip}'| \end{Bmatrix}; \begin{Bmatrix} arg\{U_{i1}'\} \\ arg\{U_{i2}'\} \\ \vdots \\ arg\{U_{ip}'\} \end{Bmatrix}; \begin{Bmatrix} f_{i1} \\ f_{i2} \\ \vdots \\ f_{ip} \end{Bmatrix} \tag{5.20}$$

Starting from the identified interharmonic frequencies $f_{i1}, f_{i2}, \ldots, f_{ip}$ and applying Eq.(5.10),the corresponding BFRP for each phasor referenced to DCH signal can be determined. Considering that the slip value employed to generate the RAH signal from the DCH signal is s=N, and that the fundamental frequency f is set equal to the network nominal frequency(50Hz), Eq.(5.10) can be rewritten as follows:

$$\delta_i = \mathrm{s} \cdot \frac{f'}{f} \cdot \frac{360}{N'} = N \cdot \frac{f'}{50} \cdot \frac{360}{N} = 7.2 \cdot f_i \,(\text{degrees}) \tag{5.21}$$

Consequently, the parameters ϑ and K can be directly obtained from Equations (5.11) and (5.14). Using these parameters, the relationships defined in (5.12) and (5.13) are then applied to the phase and magnitude of the RAH signal phasors. The resulting quantities constitute the phasor set $U_{i1} = \{U_{i1},\ U_{i2}, \ldots, U_{ip}\}$, which defines CISH signal:

$$\underline{U}_j = \begin{Bmatrix} \underline{U}_{j1} = |\underline{U}_{j1}|\lfloor arg\{\underline{U}_{j1}\} = |\underline{U}'_{j1}| \cdot K_{i1}\lfloor arg\{\underline{U}'_{j1}\} + \vartheta_{i1} \\ \underline{U}_{j2} = |\underline{U}_{j2}|\lfloor arg\{\underline{U}_{j2}\} = |\underline{U}'_{j2}| \cdot K_{i2}\lfloor arg\{\underline{U}'_{j2}\} + \vartheta_{i2} \\ \vdots \\ \underline{U}_{jp} = |\underline{U}_{jp}|\lfloor arg\{\underline{U}_{jp}\} = |\underline{U}'_{jp}| \cdot K_{ip}\lfloor arg\{\underline{U}'_{jp}\} + \vartheta_{ip} \end{Bmatrix} \quad (5.22)$$

The estimation of the Ui' phasors, which correspond to the potential interharmonic components present in the RAH signal, is performed using the MCM. In contrast to the original CCHDF approach where interharmonic estimation relied on DFT combined with peak detection the proposed methodology adopts the Modified Covariance Method(MCM) to achieve superior interharmonic estimation performance. Because it achieves high- resolution spectral analysis using significantly reduced data sets, MCM is particularly well adapted for the protective relaying environment. It effectively addresses the critical need for the fast response times and robust real-time performance required in modern electrical power systems [35, 36]. Once the RAH signal contains sufficient samples specifically minimum of N/8 samples, which enables the detection of interharmonic components up to 400Hz, the following estimation procedure is applied:

Signal Preparation: The RAH signal segment is prepared for analysis without windowing or zero-padding, as MCM provides superior resolution without mentioned techniques.

Autoregressive Modeling: A linear predictor is an adaptive filter that forecasts the amplitude of the signal at time m, x(m), using a linear combination of P previous samples [x(m -1), …,x(m - P)] as:

$$\hat{x}(m) = \sum_{k=1}^{P} a_k \; x(m - k) \quad (5.23)$$

Where $\hat{x}(m)$ is the prediction of the signal x(m), and the vector $a^T = [a_1, \cdots, a_P]$ is the coefficient vector of a predictor of order *P*. The prediction error e(m), i.e., the difference between the actual sample x(m) and its predicted value $\hat{x}(m)$, is defined as:

$$e(m) = x(m) - \sum_{k=1}^{P} a_k \, x(m - k) \quad (5.24)$$

Where a_k is AR coefficient and e(m) is the prediction error [36].

Modified Covariance Optimization: MCM minimize the sum of forward and backward prediction errors:

$$J = \frac{1}{2} \sum_{n=p}^{N-1} \left(\left| e_f[n] \right|^2 + |e_b[n]|^2 \right) \quad (5.25)$$

This approach provides superior frequency resolution compared to standard covariance methods.

Frequency Estimation: the AR polynomial roots are calculated:

$$A(z) = 1 + \sum_{k=1}^{P} a_k \, z^{-k} \quad (5.26)$$

Frequencies of sinusoidal components correspond to the angles of roots lying close to the unit circle:

$$f_i = (\theta_i \cdot f_s)/(2\pi) \tag{5.27}$$

Where θ_i is the angle of i^{th} root of $A(z) = 1 + \sum_{k=1}^{P} a_k\, z^{-k}$.

Amplitude and Phase Estimation: For each detected frequency, amplitudes and phases are estimated using least squares technique.

Adaptive Window Processing: For each newly RAH sample, steps 2-5 are iteratively executed an adaptive observation window that expands by one sample at each iteration while preserving the required spectral resolution. The window length is progressively increased until the estimated magnitude, phase, and frequency values satisfy predefined convergence criteria, at which point the window size is considered stabilized.

Change Detection: If estimated values change significantly after stabilization, the process restarts from step 1 to detect new signal components.

This process provide highly accurate interharmonic frequency, magnitude, and phase estimation even with short data windows. Once the phasors of the RAH signal have been estimated, the CISH signal is constructed by applying the phasor relationships defined in (5.22). The generation of the CISH is performed over a window of N samples, corresponding to one fundamental period T, extending backward from the instant at which the interharmonic estimation process is initiated. This backward windowing strategy enables the reconstruction of signal values at previous time instant using information available at current instant. The procedure is the applied successively for subsequent time steps. Accordingly, the general expression of the resulting signal, formulated in terms of the estimated phasors, is given by:

$$CISH = \left|\underline{U}_{i1}\right| \cdot cos\left(2\pi f_{i1} \cdot nT_s + arg\{\underline{U}_{i1}\}\right) + \left|\underline{U}_{i2}\right| \cdot cos\left(2\pi f_{i2} \cdot nT_s + arg\{\underline{U}_{i2}\}\right) + \cdots + \left|\underline{U}_{ip}\right| \cdot cos\left(2\pi f_{ip} \cdot nT_s + arg\{\underline{U}_{ip}\}\right) \tag{5.28}$$

Ultimately, the CCH signal is derived by calculating the difference between the DCH baseline and the synthesized CISH signal. As illustrated in Figure 5.6, the resulting waveform is effectively purged of both interharmonic distortions and exponential decay components, leaving a clean representation of the system's harmonic characteristics:

$$MC - CCH[n] = DCH[n] - CISH[n] \tag{5.29}$$

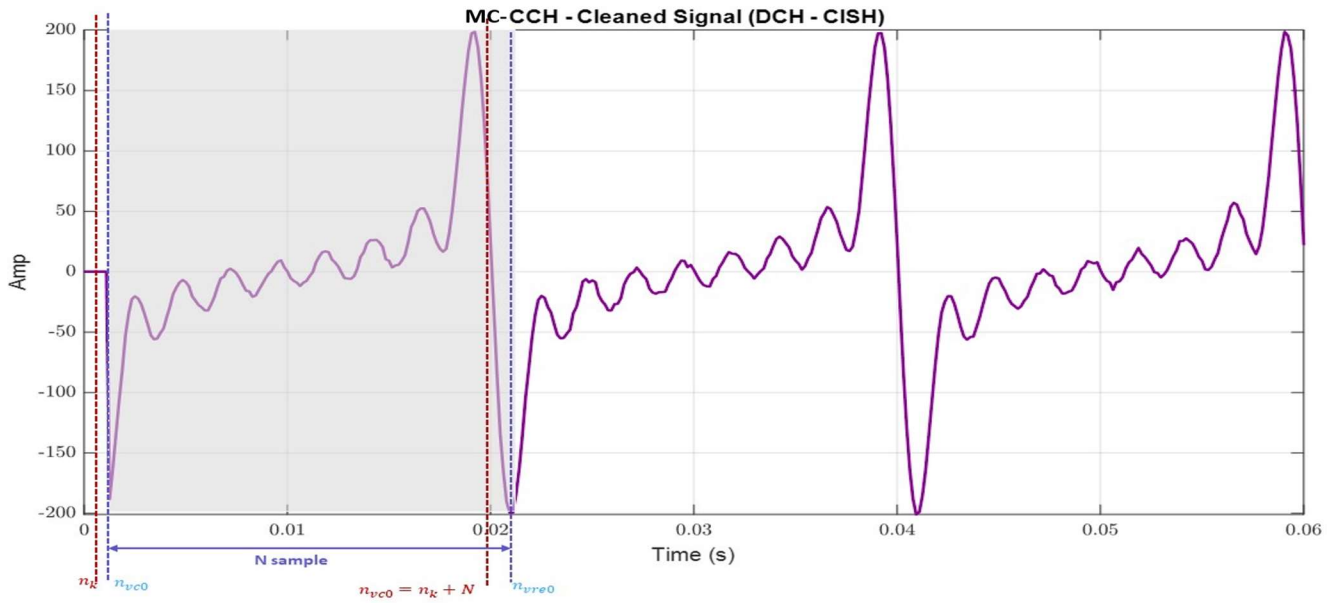

Fig. 5.6 *MC-CCH Wave.*

To get the right answer for the subtraction, we need to know the lengths of the N samples and the time interval that goes with the CISH window. The DCH signal must match the window that goes with the samples $n = n_{vc}$ and $n = n_{vre0}$. Figure 5.7 shows a simplified version of the whole process.

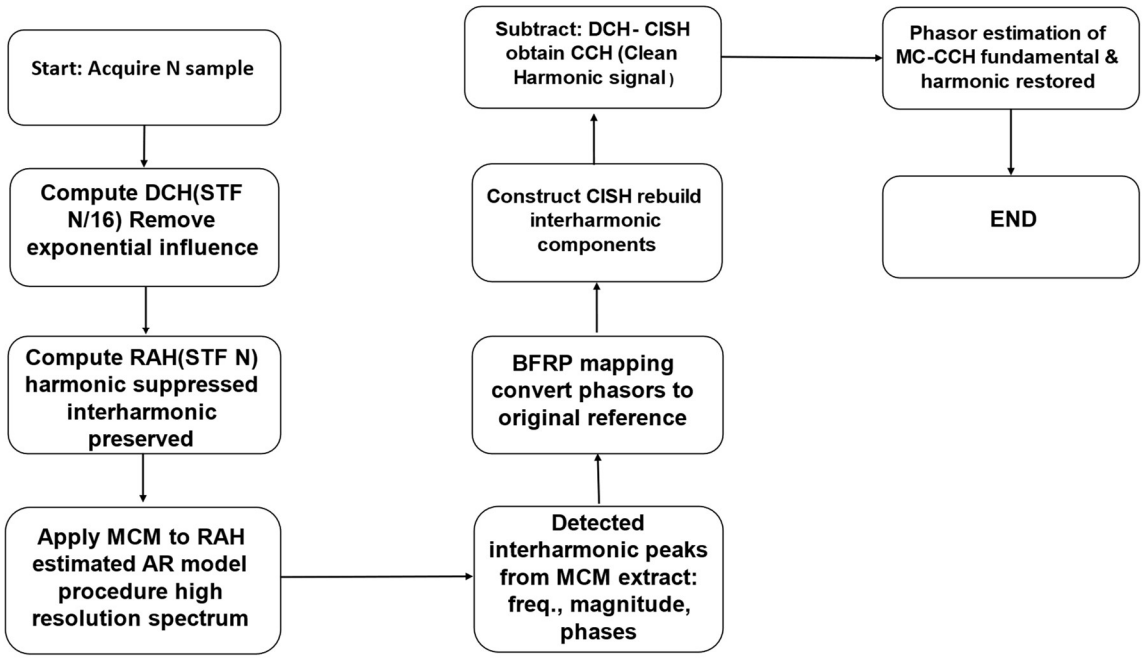

Fig. 5.7 *MC-CCHDF Wave Flow process.*

5.5 Derivation of Original Signal Phasors

The MC-CCH signal isolates the harmonic components, allowing for a direct mapping to the original signal's components via the BFRP technique. This step involves estimating the phasors of the MC-CCH wave denoted as U_1 through U_8, consistent with the antialiasing filter's suppression of higher order harmonics. To reference these values back to the original timeline, a constant sample displacement of $s = N/16$ is applied. This relationship is mathematically formalized by adapting Eq.(5.10) as follows:

$$\delta_h = s \cdot \frac{f'}{f} \cdot \frac{360}{N'} = \frac{N}{16} \cdot \frac{f_h}{50} \cdot \frac{360}{N} = 0.45 \cdot f_h \, (degrees) \tag{5.30}$$

In this formulation, $f_h = f \cdot h$ represent the discrete harmonic frequencies, where f denotes the nominal fundamental frequency (50 Hz), the harmonic index h is constrained to the integer $h = 1, 2, \ldots 8$, reflecting the bandwidth limitations imposed by the antialiasing filter.

With the requisite parameters ϑ and K in Equations (5.11) and (5.14), the BFRP transformation outlined in (5.12) and (5.13) is applied to the MC-CCH signal phasors. This procedure facilitates the recovery of following the original signal phasors, A_h , through the following derived relationships:

$$\underline{A}_h = \left|\underline{A}_h\right| \left| arg\{\underline{A}_h\} = \left|\underline{U}_h\right| \cdot K_h \left| arg\{\underline{U}_h\} + \vartheta_h \right. \right. \tag{31}$$

The derivation of the original signal phasors is synchronized with the calculation of the CCH signal. Because the MC-CCH waveform is periodic with period T , applying a standard one-cycle DFT over a window of N samples allows for the seamless extracting of fundamental and harmonic components. As the analysis window advances by the sampling interval Ts , the estimation process converges toward stable values, ensuring the reliability required for protective relaying functions.

A parallel methodology is employed to quantify the interharmonic phasors. However, whereas harmonic estimation relies on the MC-CCH signal, interharmonics analysis utilizes the referenced phasor of the CISH signal is used. Following the logic established in Equation (5.29), the formulation is adapted as follows:

$$\delta_i = s \cdot \frac{f'}{f} \cdot \frac{360}{N'} = \frac{N}{16} \cdot \frac{f_i}{50} \cdot \frac{360}{N} = 0.45 \cdot f_i \, (degrees) \tag{5.32}$$

Here, f_i denotes the set of estimated interharmonic frequencies identified in Eq.(5.20). By invoking the established BFRP relationships, the phasors A_i , representing the interharmonic components of the original signal, are derived as follows:

$$\underline{A}_i = \begin{Bmatrix} \underline{A}_{i1} = \left|\underline{A}_{i1}\right| \left| arg\{\underline{A}_{i1}\} = \left|\underline{U}'_{i1}\right| \cdot K_{i1} \left| arg\{\underline{U}'_{i1}\} + \vartheta_{i1} \right. \right. \\ \underline{A}_{i2} = \left|\underline{A}_{i2}\right| \left| arg\{\underline{A}_{i2}\} = \left|\underline{U}'_{i2}\right| \cdot K_{i2} \left| arg\{\underline{U}'_{i2}\} + \vartheta_{i2} \right. \right. \\ \vdots \\ \underline{A}_{ip} = \left|\underline{A}_{ip}\right| \left| arg\{\underline{A}_{ip}\} = \left|\underline{U}'_{ip}\right| \cdot K_{ip} \left| arg\{\underline{U}'_{ip}\} + \vartheta_{ip} \right. \right. \end{Bmatrix} \tag{5.33}$$

Chapter 6

Performance Evaluation and Simulation Analysis

6.1 Performance Evaluation and Simulation Analysis

This chapter builds upon the theoretical foundation of the MC-CCHDF algorithm established in Chapter Five, and it centers on the empirical validation of the proposed methodology. The central objective is to evaluate the filter's efficacy in meeting the demanding specifications of contemporary numerical protection relays, with a particular emphasis on accuracy, speed, and resilience in the face of severe transient disturbances. The evaluation employs two principal methodologies: first, the utilization of controlled synthetic test signals engineered to methodically integrate essential disturbance elements, including decaying DC, interharmonics, and noise; and second, a simulated fault scenario based on a validated transmission network model. Performance is then assessed against the conventional DFT and the original CCHDF technique, utilizing quantitative metrics that encompass estimation error, convergence time, and compliance with IEEE C37.118 synchro-phasor standards (TVE, FE, and RFE).

6.2 Evaluation Methodology and Test framework

The algorithm was built and evaluated in MATLAB. To ensure that the results are representative of real-world protection relays, the sampling frequency was set to 6400Hz (128 samples per cycle at 50Hz), which corresponds to modern Digital Signal Processor (DSP) capabilities in industrial relays. The analysis of the obtained results was conducted in strict accordance with IEC 61000-4-30 and 61000-4-7 standards [37, 38], which established the protocols for measuring and interpreting harmonic and interharmonic distortion. While the IEC standards prescribe an observation window of 10 cycles (equivalent to 200ms at 50Hz) for accurate spectral analysis, the proposed filter technique demonstrates a significant advantage by achieving precise phasor estimation within only a few fundamental cycles. Furthermore, the specific interharmonic components identified during the filtering process are presented in the subsequent tables for each respective test case.

6.3 Test Signal Design and Configuration

6.3.1 general Signal Model

All test signals conform to the mathematical model established in Eqs.(5.1) and (5.2), representing a comprehensive fault signal containing:

$$y(t) = C_{dc} + C \cdot e^{\frac{-nT_S}{\tau}} + \sum_{h=1}^{l} A_h \cdot \cos(2\pi f \cdot h \cdot nT_S + \alpha_h) + i[n] + z[n]$$

Here, C_{dc} represents the constant DC component, while C and τ denote the magnitude and decay time constant of exponential transient, respectively, the term $z[n]$ corresponds to additive noise contamination, and $i[n]$ characterizes interharmonic content relative to the fundamental frequency, expressed as a summation of sinusoidal components:

$$A_i \cdot \cos(2\pi f_i \cdot h \cdot nT_S + \alpha_i) \quad with \quad f_i \neq f \cdot h$$

Within this framework, A_h and A_i indicate the magnitudes, while $\alpha_h$and α_i represent the phase angles of harmonic components(Where h=1 designates the fundamental frequency), and periodic interharmonics, respectively.

6.3.2 Test Case Definitions

Three test cases of escalating complexity were created to evaluate the algorithm's performance in more demanding situations. Each case preserves a standard baseline configuration while incorporating additional interharmonic complexity.

Case1: Single Interharmonic Component.

Table 6. 1 *Characteristics of Test Signal-Case1*

Parameter	Value	Description
C_0	100	Dc offset
C_1	80	First exponential magnitude
C_2	50	Second exponential magnitude
τ_1 **(ms)**	100ms	First time constant
τ_2 **(ms)**	50ms	Second time constant
h	1-8	Harmonic order
A_h	100/h	Harmonic amplitude
f_h **(Hz)**	50 Hz	Harmonic frequency
α_h **(°)**	180h/18°	Harmonic phase angles
$Z[n]$	1% of A_1	Noise level
A_{i1}	15	Interharmonic amplitude
f_{i1}	230 Hz	Interharmonic frequency
α_{i1}	$-40°$	Interharmonic Phase

This configuration represents a moderately distorted fault signal with a high-frequency interharmonic component at 230 Hz, positioned between the 4th and 5th harmonics.

Case2: Two Interharmonic Components with Subharmonic.

Table 6. 2 *Characteristics of Test Signal-Case2*

Parameter	Value	Description
Baseline	Same as case1	DC, exponentials, harmonics, noise
A_{i1}	20	Interharmonic amplitude
f_{i1}	42 Hz	Subharmonic frequency

α_{i1}	30°	First interharmonic Phase
A_{i2}	14	Second interharmonic amplitude
f_{i2}	270 Hz	High interharmonic frequency
α_{i2}	-60°	Second interharmonic Phase

This case introduces a critical challenge: a subharmonic component at 42 Hz (84% of the fundamental frequency), which requires extended observation windows for accurate detection, combined with a high-frequency interharmonic at 270 Hz.

Case3: Three Interharmonic components.

Table 6. 3 *Characteristics of Test Signal-Case3*

Parameter	Value	Description
Baseline	Same as case1	DC, exponentials, harmonics, noise
A_{i1}	25	First interharmonic amplitude
f_{i1}	77 Hz	Low interharmonic frequency
α_{i1}	45°	First interharmonic Phase
A_{i2}	20	Second interharmonic amplitude
f_{i2}	180 Hz	Mid-range interharmonic frequency
α_{i2}	-40°	Second interharmonic Phase
A_{i3}	15	Third interharmonic amplitude
f_{i3}	370 Hz	High interharmonic frequency
α_{i3}	-30°	Third interharmonic Phase

The most complex situation involves three interharmonic components spread over the frequency spectrum. Due to its proximity to the fundamental frequency and its second harmonic, the 77 Hz component is especially demanding.

6.4 Performance Evaluation for Synthetic Test Signals

6.4.1 Case1 Results: Single Interharmonic Component

The results demonstrate that while the DFT-based approach exhibits persistent oscillations due to uncompensated exponential decay and interharmonic interference, the MC-CCHDF algorithm achieves rapid convergence to stable, accurate estimates as shown in table 6.4 related to interharmonic detection performance.

Table 6. 4 *Interharmonic Detection Performance-Case1*

Parameter	Actual Value	Estimated Value	Absolute Error
A_{i1}	15	15	0
f_{i1}	230 Hz	230	0
α_{i1}	-40°	-39.98°	0.02

Figure 6.1 presents the temporal evaluation of the original test signal and the corresponding MC-CCHDF wave for case1. The superposition of DC offset, exponential decay, harmonics, and the 230 Hz interharmonic component are all signs of severe distortion in the original signal during the first transient period. On the other hand, the MC-CCHDF wave produces a clear sinusoidal representation of the fundamental and harmonic content by effectively suppressing both the exponential transient and interharmonic contamination.

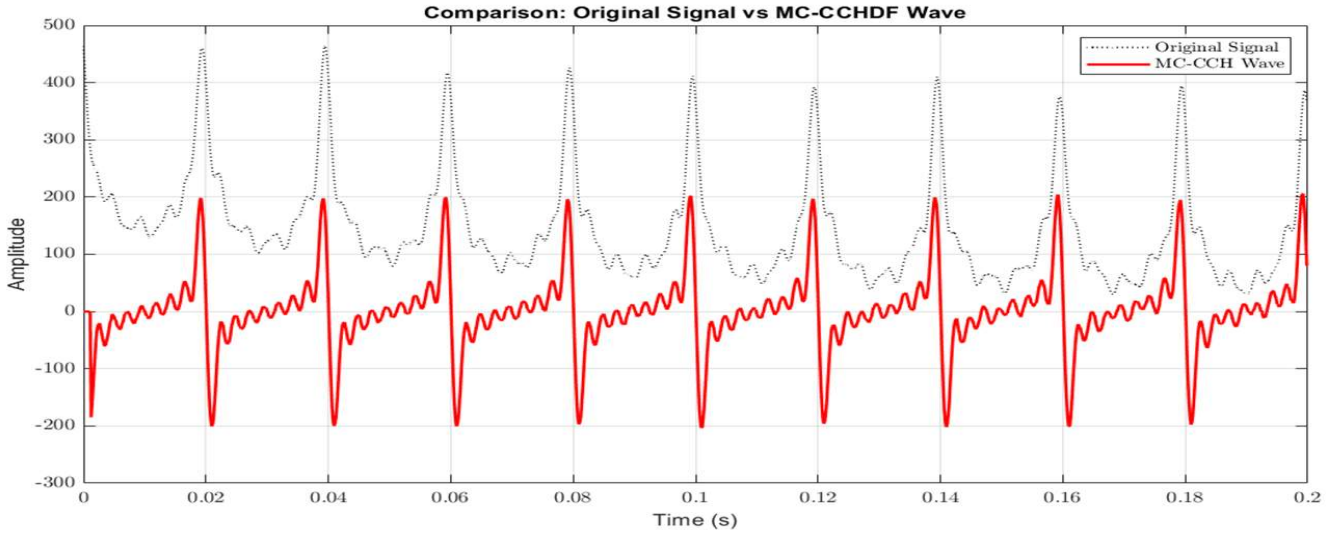

Fig. 6.1 *Original signal vs MC-CCHDF*

Figure 6.2 illustrates the fundamental magnitude and phase estimation for case1, comparing the MC-CCHDF algorithm against conventional DFT-based estimation and CCHDF.

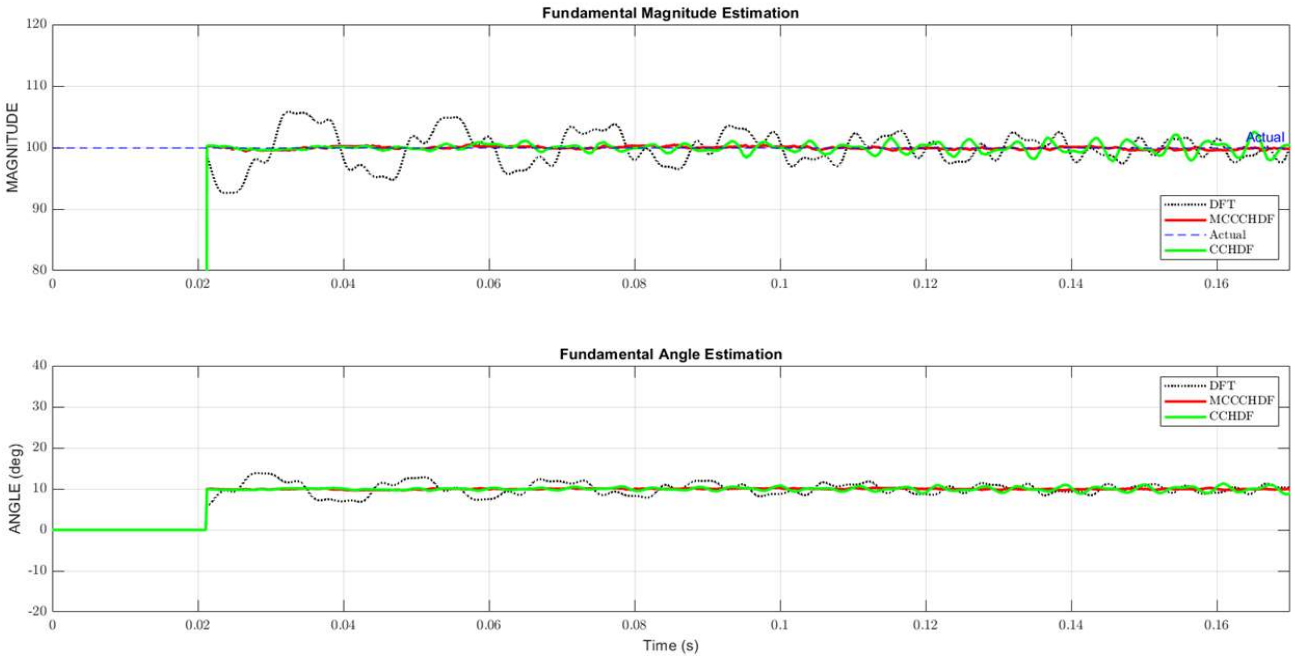

Fig. 6.2 *Fundamental Amplitude and Angle for Case 1.*

The Modified Covariance Method successfully identified the 230Hz interharmonic with exceptional accuracy. The frequency error is below the frequency resolution limit ($\Delta f = f_s/N = 50$ for N=128 samples), indicating perfect bin alignment. The magnitude and phase error are within instrumentation-grade accuracy requirements.

6.4.2 Case2 Results: Dual Interharmonic with Subharmonic

The extended convergence time reflects the adaptive windowing strategy, which requires sufficient samples to reliably characterize the 42 Hz subharmonic. Despite this requirement, the algorithm achieves stable estimates well within the 3-cycle window typically available for protection decision-making. As shown in table 6.5 subharmonic detection results.

Table 6. 5 *Interharmonic Detection Performance-Case2*

Parameter	Actual Value	Estimated Value	Absolute Error
A_{i1}	20	20.21	0.21
f_{i1}	42Hz	42.2	0.2
α_{i1}	30°	26.22	3.78
A_{i2}	14	13.98	0.02
f_{i2}	270 Hz	270	0
α_{i2}	-60°	-60.41°	0.41

The presence of a subharmonic component at 42 Hz presents a significantly more challenging scenario. Figure 6.3 and Figure 6.4 shows that the original signal exhibits beating patterns with a period of approximately 6.25 cycle (1/(50-42) = 0.125s), creating amplitude modulation that complicates phasor extraction.

The MC-CCHDF wave successfully eliminates both interharmonic components while preserving harmonic integrity. However, the convergence time is extended compared to case1 due to the lower frequency of the subharmonic component.

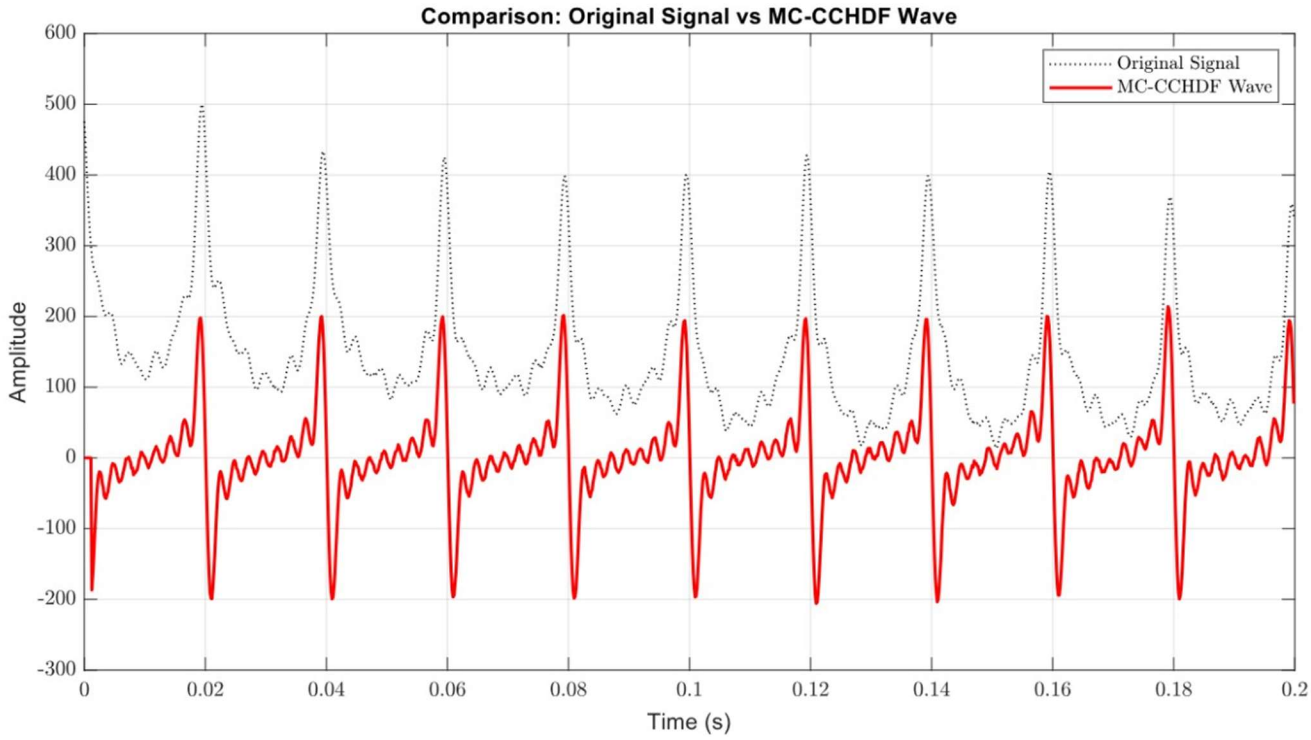

Fig. 6.3 *Original signal vs MC-CCHDF*

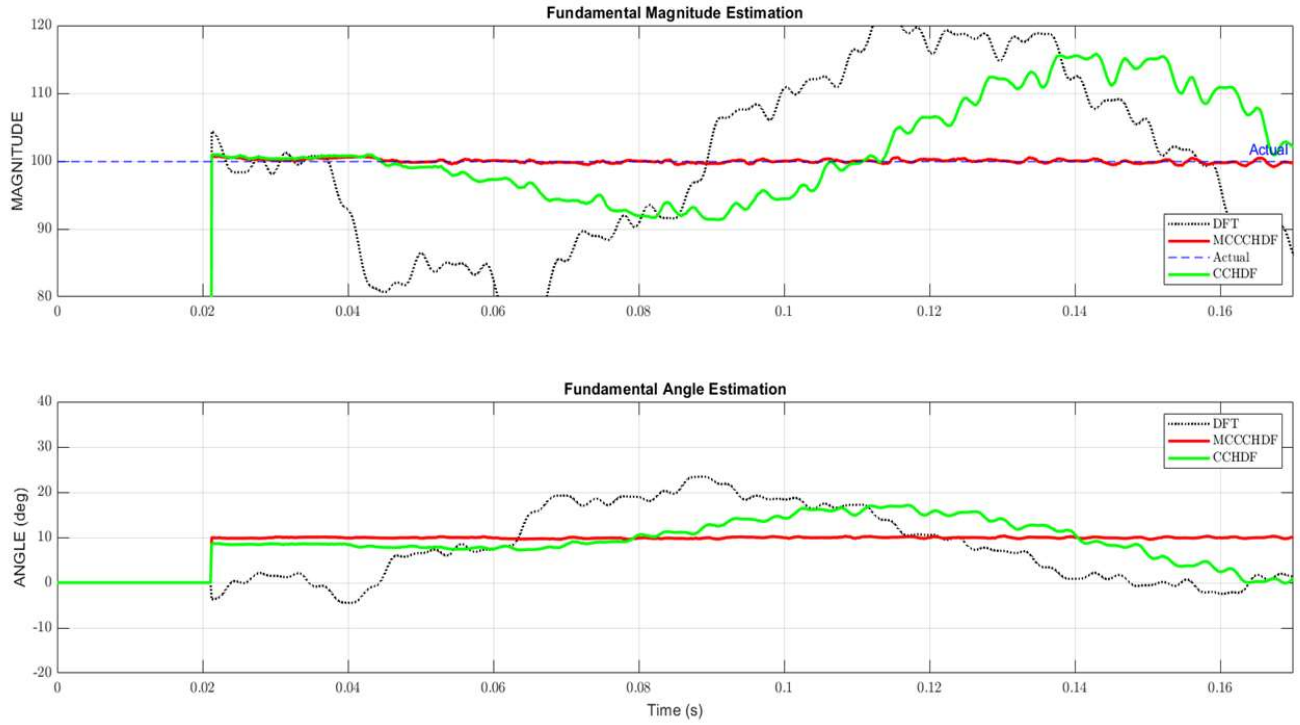

Fig. 6.4 *Fundamental Amplitude and Angle for Case 2.*

6.4.3 Case3 Results: Triple Interharmonic Components

The extended convergence time reflects the complexity of resolving three simultaneous interharmonics, particularly the 77Hz component which is only 27Hz away from the fundamental frequency. Nevertheless, the algorithm maintains stable, accurate estimates after convergence. As in table 6.6 shows interharmonic detection performance.

Table 6. 6 *Interharmonic Detection Performance-Case3*

Parameter	Actual Value	Estimated Value	Absolute Error
A_{i1}	25	24.93	0.07
f_{i1}	77Hz	77.20	0.20
α_{i1}	45°	43.30	1.70
A_{i2}	20	19.97	0.03
f_{i2}	180 Hz	180.10	0.10
α_{i2}	-40°	-40.92°	0.92
A_{i3}	15	14.86	0.14
f_{i3}	370 Hz	370.10	0.10
α_{i3}	-30°	-30.60°	0.60

Case3 represents the maximum spectral complexity evaluated in this study, with three interharmonic components at 77Hz, 180 Hz, and 370 Hz creating multi-modal interference pattern. Figure 6.5 demonstrates the despite this complexity, the MC-CCHDF algorithm successfully produces a clean auxiliary signal. Also, Figure 6.6 shows the most challenging phasor estimation scenario due to spectral congestion.

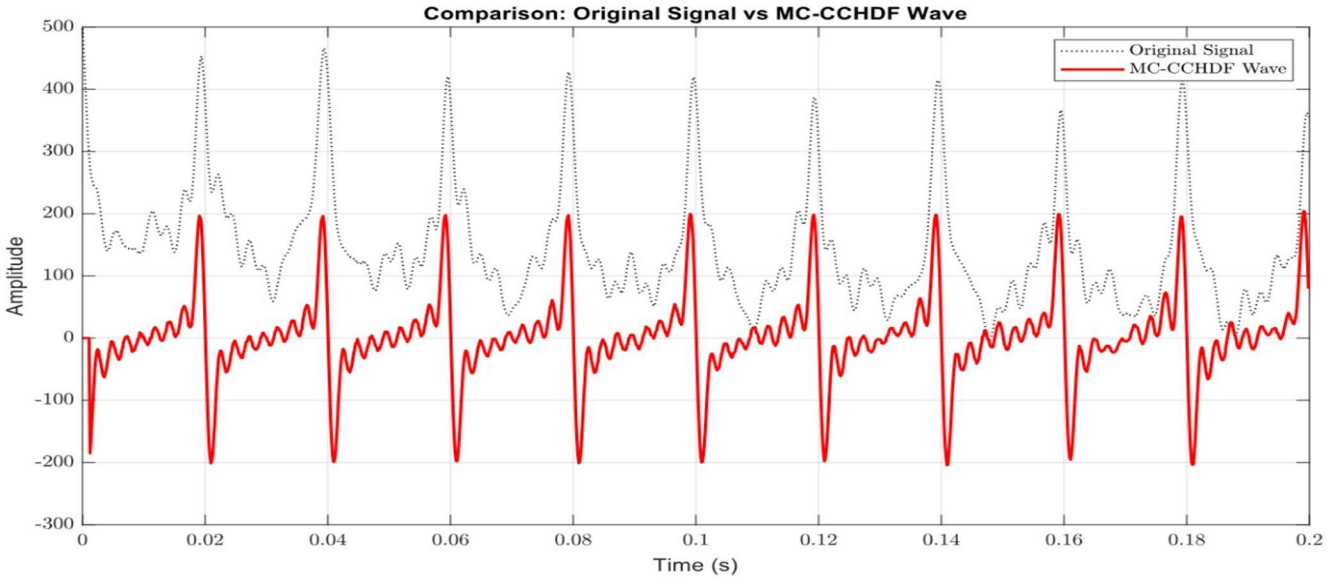

Fig. 6.5 *Original signal vs MC-CCHDF*

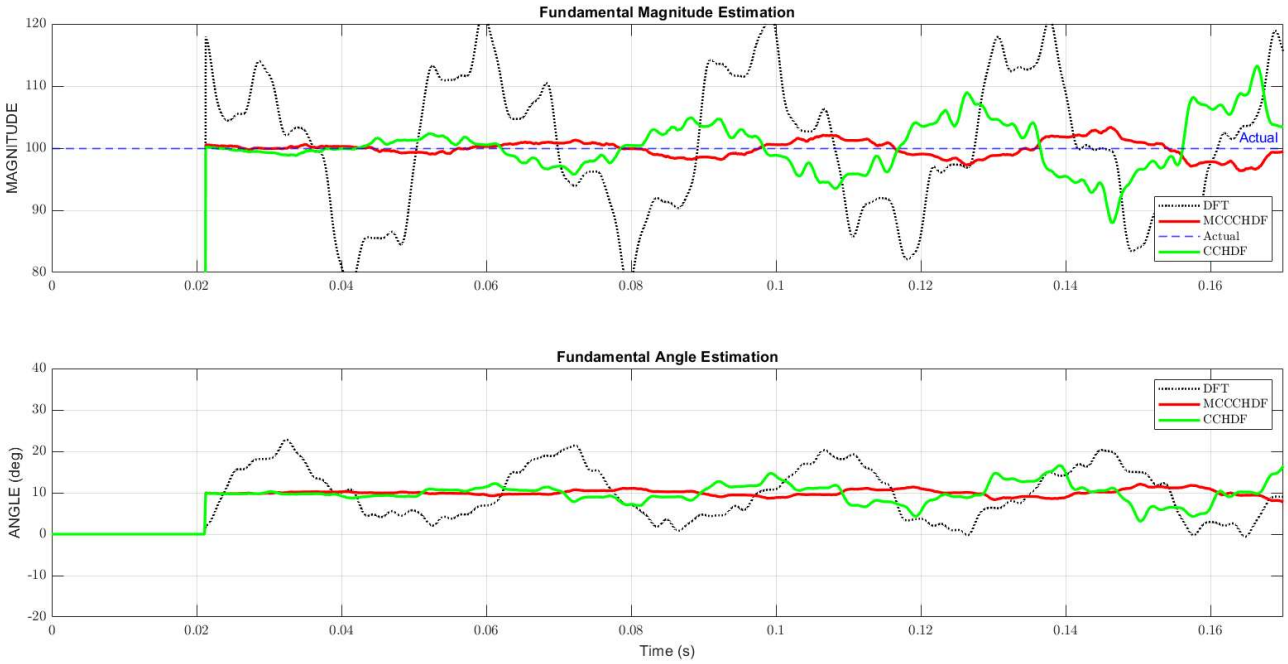

Fig. 6.6 *Fundamental Amplitude and Angle for Case 3.*

The MC-CCHDF demonstrated consistent response times across all cases. Valid output is generated after processing (*N+N/16+N/8*) samples, equivalent to slightly more than one fundamental cycle. In all scenarios, the algorithm converged well within three cycles, meeting the strict speed requirements of protection relays.

6.5 Performance Evaluation of the MC-CCHDF Method Under Dynamic and Adverse Signal Conditions

6.5.1 Increased the Harmonic and Elevated Noise

The results presented in this section correspond to a stress-test scenario in which the number of harmonic components is increased to h=15 (from baseline case of harmonic of h=8) and the additive noise is simultaneously elevated. The observation window is also extended to 0.3s (15 fundamental cycles) to accommodate a richer spectral content and permit statistically meaningful evaluation. The relationship between the original signal and the derived DCH and RAH waves is illustrated in Figure 6.7.

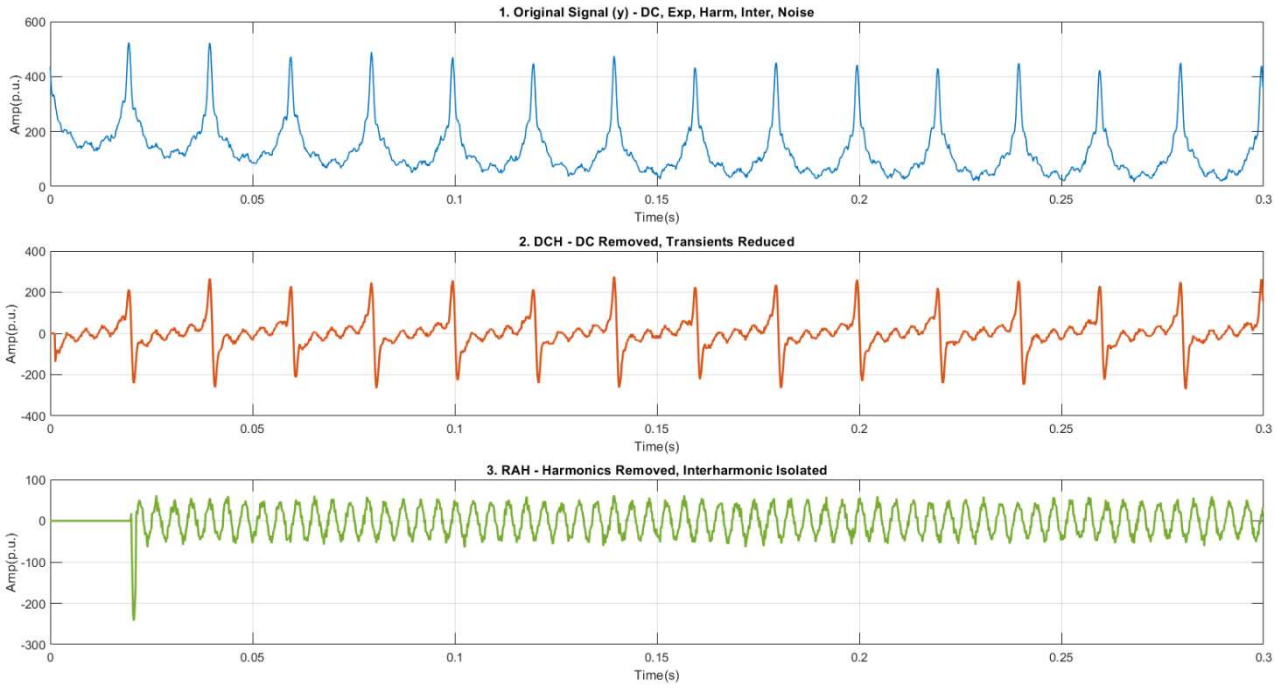

Fig. 6.7 *Robustness of DCH/RAH when Increased the Harmonic and Elevated Noise.*

The composite signal has denser harmonic content and higher peak amplitudes, approximately 520p.u. in the initial cycles, due to the superposition of fifteen harmonic components, a DC offset, and amplified noise. It remains strictly positive due to the DC bias, with more pronounced noise-induced surface roughness compared to the baseline case.

After the first stage of STF filtering, the DC component is removed and the signal is centered around zero. The residual noise is located in the inter-peak regions, but the harmonic shape with sharp periodic spikes is preserved. The peak excursions are slightly higher than the h = 8 case, ± 260p.u., because of constructive reinforcement from more harmonics.

Despite increased harmonic density and noise contamination, the second-stage STF operator effectively suppresses all fifteen integer-harmonic components while clearly isolating the 230 Hz interharmonic. The RAH envelope shows a noticeable noise layer over the dominant ±50p.u. interharmonic oscillation, yet the underlying periodic structure is clearly identifiable, demonstrating the noise-robust nature of the harmonic cancellation mechanism amid complex spectral conditions.

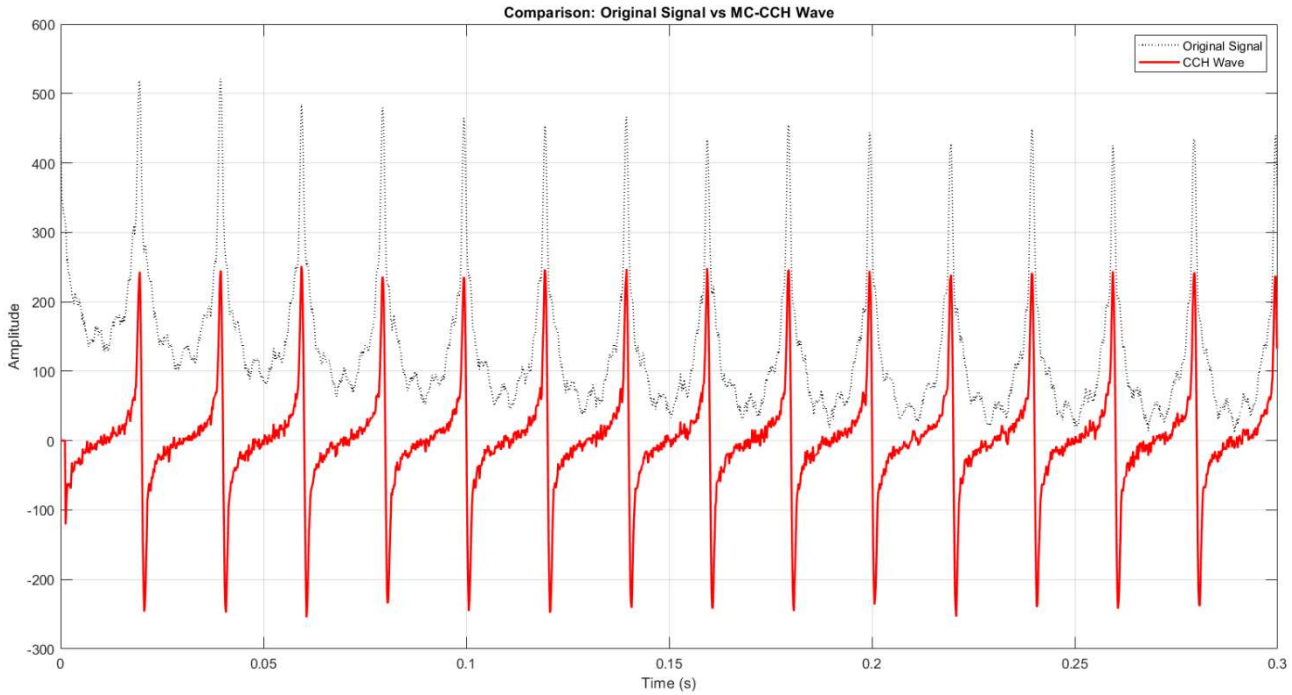

Fig. 6.8 *Original signal vs MC-CCHDF when Increased the Harmonic and Elevated Noise.*

In Figure 6.8 the overlay comparison shows the ability of the MC-CCH wave to extract the harmonic content of an original signal, despite difficult circumstances. The original trace is positively biased and reaches a peak of 520p.u. The MC-CCH wave oscillates in the range of ±260p.u. The noise envelope is higher, but the strong harmonic peaks remain regular from cycle to cycle, showing that the DC-removal and exponential-attenuation functions are intact. The precision of the phasor estimation downstream is expected to be somewhat worse than in the low-noise case.

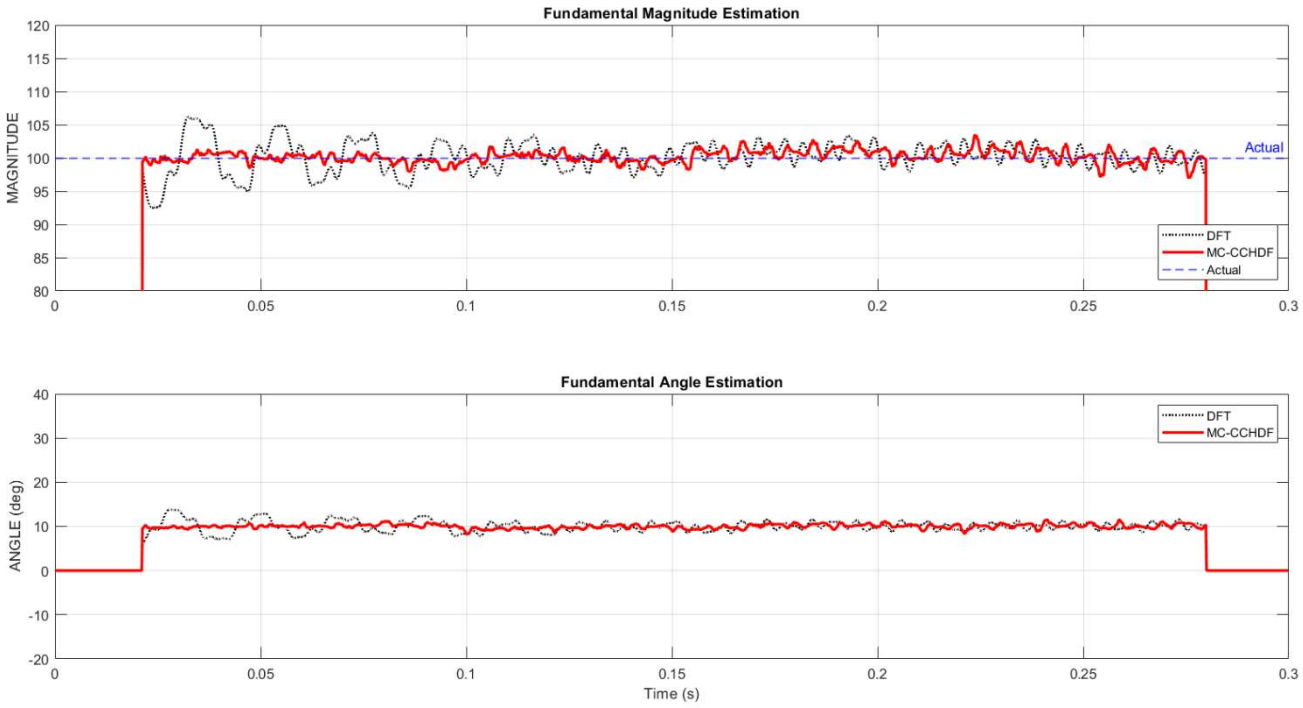

Fig. 6.9 *Fundamental Amplitude and Angle when Increased the Harmonic and Elevated Noise.*

The Figure 6.9 showed that the both estimators track the true fundamental amplitude of 100p.u. effectively within the valid time window ($0.02\ s \leq t \leq 0.28\ s$), despite a more challenging signal environment. The MC-CCHDF shows a tighter estimation band around the true value, with fluctuations within ±2p.u. post-initial transient, while the DFT demonstrates larger oscillations between 92–108p.u. due to increased harmonic leakage and noise. While both methods exhibit slightly greater ripple compared to a low-noise case, the MC-CCHDF retains its superiority over the DFT despite the adverse conditions.

6.5.2 Rapid Amplitude Changes

The test-input envelope for the experiment is shown in the Figure 6.10 in a staircase amplitude profile. The magnitude A_1 of the 50 Hz fundamental is set to 100 p.u. for 0–4 s, then drops to 60 p.u. for 4–8 s, goes back to 100 p.u. for 8–12 s, increases to 150 p.u. for 12–16 s, and finally settles to 120 p.u. for 16–20 s. Each segment is 4 s long, resulting in four discontinuous transitions at t = 4, 8, 12 and 16 s. The goal of this design is to challenge the estimator with amplitude jumps that violate the local-stationarity assumption of phasor algorithms, and test the dynamic tracking capacity of the MCCCHDF framework under fast changing steady-state settings.

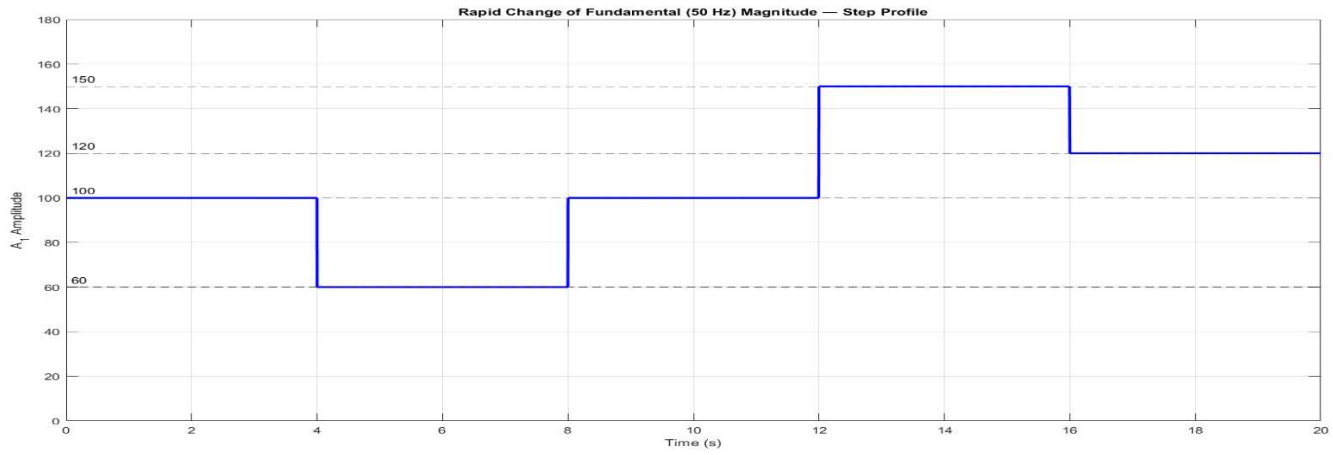

Fig. 6.10 *Rapid Change of Fundamental Amplitude.*

Figure 6.11 showed that the three panels show the steps of the MC-CCHDF front-end filtering chain. The top trace (blue) represents the raw composite signal showing its different constituents, DC offset and measurement noise, while visualizing the envelope stages. The middle trace (orange) is the output of the DCH. It does a nice job of suppressing the DC component and transient, centering the waveform around zero with a flattened envelope showing dominance of harmonic content. The bottom trace (green) shows the RAH output, where the harmonic content is mostly cancelled, revealing a low amplitude interharmonic residue with spikes at transition instants, suggestive of the sensitivity of the slip-filters to envelope changes. The traces indicate the gradual isolation of the target component before the application of the improved covariance estimation.

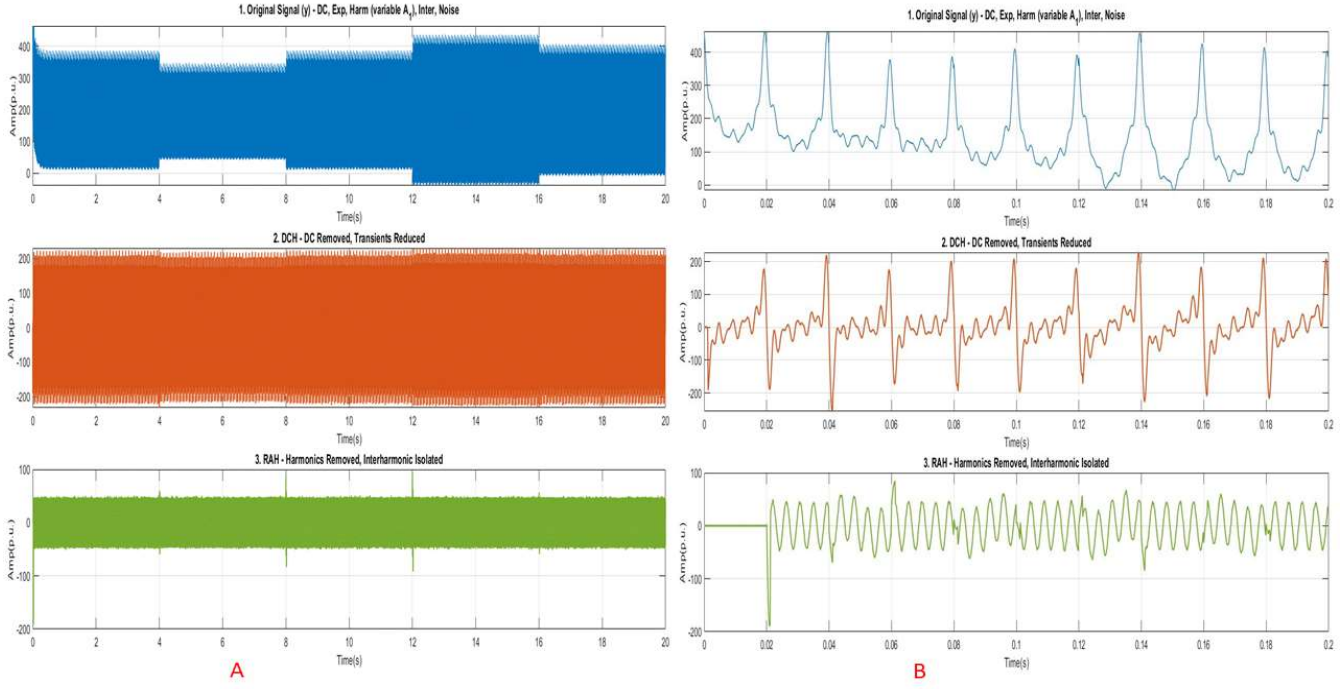

Fig. 6.11 *(a)Robustness of DCH/RAH for Rapid Change of Fundamental Amplitude, (b) magnified signals.*

Figure 6.12 showed that the comparison between the original fault signal and the MC-CCH wave demonstrates the efficiency of the processing chain in recovering the harmonic-dominant component from a contaminated raw signal. The raw signal has a time-varying envelope with a peak value of 320-440 p.u. while the MC-CCH wave is within +/- 200 p.u. with a constant envelope, suggesting the DC offset and transients are successfully removed. In addition, minor spikes of the MC-CCH wave appear at some time points as reconstruction artifacts but disappear fast, which indicates that the MCCCHDF separates well the harmonic content of the composite waveform even during the amplitude variation.

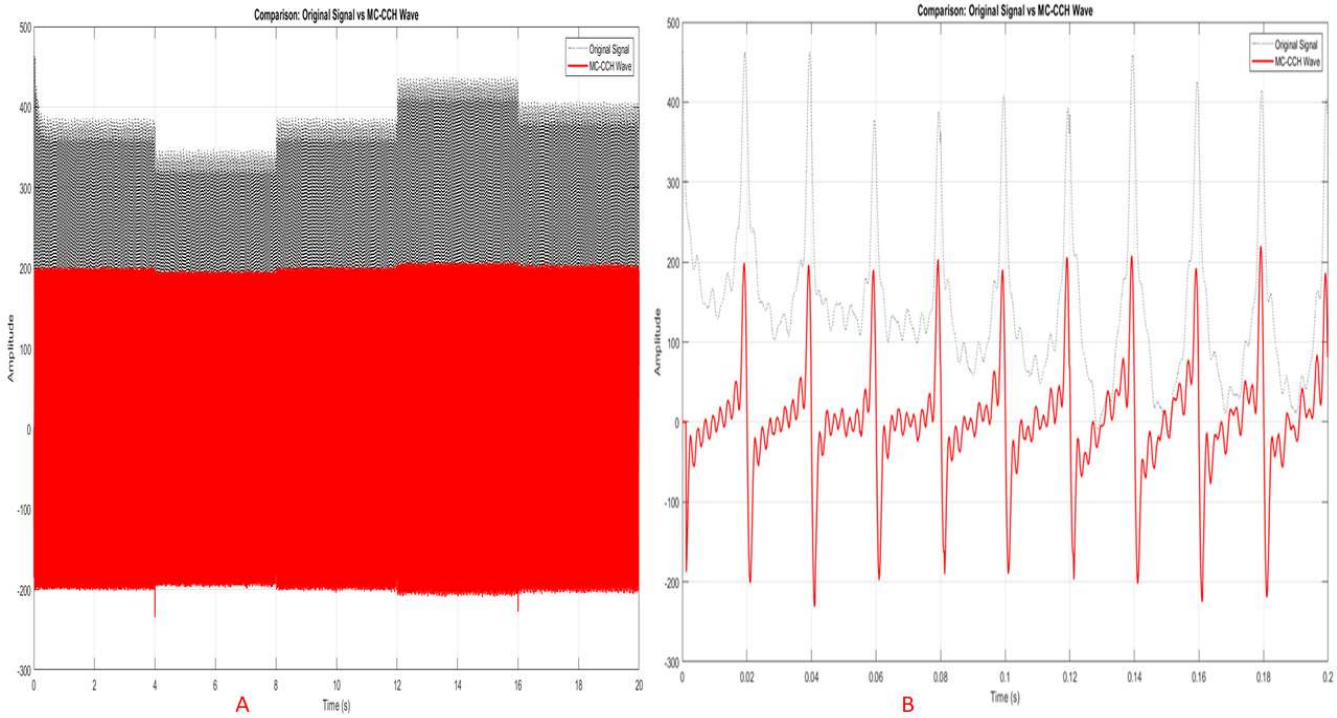

Fig. 6.12 *(a)Original signal vs MC-CCHDF for Rapid Change of Fundamental Amplitude, (b) Magnified signal.*

Figure 6.13 illustrated that both the DFT and MC-CCHDF estimators are inactive, the upper subplot compares the basic magnitude estimates provided by the standard DFT and the proposed MC-CCHDF with the ground-truth reference $A_1(t)$. Both the MC-CCHDF and DFT estimators are able to reproduce the reference staircase levels. A small jitter at higher frequencies is observed, which is attributable to noise and interharmonic residue. No systematic bias is observed. The lower subplot shows that the fundamental angle estimate is close to the +10° reference with small variances during step transitions. These differences are due to the phasor discontinuity, but settle rapidly when the new samples are present. In general, the results of both subplots show that MC-CCHDF is able to monitor the magnitude and phase accurately for rapid amplitude variations, while many traditional estimators fail to do so.

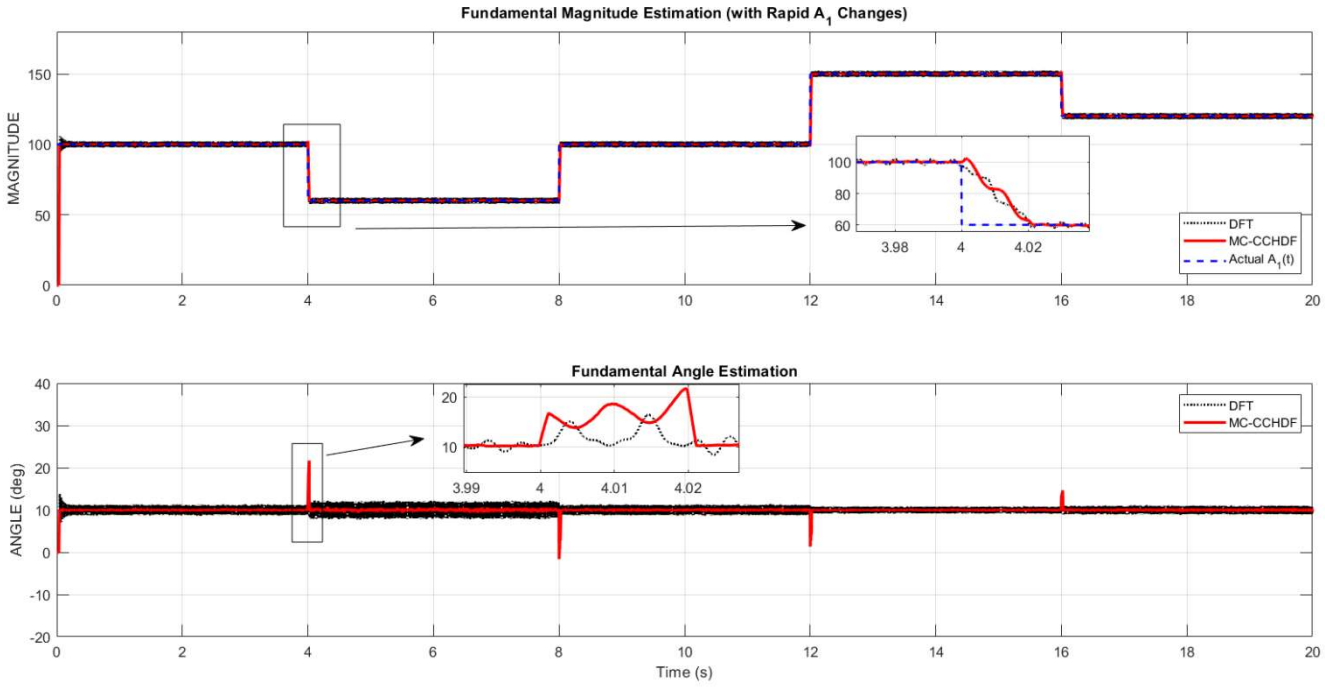

Fig. 6.13 *Fundamental Amplitude and Angle for Rapid Change of Fundamental Amplitude.*

6.5.3 Periodic Frequency Deviation

The Figure 6.14 provides a reference profile for stress testing an estimator with a sinusoidally modulated sinusoid about 50 Hz with 1 Hz deviation and a 1-sec modulation time. The frequency is between 49 Hz and 51 Hz, being off-nominal except at zero-crossings (t = 0, 0.5, 1.0, 1.5, 2.0 s) where it is momentarily 50 Hz. This profile is intended to simulate power-system situations such as generator-governor oscillations and inter-area modes, and shows a time-varying frequency. This is a hard benchmark, as static signal assumptions, in particular classical DFT, perform badly when the real frequency is not equal to the analysis center.

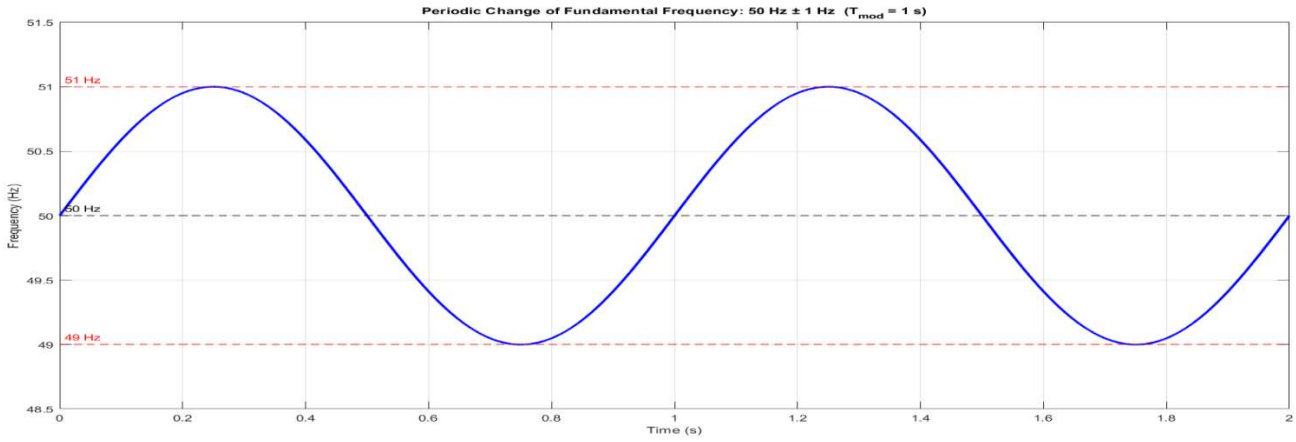

Fig. 6.14 *Periodic Frequency Deviation* **(±1 Hz)**.

The Figure 6.15 illustrated the three subplots representing the evolution of the signals along the MC-CCHDF front-end filtering cascade in frequency-modulated settings. The raw composite input in the top panel, with the DC offset and the harmonic content impacted by the frequency modulation highlighted. The center panel shows the DCH output which is efficient at removing the DC component and slow decay but still some spikes can be seen owing to spectral leakage. In the lower panel, the output of the RAH is displayed, where the harmonic content is suppressed but an interharmonic residue of low amplitude remains. The figures generally demonstrate that the STF cascade still has its signal decomposition capabilities even if the fundamental frequency deviates from nominal, although the residual ripple increases.

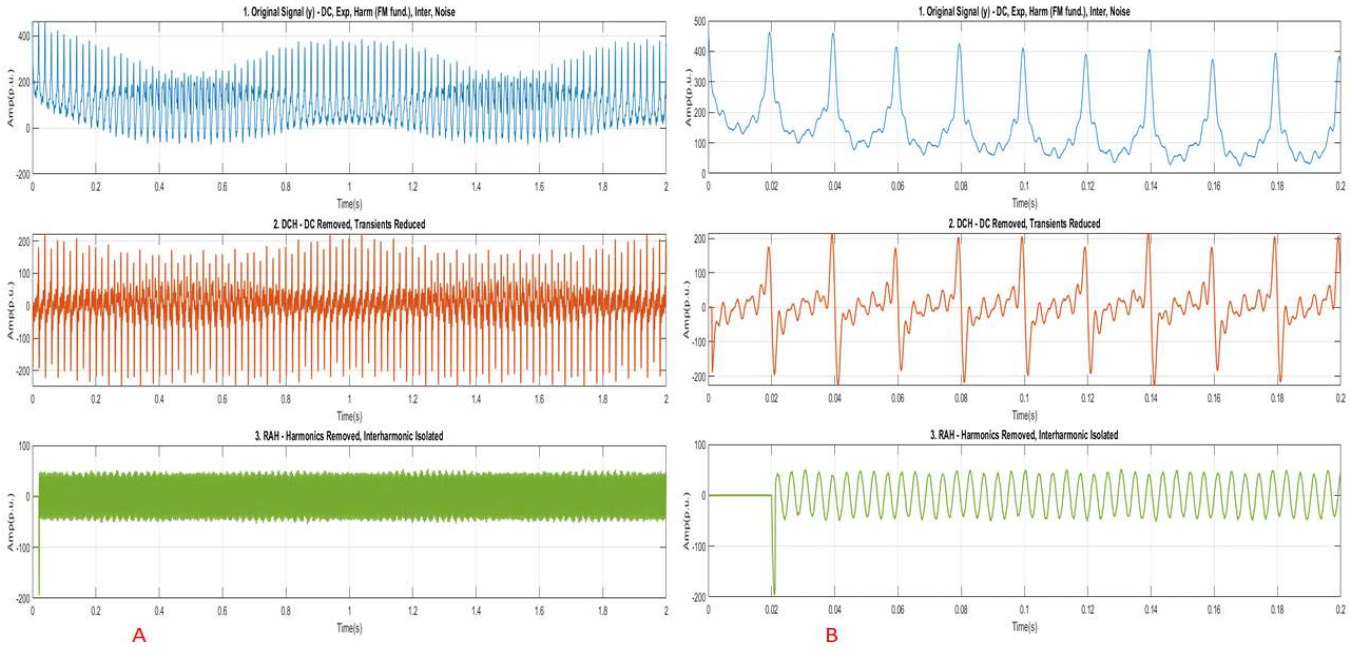

Fig. 6.15 *(a)Robustness of DCH/RAH for Periodic Frequency Deviation* **(±1 Hz)***, (b) Magnified signals*

Figure 6.16 shows the overlay plot displays the raw input signal (dotted black) compared to the MC-CCH reconstruction (solid red). The original signal exhibits a skewed envelope with peaks near +440 p.u. and rarely dipping below −100 p.u., indicating a significant DC bias along with interharmonic noise, with a detectable FM modulation period of 1 second. Post-processing, the MC-CCH wave shows symmetry around zero and remains within ±200 p.u., confirming the effective removal of DC, exponential, and interharmonic components. However, a small high-frequency ripple is present at the peaks due to spectral leakage from the DFT analysis, though it remains stable and does not accumulate, reflecting consistent numerical stability during frequency variations.

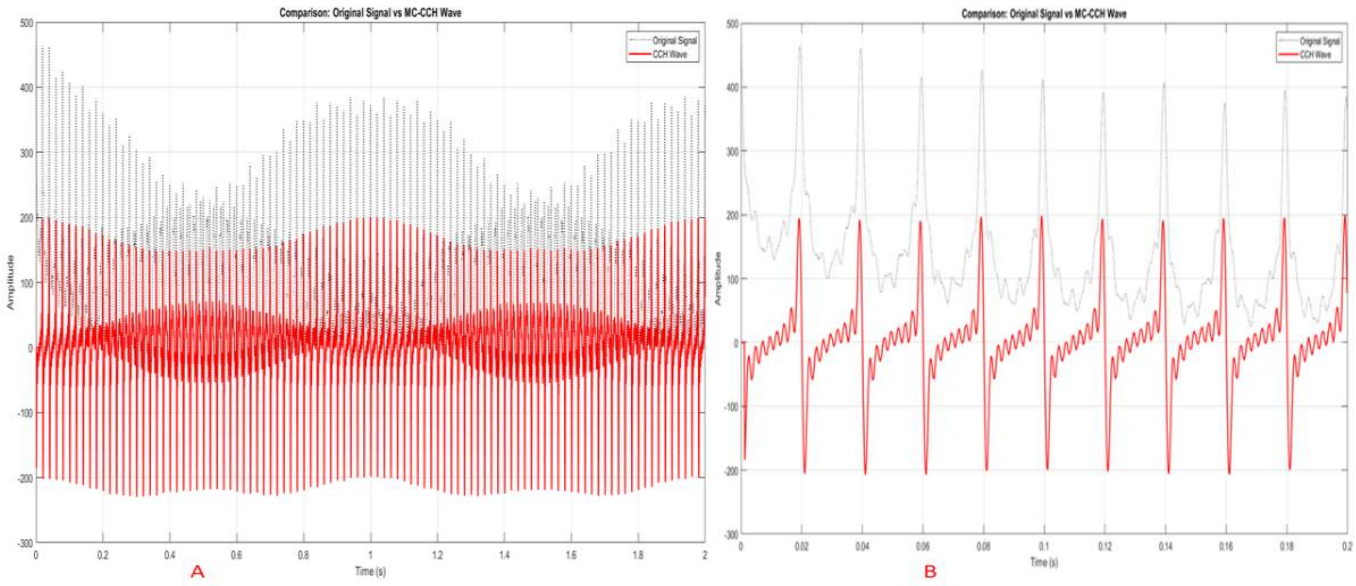

Fig. 6.16 *(a)Original signal vs MC-CCHDF for Periodic Frequency Deviation* **(±1 Hz),** *(b) Magnifying signal.*

Figure 6.17 in the top subplot the fundamental magnitude estimations of MC-CCHDF (solid red) and DFT (dotted black) are presented. Both are quite close to the genuine reference value of 100 p.u. with a variation of ±3 p.u. and slight oscillations related to a 1 s modulation period. The MC-CCHDF has a smaller band of fluctuation which means less leakage. The lower graphic shows the estimated fundamental angle when the angle is nonlinearized with an oscillation between +10° and +125° with a period of 1 s when the instantaneous frequency is different from the nominal 50 Hz . Both approaches match well with this angle profile, but the MC-CCHDF yields a smoother curve, which can offer practical benefits to applications that require exact angle data under varying conditions.

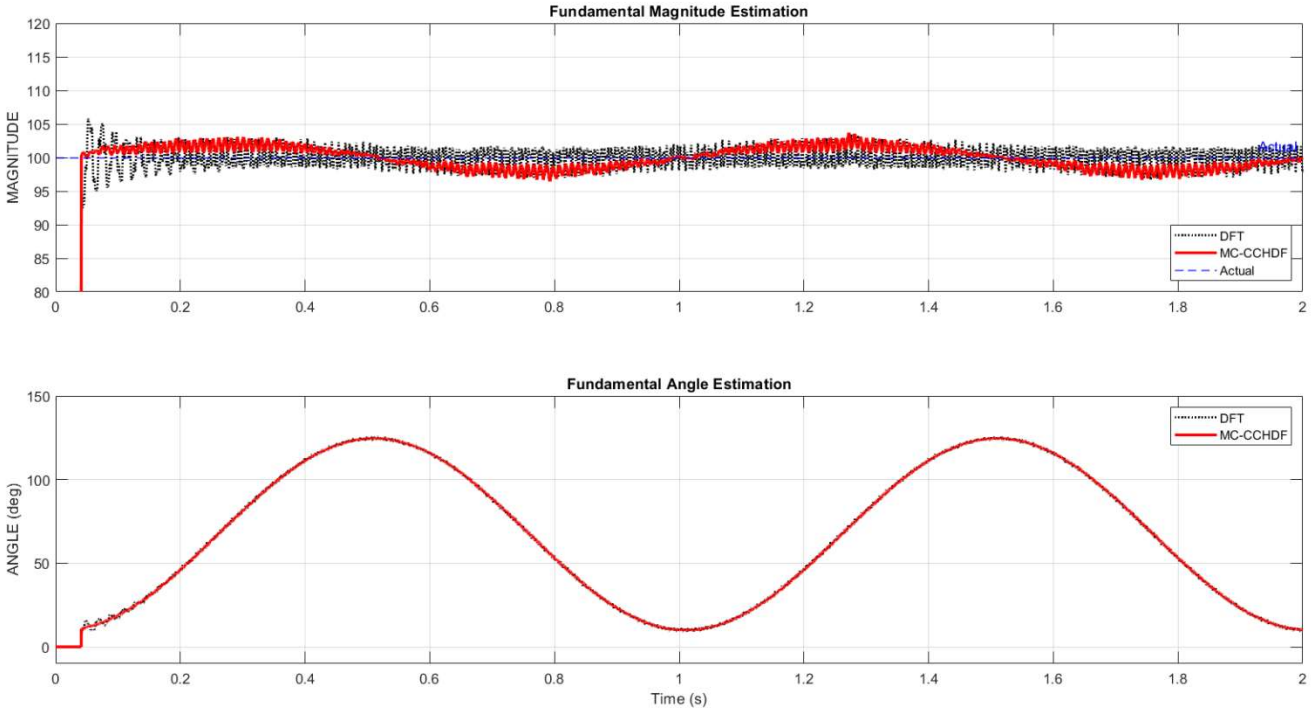

Fig. 6.17 *Fundamental Amplitude and Angle for Periodic Frequency Deviation* **(±1 Hz)**.

Figure 6.18 compares the traditional DFT with the suggested MC-CCHDF algorithm estimates with the ground-truth frequency trajectory. Both approaches can correctly follow a frequency modulation from 49 Hz to 51 Hz over a 2 s frame, and precisely reproduce a sinusoidal modulation of +/-1 Hz. The DFT exhibits a large error envelope (±0.3 Hz) due to spectral leakage. The MC-CCHDF closely follows the reference trajectory with small bias (~0.02 Hz) and less dispersion. There is some bias at the extremities of the modulation (t = 0.25 s, 1.25 s at 51 Hz; t ≈ 0.75 s, 1.75 s at 49 Hz) and a transitory initial burst at t ≈ 0.05 s as the algorithm heats up, but in general the frequency estimate is robust and less noisy than the DFT.

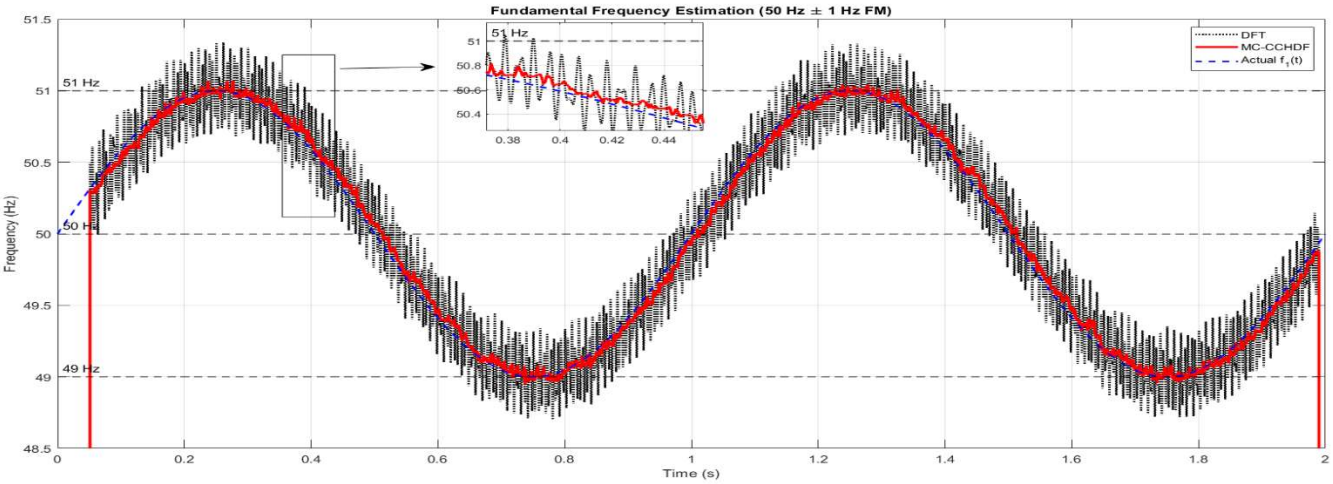

Fig. 6.18 *Estimated Fundamental Frequency for Periodic Frequency Deviation* **(±1 Hz)**.

6.6 Comparative Analysis and Error Metrics

To quantify the improvement over existing methods, the MC-CCHDF was benchmarked against the standard DFT and the original CCHDF algorithm.

6.6.1 Cumulative Estimation Error (CEE)

The CEE provides a comprehensive metric for evaluating long-term estimation accuracy and stability. Its defined as:

$$cee(n) = \frac{1}{n}\sum_{j=1}^{n}\frac{|v(j) - \hat{v}(j)|}{|v(j)|}$$

Where $v(j)$ denotes the actual parameter, and $\hat{v}(j)$ the estimated parameter. The cumulative estimation error is also a discrete variable was calculated for the fundamental phasor modulus. Figure 6.19 illustrates the results indicate that the DFT-based estimator exhibits significant error accumulation due to spectral leakage and DC offset. The original CCHDF reduces this error but shows oscillations when interharmonics are present. The proposed MC-CCHDF achieved the lowest CEE, effective suppression of distortions.

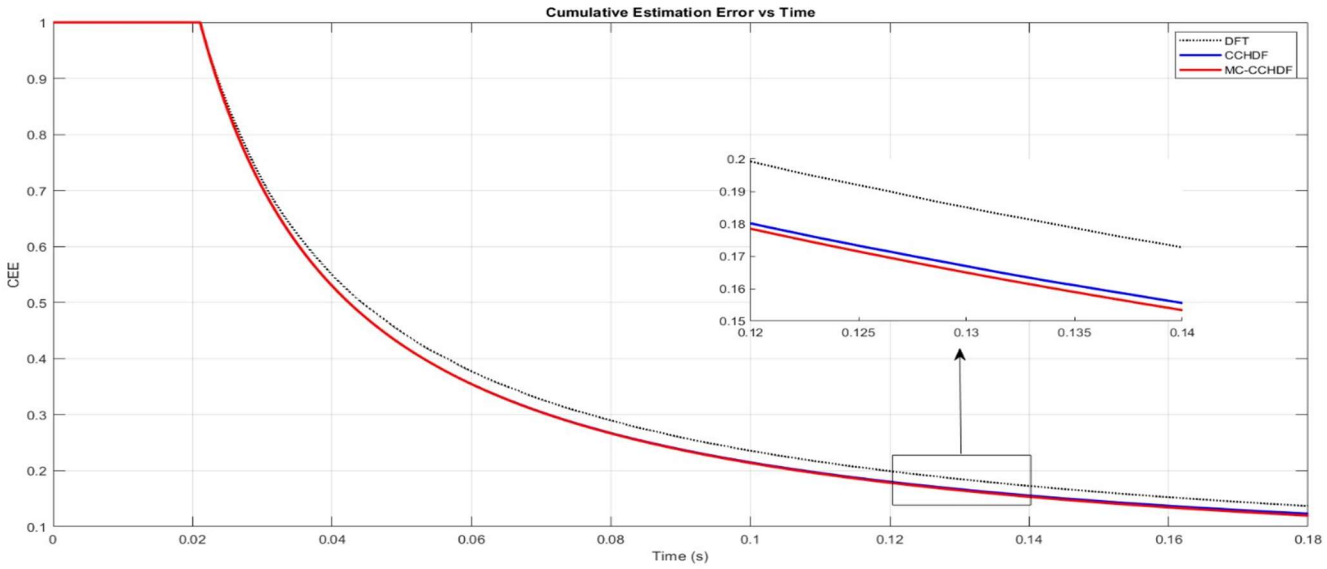

Fig. 6.19 *CEE comparative for DFT,CCHDF, and MC-CCHDF.*

6.6.2 IEEE C37.118 Compliance

The dynamic performance was evaluated using the Total Vector Error (TVE), Frequency Error (FE), and Rate-of-Change-of-Frequency(ROCOF) as in Figure 6.20 illustrates the performance indices(TVE,FE, and RFE) comparison.

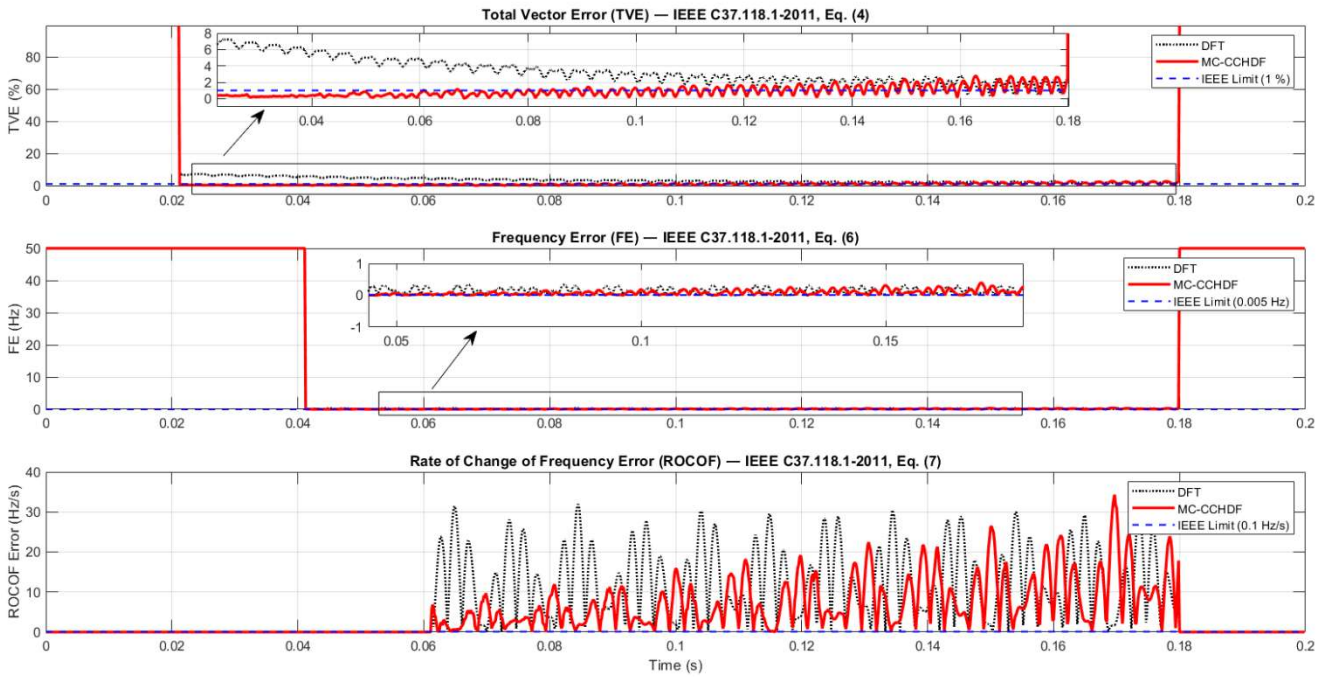

Fig. 6.20 *IEEE indices TVE, FE, and RFE comparison .*

The Total Vector Errors (TVE) illustrates both estimators, MC-CCHDF remains under 1%, whereas DFT varies between 2-5%, above the 1% M-class threshold due to spectral leakage from a 230 Hz interharmonic and diminishing DC, which has been eliminated by the C-Charm pipeline.

Both methods converge to approximately 0.04 seconds, however FE requires one additional cycle compared to TVE due to the differentiation stencil. Both approaches reach the 0.005 Hz limit, although MC-CCHDF tracks the 50 Hz reference more precisely than DFT inside the permitted window. Since FE is the least demanding of the three metrics and merely first-differences the phase, its benefit is subtle.

In this section we address the inversion of the results of the Ts-stencil and emphasize the relevance of the cycle-stencil correction. It observes that the peaks of the MC-CCHDF are 10–20 Hz/s, the peaks of the DFT are 25–35 Hz/s, and the average ROCOF error is 40–50% lower. Also, the MC-CCHDF curve is lower in mean level than DFT, which means the residual phase error after MC interharmonic cancellation is really less than DFT's structured leakage error. The earlier inversion is caused by noise-amplification by the single-sample second derivative.

The absolute ROCOF magnitudes (~10-30 Hz/s) are still beyond the M-class 0.1 Hz/s criteria - however this is expected as the test signal is intentionally adversarial (DC + double exponentials + 8 harmonics + 230 Hz interharmonic + 1% noise), not the pristine tone assumed by IEEE compliance testing. The publication-quality finding is the comparison one: under equal hard conditions, MC-CCHDF decreases TVE, FE and ROCOF error simultaneously relative to standard DFT, with the biggest relative gain on the metric most sensitive to phase quality (ROCOF).

6.7 Results for Realistic Fault Scenarios

While the synthetic test cases outlined in previous sections provide a controlled environment for validating the algorithm's mathematical robustness, the ultimate efficacy of the proposed MC-CCHDF method must be assessed under conditions that emulate actual power system topology and fault physics. To bridge the gap between theoretical validation and practical application, this section evaluates the filter's performance using a fault signal generated from a verified MATLAB-based transmission network model.

The simulation model represents a high-voltage transmission network consist of 246km three-phase line operating in parallel with 78km line. To generate a transient signal with realistic spectral characteristics, a single-phase-to-earth fault was applied at a distance of 100km from the measuring point along the main line. This topology produces a fault current waveform that is physically representative of real-world protection scenarios, comprising both a steady-state pre-fault interval and a highly distorted post-fault interval dominated by exponential decays and decaying DC offsets.

Figure 6.21 presents a temporal comparison of the original fault current against the processed MC-CCHDF waveform. As illustrated in the figure, At t = 0.1 s, phase A exhibits a large upsurge of the phase current with a peak value of around 10 kA and an asymmetric decreasing offset, whereas phases B and C show the stable sinusoidal phase currents of about 1.8 kA. This is consistent with a Single Line-to-Ground (SLG) fault when the only conductor carrying the ground-return current is the defective one. After removal of the DC/exponential transient, the MC-CCH wave on phase A well represents the post-fault component, suggesting that Equation 17 works well with no residual offset drift.

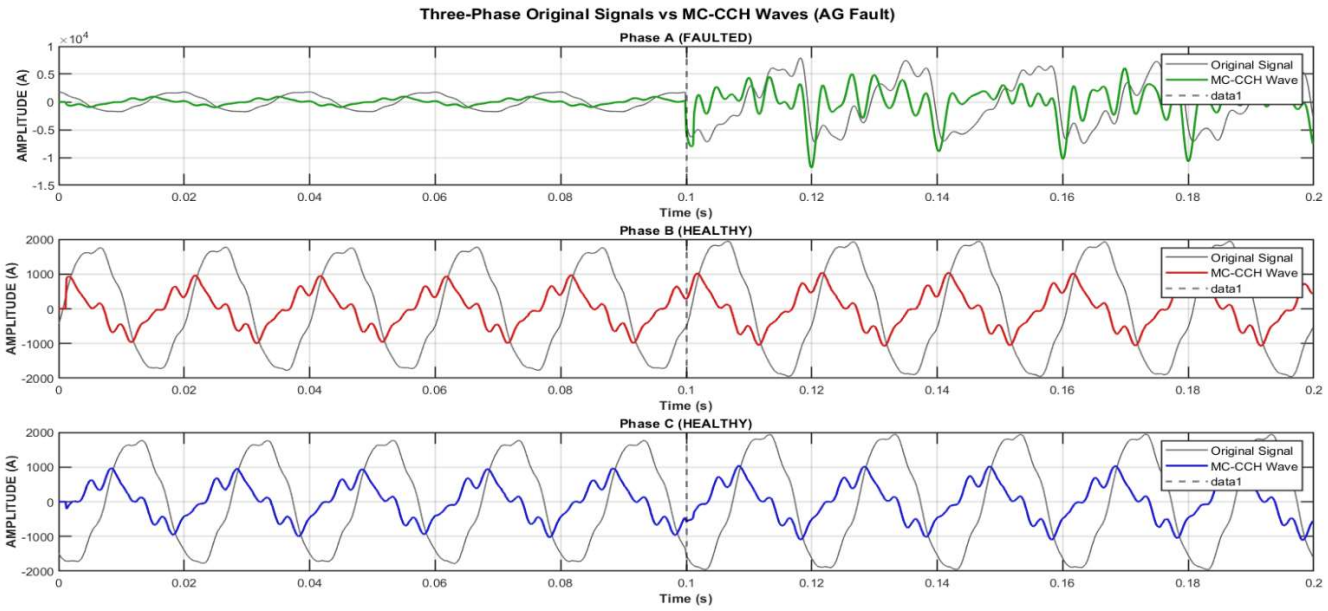

Fig. 6.21 *Original and MC-CCH waves of Single Phase to Ground Fault.*

Further insight into dynamic performance of the algorithm is provided by analyzing the estimated fundamental phasors, shown in Figure 6.22 depicts the magnitude and phase angle of the fundamental component throughout the fault event. Phase A increases from approximately 1.8 kA to 6 kA, aligning

with the fault current target. The MC-CCHDF estimate settles more quickly and exhibits less transient overshoot than the DFT during the fault-inception window from 0.09 to 0.11 seconds, thanks to the BFRP correction compensating for bin leakage in DFT. A residual ripple of around 100–200 A is observed in steady-state post-fault, likely due to a 230 Hz arc interharmonic. Healthy phases remain stable at approximately 1.8 kA, showing only a 5–10% rise from the unbalance, consistent with the parameterization of the healthy branch.

Phase A shows a ~80° lagging swing, typical of a predominantly inductive fault route, and the MC-CCHDF tracks cleanly through this transition. Phases B and C are still at ~−100° and ~+140°, respectively, 120° apart, hence the fault has no effect on the healthy-phase phasors. This is a critical factor on which the 67N directional element depends.

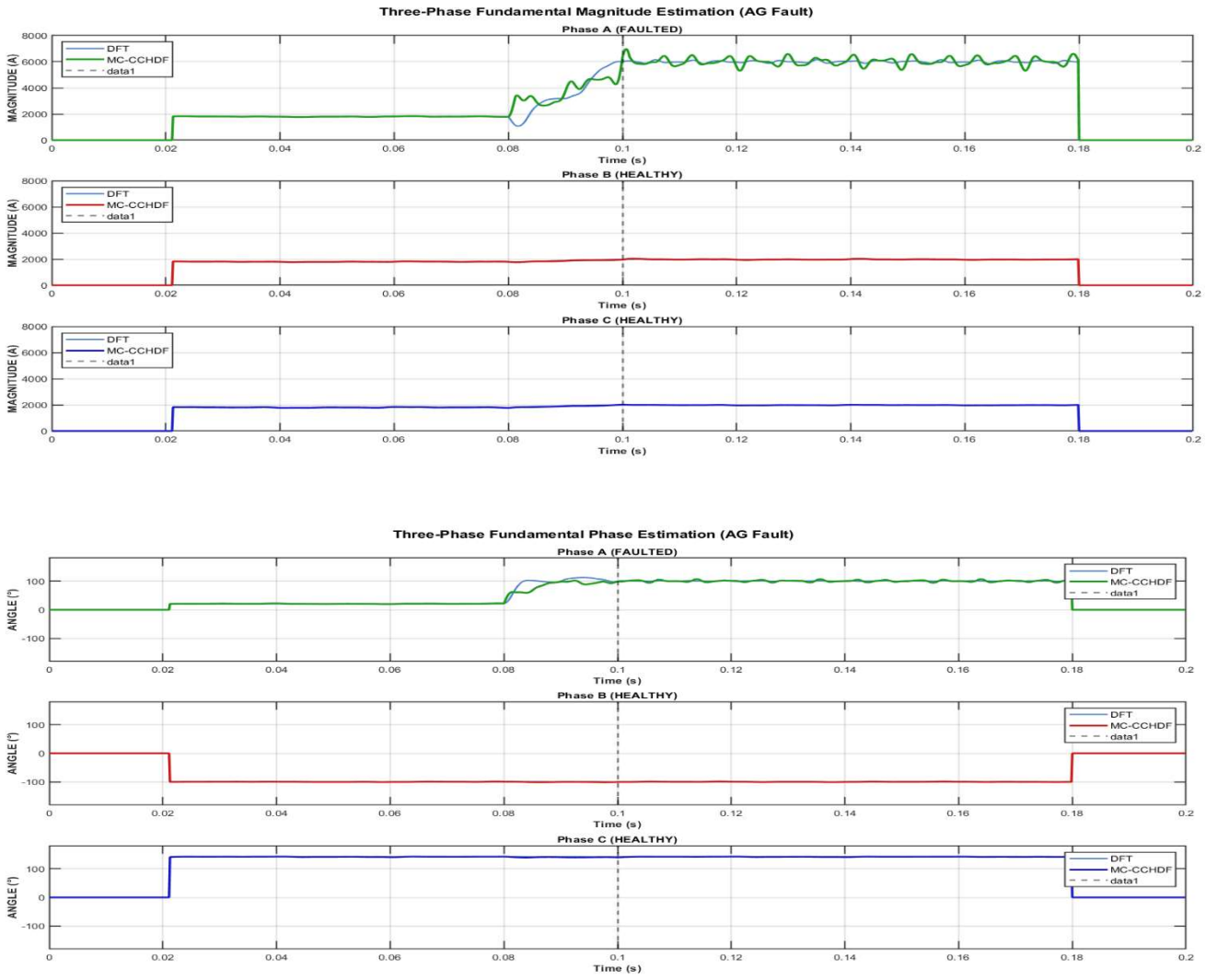

Fig. 6.22 *Fundamental Magnitude and Phase of Single Phase to Ground Fault.*

The Figure 6.22 illustrates the BCG fault topology shows phase A as a healthy sinusoid at ~1.8 kA peak, while phases B and C experience fault currents. Phase B's signal is skewed upward post-fault, reaching +15 kA and -5 kA, whereas phase C is skewed downward with +10 kA and -11 kA. The

inception angles lead to a positive DC offset on phase B and a negative on phase C. The MC-CCH waves confirm the D-Charm stage has effectively removed these DC components.

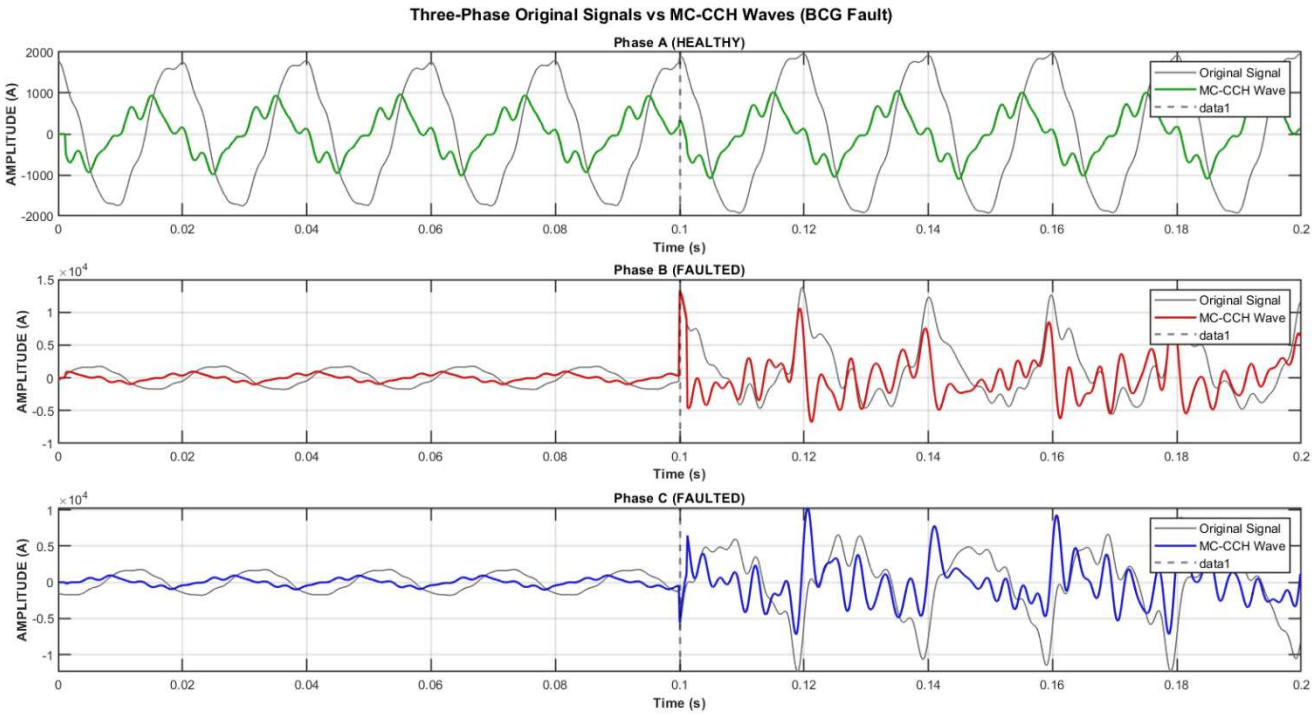

Fig. 6.23 *Original and MC-CCH waves of Two Phase to Ground Fault.*

Figure 6.23 illustrates the fundamental magnitude and phase estimation; Phase A remains steady at 1.8-2 kA with a little ~10% rise due to the built-in imbalance factor. After the fault, the phases B and C go to approximately 6 kA which is the desired fault current level. The MC-CCHDF approach (thick red/blue) tracks the transition more accurately than DFT (thin blue lines) with much reduced overshoot at the first peak, especially in phase B at t = 0.1 s, where DFT spikes to almost 8 kA before stabilizing. Equal magnitudes of the post-fault currents in phase B and C are indicative of the fault type of BCG. For BC fault, the current magnitudes will be equal but in anti-phase configuration.

Phase A remains stable at ~+20°, while Phase B shifts from ~−100° (~−120° load) to ~−15°, and Phase C moves from ~+140° to ~−140°, exhibiting a discontinuous shift at t ≈ 0.083 s due to a wrap-around at the ±180° boundary. The post-fault angles of B and C display an almost exact 180° difference, consistent with the expected phase-opposition at the fault point during a two-phase-to-ground fault with ground return.

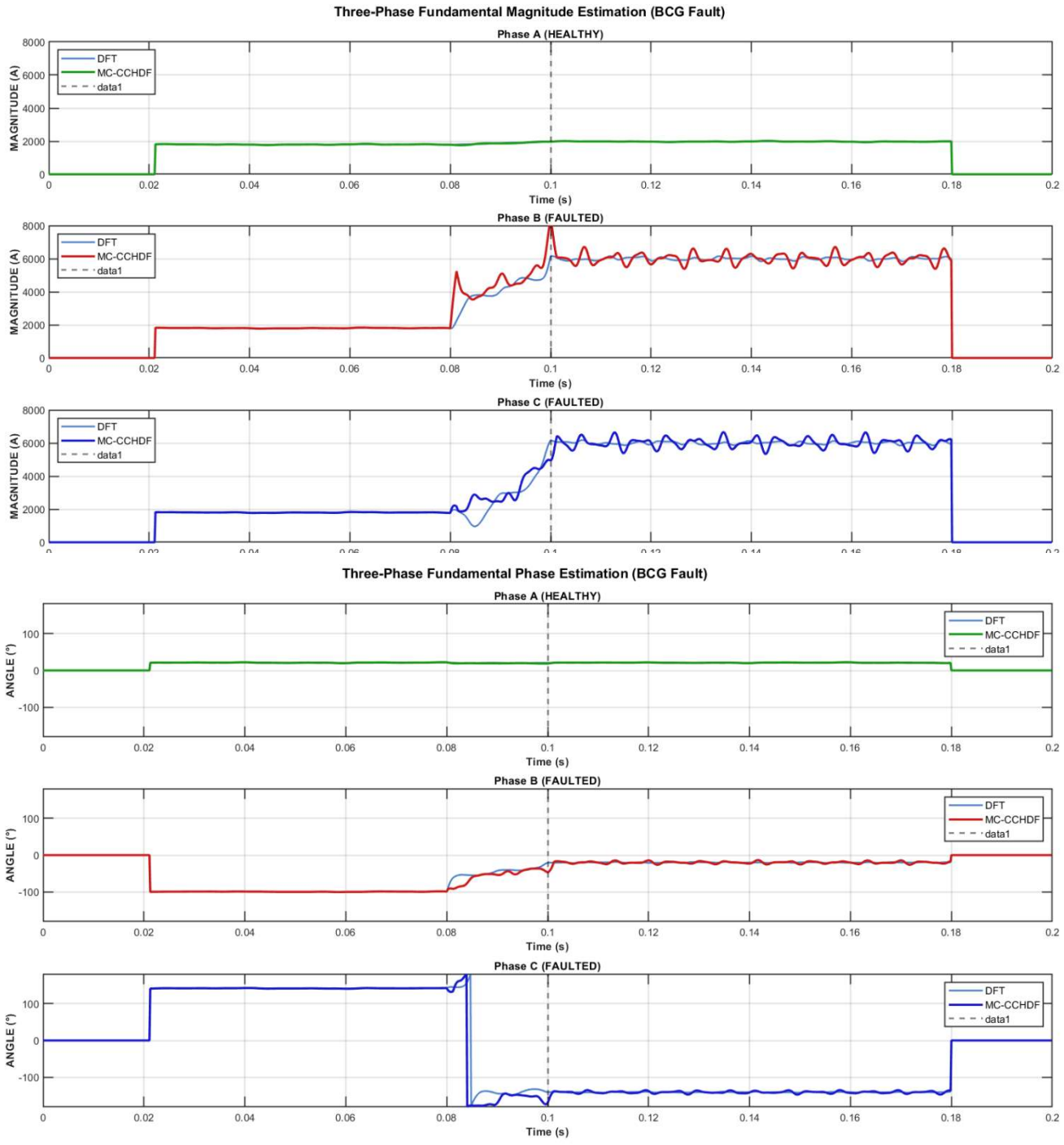

Fig. 6.24 *Fundamental Magnitude and Phase of Two Phase to Ground Fault.*

Figure 6.25 illustrates the three-phase signals are symmetrical after the fault and the waveforms of the signals are obviously asymmetrical. The waveform for phase A is almost symmetric around zero, phase B has a positive bias and phase C has a negative bias as expected from the DC-offset behavior. The DC offsets of each phase total up to zero resulting in the collapse of |I0| as seen in Figure 20. The MC-CCH wave also proves that the D-Charm stage effectively eliminated the opposite DC components in each phase.

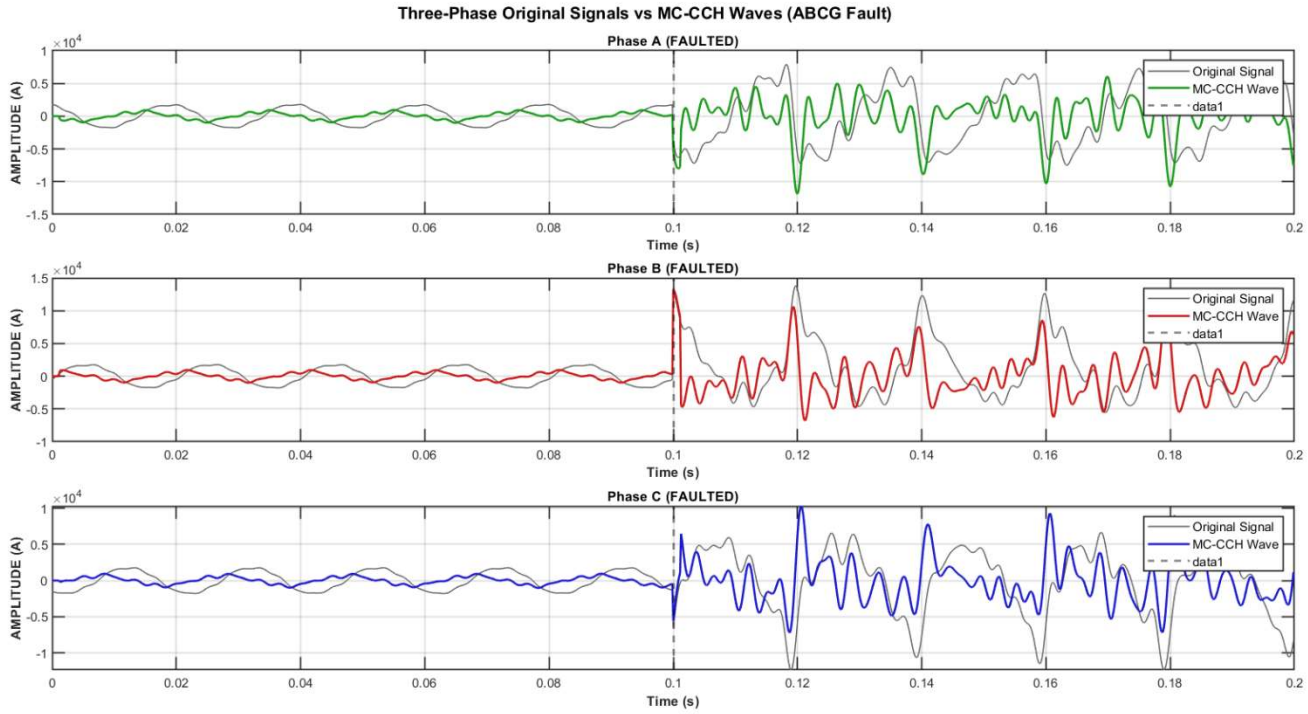

Fig. 6.25 *Original and MC-CCH waves of Three Phase to Ground Fault.*

All three phases show a fault current of about 6 kA, which indicates a balanced fault. The cleanest trajectory at inception occurs in Phase A, due to the minimum DC offset, which allows for the fast Fourier transform (DFT) and Multi-Channel Complex Harmonic DFT (MC-CCHDF) analysis. Phase B features a small MCCCHDF spike about 0.1 seconds with an 8kA overshoot as it responds to a large positive DC offset, and Phase C exhibits a similar pattern. At the end of one full cycle all phases meet at the textbook 3LG state at around 6 kA.

Each phase has a large rotation of ~80° after the faulting event, phase A from +20° to +100°, phase B from -100° to -15° and phase C from +140° to -140° . Importantly, the 120° phase displacement between the conductors is maintained during the fault . This means that the three phasors turn together as a rigid group, which is indicative of a balanced fault, and maintains the symmetry of the system despite the higher currents. As shown in Figure 6.26.

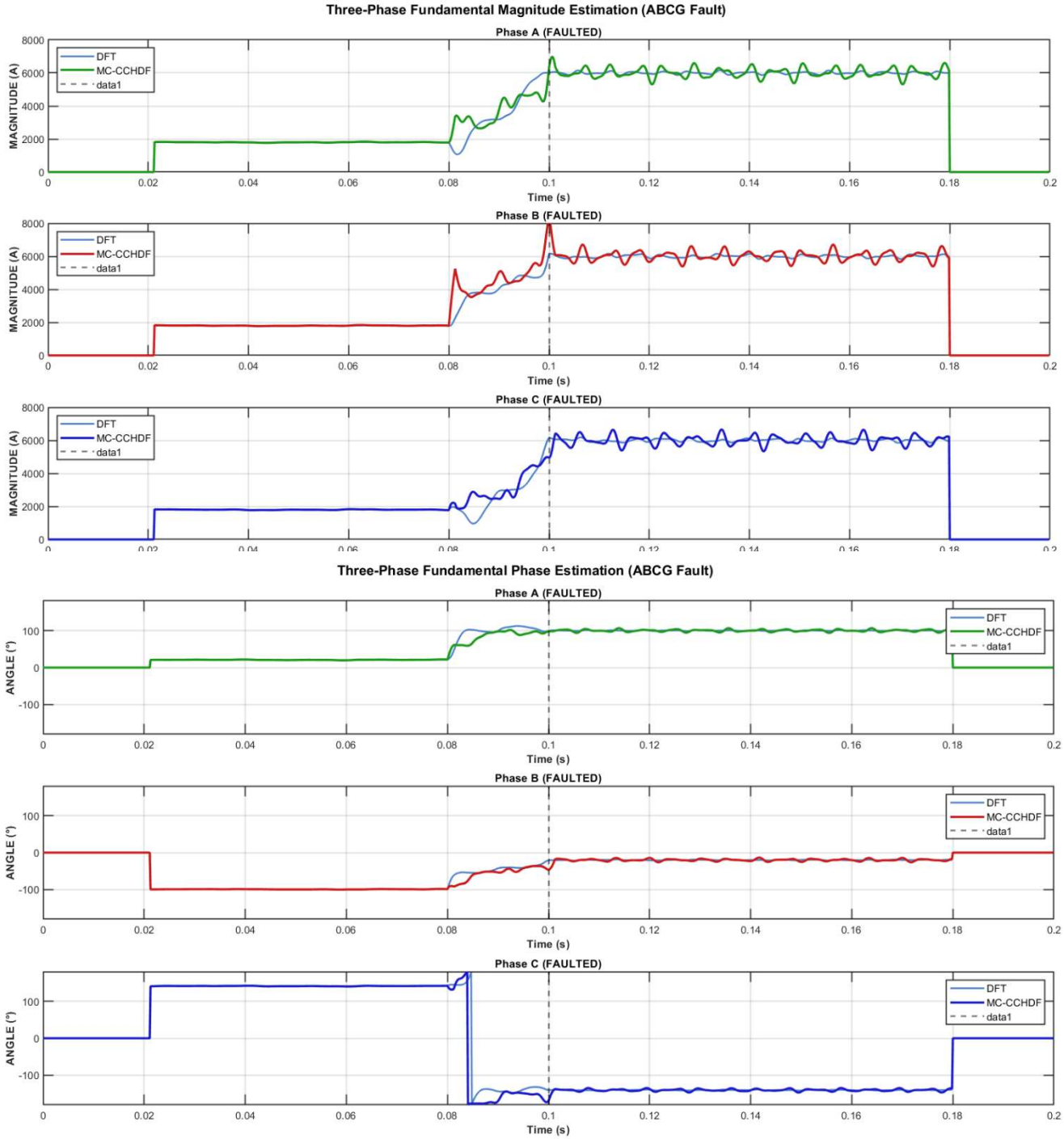

Fig. 6.26 *Fundamental Magnitude and Phase of Three Phase to Ground Fault.*

In summary, the application of the MC-CCHDF to a realistic transmission line fault model confirms the algorithm's capability to handle complex, physically accurate transient phenomena. By delivering a cleaned waveform and stable phasor estimates within the first cycle post-fault, the method demonstrates a high degree of reliability and readiness for deployment in modern digital protection relays.

Chapter 7

Conclusions

7 Conclusions

A novel method, the Modified Covariance- assisted Clean Characteristically Harmonic Digital Filter (MC-CCHDF), has been developed and presented in this work to provide more stable and accurate way to estimate fundamental and interharmonic phasor during power system faults. The proposed approach was evaluated using numerically generated signals representative of realistic transmission line fault conditions, including harmonics, interharmonics, decaying DC components, and measurement noise.

The proposed method achieves a characteristic harmonic signal that is effectively free from both exponential and interharmonic components, enabling reliable phasor estimation under highly non-stationary conditions. By integrating the Modified Covariance spectral estimation technique within the established DCH, RAH, CISH, and CCH signal decomposition structure, the method significantly enhances frequency resolution and robustness compared to classical DFT-based implementation. This improvement is particularly evident in scenarios involving closely spaced or multiple inter-harmonic components, where conventional estimators exhibit oscillatory behavior and show convergence.

The results demonstrate that the MC-CCHDF framework preserves the essential periodic information of the original signal while minimizing the influence of noise and transient disturbances. The estimated magnitude and phase of the fundamental component converge rapidly after fault inception and remain stable phasors accurately, even under severe spectral distortion.

Performance assessment using cumulative estimation error and IEEEC37.118 dynamic indices (TVE,FE, and ROCOF) confirms the superior behavior of the proposed approach. The MC-CCHDF method consistently exhibits reduced instantaneous errors and negligible long term error accumulation, indicating strong numerical stability and suitability for protection-oriented applications. Compared with the conventional DFT and the original CCHDF- based method, the MC-CCHDF framework achieves im-proved dynamic tracking and smoother frequency-related responses.

An important advantage of the MC-CCHDF lies in its structural flexibility. The MC-CCHDF framework is open and modular, allowing alternative spectral estimation techniques to be incorporated within the same signal decomposition architecture while preserving the biunivocal frequency relationship of phasors. Furthermore, the method is independent of the fault inception instant and remains valid for different sampling rates, making it compatible with modern DSP platforms employed in numerical protection relays.

The reduced data window required for stable estimation makes the proposed method particularly attractive for protection and post-fault analysis applications, where only a limited number of samples may be available between fault inception and clearing. Consequently, the MC-CCHDF approach can support reliable operation of protection, monitoring, and fault location functions under both steady-state and transient conditions.

Overall, the obtained results confirm that the proposed MC-CCHDF method provides a precise, stable, and computationally viable solution for advanced digital protection and surveillance systems, offering a clear improvement over existing techniques reported in the literature.

A. Appendix A (Examination of Instantaneous and Averaged Sampling Methodologies)

This investigation's primary aim to mathematically establish whether practical sampling implementations(employing "Sample-and-Hold") introduce spectral distortion relative to ideal sampling. Recall that ideal sampling permits baseband recovery through low-pass filter equivalent to rectangular function with bandwidth F_s.

By starting with natural sampling, regular and averaged sampling techniques can be analyzed. In natural sampling, pulse amplitudes continuously track input signal amplitude throughout the pulse duration τ_p. While natural sampling remains practically unimplementable, it serves as an essential intermediate analytical step for comprehending the two practical sampling approaches.

The periodic pulse train with period T_s and pulse width admits mathematical representation using the gate function $\prod_{\tau_p}(t)$ as follows:

$$i_{Ts,\tau_p}(t) = \sum_{n=-\infty}^{\infty} \prod_{\tau_p}(t - nT_s) \qquad (A-1)$$

Through the use of Dirac comb's periodization property and the convolution operation, the signal $i_{Ts,\tau_p}(t)$ can be transformed into a more appropriate representation:

$$i_{Ts,\tau_p}(t) = \prod_{\tau_p}(t) * \sum_{n=-\infty}^{\infty} \delta(t - nT_s) \qquad (A-2)$$

Consequently, the frequency spectrum of the signal defined in Eq.(A-2) can be expressed as follows:

$$I_{Ts,\tau_p}(f) = \left[\tau_p \cdot \frac{sin(\pi\tau_p f)}{n\pi\tau_p f}\right] \cdot F_s \cdot \sum_{n=-\infty}^{\infty} \delta(f - nF_s)$$

$$\tau_p \cdot F_s \cdot \sum_{n=-\infty}^{\infty} \frac{sin(n\pi\tau_p F_s)}{n\pi\tau_p F_s} \cdot \delta(f - nF_s) \qquad (A-3)$$

In the context of natural sampling, the sampled signal $x_{s,n}(t)$ is derived by multiplying the input signal $x(t)$ by the periodized gate function presented in Eq.(A-2):

$$x_{s,n}(t) = x(t) \cdot i_{Ts,\tau_p}(t) = \prod_{\tau_p}(t) * \sum_{n=-\infty}^{\infty} \delta(t - nT_s) \qquad (A-4)$$

Using the relationship from Eq.(A-3), we can derive the spectrum $X_{s,n}(f)$ of the signal $x_{s,n}(t)$:

$$X_{s,n}(f) = X(f) * I_{Ts,\tau_p}(f) = \tau_p \cdot F_s \cdot \sum_{n=-\infty}^{\infty} \frac{sin(n\pi\tau_p F_s)}{n\pi\tau_p F_s} \cdot X(f - nF_s) \qquad (A-5)$$

By applying Eq.(A-5), we can define the relationship between the input signal spectrum $X(f)$ and the sampled signal's baseband $X_{s,n,b}(f)$ as:

$$X_{s,n,b}(f) = \tau_p \cdot F_s \cdot X(f) \qquad (A-6)$$

Eq.(A-6) shows that an optimal low-pass filter can precisely reconstruct the original signal spectrum in the situation of natural sampling. The proportional relationship between the two spectra confirms that this sampling method introduces no distortion; rather, it effectively corresponds to an extension of the signal's observation period. Since ideal natural sampling is often impractical to implement, this study focuses on scenarios involving a specific pulse width τ_p . in such cases, we consider an approximation of the signal amplitude "held" during the sampling interval. The mathematical formulation for the regular sampling process is expressed as:

$$x_{s,r}(t) = \sum_{n=-\infty}^{\infty} x(nT_s) \prod\nolimits_{\tau_p} (t - nT_s) \qquad (A-7)$$

As demonstrated by Eq.(A-7), applying this sampling technique to the input signal $x(t)$ corresponds to the periodic application of a gate function. In this process, the amplitude of the input signal is held constant at the instant $t = nT_s$ for a duration τ_p. Consequently, the expression can be reformulated as:

$$x_{s,r}(t) = [\, x(t) \cdot \sum_{n=-\infty}^{\infty} \delta(t - nT_s)] * \prod\nolimits_{\tau_p} (t) \qquad (A-8)$$

Therefore, the spectrum of the signal $x_{s,r}(t)$ can be written as:

$$X_{s,r}(f) = [\, X(f) * (\, F_s \cdot \sum_{n=-\infty}^{\infty} \delta(f - nF_s))] \cdot [\frac{sin(\pi\tau_p f)}{\pi\tau_p f}\,]$$

$$= \tau_p \cdot F_s \cdot \frac{sin(\pi\tau_p f)}{\pi\tau_p f} \sum_{n=-\infty}^{\infty} X(f - nF_s) \qquad (A-9)$$

Following the previous method, the baseband part of $X_{s,r}(f)$ is separated using a low-pass filter, represented by the rectangular function $F_s(f)$, this results in the following expression:

$$X_{s,r,b} = \tau_p \cdot F_s \cdot \frac{sin(\pi\tau_p f)}{\pi\tau_p f} \cdot X(f) \qquad (A-10)$$

Apart from the scaling factor $\tau_p F_s$, the baseband component does not exactly replicate the original spectrum $X(f)$ because its amplitude is modulated by the $sinc(\tau_p f)$ function. As a result, the standard sampling method induces spectral distortion. However, this distortion is minor when the ratio τ_p / T_s is

small. This same analytical approach can be applied to average sampling. In this configuration, since the samples $x_{s,a}(nT_s)$ represent the mean value of $x(t)$ over the interval τ_p , the n^{th} sample is formulated as:

$$x_{s,a}(nT_s) = \frac{1}{\tau_p} \cdot \int_{nT_s-\tau_p/2}^{nT_s+\tau_p/2} x(t)\, dt \qquad (A-11)$$

Applying the boxcar function defined in Eq.(A-11) yields the following relationship:

$$x_{s,a}(nT_s) = \frac{1}{\tau_p} \cdot \int_{nT_s-\tau_p/2}^{nT_s+\tau_p/2} \prod\nolimits_{\tau_p}(t-nT_s)\, x(t)\, dt \qquad (A-12)$$

Since Eq.(A-12) expresses the convolution product of $x(t)$ with $\prod_{\tau_p}(t)$, it follows that:

$$x_{s,a}(nT_s) = \frac{1}{\tau_p} \cdot \left[\prod\nolimits_{\tau_p}(t) * x(t)\right] \cdot \delta(t-nT_s) \qquad (A-13)$$

Eq.(A-13) defines the sampled signal $x_{s,a}(t)$ as follows:

$$x_{s,a}(t) = \frac{1}{\tau_p} \cdot \sum_{n=-\infty}^{\infty} \left[\prod\nolimits_{\tau_p}(t) * x(t)\right] \cdot \delta(t-nT_s) \qquad (A-14)$$

By employing the Discrete-Time Fourier Transformer(DTFT) in accordance with the Plancherel theorem, the spectrum $X_{s,a}(f)$ of the signal $x_{s,a}(t)$ is derived as follows:

$$X_{s,a}(f) = \frac{1}{\tau_p} \cdot [\tau_p \cdot \frac{sin(\pi\tau_p f)}{\pi\tau_p f} \cdot X(f)] * [\, F_s \cdot \sum_{n=-\infty}^{\infty} \delta(f-nF_s)]$$

$$= F_s \cdot \sum_{n=-\infty}^{\infty} \frac{sin\left(\pi\tau_p(f-nF_s)\right)}{\pi\tau_p(f-nF_s)} \cdot X(f-nF_s) \qquad (A-15)$$

Following the same procedure as before, separating the baseband component of $X(f)$ results in the following:

$$X_{s,r,b}(f) = F_s \cdot \frac{sin(\pi\tau_p f)}{\pi\tau_p f} \cdot X(f) \qquad (A-16)$$

B. Appendix B (Utilization of the Full-Cycle DFT Algorithm for Phasor Estimation Under Off-Nominal Frequency Conditions)

The effects of spectral leakage on the DFT-based phasor estimator can be demonstrated mathematically. For this analysis, consider a sinusoidal input signal with an off-nominal angular frequency $\omega = 2\pi f$, defined by the relation $\omega = \omega_0 + \Delta\omega$. The m^{th} harmonic of this signal is expressed as:

$$x(t) = X_1 \cos(\omega t + \emptyset_1) + X_m \cos(m\omega t + \emptyset_m) \qquad (B-1)$$

Extracting the real component of the exponential term allows Eq.(B-1) to be reformulated as:

$$x(t) = \sqrt{2}\, Re\left\{\frac{X_1}{2}\, e^{j\emptyset_1} e^{j\omega t}\right\} + \sqrt{2}\, Re\left\{\frac{X_m}{2} e^{j\emptyset_m} e^{jm\omega t}\right\} \qquad (B-2)$$

According to Eq.(B-2), the accurate phasor representation of the fundamental frequency is $\overline{X_1} = \sqrt{X_1^2}\, e^{j\emptyset_1}$, while the m^{th} harmonic is represented by $\overline{X_m} = \sqrt{X_m^2}\, e^{j\emptyset_m}$. When we substitute these formulas into Eq.(B-2), we get the following result:

$$x(t) = \sqrt{2}\, Re\left\{\overline{X_1} e^{j\omega t}\right\} + \sqrt{2}\, Re\left\{\overline{X_m} e^{jm\omega t}\right\} \qquad (B-3)$$

The real component of a complex number is determined by averaging the complex number with its conjugate. This yields the subsequent outcome:

$$x(t) = \frac{\sqrt{2}}{2}\left\{\overline{X_1} e^{j\omega t} + \overline{X_1^*} e^{j\omega t}\right\} + \frac{\sqrt{2}}{2}\left\{\overline{X_m} e^{jm\omega t} + \overline{X_m^*} e^{jm\omega t}\right\} \qquad (B-4)$$

In contrast, the non-recursive DFT phasor estimate for a particular harmonic m, computed at sample time r, is articulated as follows:

$$\bar{X}_m^{(r)} = \frac{\sqrt{2}}{N} \sum_{n=r}^{r+N-1} x(n\Delta t)\, e^{-jnm\omega_0\Delta t} \qquad (B-5)$$

By applying the sampling procedure to the input signal defined in Eq.(B-4), where $t = n\Delta t$ and $\Delta t = 1/Nf_0$ the fundamental phasor $x(t)$ is calculated using the non-recursive DFT as follows:

$$\bar{X}^{(r)} = \frac{1}{N} \sum_{n=r}^{r+N-1} \left\{\overline{X_1} e^{j\omega n\Delta t} + \overline{X_1^*} e^{j\omega n\Delta t}\right\} e^{-jn\omega_0\Delta t} + \frac{1}{N} \sum_{n=r}^{r+N-1} \left\{\overline{X_m} e^{jm\omega n\Delta t} + \overline{X_m^*} e^{jm\omega n\Delta t}\right\} e^{-jnm\omega_0\Delta t}$$

$$\overline{X}^{(r)} = \frac{1}{N}\sum_{n=r}^{r+N-1}\left\{\overline{X_1}e^{j(\omega-\omega_0)n\Delta t} + \overline{X_1^*}e^{j(\omega+\omega_0)n\Delta t}\right\}e^{-jn\omega_0\Delta t}$$

$$+\frac{1}{N}\sum_{n=r}^{r+N-1}\left\{\overline{X_m}e^{jm(\omega-\omega_0)n\Delta t} + \overline{X_m^*}e^{jm(\omega+\omega_0)n\Delta t}\right\}e^{-jnm\omega_0\Delta t}$$

$$\overline{X}^{(r)} = \frac{1}{N}\sum_{n=r}^{r+N-1}\overline{X_1}e^{j\frac{2\pi\Delta f}{Nf_0}n} + \frac{1}{N}\sum_{n=r}^{r+N-1}\overline{X_1^*}e^{-j\frac{2\pi(\Delta f+2f_0)}{Nf_0}n}$$

$$+\frac{1}{N}\sum_{n=r}^{r+N-1}\overline{X_m}e^{j\frac{2\pi\Delta f}{Nf_0}mn} + \frac{1}{N}\sum_{n=r}^{r+N-1}\overline{X_m^*}e^{-j\frac{2\pi(\Delta f+2f_0)}{Nf_0}mn} \qquad (B-6)$$

Eq.(B-6) can be simplified by substituting the variable *n* with *k*, where *k*=*n*-*r*, resulting the following expression:

$$\bar{X}_r = \frac{1}{N}\overline{X_1}e^{j\frac{2\pi\Delta f}{Nf_0}r}\sum_{k=0}^{N-1}e^{j\frac{2\pi\Delta f}{Nf_0}k} + \frac{1}{N}\overline{X_1^*}e^{-j\frac{2\pi(\Delta f+2f_0)}{Nf_0}r}\sum_{k=0}^{N-1}e^{-j\frac{2\pi(\Delta f+2f_0)}{Nf_0}k}$$

$$= \frac{1}{N}\overline{X_m}e^{j\frac{2\pi\Delta f}{Nf_0}r}\sum_{k=0}^{N-1}e^{j\frac{2\pi\Delta f}{Nf_0}mk} + \frac{1}{N}\overline{X_m^*}e^{-j\frac{2\pi(\Delta f+2f_0)}{Nf_0}r}\sum_{k=0}^{N-1}e^{-j\frac{2\pi(\Delta f+2f_0)}{Nf_0}mk} \qquad (B-7)$$

Here's how to find the sum of the geometric series that includes the exponential function:

$$\sum_{k=0}^{N-1}e^{jk\theta} = \frac{1-e^{jN\theta}}{1-e^{j\theta}} = \frac{sin\frac{N\theta}{2}}{sin\frac{\theta}{2}}e^{\frac{j(N-1)\theta}{2}} \qquad (B-8)$$

Consequently, Eq.(B-8) allows the phasor estimate $\overline{X}^{(r)}$ to be expressed as a function of the fundamental and m^{th} harmonic phasors, along with their complex conjugates. Each of these component is weighted by a specific complex factor, as shown below:

$$\bar{X}^{(r)} = \bar{P}^{(r)}\bar{X}_1 + \bar{Q}_1{}^{(r)}\bar{X}_1^* + \overline{P_m}^{(r)}\bar{X}_m + \overline{Q_m}^{(r)}\bar{X}_m^* \qquad (B-9)$$

With:

$$\bar{P}_1^{(r)} = \frac{sin\left(\frac{\pi\Delta f}{f_0}\right)}{N\,sin\left(\frac{\pi\Delta f}{Nf_0}\right)} e^{j\pi\frac{(N-1)}{N}\frac{\Delta f}{f_0}} e^{j\frac{2\pi\Delta f}{Nf_0}r} \qquad (B-10)$$

$$\bar{Q}_1^{(r)} = \frac{sin\left(\left(\frac{\pi}{f_0}\right)(\Delta f+2f_0)\right)}{N\,sin\left(\frac{\pi\Delta f}{Nf_0}+\frac{2\pi}{N}\right)} e^{-j\pi\frac{(N-1)}{N}(\Delta f+2f_0)} e^{-j\frac{2\pi}{Nf_0}(\Delta f+2f_0)r} \qquad (B-11)$$

$$\bar{P}_m^{(r)} = \frac{sin\left(\frac{\pi\Delta f}{f_0}\right)}{N\,sin\left(\frac{\pi\Delta f}{Nf_0}\right)} e^{j\pi\frac{(N-1)}{N}\frac{\Delta f}{f_0}m} e^{j\frac{2\pi\Delta f}{Nf_0}r} \qquad (B-12)$$

$$\bar{Q}_m^{(r)} = \frac{sin\left(\left(\frac{\pi}{f_0}\right)(\Delta f+2f_0)\right)}{N\,sin\left(\frac{\pi\Delta f}{Nf_0}+\frac{2\pi}{N}\right)} e^{-j\pi\frac{(N-1)}{N}(\Delta f+2f_0)m} e^{-j\frac{2\pi}{Nf_0}(\Delta f+2f_0)r} \qquad (B-13)$$

In power systems, where the frequency typically fluctuates slightly around its nominal value such that $\Delta f = f - f_0 \approx 0$, the expression for the resultant phasor $\bar{X}^{(0)}$ at sample time r=0 can be simplified. This is achieved by calculating the limit of the previously mentioned factor $\bar{P}_1^{(0)}$ as Δf approach zero:

$$\lim_{\Delta f\to 0} \bar{P}_1^{(0)}(\Delta f) = \lim_{\Delta f\to 0}\left(\frac{sin\left(\frac{\pi\Delta f}{f_0}\right)}{N\,sin\left(\frac{\pi\Delta f}{Nf_0}\right)} e^{j\pi\frac{(N-1)}{N}\frac{\Delta f}{f_0}} e^{j\frac{2\pi\Delta f}{Nf_0}r}\right)$$

$$= \lim_{\Delta f\to 0}\left(\frac{sin\left(\frac{\pi\Delta f}{f_0}\right)}{N\,sin\left(\frac{\pi\Delta f}{Nf_0}\right)} e^{j\pi\frac{(N-1)}{N}\frac{\Delta f}{f_0}} e^{j\frac{2\pi\Delta f}{Nf_0}r}\right)$$

$$\approx \frac{1}{N} \times \frac{\left(\frac{\pi\Delta f}{f_0}\right)}{\left(\frac{\pi\Delta f}{Nf_0}\right)} \times 1 \times 1 \approx 1 \qquad (B-14)$$

The same procedure applied to the $\bar{Q}_1^{(0)}$ factor results in expression:

$$\lim_{\Delta f \to 0} \bar{Q}_1^{(0)}(\Delta f) = \lim_{\Delta f \to 0} \left(\frac{sin\left(\left(\frac{\pi}{f_0}\right)(\Delta f + 2f_0)\right)}{N\, sin\left(\frac{\pi \Delta f}{N f_0} + \frac{2\pi}{N}\right)} e^{-j\ \frac{(N-1)}{N}(\Delta f + 2f_0)}\, e^{-j\frac{2\pi}{N f_0}(\Delta f + 2f_0)r} \right)$$

$$\approx \frac{\pi \Delta f}{N f_0\, sin\left(\frac{2\pi}{N}\right)} \qquad (B-15)$$

In summary, the $\bar{P}_1^{(0)}$ factor can be neglected solely when frequency deviations are minimal. On the other hand, the $\bar{Q}_1^{(0)}$ factor needs to be considered as soon as the power system frequency start to change. Therefore, Eq.(B-9) can be simplified to the following from:

$$\bar{X}^{(0)} = \bar{X}_1 + \frac{sin\left(\left(\frac{\pi}{f_0}\right)(\Delta f + 2f_0)\right)}{N\, sin\left(\frac{\pi \Delta f}{N f_0} + \frac{2\pi}{N}\right)} e^{-j\pi\frac{(N-1)}{N f_0}(\Delta f + 2f_0)}\, \bar{X}_1^* \qquad (B-16)$$

While a qualitative analysis of the complex gains $\bar{P}_1^{(0)}$ and $\bar{Q}_1^{(0)}$ has been presented, this investigation does not clarify whether minor frequency deviations critically impact phasor estimation accuracy. Furthermore, sampling rate influences these factors, as described in Appendices B equations. Therefore, these two factors require independent by holding one variable constant while varying the other, and vice versa. Initially, consider a power system nominal frequency f_0 at 50Hz, with a fixed sampling rate F_s *=2,400*Hz, resulting in N=48 samples per-nominal cycle. Under this configuration, the magnitude and phase responses of both complex gains can be plotted for a frequency deviation of $\pm 10Hz$:

For the P_1 factor, attenuation increases with the frequency deviation magnitude. However, within a $\pm 2Hz$ range, magnitude remains approximately unity, with maximum attenuation of approximately 99.8% at $\Delta f = 2Hz$. Consequently, for typical power system frequency excursions, P_1 does not affect the magnitude of X_0, as shown in Eq.(B-15). Nevertheless, within the same deviation range, the phase angle P_1 varies linearly, introducing a phase shift to the resultant phasor requiring consideration.

For the Q1 factor, conclusions differ somewhat. First, its magnitude exhibits approximately linear variation, increasing proportionally with frequency deviation. Second, it introduces larger phase shifts than the P1 factor, with 15-degree phase angle at nominal frequency varying linearly. Finally, despite small magnitude values, the Q1 factor cannot be neglected like its counterpart. Indeed, complex gain Q1, having frequency near the second harmonic, introduces oscillations at angular velocity $2\omega_0$ rad/s affecting both magnitude and phase angle of phasors P1X1. The figure depicts these oscillation amplitudes. For example, merely 0.5Hz frequency deviation introduces ripple amplitude of 0.0042p.u., corresponding to 0.0084p.u. peak-to-peak, on resultant phasor X0, while P1 factor effects remain insignificant.

In the end, consider a +1Hz frequency deviation example to illustrate sampling rate effects on complex gains P1 and Q1. Plotting magnitude and phase angle as functions of sample count N reveals: The figure demonstrates that P1 remains relatively unaffected by sampling rate, although phase angle exhibits slight increase with increasing rate. However, introduced variations are on the millidegree order

across wide sampling rate ranges, indicating phase shift remains essentially constant regardless frequency. Conversely, the Q1 factor displays considerably greater sensitivity to sampling frequency, through exclusively regarding phase angle.

C. APPENDIX C (MODIFIED COVARIANCE METHOD (MCM))

It was demonstrated in appendix C that the best forward predictor for an AR(p) process is

$$\hat{x}[n] \; = \; -\sum_{k=1}^{p} a[k] \; x(n - \; k) \qquad (C.1)$$

The optimal backward prediction, however, is

$$\hat{x}[n] \; = \; -\sum_{k=1}^{p} a^{*}\,[k]\, x(n + \; k) \qquad (C.2)$$

where the AR filter parameters are represented by the $a[k]$. The white noise variance σ^2 is the minimum prediction error power in either scenario. By reducing the average of the estimated forward and backward prediction error powers, the modified covariance approach calculates the AR parameters,

$$\hat{\rho} \; = \; \frac{1}{2} \, (\hat{\rho}^{f} \; + \; \hat{\rho}^{b}) \qquad (C.3)$$

Where:

$$\hat{\rho}^{f} \; = \; \frac{1}{N - p} \sum_{n=p}^{N-1} \left| x[n] \; + \sum_{k=1}^{p} a[k] x[n - k] \right|^{2} \qquad (C.4)$$

$$\hat{\rho}^{b} \; = \; \frac{1}{N - p} \sum_{n=0}^{N-1-p} \left| x[n] \; + \sum_{k=1}^{p} a^{*}[k] x[n + k] \right|^{2} \qquad (C.5)$$

The summations are limited to the prediction errors involving observed data samples, just like in the covariance technique. The prediction error power estimate obtained by "flipping the data record around" and complex conjugating it (i.e., letting $\acute{x}[0] = x^{*}[N - 1], \acute{x}[1] = x^{*}[N - 2],$ etc.) and applying a forward predictor to this new data set is known as $\hat{\rho}^{b}$. We have some "extra" data points in this way, which means we have more prediction errors to average. Keep in mind that the range of the summations will cause the forward and backward prediction error estimates for every set of $a[k]$'s to differ slightly. Combining the prediction errors of the forward and backward AR models is also comparable to this process. We can differentiate $\hat{\rho}$ with regard to the real and imaginary parts of $a[k]$ for $k = 1, 2, \ldots, p$ in order to minimize (C.3). As an alternative, we can utilize the complex gradient connection provided as

$$\frac{\partial \hat{\rho}}{\partial a[l]} = \frac{1}{N-p}\left[\sum_{n=p}^{N-1}\left(x[n] + \sum_{k=1}^{p} a[k]\,x[n-k]\right)x^*[n-l] + \sum_{n=0}^{N-1-p}\left(x^*[n] + \sum_{k=1}^{p} a[k]x^*[n+k]\right)x[n+l]\right] \qquad (C.6)$$

= 0 l =1,2,……,p.

After a little simplifying, this becomes

$$\sum_{k=1}^{p} \hat{a}[k]\left(\sum_{n=p}^{N-1} x[n-k]\,x^*[n-l] + \sum_{n=0}^{N-1-p} x^*[n+k]x[n+l]\right) \qquad (C.7)$$

$$= -\left(\sum_{n=p}^{N-1} x[n-k]\,x^*[n-l] + \sum_{n=0}^{N-1-p} x^*[n+k]x[n+l]\right)$$

For l= 1, 2, …., p. Letting.

$$c_{xx}[j,k] = \frac{1}{2(N-p)}\left(\sum_{n=p}^{N-1} x^*[n-j]x[n-k] + \sum_{n=0}^{N-1-p} x[n+j]\,x^*[n+k]\right) \qquad (C.8)$$

The equation (C.7) is writing as identical matrix form as

$$\begin{bmatrix} c_{xx}[1,1] & c_{xx}[1,2] & \dots & c_{xx}[1,p] \\ c_{xx}[2,1] & c_{xx}[2,2] & \dots & c_{xx}[2,p] \\ \vdots & \vdots & \ddots & \vdots \\ c_{xx}[p,1] & c_{xx}[p,2] & \dots & c_{xx}[p,p] \end{bmatrix}\begin{bmatrix} \hat{a}[1] \\ \hat{a}[2] \\ \vdots \\ \hat{a}[p] \end{bmatrix} = -\begin{bmatrix} c_{xx}[1,0] \\ c_{xx}[2,0] \\ \vdots \\ c_{xx}[p,0] \end{bmatrix} \qquad (C.9)$$

The white noise variance estimate is

$$\hat{\sigma}^2 = \hat{\rho}_{MIN} = \frac{1}{2(N-p)}\left[\sum_{n=p}^{N-1}\left(x[n] + \sum_{k=1}^{p} \hat{a}[k]\,x[n-k]\right)x^*[n] + \sum_{n=0}^{N-1-p}\left(x^*[n] + \sum_{k=1}^{p} \hat{a}[k]x^*[n+k]\right)x[n]\right]$$

Finally (C.6) is

$$\hat{a}^2 = c_{xx}[0,0] + \sum_{k=1}^{p} \hat{a}[k]\, c_{xx}[0,k] \qquad (C.10)$$

where (C.8) defines $c_{xx}[j,k]$. The definition of $c_{xx}[j,k]$, the autocorrelation estimator, is the only difference between the modified covariance technique and the covariance method. The linear equations can be solved using the Cholesky decomposition since the matrix in (C.9) is hermitian ($c_{xx}[j,k] = c_{xx}{}^{*}[j,k]$) and positive definite (except from the pure sinusoid case). The improved covariance approach is implemented by a computer program called COVMCOV. The unique structure of the equations is exploited in a more computationally efficient method of solving the equations devised by Marple [1980]. Similar to the covariance technique, data with *p - 1* or fewer sinusoids will result in a singular matrix. Perfect frequency estimates for *p* sinusoids can be obtained using the modified covariance approach. Although the predicted poles typically lie inside the unit circle in practice, the modified covariance technique does not ensure a reliable all-pole filter. Nuttall [1976] first presented the forward-backward method for estimating AR parameters, and Ulrych and Clayton [1976] independently proposed the least squares methodology.

High-resolution, statistically stable spectral estimates seem to be produced by the modified covariance approach [Nuttall 1976, Kay 1983, Shon and Mehrota 1984]. Computer simulations have revealed several desired characteristics of the estimator for data that consists of sinusoids in white noise. Compared to many other AR spectral estimators, the typical movement of an AR spectral estimate's peaks from the actual frequency positions caused by additive observation noise seems to be less noticeable [Swingler 1979A]. Additionally, there is a significant decrease in the peak position dependency on the beginning sinusoidal phase [Chen and Stegen 1974] [Ulrych and Clayton 1976]. The modified covariance approach [Kay and Marple 1979, Marple 1980] has never shown spectral line splitting, when a single sinusoidal component gives rise to two different spectral peaks [Fougere et al. 1976, Herring 1980]. Section 7.10 gives examples of spectral estimation performance for nonsinusoidal processes.

References

1. Phadke, A.G. and J.S. Thorp, Computer relaying for power systems. 2009: John Wiley & Sons.
2. Jia, T., L. Yao, and G. Yang, A new fault location method for high-voltage transmission lines based on ICEEMDAN-MSA-ConvGRU model. IET Generation, Transmission & Distribution, 2024. 18(16): p. 2650-2668.
3. Parpaei, M., H.A. Abyaneh, and F. Razavi, An innovative method to eliminate multiple exponentially decaying DC components based on the discrete Fourier transform in the numerical distance relay. IET Generation, Transmission & Distribution, 2022. 16(18): p. 3617-3635.
4. Vlahinić, S., D. Brnobić, and D. Vučetić, Measurement and analysis of harmonic distortion in power distribution systems. Electric Power Systems Research, 2009. 79(7): p. 1121-1126.
5. Altintasi, C., et al., Power system harmonic and interharmonic estimation using Vortex Search Algorithm. Electric Power Systems Research, 2020. 182: p. 106187.
6. Ghafari, C., Innovative numerical protection relay design on the basis of Sampled Measured Values for Smart Grids. 2016, Université Grenoble Alpes.
7. Rana, M.M., Least mean square fourth based microgrid state estimation algorithm using the internet of things technology. PloS one, 2017. 12(5): p. e0176099.
8. Riahinia, S., et al. Recursive Least-Square-Based Parameter Estimation for Dynamic State Estimation in Power Grids. in 2023 IEEE 2nd Industrial Electronics Society Annual On-Line Conference (ONCON). 2023. IEEE.
9. Silva, K.M. and B.F. Küsel. Phasor estimation using a modified sine filter combined with an adaptive mimic filter. in International Conference on Power Systems Transients. 2011.
10. Ogar, V.N., Modelling of a protective scheme for AC 330 kV transmission line in Nigeria. 2023, University of Glasgow.
11. Daang, J.A.M., A.M. Omas-as, and E.R. Arboleda, Advancements in Fault Detection Techniques for Transmission Lines: A Literature Review. 2024.
12. Arboleda, E.R., J.A.M. Daang, and A.M. Omas-as, Advancements in Fault Detection Techniques for Transmission Lines: A. 2024.
13. Vannesjö, A., Using DFT-Based Filter Topologies for High Power Transformer Analysis: Theoretical and Experimental Assessment of Windowing Techniques in DFT-Based Filters. 2025.
14. Ray, P.K., et al., Detection of faults in a power system using wavelet transform and independent component analysis, in Computer, Communication and Electrical Technology. 2017, CRC Press. p. 227-231.
15. Charfi, F., K. Haddad, and B. Francois. Power system fault monitoring using wavelet transform. in 2004 IEEE 35th Annual Power Electronics Specialists Conference (IEEE Cat. No. 04CH37551). 2004. IEEE.
16. Ahmed, N., et al., Fault detection through discrete wavelet transform in overhead power transmission lines. Energy Science & Engineering, 2023. 11(11): p. 4181-4197.
17. Mohd Amiruddin, A.A.A., et al., Neural network applications in fault diagnosis and detection: an overview of implementations in engineering-related systems. Neural Computing and Applications, 2020. 32(2): p. 447-472.
18. Heo, S. and J.H. Lee, Fault detection and classification using artificial neural networks. IFAC-PapersOnLine, 2018. 51(18): p. 470-475.

19. Muthamizhan, T., M. Aijaz, and D.C. Sekhar, Wavelet-ANN based detection of fault location of hybrid renewable energy sources connected power transmission system. International Journal of Renewable Energy Research (IJRER), 2024. 14(3): p. 551-562.
20. Shekar, S.C. and S.R. Salkuti, Wavelet-ANN Based Detection of Fault Location of Renewable Energy Sources Integrated Power Transmission System, in Energy and Environmental Aspects of Emerging Technologies for Smart Grid. 2024, Springer. p. 599-627.
21. Karmacharya, I.M. and R. Gokaraju, Fault location in ungrounded photovoltaic system using wavelets and ANN. IEEE Transactions on Power Delivery, 2017. 33(2): p. 549-559.
22. Singh, S.V.P., et al., Fault detection and classification using wavelet and ANN in DFIG and TCSC connected transmission line. arXiv preprint arXiv:2308.09046, 2023.
23. Ankar, S. and A. Yadav. Wavelet-ANN based fault location scheme for bipolar CSC-based HVDC transmission system. in 2020 First International Conference on Power, Control and Computing Technologies (ICPC2T). 2020. IEEE.
24. Morais, A., et al., Numerical distance relaying algorithm based on Mathematical Morphology and Least-Squares Curve Fitting method. Electric power systems research, 2011. 81(5): p. 1144-1150.
25. Narang, J.K. and B. Bag. Detection of cyber-attacks in smart power transmission system using mathematical morphology and autoencoder. in 2022 2nd Asian Conference on Innovation in Technology (ASIANCON). 2022. IEEE.
26. Wu, Q.-H., Z. Lu, and T. Ji, Protective relaying of power systems using mathematical morphology. 2009: Springer.
27. Marz, M.B. Interharmonics: What they are, Where they come from and What they do. in Minnesota Power Syst. Conf. Pap. 2016.
28. Chen, L., et al., An interharmonic phasor and frequency estimator for subsynchronous oscillation identification and monitoring. IEEE Transactions on Instrumentation and Measurement, 2018. 68(6): p. 1714-1723.
29. Xiang, P., et al., A Phasor Estimation Algorithm Based on Iterative Filtering to Remove the Decaying Direct Current Component. IEEE Access, 2024.
30. Dam, H.H., et al., Iterative method for the design of DFT filter bank. IEEE Transactions on Circuits and Systems II: Express Briefs, 2004. 51(11): p. 581-586.
31. Mojiri, M., M. Karimi-Ghartemani, and A. Bakhshai, Estimation of power system frequency using an adaptive notch filter. IEEE transactions on instrumentation and measurement, 2007. 56(6): p. 2470-2477.
32. Vazquez, J., et al., Phasor Estimation of Transient Electrical Signals Composed of Harmonics and Interharmonics. Energies, 2021. 14(16): p. 5166.
33. Venkata, S., et al., Computer-aided relay protection coordination. 1988, Electric Power Research Inst., Palo Alto, CA (USA); Washington Univ ….
34. Udren, E. and M. Sackin, Relaying features of an integrated microprocessor-based substation control and protection system. Development in Power System Protection, 1980: p. 97-101.
35. Phadke, A. Digital Protection Techniques and Substation Functions. in Cigré Symposium. 1989.
36. Kezunovic, M., Digital protective relaying algorithms and systems—an overview. Electric Power Systems Research, 1981. 4(3): p. 167-180.
37. STEINllETZ, C.P., COMPLEX QUANTITIES AND THEIR USE IN ELECTRICAL ENGINEERING. 1893.
38. Lawrenz, F. and N. Kipnis, Hands-on history of physics. Journal of Science Teacher Education, 1990. 1(3): p. 54-59.
39. Fourier, J.B.J., Théorie analytique de la chaleur. 1888: Gauthier-Villars et fils.
40. Yalla, M.V., Method and system for providing protective relay functions. 1997, Google Patents.

41. Wang, L., Frequency responses of phasor-based microprocessor relaying algorithms. IEEE Transactions on power delivery, 1999. 14(1): p. 98-109.
42. Sachdev, M. and M. Nagpal, A recursive least error squares algorithm for power system relaying and measurement applications. IEEE Transactions on Power Delivery, 2002. 6(3): p. 1008-1015.
43. Schweitzer, E.O. and D. Hou. Filtering for protective relays. in IEEE WESCANEX 93 Communications, Computers and Power in the Modern Environment-Conference Proceedings. 1993. IEEE.
44. Holtbecker, H., Testing philosophy and simulation techniques. Nuclear Engineering and Design, 1977. 42(1): p. 75-87.
45. Sanders, M.P., Protective Relaying: Principles and Applications [Book Reviews]. IEEE Power and Energy Magazine, 2015. 13(5): p. 89-90.
46. Carpentieri, L. and M. Guenego, CT/VT for Fusion project. User's manual. Characteristics. Technical report, 07 2013.
47. Poberezhskiy, Y. and G. Poberezhskiy, Signal digitization and reconstruction in digital radios. 2018: Artech House.
48. Su, K.L., Analog filters. 2012: Springer Science & Business Media.
49. Bennett, W.R., Spectra of quantized signals. The Bell System Technical Journal, 1948. 27(3): p. 446-472.
50. Hauser, M.W., Principles of oversampling A/D conversion. Journal of the Audio Engineering Society, 1991. 39(1/2): p. 3-26.
51. D'Antona, G. and A. Ferrero, Architecture and Performance of DSP-Based Instruments. Digital Signal Processing for Measurement Systems: Theory and Applications, 2006: p. 83-113.
52. Vaseghi, S.V., Multimedia signal processing: theory and applications in speech, music and communications. 2007: John Wiley & Sons.
53. Tierney, D., et al. Performance of generator protection relays during off-nominal frequency operation. in 2014 67th Annual Conference for Protective Relay Engineers. 2014. IEEE.
54. Benmouyal, G., An adaptive sampling-interval generator for digital relaying. IEEE Transactions on Power Delivery, 2002. 4(3): p. 1602-1609.
55. Benmouyal, G., E. Schweitzer, and A. Guzmán. Synchronized phasor measurement in protective relays for protection, control, and analysis of electric power systems. in 57th Annual Conference for Protective Relay Engineers, 2004. 2004. IEEE.
56. Benmouyal, G., System and method for exact compensation of fundamental phasors. 2005, Google Patents.
57. Robinson, P. Reliability considerations of overspeed protection for turbine generators. in IEE Colloquium on Case Studies in Industrial Control. 1990. IET.
58. Morrow, D., B. Fox, and P. Toner. Low-cost under-frequency relay for distributed load shedding. in 1991 Third International Conference on Power System Monitoring and Control. 1991. IET.
59. Akke, M., Frequency estimation by demodulation of two complex signals. IEEE Transactions on Power Delivery, 2002. 12(1): p. 157-163.
60. Phadke, A.G., J.S. Thorp, and M.G. Adamiak, A new measurement technique for tracking voltage phasors, local system frequency, and rate of change of frequency. IEEE transactions on power apparatus and systems, 2007(5): p. 1025-1038.
61. Girgis, A.A. and W.L. Peterson, Adaptive estimation of power system frequency deviation and its rate of change for calculating sudden power system overloads. IEEE Transactions on Power Delivery, 2002. 5(2): p. 585-594.
62. Begovic, M.M., et al., Frequency tracking in power networks in the presence of harmonics. IEEE Transactions on Power Delivery, 1993. 8(2): p. 480-486.

63. Giray, M. and M. Sachdev, Off-nominal frequency measurements in electric power systems. IEEE Power Engineering Review, 2007. 9(7): p. 42-43.
64. Kasztenny, B. A new method for fast frequency measurement for protection applications. in 13th International Conference on Developments in Power System Protection. 2016.
65. Ristic, M., I. Voloh, and Z. Zhang. How frequency measurements can impact security of frequency elements in digital relays. in 2011 64th Annual Conference for Protective Relay Engineers. 2011. IEEE.
66. Sachdev, M.S. and R. Das, Understanding microprocessor-based technology applied to relaying. Report of Working Group I-01 of the Relaying Practices Subcommittee, 2009: p. 1-79.
67. Phadke, A.G. and J.S. Thorp, Phasor estimation at off-nominal frequency inputs, in Synchronized phasor measurements and their applications. 2017, Springer. p. 47-72.
68. Phadke, A.G. Synchronized phasor measurements-a historical overview. in IEEE/PES transmission and distribution conference and exhibition. 2002. IEEE.
69. Phadke, A., J. Thorp, and K. Karimi, State estimationwith phasor measurements. Power Systems, IEEE Transactions on: p. 233-238.
70. Phadke, A.G., Synchronized phasor measurements in power systems. IEEE Computer Applications in power, 2002. 6(2): p. 10-15.
71. Phadke, A. and J. Thorp. History and applications of phasor measurements. in 2006 IEEE PES Power Systems Conference and Exposition. 2006. IEEE.
72. Phadke, A., et al., Synchronized sampling and phasor measurements for relaying and control. IEEE Transactions on Power Delivery, 1994. 9(1): p. 442-452.
73. Adamiak, M., et al., Wide area protection—Technology and infrastructures. IEEE Transactions on Power Delivery, 2006. 21(2): p. 601-609.
74. Martin, K.E., et al., IEEE standard for synchrophasors for power systems. IEEE Transactions on Power Delivery, 1998. 13(1): p. 73-77.
75. Andersson, G., et al., Causes of the 2003 major grid blackouts in North America and Europe, and recommended means to improve system dynamic performance. IEEE transactions on Power Systems, 2005. 20(4): p. 1922-1928.
76. Moraes, R.M., et al., PMU interoperability, steady-state and dynamic performance tests. IEEE Transactions on Smart Grid, 2012. 3(4): p. 1660-1669.
77. Usman, M.U. and M.O. Faruque, Applications of synchrophasor technologies in power systems. Journal of Modern Power Systems and Clean Energy, 2019. 7(2): p. 211-226.
78. Martin, K.E., Synchrophasor measurements under the IEEE standard C37. 118.1-2011 with amendment C37. 118.1 a. IEEE Transactions on Power Delivery, 2015. 30(3): p. 1514-1522.
79. Frazao, R.J.A., PMU based situation awareness for smart distribution grids. 2015, Université Grenoble Alpes.
80. Relays, M., Measuring Relays and Protection Equipment—Part 118-1: Synchrophasor for Power Systems—Measurements. IEEE Standard, 2018: p. 60255-118.
81. Phadke, A., et al., The wide world of wide-area measurement. IEEE Power and Energy Magazine, 2008. 6(5): p. 52-65.
82. Terzija, V., et al., Wide-area monitoring, protection, and control of future electric power networks. Proceedings of the IEEE, 2010. 99(1): p. 80-93.
83. Fadiran, J., S. Chowdhury, and S. Chowdhury. A multi-criteria optimal phasor measurement unit placement for multiple applications. in 2013 IEEE Power & Energy Society General Meeting. 2013. IEEE.
84. Salehi, A., et al., Developing an optimal framework for PMU placement based on active distribution system state estimation considering cost-worth analysis. IEEE Access, 2023. 11: p. 12088-12099.

85. Kasztenny, B., W. Premerlani, and M. Adamiak. Synchrophasor Algorithm Allowing Seamless Integration with Today's Relays. in 2008 IET 9th International Conference on Developments in Power System Protection (DPSP 2008). 2008. IET.
86. De La Ree, J., et al., Synchronized phasor measurement applications in power systems. IEEE Transactions on smart grid, 2010. 1(1): p. 20-27.
87. Dotta, D., et al. A matlab-based PMU simulator. in 2013 IEEE Power & Energy Society General Meeting. 2013. IEEE.
88. Benco, J.P., et al., Generator protection system and method for phasor estimation and frequency tracking during frequency ramping. 1998, Google Patents.
89. Nguyen, T. and X. Li. A fast and accurate method for estimating power systems phasors using DFT with interpolation. in 2006 IEEE Power Engineering Society General Meeting. 2006. IEEE.
90. Harris, F.J., On the use of windows for harmonic analysis with the discrete Fourier transform. Proceedings of the IEEE, 2005. 66(1): p. 51-83.
91. Jain, V.K., W.L. Collins, and D.C. Davis, High-accuracy analog measurements via interpolated FFT. IEEE Transactions on Instrumentation and Measurement, 2007. 28(2): p. 113-122.
92. Grandke, T., Interpolation algorithms for discrete Fourier transforms of weighted signals. IEEE transactions on instrumentation and measurement, 2007. 32(2): p. 350-355.
93. Belega, D. and D. Petri. Accuracy of the synchrophasor estimator provided by the interpolated DFT algorithm. in 2012 IEEE International Instrumentation and Measurement Technology Conference Proceedings. 2012. IEEE.
94. Belega, D. and D. Petri, Accuracy analysis of the multicycle synchrophasor estimator provided by the interpolated DFT algorithm. IEEE Transactions on Instrumentation and Measurement, 2013. 62(5): p. 942-953.
95. Belega, D., D. Macii, and D. Petri, Fast synchrophasor estimation by means of frequency-domain and time-domain algorithms. IEEE Transactions on Instrumentation and Measurement, 2013. 63(2): p. 388-401.
96. Kay, S.M., Modern spectral estimation. 1988: Pearson Education India.
97. Vaseghi, S.V., Advanced digital signal processing and noise reduction. 2008: John Wiley & Sons.
98. Abed, A., et al. Efficiency of post-processing in PMU based state estimation of renewable energy microgrids. in 2023 IEEE Belgrade PowerTech. 2023. IEEE.
99. Alwan, N. and V. Papic, Phasor Estimation of Transient Electrical Signals Using Modified Covariance Enhanced Cleaned Characteristic Harmonic Filtering in Protection Relay. Energies, 2026. 19(3): p. 711.
100. Djurišić, Ž.R., M.B. Djurić, and V.D. Papić, An algorithm for three-phase power system frequency measurement. Electrical Engineering, 2024. 106(4): p. 4591-4602.
101. Đurišić, Ž. and V. Papić, Power system frequency tracking based on LES technique with constant matrix. Measurement, 2018. 114: p. 308-321.

Biography

NATHEER AHMED ALWAN was born on March 07, 1981, in Mosul – Iraq. He finished elementary and high school in 2001 in Mosul. And in 2001, he enrolled the Faculty of Science at the University of Technology in Baghdad, where he received a Bachelor's degree in Electrical Engineering from Technical Education department in 2005. Then He enrolled the Master studies in 2015, in the department of Electrical and Electronics at the School of Electrical Engineering, University of Turkish Aeronautical Association, he graduated with an overall average score of 8.8, where he defended his Master's thesis on October 25, 2017, entitled "Effect of Flexible AC Transmission System (FACTS) Devices on Distance Relay Performance in a Transmission line" under the mentorship of Prof.Dr. Doğan ÇALIKOĞLU. Later Mr. ALWAN enrolled in doctoral studies at the Department of Electrical Engineering and Computing, School of Electrical Engineering, Belgrade University, in 2021-2026, he is a third-year Ph.D. student and passed all exams with a grade point average of 9.71.

The candidate has developed his experience in a variety of technical tools, including AutoCAD, MATLAB, Multisim, and Visio, as well as proficiency in Microsoft Office applications such as Word, Access, Excel, and PowerPoint. Additionally, the candidate has a solid foundation in computer hardware and software maintenance. Throughout his career, He has led multiple critical projects, such as the installation, testing, and operation of 33/11 KV electrical substations in Mosul City, and site supervisor of installation AL Qayyarah Gas power plant(6x125 MW-E9). Also, he worked as a Supervising the rehabilitation ALQAYYARAH Gas Power Plant which executed by USA .GE. company (General Electric Company).

Publications:

1. Abed, Amir, Natheer Alwan, Munther H. Abed, and Goran Dobric. "Efficiency of post-processing in PMU based state estimation of renewable energy microgrids." In 2023 IEEE Belgrade PowerTech, pp. 01-06. IEEE, 2023. doi: 10.1109/PowerTech55446.2023.10202834.
2. Alwan, Natheer, and Veljko Papic. 2026. "Phasor Estimation of Transient Electrical Signals Using Modified Covariance Enhanced Cleaned Characteristic Harmonic Filtering in Protection Relay" Energies 19, no. 3: 711. https://doi.org/10.3390/en1903071.
3. Alwan, Natheer, and Veljko Papic "Evaluation the Modified Covariance Method Performance with Cleaning Characteristic Harmonic Digital Filter in Protection Relay" ETRAN Conference, Silver Lake, Serbia, June.2026.

Изјава о ауторству

Име и презиме аутора Назир Алван (Natheer Ahmed Alwan)

Број индекса 2021/5049

Изјављујем

да је докторска дисертација под насловом

Естимација фазора у релејној заштити коришћењем модификоване коваријантне методе

- резултат сопственог истраживачког рада;
- да дисертација у целини ни у деловима није била предложена за стицање друге дипломе према студијским програмима других високошколских установа;
- да су резултати коректно наведени и
- да нисам кршио/ла ауторска права и користио/ла интелектуалну својину других лица.

Потпис аутора

У Београду, _____

_____

образац изјаве о истоветности штампане и електронске верзије докторског рада

Изјава о истоветности штампане и електронске верзије докторског рада

Име и презиме аутора _____Назир Алван (Natheer Ahmed Alwan)_____

Број индекса _____2021/5049_____

Студијски програм _____Докторске академске студије_____

Наслов рада __Естимација фазора у релејној заштити коришћењем модификоване коваријантне методе

Ментор _____др Вељко Папић_____

Предложени ментор:

__др Вељко Папић, ванредни професор

Изјављујем да је штампана верзија мог докторског рада истоветна електронској верзији коју сам предао/ла ради похрањивања у **Дигиталном репозиторијуму Универзитета у Београду.**

Дозвољавам да се објаве моји лични подаци везани за добијање академског назива доктора наука, као што су име и презиме, година и место рођења и датум одбране рада.

Ови лични подаци могу се објавити на мрежним страницама дигиталне библиотеке, у електронском каталогу и у публикацијама Универзитета у Београду.

Потпис аутора

У Београду, _____

_____

образац изјаве о коришћењу

Изјава о коришћењу

Овлашћујем Универзитетску библиотеку „Светозар Марковић“ да у Дигитални репозиторијум Универзитета у Београду унесе моју докторску дисертацију под насловом:

“Естимација фазора у релејној заштити коришћењем модификоване коваријантне методе”

која је моје ауторско дело.

Дисертацију са свим прилозима предао/ла сам у електронском формату погодном за трајно архивирање.
Моју докторску дисертацију похрањену у Дигиталном репозиторијуму Универзитета у Београду и доступну у отвореном приступу могу да користе сви који поштују одредбе садржане у одабраном типу лиценце Креативне заједнице (Creative Commons) за коју сам се одлучио/ла.

1. Ауторство (CCBY)
2. Ауторство – некомерцијално (CCBY-NC)
3. Ауторство – некомерцијално – без прерада (CCBY-NC-ND)
4. Ауторство – некомерцијално – делити под истим условима (CCBY-NC-SA)
5. Ауторство – без прерада (CCBY-ND)
6. Ауторство – делити под истим условима (CCBY-SA)

(Молимо да заокружите само једну од шест понуђених лиценци.
Кратак опис лиценци је саставни део ове изјаве).

Потпис аутора

У Београду, _____